New perspectives on thermal and hyperthermal oxidation of Si surfaces

Proefschrift voorgelegd tot het behalen van
de graad van doctor in de Wetenschappen aan
de Universiteit Antwerpen te verdedigen door

Umedjon Khalilov

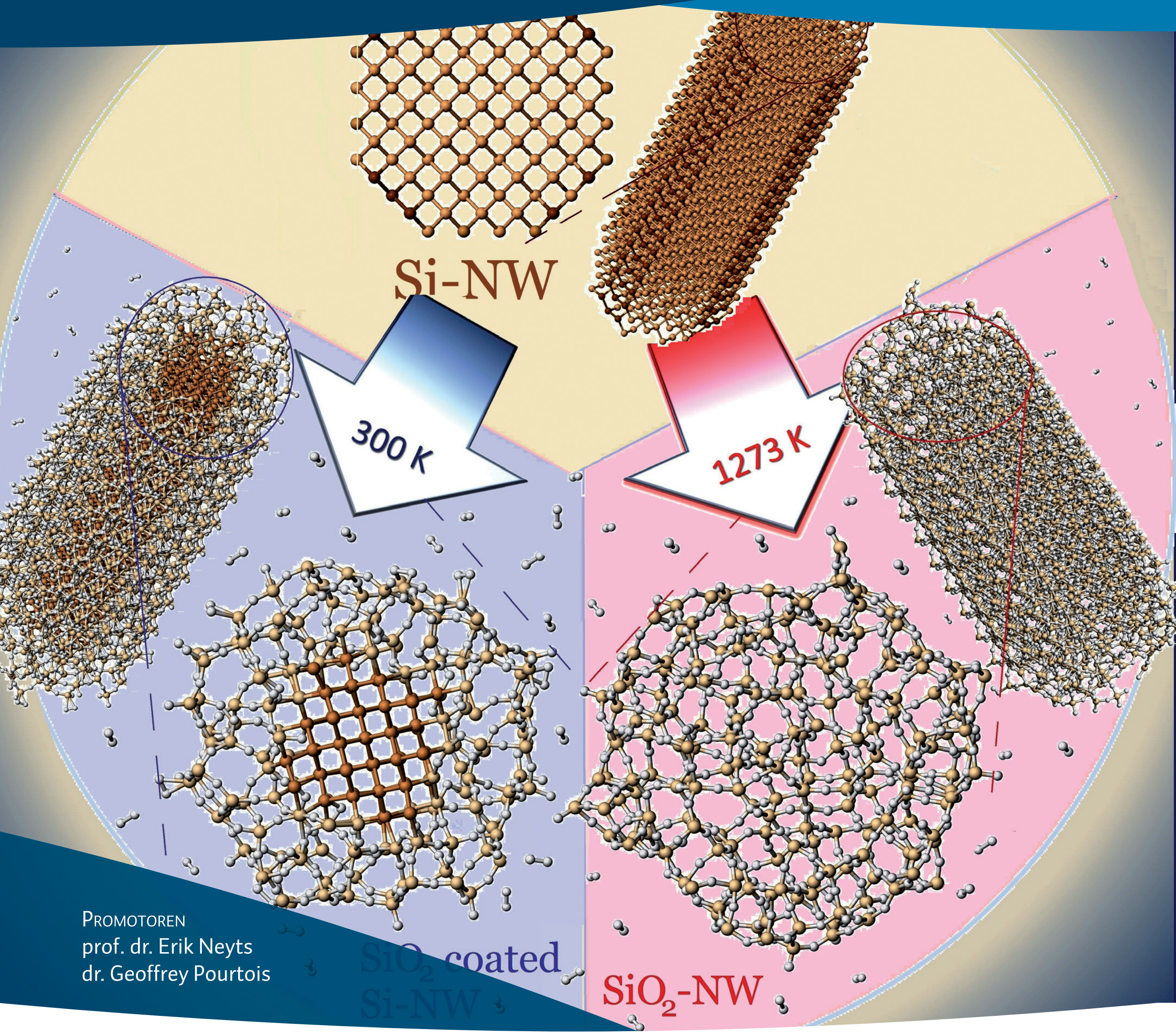

Promotoren
prof. dr. Erik Neyts
dr. Geoffrey Pourtois

Faculteit Wetenschappen
Departement Scheikunde
Antwerpen 2013

Universiteit
Antwerpen

Faculteit Wetenschappen

Departement Chemie

New perspectives on thermal and hyperthermal oxidation of Si surfaces

Nieuwe perspectieven in thermische en hyperthermische oxidatie van Si oppervlakken

Proefschrift voorgelegd tot het behalen van de graad van doctor in de Wetenschappen aan de Universiteit Antwerpen te verdedigen door

Umedjon KHALILOV

Promotor: Prof. Dr. Erik NEYTS

Co-promotor: Dr. Geoffrey POURTOIS

Antwerpen, 2013

Contents

II RESULTS AND DISCUSSIONS

a. Hyperthermal oxidation of Si surfaces:

b. Thermal oxidation of small Si-NWs:

III SUMMARY – SAMENVATTING

Acknowledgements

Apart from my own efforts, the success of this project is also due to the encouragement and guidance of many others, whom I have worked with in my scientific life. This research work would not have been possible without their help and support. It gives me great pleasure to expressing my gratitude to all those people.

First of all, I would like to express my greatest thanks to my supervisor, Prof. Dr. Erik Neyts. He taugh me everything in detail, also when he had a very busy schedule. Erik, I can honestly say that your behaviour is an excellent example for me. Heartfelt thanks for your patience, careful attention for detail and friendly support as well as for your belief in me!

Utmost gratitude go to my second supervisor, Dr. Geoffrey Pourtois. His many useful (scientific) advices always helped me. He shared his knowledge, his ideas, and numerous tips all of which culminated in the completion of this work. Geoffrey, thank you very much! Also, the Interuniversity Microelectronics Centre (IMEC) is acknowledged for the financial support.

I would also like to express my deep respect and great appreciation to Prof. Dr. Annemie Bogaerts, head of research group PLASMANT. Annemie, I feel proud that I could be a member of your research group. I learnt many nice things from you. *Hartelijk bedankt voor uw ontelbare momenten van hulp en vriendelijke ondersteuning*!

During my PhD period, I also spend an interesting time with my groupmates Stefan, David, Maksudbek, Wesley, Maryam, Péter, Stijn, Robby, Mujahid, Christophe, Stefaan, Wouter van G., Wouter W., as well as Ramses, Johan, Koen and Marieke. I had great pleasure working with you! *Maksudbek, do'stona yordamlaringizdan behad minnatdorman!* I would also like to express my thanks to former PLASMANT members: Maxie, Ming, Shuxia, Steluta, Helmut, Tom, Violeta, Fujun, Axel, Evi, Asliddin, Neyda and others, who I forgot to mention, for their friendly advices and help.

Special thanks should be given to Luc Van't dack for adminstrative and technical support. He as well as David Roet are acknowledged for setting up FistUA and making computational research easier and faster.

It is also my pleasure to thank Nelly Suijkerbuijk for taking care of all non-scientific tasks.

I also acknowledge the Turing HPC infrastructure at the CalcUA core facility of the Universiteit Antwerpen (UA), a division of the Flemish Supercomputer Center VSC, funded by the Hercules Foundation, the Flemish Government (department EWI) and the UA for calculation support.

I also wish to express my sincere gratitude to Prof. Dr. A. C. T. van Duin for sharing his ReaxFF code, which I used for all my Molecular Dynamics calculations applied in this work. Utmost thanks also for interesting discussions and fruitfull advices as well as the nice co-operation.

I would also like to show my greatest appreciation to Prof. Dr. Abdiravuf Dzhurakhalov for his sincere advices and nice recommendations, which gave me the opportunity to get into contact with the PLASMANT group. *Mening muvaffaqiyatlarim sizning sa'yi harakatlaringiz mahsulidir. Katta raxmat!*

Furthermore, I would also like to thank my teachers, friends and previous collegues. In particular, special thanks to Prof. Dr. Nazar Turaev, Dr. Hotam Ashurov and Dr. Flura Jurabekova for supportive guidance and kindly advices. Also, my sincere thanks go to my friend Dr. Golibjon Berdiyorov for his friendly support as well as useful ideas.

Most importantly, I am forever indebted to my beloved parents, Boymamat Uljaev and Norxoloy Boboniyozova, for their blessings, support and encouragements in every step of my life. I am very much indebted to my family, my wife Dilfuza and daugthers Dildora, Dinora and Soliha for their understanding, endless patience and encouragement when it was most required.

Umedjon Khalilov,
January 2013

Part I

BACKGROUND

Chapter 1

Si & SiO_2 and their application

1.1 Silicon and its oxide

1.1.1 Silicon manufacture

Silicon (Si) is the eighth most common element in the universe by mass, but very rarely occurs as the pure free element in nature. It is most widely distributed in dusts, sands, planetoids, and planets as various forms of silicon dioxide (SiO_2) or silicates. It is a non-toxic material and is possibly the most studied material in the history of mankind [1, 2]. Si is a tetravalent metalloid, less reactive than its chemical analog carbon, the nonmetal directly above it in the periodic table, but more reactive than germanium, the metalloid directly below it in the table. Si is used mainly in the microelectronics industry and thus constitutes a technologically very important material [3]. It is often said that understanding silicon and its role in electronic materials is similar to understanding iron and its role in metallurgy. Especially for the semiconductor technology, its polycrystalline and crystalline forms are of importance, which are produced from its oxide SiO_2. Essentially, the Si production is as follows. First, metallurgical grade (MG) silicon is produced by heating the SiO_2 with carbon (coke) at 2100 K:

$$2C + SiO_2 \rightarrow Si + 2CO \tag{1.1}$$

In the second step, MG silicon is purified through a chemical reaction to produce a silicon-bearing gas of trichlorosilane ($SiHCl_3$)

$$Si + 3HCl \rightarrow SiHCl_3 + H_2 \tag{1.2}$$

Then raw polycrystalline silicon (or semiconductor grade silicon) is created by mixing refined trichlorosilane with hydrogen gas in a reaction furnace at approximately 1400 K and allowing the polycrystalline silicon to grow on the surface of electrically heated tantalum hollow metal wicks:

$$SiHCl_3 + H_2 \rightarrow Si + 3HCl \tag{1.3}$$

Subsequently, the polycrystalline silicon tubes are refined by dissolving them in hydrofluoric acid to produce polysilicon ingots. Because polycrystalline silicon has randomly oriented crystallites, it does not have the electrical characteristics necessary for semiconductor device fabrication. It must first be transformed into *single crystal silicon* using a process called Crystal Pulling, which was invented by the Polish scientist J. Czochralski in 1916. In this process, polysilicon material is melted, held at close to 1415°C, and a single crystal seed is used to start the crystal growth. Although many growth methods are used for producing Si wafers, most wafers used for integrated circuit (IC) technologies are fabricated using the Czochralski (CZ) method [4]. This growth method allows producing large diameter crystals, from which large diameter wafers can be cut.

1.1.2 Si crystal and its (100) surface

Si single crystal is probably the most important technological material of the past decades, that is, the “silicon era” [1, 3]. It is often used in semiconductor device fabrication. The monocrystalline Si is also the key element of solar cells. Si has a diamond-like face centred structure. The unit cell (with a unit cell parameter a = 5.43 Å) of crystalline silicon is cubic as shown in figure 1.1.

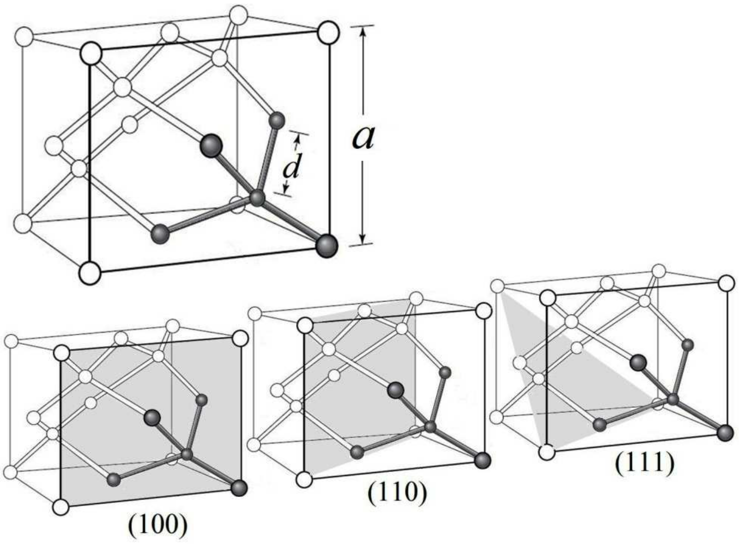

Figure 1.1 *Si single-crystal structure and its tree crystal planes.*

The diamond-like cubic structure of Si consists of two interpenetrating face-centered cubic lattices, with one offset ¼ of a cube along the cube diagonal. It may also be described as face centered cubic lattice in which half of the tetrahedral sites are filled while all the octahedral sites remain vacant. In the crystal, each Si atom has four nearest neighbors. The shortest interatomic distance ($d_{si\text{-}si}$ = 2.35 Å) is determined from the unit cell parameter as $d = \frac{\sqrt{3}}{4}a$. The standard notation for crystal planes is based on the cubic unit cell.

There has been considerable theoretical and experimental interest in the electronic and geometric structure of the silicon surface. Especially the Si(100) surface is of particular importance for microelectronics, because most Si devices are formed on this surface and its reconstructions are simple compared to those of other surfaces as shown in Figure 1.1.

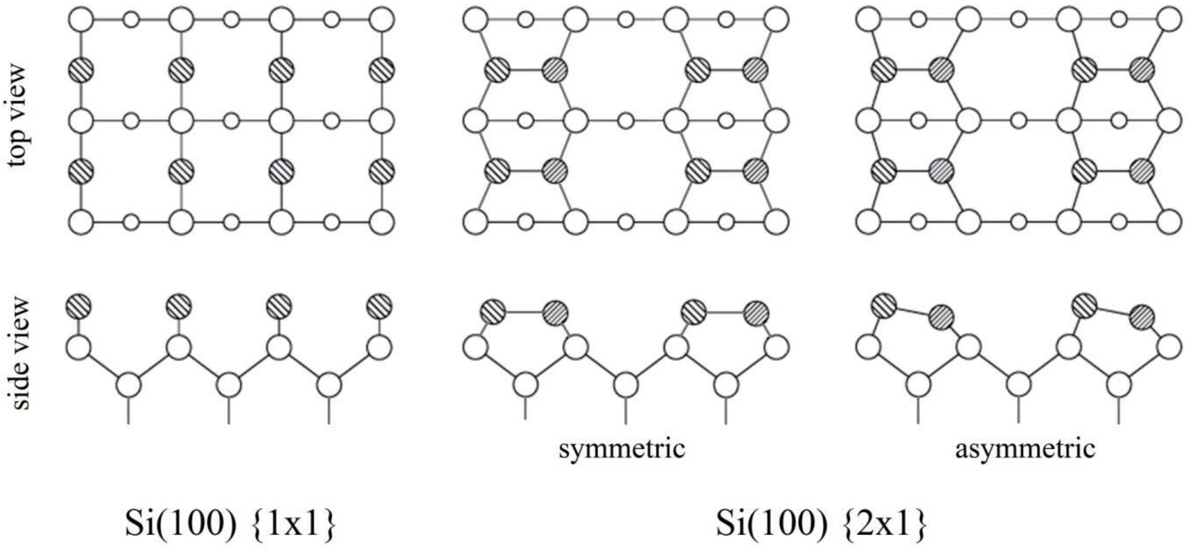

Figure 1.2 *(a) Non-reconstructed (Si(100) {1x1}) and (b) (2x1) reconstructed Si(100) surfaces (Si(100) {2x1}) of Si single-crystal. The Si(100) {2x1} surface is constructed by either symmetrical or asymmetrical oriented Si dimers.*

This surface consists of silicon atoms having two dangling bonds (see figure 1.2). However, low-energy-electron diffraction (LEED), scanning-tunneling-microscopy measurements [5] and He diffraction measurements [6] show that the {1x1} terminated-structure is unstable and reconstructs into either a lower-energy {2x1} or {4x2} structure [7, 8]. In the {2x1} reconstructed Si (100) surface, the energy of surface atoms is lowered considerably by forming Si mutual bond (dimers) [7]. Ramstad et al. [8] reported that the energy difference between ideal {1x1} and reconstructed {2x1} surfaces is about -1.8 eV/dimer. Furthermore, the Si dimers can in the reconstructed surface be positioned as either symmetric or asymmetic, i.e., located parallel or non-parallel to the surface as shown in Figure 1.2 [8, 9]. First-principle calculations showed that, however, the energy difference between the surfaces, which consist of either symmetric or asymmetric dimers is small (-0.12 eV/dimer [8] or -0.02 eV [9]). In this work, the Si (100) {2x1} surface with symmetric dimers was chosen.

1.1.3 Silicon dioxide

Si crystal is a key material for electronic and semiconductor devices. In the silicon industry, however, it would not be the "miracle material" without its oxide SiO_2. Thus, since the rise of the semiconductor technology, from 1970's to the end of the millennium, SiO_2 was also a key material. Several excellent properties of SiO_2 are in a large part responsible for enabling the microelectronics revolution [10], as described below.

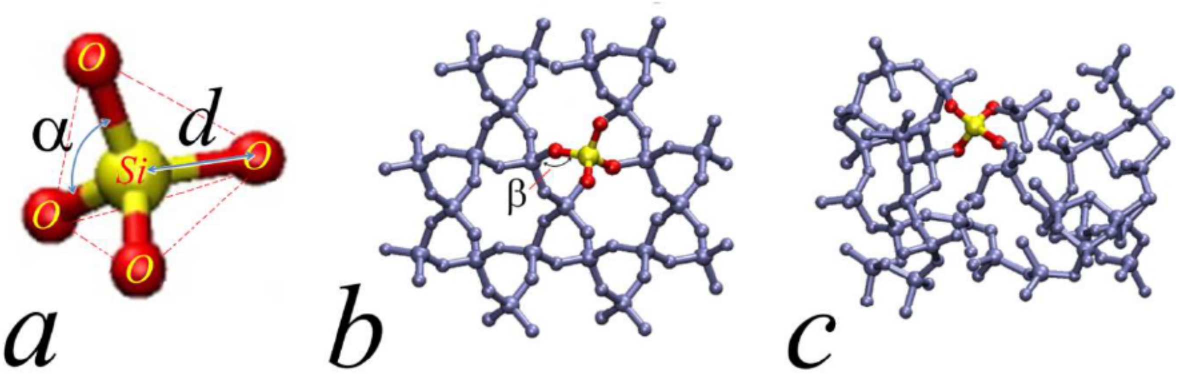

Figure 1.3 *SiO_2 (silica) molecule (a). Silica molecules in the crystalline (b) and amorphous (c) silica structures. The Si-O bond distance is denoted by d, and α and β indicate O-Si-O and Si-O-Si bond angles, respectively.*

Silicon dioxide (SiO_2) is also called silica. As shown in figure 1.3a, a silica (SiO_2) unit has a tetrahedral structure and is rather rigid. Each silicon atom can bind to four oxygen atoms, and this gives rise to a giant covalent network structure in which each Si is bonded to four oxygen atoms and each oxygen atom to two silicon atoms. Due to the strong covalent bond between silicon and oxygen in the tetrahedral structure, silicon dioxide is very hard and rigid and has a very high melting point of about 1700°C [1, 11]. Due to the absence of free electrons in the molecular structure, silicon dioxide is a very bad conductor of electricity, and acts as an insulator. Silica comes in two main forms, i.e., crystalline c-SiO_2 (figure 1.3 b) and amorphous a-SiO_2 (figure 1.3 c). For both cases, the bond distance d between Si and O is about 0.16 nm, but the Si-O-Si (α) and O-Si-O (β) bond angles depend on their structures [12]. In the gaseous state, silicon dioxide forms linear O=Si=O molecules as well.

In nature, silica is commonly found in crystalline form. There are 13 different allotropes of SiO_2 crystals. The physical properties might be different but the chemical properties remain the same, irrespective of the structure. The most common structure, which is stable at room temperature and ambient pressure, is "low quartz" or α-quartz (figure 1.3b). Quartz is used in the glass industry as a raw material for manufacturing glass [11]. It is also used in transducers because of its piezoelectric properties [13]. Furthermore, it is also used for making optical fibers [14]. In addition to quartz, there are many other crystalline forms of silicon dioxide found in nature, under different temperature and pressure conditions. In high temperature conditions, silica is found in the form of tridymite and cristobalite, whereas in regions of high pressure, it is found as seifertite and coesite.

Due to its ability to absorb moisture, silica is used as a desiccant as well. Both crystalline and amorphous silicas are very stable and chemically inert. Therefore, they essentially protect the Si or the whole integrated circuit from rapid deterioration in a chemically hostile environment. Especially a-SiO_2 is commonly used in the IC technology [12, 15].

1.1.4 Amorphous silica

Amorphous silica (a-SiO_2) is a homogeneous and isotropic material, which is mostly used in semiconductor circuits to isolate different conducting regions [3, 16]. The amorphous silica structure (shown in figure 1.3 c), is somewhat different from its crystalline form (c-SiO_2), showing a wide Si-O-Si angle distribution in the range 120° - 180°. The Si-O, O-O, and Si-Si bonds are about 1.6, 2.5, and 3.2 Å, respectively. The silica mass density is somewhat lower (2.2 $g\cdot cm^{-3}$) than the density of c-SiO_2 (> 2.4 $g\cdot cm^{-3}$). It has high resistivity (10^{18} $\Omega\cdot cm$), excellent dielectric strength (10^7 $V\cdot cm$), and large band gap energy (8.9 eV). Also, the thermal expansion coefficient of a-SiO_2 is considerably lower than that of c-SiO_2 [16]. Because of the excellent dielectric (i.e., relative dielectric constant is in the range of 3.7-3.9) and other properties it can be used as a gate oxide in transistors, a dielectric in integrated capacitors, an insulator in computer chips, and so on [17]. It is also relatively easy to structure, i.e. unwanted silica layers can selectively be removed. Moreover, the *a*-SiO_2 is relatively easy to make with several quite different methods, thus allowing a large degree of process freedom. Thanks to thermal oxidation, *a*-SiO_2 is easily grown on *c*-Si wafers with a low defect density interface, even at the nanometer scale [2, 12, 15]. The *a*-SiO_2|*c*-Si structure and its interface are the key investigated subjects in this work.

1.2 Thermal oxidation of planar Si

1.2.1 Dry and wet oxidation

In microfabrication (i.e., fabrication of miniature structures at the micrometer scale) thermal Si oxidation is a way to produce a thin layer of SiO_2 on the Si surface [12]. The SiO_2 is easily grown at high temperatures where the reaction of silicon with oxygen to form SiO_2 is relatively fast. Thermal oxidation of silicon is usually performed in furnaces at a temperature between 800°C and 1200°C. A single furnace accepts many wafers at the same time, in a specially designed quartz rack (called a "boat"). For example, layers of oxide 0.1 μm thick can be grown in about one hour at 1000^oC. As mentioned in the previous section, a low defect density interface between SiO_2 and Si is formed in the oxidation. GaAs and Ge, two other commonly used semiconductors, do not form such high quality, stable oxide layers with an almost perfect interface, making IC fabrication, and especially Metal-Oxide-Semiconductor (MOS) technology, much more difficult when using these materials.

Two process types, called wet and dry oxidation, are widely used in thermal Si oxidation [3, 12]. Thus, the oxidation is performed using either water vapor (usually UHP steam) or molecular oxygen as the oxidant in wet or dry oxidation, respectively. The corresponding oxidation reactions that can occur are:

$$\mathrm{Si\ (s) + 2H_2O\ (g) \rightarrow SiO_2\ (s) + 2H_2\ (g)} \tag{1.4}$$

$$\mathrm{Si\ (s) + O_2\ (g) \rightarrow SiO_2\ (s)} \tag{1.5}$$

The growth rate in wet oxidation is about ten times faster than in dry oxidation and is used for getting thick oxides in the aforementioned temperature range. On the other hand, dry oxidation, which is based on O_2 reacting with the Si surface, is commonly applied to obtain thin oxides. Although the oxide growth is rather slow, it is easily controlled in the dry oxidation process. In this process, the interaction of O with the Si surface is known to depend on temperature, time, and O_2 pressure. Indeed, the oxidation temperature and oxidant pressure can control the adsorption/desorption rate during the oxidation [18, 19]. In the low temperature-high pressure regime, O interaction with the surface results in oxide growth (passive oxidation) [19], while in the high temperature-low pressure regime, surface etching via volatile SiO formation (active oxidation) [18], also known as disproportionation, occurs:

$$2\mathrm{Si}\ (s) + \mathrm{O_2}\ (g) \rightarrow 2\mathrm{SiO}\ (g) \tag{1.6}$$

Furthermore, it has been shown that there is a transition regime in pressure-temperature parameter space between the active and passive oxidation modes, where the surface morphology differs dramatically from that of either region. In particular, the surface becomes very rough in this region whereas under normal active and passive oxidation conditions the surface may remain flat [10, 18-21]. The silica growth mechanism in both wet and dry oxidation is successfully described theoretically by B. E. Deal and A. S. Grove in their so-called “Deal-Grove model” [22].

1.2.2 Deal-Grove model

The formation of an oxide film on Si crystal during thermal oxidation is described by the *Deal-Grove model* [22]. According to this model, the thermal oxide formation process is divided into three steps: (1) the adsorption of an oxidant (assumed to be molecular O_2 or H_2O in the case of dry or wet oxidation, respectively) on the SiO_2 surface; (2) diffusion of the oxidant through the disordered oxide film toward the Si|SiO_2 interface, and finally (3) the reaction of the oxidant at the Si surface to form a new oxide layer. It is assumed that oxidation proceeds by the inward movement of the oxidant rather than by the outward movement of Si atoms.

A schematic representation of the model is shown in figure 1.4a. The oxide formation depends on the fluxes of entering (F_1), diffusing (F_2) and reacting (F_3) oxygen, which can be determined as follows:

$$\begin{aligned} F_1 &= h(C^* - C_o) && \text{(gas transport flux)} \\ F_2 &= D\frac{C_o - C_i}{x} && \text{(diffusion flux)} \\ F_3 &= kC_i && \text{(reaction flux)} \end{aligned} \tag{1.7}$$

where h is the gas-phase transport coefficient, D is the oxidant diffusion coefficient in the oxide with thickness x, and k is the oxidant reaction coefficient at the oxide-silicon interface. C_0, C^* and C_i are the oxidant concentration at outer surface of the oxide, in equilibrium in the oxide, and at the oxide-silicon interface, respectively.

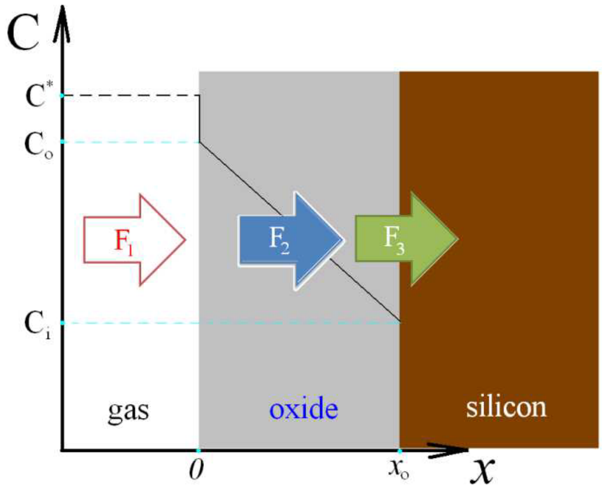

Figure 1.4 *Deal-Grove mechanism for thermal Si oxidation.*

The oxide growth rate can in the steady-state regime (F_1=F_2=F_3) be described as:

$$x^2 + Ax = B(t + \tau) \tag{1.8}$$

From equation 1.8, the oxide thickness evolution may be obtained as:

$$\frac{dx}{dt} = \frac{B}{2x+A} \tag{1.9}$$

where $A = 2D\left(\frac{1}{h} + \frac{1}{k}\right)$, $B = \frac{2DC^*}{N}, \tau = \frac{(x_0^2 + Ax_0)}{B}$, and x_0 is the initial thickness of the (preexisting) oxide, t is oxidation time and N is number of oxidant particles incorporated into a unit volume of oxide layer. Rate constants A, B and τ are known experimentally. An initial time offset (or delay time) τ is necessary to take into account the presence of an initial thick oxide layer. This "delay time" τ has been carefully studied by Massoud et al. [23, 24].

The Deal-Grove model allows us to characterize the oxidation kinetics for two limiting regimes. At long oxidation times ($t \gg \tau$) and for a thick oxide ($x^2 \gg Ax$), the oxide thickness is defined following equation 1.8 $x \cong \sqrt{Bt}$, while for a short oxidation time and for a thin oxide film ($x^2 \ll Ax$), the equation is becomes $x \cong \frac{B}{A}(t+\tau)$. Here, B and B/A are referred to as the parabolic and linear rate constants, respectively.

This model has proven to be extremely successful in reproducing a variety of experimental data describing the silicon oxidation kinetics over a wide range of substrate temperatures (700-1300°C) and oxygen partial pressures (0.1-1.0 atm). Specifically, the model allows excellent predictions for very thick oxide (> 100 nm) films and at sufficiently high oxidation temperature (> 1000 K) [18].

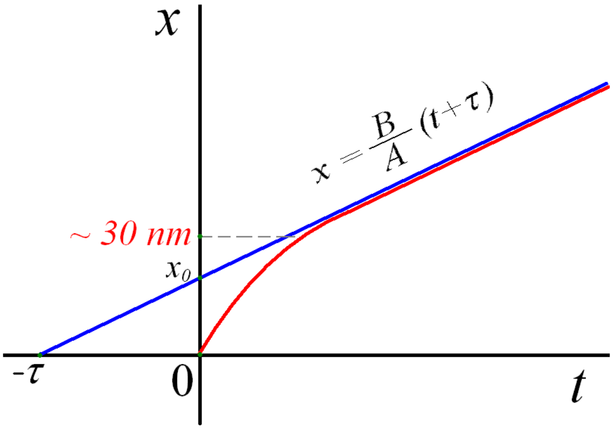

Figure 1.5 *Rapid, non-linear growth rate in the initial stage of dry oxidation.*

However, for thin oxide films (< 20 nm), an anomalous high oxidation rate was observed when compared with the prediction of the Deal-Grove model [10, 25]. It has been observed in many experiments that there is a rapid and non-linear oxide growth in the initial stage of dry oxidation [26], as presented in figure 1.5. One weakness of the Deal-Grove model is the impossibility to predict the initial stage of the oxidation growth. As shown in the figure, even with the best fit, the (approximately) first 30 nm of oxide growth cannot be reproduced with the Deal-Grove model. This is due to the fact that in this stage, the oxide growth is fast and non-linear, while the model offers only a linear fit (blue line in the figure) for such thin thicknesses [27].

The Deal-Grove model is clearly inadequate for the technologically important case of very thin oxides and experimentally an exponential law is found for the dependence of the oxide thickness on time for very short times.

Much research work has also been dedicated to elucidate the breakdown of the Deal-Grove model in the ultra-thin regime. *The Massoud model* [23, 24] is one of a number of successful extensions of the Deal-Grove model to improve the description in the ultra-thin regime. The Massoud idea is to correct the Deal-Grove model by adding some empirical terms to the growth rate. Thus, the growth rate as expressed by equation 1.9 is corrected by adding a supplementary term that exponentially decays with the oxide thickness:

$$\frac{dx}{dt} = \frac{B}{2x+A} \cdot \left[1 + C_2 exp\left(-\frac{x}{L}\right)\right] \tag{1.10}$$

where C_2 follows an Arrhenius law: $C_2 = 61.52 \cdot exp\left\{-\frac{2.56\ eV}{k_B T}\right\}$ and the oxide thickness of this additional term is controlled by the length parameter L. However, the physical origin of these terms is subject to discussion [28]. Moreover, this model fails to describe the oxidation in the low temperature regime where the oxidation reaction rate is very limited and the oxide thickness is very thin. Indeed, there is little or no experimental data for films thinner than about 20 Å [29]. Nevertheless, such very thin or ultrathin oxides (< 3 nm) are of great importance in today’s nanotechnology, especially for field-effect-transistors (FETs). Furthermore, the ultrathin Si|SiO_2 interfaces, which form the core of the *Metal-Oxide-Semiconductor* (MOS) FET gate structure, are arguably the world’s most economically and technologically important materials interfaces [3, 27].

It should also be realized that the detailed kinetics of the oxide growth process are influenced by many other factors, e.g. the *crystallographic orientation* of the Si surface, the *mechanical stress* in the oxide (which in turn depends on many process variables), the substrate *doping*, and the *initial condition* of the Si surface. Therefore, the development of this model still represents a big challenge.

1.2.3 MOSFET

Since the invention of the transistor in the 1940's, and especially since the start of the mass production of integrated circuits and microprocessors, semiconductor devices have played an ever increasing role in modern information technology as well as many other applied fields [12]. A transistor is a solid-state active device that controls current flow, and the word 'transistor' is a contraction of 'trans-resistor'. Basically, the transistor is a gated trans-resistor; that is, it is a resistor with a gate that controls the carrier density, and hence the current flow. The MOS (metal-oxide-semiconductor) technology has been emerging as the major driving force for VLSI (very-large-scale integration), which is the process of creating integrated circuits by combining thousands of transistors into a single chip [30]. The most famous MOS transistor is the metal–oxide–semiconductor field-effect transistor (MOSFET), originally used for amplifying or switching electronic signals. The first MOSFET, in which the semiconductor silicon plays a crucial role, was demonstrated by Kahng and Atalla in 1960. [31]. Silicon oxide films thermally grown on single-crystalline Si (*c*-Si) substrates in dry O_2 constitute the main material for gate dielectrics of MOS silicon devices since the advent of this technology [3, 15, 32]. Owing to a low density of electronic states at the silicon oxide/Si interface, as compared to other dielectric materials, the silicon-based MOSFET became the basic structure of stable, reliable, large scale integrated circuits. Nowadays, MOSFETs are used for random-access memory, flash memory, processors, ASICs (i.e., application-specific integrated circuits), and other applications [33].

Basic structure. As shown in the schematic respresentation of a MOSFET in figure 1.6, the field effect transistor consists of source (S) and drain (D) channel contacts, and a gate (G) electrode separated from the substrate (B) by the gate oxide. The body (or substrate) is often connected to the source terminal, making it a three-terminal device like other field-effect transistors. The *gate* is a conductive region electrically isolated from the substrate. Since the gate must provide an equipotential surface above the substrate, it must be constructed from a very conductive material. Newer technology uses poly-Si, which is grown on top of the gate oxide using a chemical vapor deposition (CVD), instead of Al. The function of the *gate oxide* is to provide a high quality insulator between the conductive gate and the substrate. Although preventing current flow from gate to substrate, the oxide layer still allows penetration of electric field from gate to substrate. The *source* and *drain* of the MOSFET are two regions with high dopant levels (e.g., by phosphorous ions or boron ions) of opposite type (*n*- and *p*-type) to the substrate immediately adjacent to the edges of the gate. The source and drain regions are normally contacted with metal (Al), separated from the gate and substrate by a dielectric isolation layer [30].

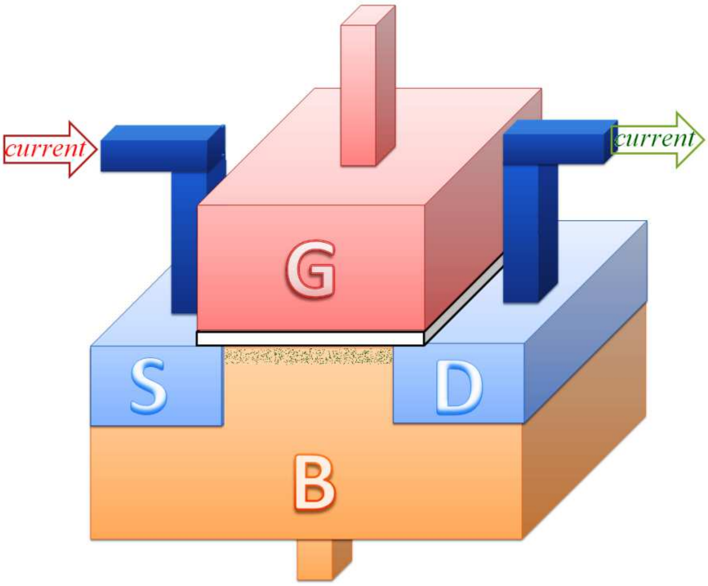

Figure 1.6 *Schematic view of a MOSFET. The gate oxide is located in between the gate (G) and the substrate or body (B). The gate voltage controls the conductivity of the B region near the gate oxide-substrate region. Flow of current occurs between the source (S) and drain (D) regions. Thus, in a MOSFET, applying a voltage perpendicular to the surface of the body B is used to control the flow of electrical current through the field effect.*

Basic working principle. The basic principle of the MOSFET is that the source-to-drain current (SD current) is controlled by the gate voltage (or electric field). The electric field induces charge (field effect) in the Si crystal at the semiconductor-oxide interface. Thus, in the MOSFET, a voltage drop across the oxide induces a conducting channel between the source and drain contacts *via* the field effect. The channel can contain electrons (called an *n*MOSFET or *n*MOS), or holes (called a *p*MOSFET or *p*MOS), opposite in type to the substrate. Therefore, *n*MOS is made from a *p*-type substrate, while the source and drain are *n*-type, whereas a *p*MOS is made from an *n*-type substrate, while the source and drain are *p*-type and the body is *n*-type. In *n*MOS FET, when the voltage on the gate is positive, electrons accumulate on the semiconductor surface making the channel between source and drain conducting and so turning the transistor from the ‘off’ (depletion-mode) into the ‘on’ (enhancement mode) state. The working principle is opposite for *p*MOS field-effect transistors [30].

1.2.4 Thermally grown oxides in MOSFETs

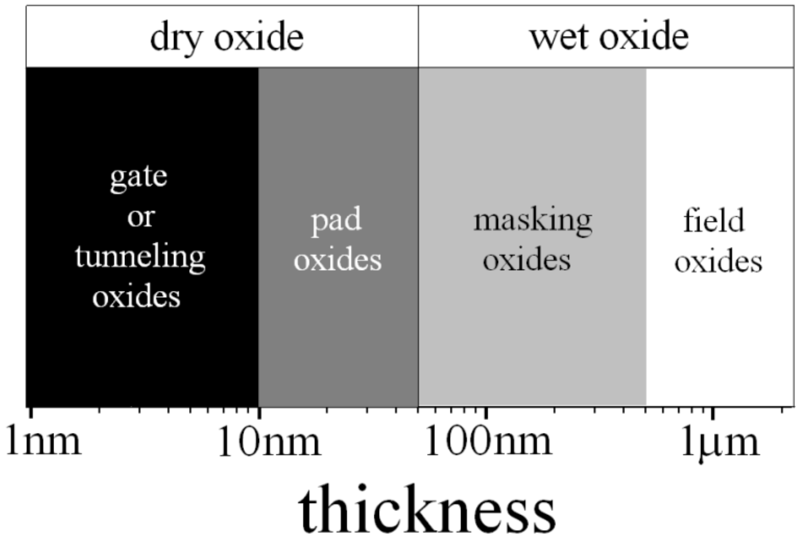

Figure 1.7 *Used oxide thicknesses in MOSFET manufacture.*

In MOSFET manufacturing, several types of oxides are grown with different thicknesses using either dry or wet oxidation. Accordingly, the oxides formed are classified as dry or wet oxides, as shown in figure 1.7. Dry oxides are excellent insulators with a thickness thinner than about 0.1 μm. Gate and thin pad oxides are referred to as dry oxides. Field and masking oxides are wet oxides. Wet oxides are good insulators with a thickness in the range of 0.5- 2.5 μm.

Typically, MOSFET fabrication starts with the formation of a so-called SiO_2 *pad oxide* on the active device region, i.e., the substrate surface where the various MOSFET elements are formed. A silicon nitride (Si_3N_4) mask is formed on the pad oxide. The MOSFET structure is surrounded by a thick layer (~ 1 μm) of insulator called the *field oxide*. The field oxide, normally silicon dioxide, isolates the gate from the substrate outside the active device region. Consequently, a *gate oxide* is formed on the active region. Prior to the gate oxide formation, the pad oxide and Si_3N_4 mask is etched. The (ultra) thin gate oxide between gate (polysilicon) and substrate (crystalline silicon) is usually

SiO_2, or can be other high-*k* insulators [34, 35]. Furthermore, a *masking oxide* is deposited on the active region using Chemical Vapor Deposition (CVD) in order to protect the open area of the Si substrate in the acive region. Thus, this oxide also separates the poly-Si gate and the Al metal contact. In particular, the oxide thickness of about 500 nm will be sufficient to mask against any contaminations.

Finally, note that many studies have demonstrated the formation of a so-called "*native oxide*" on Si in air, even at room temperture. Commonly, this native oxide layer is about 1 nm thick [36]. However, such oxides are poor insulators and thus the oxide layer is removed prior to MOSFET fabrication.

1.2.5 Ultrathin gate oxide for MOSFET

Current technological trends geared toward higher performance are driving the gate oxide thickness to shrink [12]. SiO_2 has been the preferred gate insulator for silicon MOSFET since its very beginning in the 1960's and the oxide thickness has been reduced over the years from 300 nm for 10 μm technology to 1.2 nm for 65 nm technology. Scaling of MOSFET dimensions (including transistor length, width, and the oxide thickness) is desirable for several reasons. First, for a given chip area, more and more MOSFETs can be placed. Thus, the same functionality can be realized in a smaller area, or chips can have more functionality in the same area. Second, a smaller MOSFET switches faster and consumes less power, which is desirable for maximizing the circuit speed. The downsizing of MOSFETs has been accomplished to a large part by decreasing the oxide thickness to obtain high current flows and a good short-channel control. MOS transistors featuring sub-1.5-nm ultrathin gate oxides have been fabricated [33]. Although the manufacturing of such ultrathin Si oxide growth remains a difficult issue for the microelectronics industry, it is possible to grow very thin and uniform gate oxide films with high yield. These can be produced in many ways: dry or wet oxidation, high temperatures and short oxidation times or the other way around. Furthermore, low pressure chemical vapor deposition (LPCVD), atomic layer deposition (ALD), and molecular beam epitaxy (MBE) methods, all of which have the potential for growth with sufficient interface control, are also candidates for deposition of the ultrathin gate dielectrics [10].

However, it must be kept in mind that oxide growth kinetics in this range (1.5-4 nm) are strongly dependent on processing parameters like pre-oxidation surface cleaning, substrate orientation, rapid or conventional thermal processing, and others. Furthermore, the kinetics in this thickness range are also dependent on processing parameters, like pressure, temperature and time [32]. Therefore, the experimental regime is very challenging to model. On the other hand, the current thickness of the gate dielectric is close to the fundamental limit. The need for atomic scale understanding and control thus becomes even more critical [15, 32, 33, 37-39]. Therefore, the precise control of the ultrathin gate thickness is one of challenge tasks for further MOS device technologies [12]. Unfortunately, thermal oxidation fail to provide such control of very thin oxide thickness and therefore, searching other growth methods than thermal may also be useful. Oxidation of a Si substrate using energetic (< 100 eV) oxygen species (i.e., *hyperthermal oxidation*) has been envisaged as an alternative method for growing and controlling ultrathin gate oxides, even at relatively low temperatures [40].

1.3 Hyperthermal oxidation of planar Si

1.3.1 Hyperthermal energy range

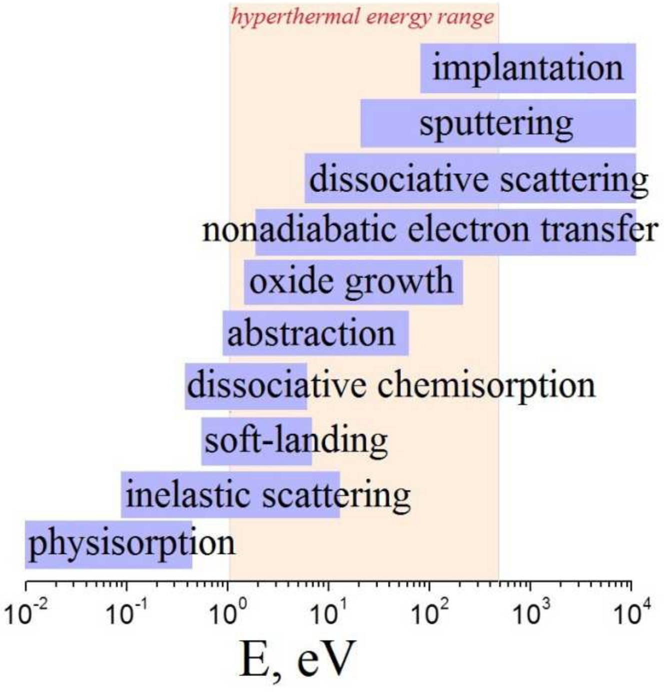

Figure 1.8 *Fundamental processes associated with projectile-surface collisions around the hyperthermal energy range, based on [41].*

When an atom or a molecule interacts with a surface, several processes can occur depending on the chemical nature of the incident particle and the geometric and electronic structure of the surface. Some of the more common events that can occur when the hyperthermal projectile atom (molecule) strikes with a surface target are shown in figure 1.8.

At thermal conditions, desorption and decomposition often compete with surface chemical reactions, often leaving the experimentalist with limited control over the distribution of products. However, hyperthermal translational energies, which vary in the range of about 1-500 eV, are sufficient to activate a number of fundamental chemical processes in the near-surface region, including nonadiabatic electron transfer, dissociative scattering, abstraction and processes related to ion beam deposition [41, 42]. In that case, the initial properties of the incoming particle, i.e., the translational energy, internal energy etc., may contribute significantly to the dynamical processes on the surface even after the first interaction with the surface [43]. Furthermore, tuning the incident energy in the hyperthermal range and selecting the projectile type can provide control over several of the processes shown in the figure. Such controlled low-energy (< 100 eV) ion beams provide a unique opportunity for investigating the chemistry and physics of hyperthermal species with surfaces and for exploring unique applications of beam-surface interactions [44]. Indeed, the energetic reagents are being used to modify surfaces and this can open novel routes for industrial applications, in which implantation, sputtering, etching and other processes are commonly used [41, 45].

Currently, interest in hyperthermal oxidation as an alternative to thermal oxidation is rapidly increasing, especially for semiconductor applications. Furthermore, since silicon oxide is commonly employed as a protective transparent coating in spacecraft applications, the study of the surface reaction of energetic oxygen species as dominant components of the low-Earth orbital (LEO) is also important [43, 46]. As a result, many investigations were recently devoted to this topic, in order to elucidate the fundamental aspects of the hyperthermal impact and oxidation process [43, 46-52]. Such investigations can experimentally be carried out by using a laser detonation hyperthermal (i.e., in the energy range 1 – 15 eV) atomic beam source [40, 53, 54].

1.3.2 Laser Detonation Source

The laser detonation-type oxygen atom beam source was originally invented by *Physical Sciences, Inc.* in order to simulate hyperthermal oxygen atom (with a translation energy of approximately 4.6 eV) reactions with materials in low Earth orbit, located at an altitude of 200-300 km [53, 54]. The beam source is based on a laser-induced detonation phenomenon, which can generate a pulsed oxygen atom beam with a velocity of about 8 km/s and fluxes of approximately 10^{15} atom/cm^2 per pulse on a large area (~1000 cm^2). A schematic of an original laser detonation-type hypethermal oxygen atom beam source is shown in figure 1.9.

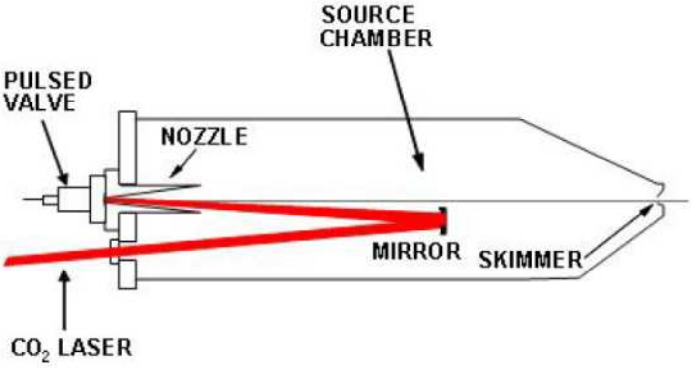

Figure 1.9 *Schematic diagram of the laser detonation source used to create hyperthermal neutral beams.*

The operation principle of the source is as follows: pure oxygen gas is introduced into a nozzle through a piezo-driven pulsed supersonic valve at a repetition rate of 2 Hz. A giant laser pulse from a carbon dioxide laser (wavelength: 10.6 μm, output power: 5-7 J/pulse), which enters the source chamber through a ZnSe window, is focused on the oxygen gas at the water-cooled, gold-plated copper nozzle. By absorbing the laser energy, a high-density and high temperature (> 20000 K) oxygen plasma is formed at the nozzle. Once the plasma is formed, it propagates and absorbs laser energy in the tail of the laser pulse. This plasma propagation is along the incident laser axis, and oxygen molecules are decomposed and accelerated at the shockfront of the plasma propagation. Thus, an intense hyperthermal atomic oxygen beam pulse is formed due to efficient ion-electron recombination in the nozzle as the plasma cools. Alignment of a rotatable mass spectrometer detector with the beam axis is used to characterize the beam source [55].

Modification versions of the beam source have been presented as well [56]. Now, the beam source also generate other energetic neutral atoms (rare gas, C, F, N, S, Cl, etc.) and molecules (O_x, C_xH_x, C_xO_x, N_xO_x, etc.) beams by selecting the source gas (for instance, a hyperthermal oxygen atom beam is generated using oxygen molecule as a source gas). Because of the unique properties of the beam source, the hyperthermal neutral atom beams have also been used to investigate fundamental gas-gas [57] and gas-surface [58] chemical reactions.

1.3.3 Ultrathin SiO_2 growth by hyperthermal oxygen

As mentioned in previous sections, the growth of ultrathin silica layers on Si-crystals at low temperature is important for the fabrication of microelectronics devices such as the MOSFET, as well as photovoltaic devices (solar cells, optical fibers, etc.) [15, 20, 38]. In such thin films, a significant portion of the film is occupied by the transition layer at the $Si|SiO_2$ interface, degrading the dielectric properties, the light absorption efficiency, and hence the performance of the devices [15, 37].

The laser detonation oxygen-beam source has already successfully been used to fabricate such ultrathin SiO_2 film on Si surfaces at room temperature [40]. This atom-beam source provides the O atoms with a translational energy up to 10 eV. Indeed, it was discovered that the reaction of hyperthermal oxygen species (O, O_2) with a surface has unique properties compared to ordinary high temperature oxidation, i.e., a very thin oxide film can be formed even at room temperature [47-51]. Furthermore, it is found that precise control over the ultrathin silica formed is possibly by tuning the translation energy of incident species or by changing their incident angle [43, 51]. Moreover, the oxide thickness as obtained in the hyperthermal oxidation process depends also on the type of oxygen species. Experiments in this oxidation energy region show that the thickness of the oxide formed by atomic oxidation should increase as compared to the thickness of the oxide created by O_2. For optimal device performance, the thickness of the interfacial region consisting of suboxides, SiO_x ($x<2$), formed by atomic oxidation, should be reduced as much as possible. Oxidation by oxygen molecules produces a 0.2-1 nm region consisting of suboxides (between Si^0 and Si^{4+}) [46, 59].

While many experimental works are devoted to unravelling the hyperthemal Si oxidation process, many aspects are still poorly understood. For example, while the direct oxidation mechanism has been properly elucidated at room temperature, it has not been studied yet at other growth temperatures. Furthermore, the probabilities for penetration, desorption and implantation during the initial oxidation stage have not yet been investigated in full detail [60, 61]. Moreover, the morphology of the hyperthermal Si|SiO_2 interface is at present not clear. Also, self-limiting oxidation at low temperature, as induced by interfacial stresses, has not often been studied. Understanding the growth process at the atomic-scale (i.e., oxidation kinetics and dynamics, transport phenomena during oxidation, etc.) of ultrathin silicon dioxide is also important [20, 62]. In this work, I have therefore investigated the hyperthermal Si oxidation in order to study the interface and the relevant processes at the atomic scale using molecular dynamics simulations.

1.4 Si nanowire (Si-NW) oxidation

1.4.1 Fabrication of Si-NWs

Silicon nanowires (Si-NWs) are cylindrical single crystal structures with a diameter in order of a nanometer and a length of several hundred nanometers. As a new class of nanomaterials, they are currently the subject of extensive research with several hundreds of papers published annually in the field. In the past decade, the interest in Si-NWs has increased tremendously, as they are being used extensively in nanoscale electronic devices [63, 64], including nanowire field-effect transistors (FET), thin film transistors [63 - 67], photovoltaic devices [68], including thin-film solar cells [69] as well as nanowire-based electrochemical biosensors [70, 71] etc. Therefore, several growth methods of Si-NWs have been reported, analyzing general aspects of their growth [72].

Si-NWs can be fabricated by two routes: so-called "*top-down*" and "*bottom-up*" fabrication techniques. Figure 1.10 shows the essence of top-down and bottom-up manufacturing.

In the "top-down" approach, the process starts on a thin Si wafer. The wafer is cleaned, coated, and preferentially etched. The total process consists of a large number of steps, including crystal growth, lithography (electron beam lithography or scanning probe lithography), deposition, etching, ion implantation, electrophoresis and so on [73] before the desired shape or product is complete. Thus, the approach involves molding or etching materials into smaller components.

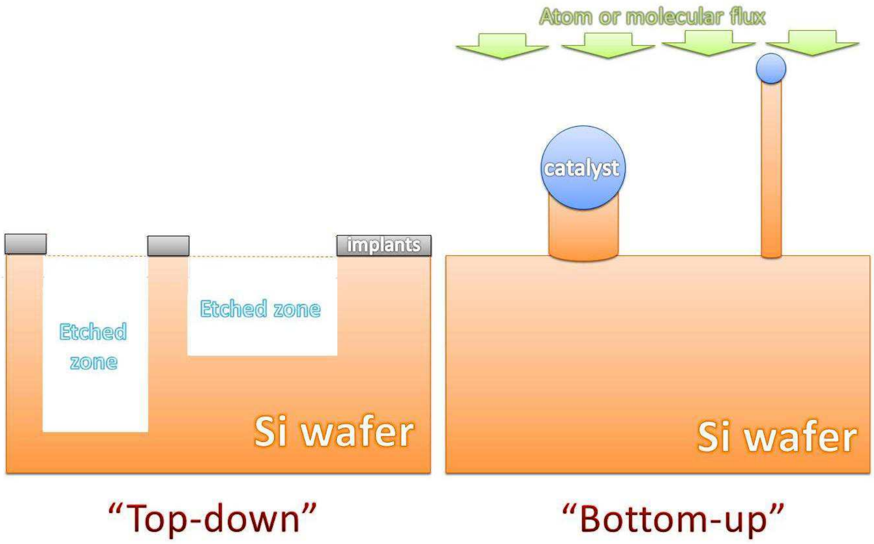

Figure 1.10 *"Top-down" and "Bottom-up" Si nanowire fabrication techniques.*

On the other hand, in the "bottom-up" technique, the end product is essentially formed by merging or combining small items to bigger ones. The "bottom-up" growth technique is widely used for Si-NW fabrication. The Vapor–Liquid–Solid (VLS) mechanism of the Chemical Vapor Deposition (CVD) growth technique,, first proposed by Wagner and Ellis [74] in the mid-1960s, is the one of the most widely adopted growth mechanisms based on the "bottom-up" concept. The VLS mechanism essentially consists of three steps: (i) the adsorption of a gaseous growth precursor (Vapor, V) on the surface of a nanoparticle; (ii) diffusion of Si-atoms through the liquid body of the nanoparticle (Liquid, L); (iii) extrusion of the nanowire in solid form (Solid, S). Analogous to the VLS mechanism, a vapor–solid–solid (VSS) mechanism in CVD has also been proposed [72]. This mechanism applies to wire growth catalyzed by a solid catalyst particle instead of a liquid catalyst droplet. Although these mechanisms strongly depend on the catalyst material and temperature, they are applicable over a wide range of sizes, from wires several hundreds of micrometers thick down to nanowires of just a few nanometers in diameter [72]. Beside of CVD-based growth mechanisms, many other techniques, including Molecular Beam Epitaxy (MBE), Laser Ablation (LA), Annealing in Reactive Atmosphere, and Evaporation of SiO, Solution-Based

Techniques have also been developed for "bottom-up" SiNW growth [72, 75, 76].

Comparing with the "top-down" approach, the "bottom-up" approach has a number of advantages: it allows synthesizing Si-NWs of higher crystallinity, better control over the dopant density, the formation of (controllably) thin silicon oxide sheaths, and easily controlled diameters for the nanowire based transistors in a cost-effective preparation [71]. Applying Si-NW as building blocks of transistors opens up a new route for Si technology. Transistors based on Si-NWs have indeed already shown promising potential to revolutionize the applications of electronic, optical, chemical and biological devices [63-70]. One of such transistors is Si nanowire based field-effect transistor.

1.4.2 Si-NW FET

Although new candidates are also being searched for in today's nanotechnology, silicon technology is still the most reliable and cost-efficient way to fabricate large microelectronic circuits [39]. To directly address the scaling challenge, semiconducting nanowires such as Si-NWs, have been thoroughly investigated because of their compatibility with today's microelectronics industry and their potential in replacing conventional planar MOSFET structures. Specifically, devices based on Si-NWs are attractive candidates for the pursuit of the miniaturization of MOSFET transistors with gate lengths below 22 nm and for the development of innovative architectures. Experimental results showed that Si-NW Field-Effect-Transistor (FET) exhibited higher hole mobility, higher transconductance, more ideal subthreshold behavior, better gate control and better short channel performance than traditional planar MOSFETs [77]. In addition, comparison of scaled Si-NW FET transport parameters with those of state-of-the-art planar MOSFETs show that Si-NWs have the potential to substantially exceed those of conventional devices, and thus could be ideal building blocks for future nanoelectronics [77].

Figure 1.11 presents a schematic representation of Si NW FETs: already being used "top-gated" (top) and envisaged "wrap-gated" (bottom) transistors. In the already existing setup, the FET is supported on an oxidized silicon substrate with the underlying conducting silicon used as a global back gate electrode to vary the electrostatic potential of the NW (B). In a typical NW FET device, two metal contacts, which correspond to source and drain electrodes, are defined by electron beam lithography followed by evaporation of suitable metal contacts. Current vs. source-drain voltage and current vs. gate voltage is then recorded for a NW-FET to characterize its electrical properties.

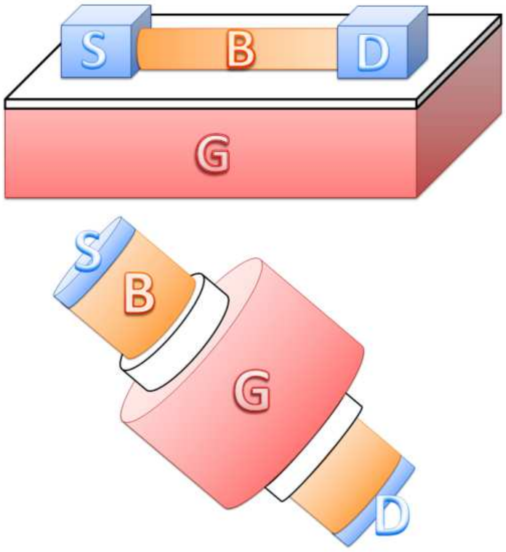

Figure 1.11 *Schematic views of two types of the Si nanowire (Si-NW) FETs: "top-gated" (top) and "wrap-gated" (bottom) transistors. The gate oxide is located in between the gate (G) and body, i.e., the Si-NW (B). Current flow occurs between the source (S) and drain (D) trough nanowire. Gate voltage controls the current.*

As mentioned in the previous section, Si-NW can be grown in either top-down or bottom-up mode. Thus, fabrication of Si-NW FETs is based on these growth methods. In a top-down technique, the Si-NW FET is fabricated by physically etching a single-crystalline silicon wafer through lithographic processes combined with an electron-beam technique [78]. On the other hand, the "bottom-up" process starts with the growth of a Si-NW , normally in a CVD setup via the VLS mechanism, followed by Si-NW deposition/alignment on a silicon substrate and finally device fabrication via the photolithographic or electron-beam lithographic procedures [79]. A "top-gated" Si-NW FET is prepared using both fabrication techniques while the the "wrap-gated" transistor fabrication is mostly based on the bottom-up approach. In the latter type of Si-NW FET, a Si core-oxide shell structure plays the role the "body"-"gate oxide" system. Such a "core-shell" structure is typically obtained by monitoring the oxidation time and temperature in a thermal Si-NW oxidation process, in which the nanowire diameter is carefully selected [67, 80]. The oxidation process is typically self-limiting. Control over this oxidation process is critical, since thermal oxidation is a mandatory step to form the gate oxide or to reduce the wire diameter.

1.4.3 Self-limiting oxidation

As mentioned above, silicon oxide nanowires, produced by oxidizing Si-NWs, have many applications due to their electrical, mechanical and optical properties. Silicon oxide is an electrically insulating material and can emit stable blue light [81]. Conventional glass fibers are used in the reinforcement of composites and nanowires could find similar use [69]. Therefore, the oxidation of Si-NWs is studied by a large number of groups working on various aspects of the process as well as on the properties and applications of the resulting wires.

Self-limiting oxidation of Si nanowires and spheres on the micro-scale is of considerable importance, for instance for the design of metal-oxide-semiconductor (MOS) devices [66, 73, 82-85], such as wrap-gated [86] and top-gated [67] FETs as mentioned in previous section. The early work on self-limiting oxidation performed by Liu et al. [73] analyzed the dry thermal oxidation of Si-NWs starting from an initial nanowire diameter of ~30 nm. These authors suggested that the final Si core diameter can be controlled by the oxidation temperature. Self-limiting oxidation was mechanistically explained by a so-called retarded oxidation process of Si nanowires [87]. It was found that such oxidation behavior strongly depends on the nanowire curvature, the sign of curvature (i.e., convex or concave) and the growth temperature. Various modeling efforts and analyses regarding this effect have been presented [67, 83-89]. Since the Deal-Grove model [22] is only valid for the oxidation of planar bulk silicon, some modifications need to be applied for describing such two dimensional (cylindrical) structures, as outlined in detail for wet oxidation by Kao and co-workers [82]. This model has successfully elucidated the self-limiting oxidation in Si-NWs with diameters in the micrometer scale, and will be explained in the next section.

On the other hand, small-diameter (< 10 nm) Si-NWs are potentially very attractive because of the quantization of the electronic structure [65, 66]. Normally, such Si-NWs are obtained by oxidizing a large nanowire and subsequently removing the oxide layer [90-92]. Oxidation has been used to reduce the Si-NWs diameter below the Bohr exciton radius to obtain visible photoluminescence due to quantum confinement effects. Interestingly, in this case, the band gap becomes size dependent and increases as the size of the nanostructure decreases. As established by Ma and co-workers [65], the Si-NW band gap can be increased up to 3.5 eV by reducing their diameter to less than 3 nm. This indicates the possibility of developing Si-NW materials with a controllable band gap. For exploiting these characteristics in actual applications, obtaining an accurate control over the oxidation process is clearly critical, which, however, is difficult to achieve [93]. The mechanisms of the small diameter nanowire oxidation have therefore been studied extensively [67, 87-89, 93, 94].

Once the self-limiting oxidation is established for small Si-NWs, the understanding of the stress dependence will be useful for controlling non-planar oxidation large scale integrated processes [73]. The residual stress results in self- (or stress-) limiting oxidation when the strain energy at the interface is larger than the energy gain for the ambient oxygen to diffuse and oxidize the inner Si. Because the oxide should expand more to accommodate the volume expansion in thinner Si-NWs, the self-limiting oxidation is more significant in Si-NWs with smaller diameters [73]. According to the Kao model [82], compressive stresses normal to the Si|SiO_2 interface reduce the interfacial reaction rate compared to a planar Si surface, whereas tensile stresses generated within the oxide shell reduce the effective oxide viscosity and enhance the oxygen diffusivity and solubility [93].

1.4.4 Kao model

The Kao model [82] is a popular extension of the traditional Deal-Grove model for wet oxidation of non-planar (curved) Si surfaces. As discussed in the previous section, the oxidation planar Si surfaces (see *eq 1.8*) can be quantified in the Deal-Grove mechanism [22] as follows:

$$\frac{dx}{dt} = \frac{B}{2x+A} = \frac{C^*/N}{\frac{1}{k}+\frac{1}{h}+\frac{1}{D}x} \qquad (1.11)$$

where h is the gas-phase mass transport coefficient, D is the oxidant diffusion coefficient in the oxide with thickness x,and k is the oxidant reaction coefficient at the oxide-silicon interface. Finally, C^* is the oxidant concentration in equilibrium in the oxide and N is the number of oxidant particles required to form a cubic unit of oxide. From this formula, the growth rate is determined by k, the surface reaction rate constant for thinner oxides. Consequently, it will be dominated by x/D in the diffusion-controlled regime when the oxide is thick.

Experimentally, the oxidation kinetics has been observed to be strongly dependent on the size and the geometry of the micro- and nano-objects. Using this generalized Deal-Grove approach, Kao et al. [82] found that the oxidation rate at the Si|SiO$_2$ interface for the oxidation of non-planar Si surfaces can be described as:

$$\frac{dx}{dt} = \frac{C^*/N}{\frac{1}{k}+\frac{1}{h}\frac{a}{b}\pm\frac{1}{D}a\log\left(\frac{b}{a}\right)} \tag{1.12}$$

where a and b are the radii of the curved Si and oxide surface, respectively. The "+" sign denotes convex structures (e.g., Si-NW) and "-" sign concave structures (e.g., Si nanorings). The equation describes the rate at which the new oxide grows at the interface. This growth rate is a logarithmic function of the radii of the silicon and oxide surfaces, both changing with time. Therefore, the oxide thickness can no longer be described by the simple linear (B/A) and para-

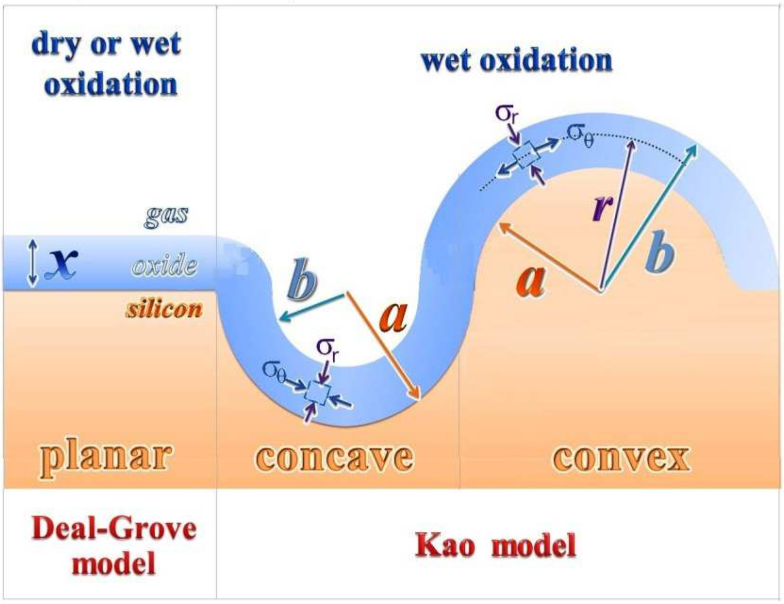

Figure 1.12 *Deal-Grove and Kao models for thermal oxidation of planar and curved Si surfaces, respectively.*

bolic (*B*) rate constants of the Deal-Grove oxidation model. Figure 1.12 shows both Deal-Grove and Kao models for the oxidation of planar and curved Si surfaces, respectively.

Another major achievement of this work is the including of *stress/pressure effects* in the Deal-Grove approach. It is well known that the formation of new oxide at the silicon surface requires a volume expansion, because the volume of an oxide or SiO_2 molecule (Ω_{SiO_2} = 45 $Å^3$) is more than twice as large than the volume of a silicon atom (Ω_{Si} = 20 $Å^3$). The resulting stress in the strained oxide significantly influences the oxygen diffusion. Furthermore, in this model, the oxide is assumed to behave as a "viscous fluid", i.e., the oxide viscosity is extremely high and its velocity very low. Therefore, non-planar two-dimensional viscous deformation of the oxide produces large stresses, in addition to the stress that already develops in planar oxidation. The viscous stresses, i.e., radial (or normal) and tangential (or hoop) stresses are expressed as follows:

$$\sigma_r(r) = 2\eta\xi\left(\frac{1}{b^2} - \frac{1}{r^2}\right) \tag{1.13}$$

$$\sigma_\theta(r) = 2\eta\xi\left(\frac{1}{b^2} + \frac{1}{r^2}\right) \tag{1.14}$$

where η is the viscosity of the oxide, ξ is the velocity coefficient and it is derived from the oxide growth rate at interface as $\xi = a\frac{kC_i}{N}\left(\frac{\Omega_{SiO_2} - \Omega_{Si}}{\Omega_{SiO_2}}\right)$, C_i is oxidant concentration at the Si|SiO_2 interface, and *r* is the distance from the center of curvature to a cubic unit of oxide where stresses are calculated. Because the oxide is a viscous fluid, the calculation of the hydrostatic pressure *p* is also important. According to fluid mechanics, the pressure is equal to the average viscous stress on a control volume in the fluid:

$$p = \frac{1}{2}(\sigma_r + \sigma_\theta) \tag{1.15}$$

In the oxidation of Si surfaces, the oxidant reaction rate (*k*) is assumed to be affected by the stress, while the oxidant diffusion (*D*), the oxidant solubility at the SiO_2 surface (C^*) and the oxide viscosity are dependent on the pressure, in the following way:

$$k = k_0 \cdot exp\left\{-\frac{\sigma_r(\Omega_{SiO_2}-\Omega_{Si})}{k_B T}\right\} \tag{1.16}$$

$$D = D_0 \cdot exp\left\{-\frac{pV_a}{k_B T}\right\} \tag{1.17}$$

$$C^* = C_0^* \cdot exp\left\{-\frac{pV_s}{k_B T}\right\} \tag{1.18}$$

$$\eta = \eta_0 \cdot exp\{\alpha \cdot p\} \tag{1.19}$$

where k_0 is the stress-free oxidant reaction coefficient, D_0 is the diffusion coefficient at a pressure of 1 atm, C_0^* is zero-pressure solubility, V_a and V_s are the activation volume of diffusivity and solubility, respectively, η_0 is the viscosity at zero pressure and α is an empirical parameter. Also, k_B is the Boltzmann constant, T is the temperature.

Because the radial stress is compressive in both convex and concave structures, the oxidation rate is lowered through the reduced surface reaction rate coefficient k. Under high pressure, the oxidant diffusivity and solid solubility are reduced and the oxide viscosity increases. Due to including the stress and pressure terms in *eq 1.12*, Kao and co-workers successfully explained the retardation effect (i.e., self-limiting oxidation) observed for the oxidation of cylindrical structures, which depends on the growth temperature, the radius (or the curvature) and the sign of curvature (convex or concave). This effect is of concern for the design of, e.g., Si-NW field-effect-transistors as described before.

Kao and colleagues concluded that the oxide growth on a curved surface approaches that on a planar surface when the oxide is thin or the radius is large. For thick oxides or small radii, the oxidation strongly depends on the surface curvature. Specifically, oxidation is faster on a convex surface than on a planar surface, and in contrast,whereas a concave surface oxidizes slower. Furthermore, convex surfaces are predominantly controlled by the surface reaction rate (k), while concave surfaces are mostly controlled by the oxygen diffusion (D), which strongly depend on the normal stress and hydrostatic pressure, respectively.

Although this model successfully describes wet oxidation of curved Si surfaces, it suffers from certain limitations. For instance, the model fails to describe the fast initial growth regime for dry oxidation [23]. Indeed, the oxidation rate in the nanoscale regime is not accurately described by this micro-scale model although the model has been extended into the nanometer scale [84, 85, 95.]. Furthermore, the self-limiting behaviour of the dry oxidation of small-diameter Si-NWs has not been investigated using this model.

Chapter 2

Computational methodologies

Nowadays *computer simulation methods* are powerful tools used in many fields of research. One specific advantage is its ability to “bridge” theory and experiments. In a so-called “computer experiment”, parameter values or parameter interdependencies can be resolved, which might be diffult or impossibe to do in a real experiment. Moreover, computer experiments often also allow comparison with real experiments and, consequently, validating (or falsifying) the model underpinning the simulation. Finally, computer simulations allow macroscopic observables to be calculated from microscopic behaviour, through the laws of statistical mechanics.

2.1 Statistical mechanics

The microscopic state (“microstate”) of a physical system is connected to the macroscopic world (“macrostate”) by *statistical mechanics*. In statistical mechanics, the microstate is the state of the system, as defined in terms of the behaviour of all constituent atoms. It is typically represented by a particular point A of the phase space of the system. For example, in a system of N atoms, the phase space is defined by $6N$ coordinates, i.e., $3N$ positions $\boldsymbol{r}$ and $3N$ momenta $\boldsymbol{p}$ at a given instant of time t. A particular point is phase space must then be time-dependent, i.e., A=A(t). The macrostate is the state of the system as defined by macroscopic parameters, e.g., temperature, pressure, internal energy etc.

A key concept in statistical mechanics is the *ensemble*. An ensemble is a collection of microstates of the system, all having in common one or more extensive properties. As a model of the physical system, the computer simulation is carried out to calculate the property or properties of interest. These properties are averaged over a large number of atoms in the simulation or averaged over time. In statistical mechanics, the corresponding observable is determined from the ensemble average. However, calculating a (true) ensemble average may be expensive or even unattainable in the computer experiment. This problem is alleviated by the ergodic hepothesis, which is one of the fundamental axioms of statistical mechanics. In accordance with this hypothesis, the ensemble average is equal to the time average:

$$\langle A\rangle_{ensemble} = \langle A\rangle_{time} = \lim_{\tau\to\infty} \frac{1}{\tau}\int_0^\tau A(t)dt \qquad (2.1)$$

where the notation <…> indicates the average.

2.2 Computer simulation methods

At the atomic scale, computer simulations are often limited with respect to attainable time and length scales. The two main simulation techniques in this domain are *Molecular Dynamics (MD)* and *Monte-Carlo (MC)* methods, either in classical of in *ab-initio* flavor.

Monte Carlo is a stochastic method, based on the concept of statistical mechanics. In the so-called Metropolis algorithm (MMC), the energy change from step n to $n+1$ is used as a trigger to accept or reject the new configuration. Moves towards a lower energy are always accepted, while those to a higher energy are accepted with a Boltzmann probability. Although the concept of physical time does not exist in the MC method (except kinetic MC (kMC) and UFMC), it is the method of choice for simulating a gas or other low density systems [96]. KMC and MMC algorithms have also been widely used in thin film growth processes. It should be pointed out, however, that this method has some disadvantages. For example, the random moves in the MC simulation can easily lead to (unphysical) barrier crossings. Thus, in order to obtain accurate results on long time scales, companion investigations of the system are sometimes being performed using on-the-fly kMC or accelerated Molecular Dynamics (MD) [97].

In contrast to MC, classical MD is a deterministic method, which is based on the integration of the equations of motion of the atoms. Interactions between atoms are described using an appropriate interatomic potential. Since its invention in the 1950's [98], it has been used to investigate a wide range of problems in many different research fields, including statistical mechanics and physics (theory of liquids, correlated many-body motion, properties of statistical ensembles, structure and properties of small clusters, phase transitions, etc.), chemistry and biology (molecular structures, chemical reactions, drug design, vibrational relaxation and energy transfer, structure of membranes, dynamics of large biomolecules, protein folding, etc.), material science (defects in crystals, microscopic mechanisms of fracture, surface reconstruction, melting and faceting, film growth, friction etc) and so on. However, MD has some disadvantages as well, i.e., (1) description of the electronic (quantum) or excited states is difficult; (2) accuracy of chemical reactions (bond breaking/forming) is lower than DFT or quantum-chemical methods; and finally (3) the attainable time scale is limited to the nanosecond or perhaps microsecond range. The application of DFT-based MD, as pioneered more than thirty years ago by the work of R. Car and M. Parinello [99], showed the possibility to model many technological important processes in material processing or chemistry with good accuracy. The two other issues, however, remain challenging topics for future developments.

In this work I used classical reactive MD simulations, which reactive force-field is apllied in classical MD, to model Si and Si/O system in order to study the Si oxidation and related processes.

2.3 Classical Molecular Dynamics

2.3.1 Newtonian dynamics

Molecular dynamics (MD), as mentioned above, is a deterministic method, in which the state of the system at any future time can in principle be predicted from its current state. In a MD simulation, successive configurations of the N atoms in a volume V are generated by integrating Newton's laws of motion, which can be formulated as follows:

(1) A particle moves with constant velocity in a straight line if no force acts upon it (*Newton's first law*).
(2) A force acting on the particle changes its momentum and thus accelerates it, i.e., $\boldsymbol{F} = \frac{d\boldsymbol{p}}{dt} = m\boldsymbol{a}$ (*Newton's second law*)
(3) Action induces a reaction equal in magnitude but opposite in sign, i.e., $\boldsymbol{F}_{ij} = -\boldsymbol{F}_{ji}$ (*Newton's third law*).

However, in reality, an atom is quantum particle displaying wave-corpuscular behaviour. It's complete behaviour is described by the *Schrödinger equation* [100] and thus its motion cannot be accurately described by classical mechanics. In principle, the Schrödinger equation should be solved to find the total wavefunction ψ which tells us everything about the system. Except for the simplest systems, this is not possible analytically. Application of the so-called *Born-Oppenheimer* approximation [101], however, allows to find approximate solutions. It assumes that the electrons follow the motion of the atomic nuclei instantly. According to this approximation, MD treats the atomic nuclei (or atoms) as *classical* particles and assumes that the electrons are permanently in their ground state, such that the atomic interactions can be described by interatomic potentials dependent on the positions of the nuclei only. Newton dynamics then describe the nuclear motion. This approach can also be justified via the *De Broglie wavelength* and the *Heisenberg uncertainty principle* (see *e.g.*,[102]).

The *De Broglie thermal wavelength* Λ is defined as follows:

$$\Lambda = \frac{h}{\sqrt{2\pi m k_B T}} \tag{2.2}$$

where h is the Planck constant ($6.626069 \cdot 10^{-34}$ J·s) and k_B is Boltzmann constant ($1.3806503 \cdot 10^{-23}$ J·K^{-1}). In the case of Si ($m = 4.6637 \cdot 10^{-26}$ kg) at a temperature in the range T = 300 K - 1200 K, the wavelength is in the range 0.19 Å to 0.095 Å. In the case of oxygen ($m = 2.657 \cdot 10^{-26}$ kg), which is sligtly lighter than Si, the wavelength is 0.126 Å and 0.252 Å for high (1200 K) and low (300 K) temperatures, respectively [12]. Quantum effects are typically only of importance when Λ is much larger than the interatomic distance. In this work, crystalline Si and amorphous SiO_2 are used. The nearest neighbor interatomic distance in a Si crystal is in the range of 2-3 Å. In SiO_2, Si-O, O-O and Si-Si distances are about 1.6 Å, 2.6 Å and 3.1 Å, respectively. From the numbers above, can be therefore concluded that we can safely apply Newton equations in our case.

Another indicator for the validity of MD is *the Heisenberg uncertainty principle*. Accordingly to this principle, the position $\boldsymbol{r}$ and momentum $\boldsymbol{p}$ of a particle cannot be simultaneously measured with an arbitrary accuracy. The principle can be formulated as:

$$\Delta\boldsymbol{p} \cdot \Delta\boldsymbol{r} \geq \frac{h}{2\pi} \tag{2.3}$$

We can thus find the uncertainty in the momentum of a Si (or O) atom as $1.0546 \cdot 10^{-23}$ kg·m·s^{-1} and and a corresponding energy of about 0.007 eV (0.013 eV), if we accept an uncertainty in its position in the order of 0.1 Å, which is much smaller than any bond length considered in this work. It can thus be seen that this energy value is much smaller than any bond strength considered.

In Newtonian dynamics, the atom trajectory is obtained by integrating the equations of motion:

$$\boldsymbol{F}_i = m_i \boldsymbol{a}_i = m_i \frac{d\boldsymbol{v}_i}{dt} = m_i \frac{d^2 \boldsymbol{r}_i}{dt^2} \tag{2.4}$$

where m_i, $\boldsymbol{r}_i$, $\boldsymbol{v}_i$ and $\boldsymbol{a}_i$ are the mass, position, velocity and acceleration of atom i in a Cartesian coordinate system, respectively. Integration algorithms are described in *subsection 2.3.2*. The force $\boldsymbol{F}_i$ that acts on each atom i accelerates the particle i, which in turn leads to a new position, velocity, and acceleration. Forces are derived as the negative gradients of the potential energy (interaction potential) U with respect to atomic positions:

$$\boldsymbol{F}_i = \nabla_{\boldsymbol{r}_i} U(\boldsymbol{r}_1, \dots, \boldsymbol{r}_N) \tag{2.5}$$

The key difficulty in any MD simulation, is therefore to construct (or select) an appropriate interatomic potential. The most widely used interatomic potentials for the Si and/or Si-O system are discussed in *subsection 2.3.7*.

2.3.2 Integration algorithms

Many different algorithms have been presented for numerically solving the Newton’s equation of motion. There are three criteria for the integration algorithm:

(1) conserve total energy and momentum;
(2) be time-reversible;
(3) permit a long time step.

One suitable algorithm complying with these three criteria is the Verlet integration, as popularized in molecular dynamics by the French physicist Loup Verlet in 1967 [103]. The basic idea of *the Verlet algorithm* is to write two third-order Taylor expansions for the positions $\boldsymbol{r}$, one forward and one backward in time. Calling $\boldsymbol{v}$ the velocities, $\boldsymbol{a}$ the accelerations, and $\boldsymbol{b}$ the third derivatives of $\boldsymbol{r}$ with respect to *t*, one has:

$$\boldsymbol{r}(t+\Delta t) = \boldsymbol{r}(t) + \boldsymbol{v}(t)\Delta t + \frac{1}{2}\boldsymbol{a}(t)\Delta t^2 + \frac{1}{6}\boldsymbol{b}(t)\Delta t^3 + O(\Delta t^4) \tag{2.6}$$

$$\boldsymbol{r}(t-\Delta t) = \boldsymbol{r}(t) - \boldsymbol{v}(t)\Delta t + \frac{1}{2}\boldsymbol{a}(t)\Delta t^2 - \frac{1}{6}\boldsymbol{b}(t)\Delta t^3 + O(\Delta t^4) \tag{2.7}$$

Adding the two expressions (*eqs 2.6* and *2.7*) gives

$$\boldsymbol{r}(t+\Delta t) = 2\boldsymbol{r}(t) - \boldsymbol{r}(t-\Delta t) + \boldsymbol{a}(t)\Delta t^2 + O(\Delta t^4) \tag{2.8}$$

where Δt is time step and $O(\Delta t^4)$ is the *truncated error*. These errors are intrinsic to the algorithm and do not depend on the implementation. *Round-off errors* (e.g., related to the finite number of digits used in computer arithmetics) are associated with a particular implimentation of the algorithm. Both errors can only be reduced by decreasing time step Δt, as discussed in *subsection 2.3.6*.

Important advantages of the Verlet algorithm are that the algorithm is straightforward, and the storage requirements are modest. The disadvantage is that the algorithm is of moderate precision. Also, anoter problem with this version of the Verlet algorithm is that velocities are not directly generated, which are required to compute the kinetic energy *K*, whose evaluation is necessary to test the conservation of the total energy *E*. To overcome this difficulty, several alternative algorithms have been developed. Beeman's algorithm and predictor-corrector approaches are also widely used integration techniques. The *Beeman integration scheme* is closely related to the Verlet algorithm. The advantage of this algorithm is that it provides a more accurate expression for the velocities and produces a better energy conservation. The disadvantage is that the more complex expressions make the calculation more expensive.

As mentioned above, conservation of energy is an important criterion in the choice of the integration algorithm. The potential energy *U* and the kinetic energy *K* fluctuate around their respective average values such that the total system energy *E* or system's Hamiltonian $H = K + U$ remains constant. Note that total system energy does not change in time, if Newton's equations are exactly integrated. Two "kinds" of energy conservation may be discerned: short-term and long-term energy conservation. In short-time energy conservation, in which the fluctuation of the total energy is considered from step to step, the Verlet-like algorithms are not overly accurate. An algorithm which performs better in this respect is the so-called *Gear predictor-corrector approach* [104], which tries to use the new forces after a time step to back-correct for the extrapolation in time. In long-time energy conservation, one monitors the energy drift over extended periods of simulation time. In this respect, the Verlet-like algorithms perform very well. The Verlet-like algorithms, including the leap-frog algorithm [105] and the velocity-Verlet algorithm [106], are therefore often the methods of choice for long time calculations. Their success lies in their time efficiency and ease of implementation. The advantage of the *leap-frog algorithm* is that the velocities are explicitly calculated, however, the disadvantage is that they are not defined at the same time as the positions, i.e., the positions and velocities are not synchronized. This means that is not possible to calculate the potential and kinetic energies at the same time. This makes it awkward to evaluate the total system energy (kinetic + potential) at the same time step.

The MD calculations presented in this thesis are based on *the velocity Verlet algorithm* [106]. This algorithm is typically implemented as a three-stage procedure. The standard implementation scheme of this algorithm is:

Calculate position $\boldsymbol{r}(t+\Delta t) = \boldsymbol{r}(t) + \boldsymbol{v}(t)\Delta t + 0.5\boldsymbol{a}(t)\Delta t^2$
Derive acceleration $\boldsymbol{a}(t+\Delta t)$ *from the interaction potential using* $\boldsymbol{r}(t+\Delta t)$
Calculate velocity $\boldsymbol{v}(t+\Delta t) = \boldsymbol{v}(t) + 0.5[\boldsymbol{a}(t) + \boldsymbol{a}(t+\Delta t)]\Delta t$

This algorithm shows an excellent long-time energy conservation, allows the simulateous calculation of potential energy and kinetic energy, shows a reduced error on the velocities compared to the basic Verlet scheme, and is not necessarily more memory consuming than the other Verlet-like algorithms. As a result, this algorithm is perhaps the most widely used integration scheme in MD simulations.

2.3.3 Boundary conditions

Molecular Dynamics is typically applied to relatively small systems containing 10^2–10^7 atoms. Thus, the number of atoms in any MD simulations is small compared to any macroscopic material. Even the simulation of 1 mole of material, containing 6.022 x 10^{23} atoms, using a simple interatomic potential, would take tens of years or a century. Thus, MD simulations inherently face a length scale problem. This problem may be partially resolved by applying certain boundary conditions to the computational cell to mimic an infinite structure.

Various types of boundary conditions have been presented depending on the kind of process to be simulated [107]. When applying *free boundaries (or no boundaries) ("free boundary condition", FBC)*, the cell is surrounded by vacuum. *FBC* is typically used for studying clusters and molecules. Free boundary conditions may in certain cases also be appropriate for ultrafast processes e.g. fast ion/atom bombardment, as the effect of the boundaries is not important due to the short time-scale of the involved processes. In *rigid boundary conditions (RBC)*, atoms at the boundaries of the cell are fixed, in contrast to *FBC*. However, such boundaries are clearly unphysical and may introduce artifacts in the simulation results. Therefore *RBC* are typically only used in combination with other conditions, e.g., stochastic [108, 109] and periodic boundary conditions [110, 111], which is also called as *mixed boundary conditions (MBC)* [107].

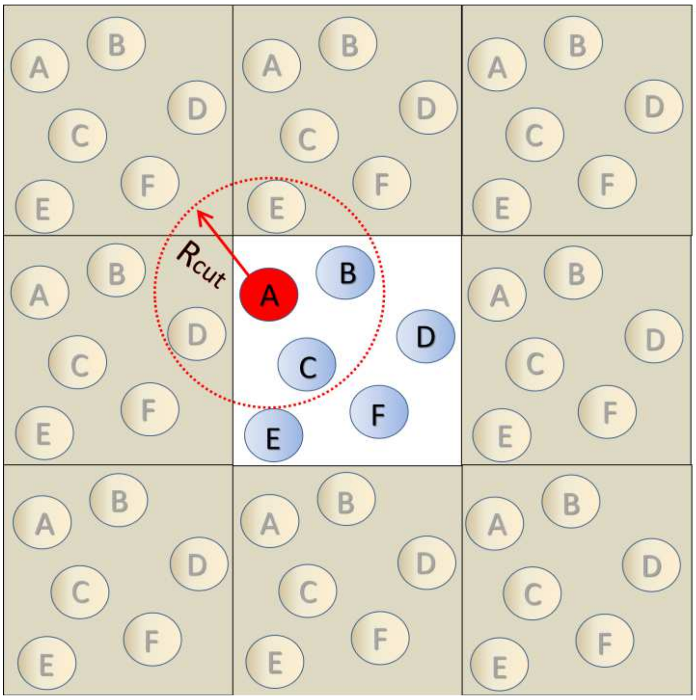

Figure 2.1 *Periodic boundary condition and "minimum image criterion"*

Periodic boundary conditions (PBCs) are the most popular choice of boundary conditions. They are used to simulate processes in a bulk material while keeping the number of atoms limited. The implementation of *PBC* is very simple: the original box or the computational cell (white rectangle) is surrounded by translated copies of itself (figure 2.1). In other words, if an atom in the cell is located at position ***r*** in the box, PBC bring into existence an infinite set of atoms located at $\boldsymbol{r} + l\boldsymbol{a} + m\boldsymbol{b} + n\boldsymbol{c}$, $(l, m, n = -\infty,+\infty)$,where *l, m, n* are integer numbers, and ***a***, ***b***, ***c*** the cell vectors. All atoms in the computational cell are thus replicated throughout space to form an infinite lattice. Each particle in the computational cell is interacting not only with the other particles in the computational box, but also with their images in the adjacent boxes. The choice of the position of the original box (or computational cell) has no effect on the forces or the behavior of the system. If an atom leaves the central box, its replica enters the central box from the other side, and thus the number of atoms in the central box is conserved. However, there are some *limitations* to the use of *PBC*:

(1) The characteristic size of any structural feature in the system or the characteristic length-scale of any important effect should be smaller than the size of the computational cell. For example, in the simuation of the oxide growth on the Si crystal, the selected box volume should be several times bigger than the volume of a SiO_2 molecule. Otherwise, artificial stresses may be generated when silicon expands. Another example is the interaction of the hyperthermal atoms with surface. After impact, the local temperature increases significantly, reaching temperatures of 1000 K and more. The computational cell size should much bigger than the locally “hot” region.

(2) The size of the computational cell should be larger than $2R_{cut}$ (figure 2.1, dotted circle), where R_{cut} is the cutoff distance of the interatomic potential. If this criterion is fulfilled, any atom ***i*** interacts with only one image of any atom ***j***, and it does not interact with its own images. This condition is called the “minimum image criterion”. When this criterion is not fulfilled, an atom *i* may interact with its own images or with multiples images of another atom *j*, which is clearly non-physical.

In my calculations, I used *MBC*, i.e., *PBC* for one or two directions in the simulation box and *FBC* or/and *RBC* for the other direction(s). For example, in the Si crystal, bottom atoms are fixed (*RBC*), while *PBC* are applied parallel to the crystal surface (i.e., x and y axes). On the other hand, in the Si-NW model, *PBC* is applied also along the z-axe, which correspond to a unit cell length. Furthermore, surface atoms are free (*FBC*) in both cases.

Besides applying appropriate boundary conditions, it is also of importance to select a suitable simulation ensemble.

2.3.4 Thermodynamic ensembles

In statistical mechanics (*section 2.1)*, a (thermodynamic) ensemble is a collection of microscopic states (microstate) that all realize an identical macroscopic state (macrostate). From the point of view of statistical mechanics the time average of an *observable* A can be calculated in MD as follows:

$$\langle A\rangle_{time}^{MD} \simeq \frac{1}{n}\sum_{k=1}^{n} A[p^N(t_k), r^N(t_k)] \tag{2.9}$$

where n is the total number of MD-steps, $t_k=k\cdot\Delta t$ is the time after the k^{th} MD-step, and Δt is the time step (see *subsection 2.3.6*). The natural ensemble simulated by molecular dynamics is the microcanonical (isoenergetic) thermodynamic ensemble or *NVE* ensemble, in which the number particles in the box (*N*), the volume (*V*) of the box containing the system atoms and the total system energy (*E*), remain constant. In the *NVE* ensemble, the system does not exchange heat nor matter with the environment, i.e., the system is isolated. This ensemble is therefore suitable to simulate e.g. a cluster in vacuum. It does not allow, however, to control the temperature or the pressure of the system.

Therefore, techniques have been developed to simulate alternative ensembles as well. The two most commenly used ensembles are the isothermal *NVT* ensemble and the isothermal-isobaric *NPT* ensemble, where *T* and *P* represent the system temperature and pressure, respectively. In the *NVT* ensemble, the system is (artificially) in contact with an external heat bath, as explained below. In the *NPT* ensemble, the simulation box can additionally be reduced or enlarged so as to maintain a target pressure.

The equilibrium states of microcanonic, isothermal and isothermal-isobaric ensembles are characterized by a maximum in entropy (*S*), minimum in Helmholtz free energy (*E-TS*) and minimum in Gibbs free energy (*E-TS+PV*) [112], respectively Furthermore, several other ensembles, including the grand canonical (μVT), isobaric-isoenthalpic (*NPH*) and non-equilibrium ensembles are also widely used in molecular dynamics simulations for describing chemical and biologic processes. In my calculations, I use *NVE*, *NVT* and *NPT* ensembles, employing the Berendsen thermostat and barostat to control the temperature and pressure, respectively [113].

2.3.5 The Berendsen thermostat and barostat

Temperature control. The temperature of the system is related to the average kinetic energy per degree of freedom as

$$\langle K\rangle = \langle\frac{mv_{i,\alpha}^2}{2}\rangle = \frac{1}{2}k_B T, \tag{2.10}$$

Using the time average of kinetic energy, the instantaneous temperature *T(t)* may be defined as follows for a finite size system:

$$T(t) = \frac{1}{k_B N_f}\sum_{i,\alpha} m\boldsymbol{v}_{i,\alpha}^2 \tag{2.11}$$

Here, N_f is the number of degrees of freedom. While in the NVT ensemble the *T(t)* is fluctuating, the average *T* is constant. Clearly, the smaller the system, the larger the fluctuations, including fluctuations in the average system temperature. The Berendsen thermostat [113] is used for the controlling the system temperature by rescaling the velocities of the system atoms. As such, the system is weakly coupled to an external thermal bath.

The implementation of the Berendsen thermostat is very simple. Energy is removed or added to the system to maintain a constant temperature. This is accomplished by multiplying the atomic velocities with a scaling factor λ. Thus, new velocities are determined from the current velocities as $\boldsymbol{v}_i' = \lambda\boldsymbol{v}_i$. λ is defined as:

$$\lambda = \sqrt{1 + \frac{\Delta t}{\tau}\left(\frac{T_{bath}}{T(t)} - 1\right)}, \tag{2.12}$$

where τ is a coupling parameter whose magnitude determines how tightly the bath and the system are coupled together, Δt is the time step and T_{bath} is the temperature of the bath. A typical value for Δt/ τ is 0.1 [113].

Pressure control. The pressure in the system can be controlled by the application of a barostat algorithm. One particulary popular example was proposed by Berendsen and co-workers [113]. In this method, the system is coupled to a “pressure bath” (or a piston), analogous to a temperature bath. The pressure is (on average) maintained at a constant value simply by scaling the volume by a factor λ, which is equivalent to scaling the atomic coordinates by a factor $\lambda^{1/3}$:

$$\lambda = 1 - \kappa \frac{\Delta t}{\tau_P}(P(t) - P_{bath}) \tag{2.13}$$

where P_{bath} is the pressure of the bath, κ is the experimental isothermal compressibility, which is related to the volume as:

$$\kappa = \frac{1}{k_B T}\frac{\langle V^2\rangle - \langle V\rangle^2}{\langle V^2\rangle} \tag{2.14}$$

In this scheme, the new positions of the atoms can be found as $\boldsymbol{r}_i' = \lambda^{1/3}\boldsymbol{r}_i$. The instantaneous pressure can be calculated as follows:

$$P(t) = \frac{1}{V(t)}\left(Nk_B T(t) + \frac{1}{D}\langle \textstyle\sum_{i=1}^{N} r_i(t) \cdot F_i(i)\rangle\right) \tag{2.15}$$

where D is the dimensionality of the system.

Alternatively, stochastic coupling methods (e.g., Anderson [114] and Nosé-Hoover [115, 116] methods) are also commonly used methods for the control of system temperature and pressure.

2.3.6 Choosing the time step

All integration schemes (see *subsection 2.3.2*) are approximate and there are errors associated with them. As mentioned before, the Verlet algorithm has a *truncation error* proportional to $O(\Delta t^4)$ for each integration time step. Furthermore, a second type of errors is *round-off errors*, related to errors associated with a particular implementation of an algorithm and to machine precision. Both errors typically significantly increase if the chosen time step (Δt)

is too long. As a result, the MD simulation becomes unstable, i.e., the total energy will rapidly drift with time when the simulation is integrated by a large time step. In extreme cases, the atoms approach each other much too closely such that repulsive interactions become very strong, possibly leading to an "exploding" system. Therefore, for numerical stability and accuracy, one typically needs to pick a time step that is at least one order of magnitude smaller than the fastest time scale in the system. Clearly, the errors of the integration algorithms are quickly reduced by decreasing Δt. However, choosing the time step too short results in an inefficient simulation and waste of computing time.

How can we choose a suitable time step? Unfortunately, there is no standard condition for evaluating the appropriate value of the time step. In most cases, a typical test is to measure the conservation of total energy E in the microcanonical (*NVE*) ensemble, as the total energy drift will depend on the chosen time step.

However, in other thermodynamic ensembles, the (energy) criterium needs to be modified. For example in the isothermic (*NVT*) ensemble, an effective energy $\overline{H}$ can be used to verify the sampling accuracy and to play a role similar to the total energy in the *NVE* ensemble [117]. Furthermore, the appropriateness of the chosen time step also depends on the system temperature and types of system atoms. Specifically, somewhat longer time steps are allowed at lower temperatures, whereas shorter time steps should be used at higher temperatures and for lighter elements. In principle, the relevant time scale should be equal to the period of atomic bond vibrations in the system. For example, an oxygen molecule has a period of vibration of 21 fs, so a time step of the order of 1 fs would be sufficient to resolve this vibrational motion [118]. Most frequently, the time step is chosen in the range 0.05 to 10 fs, depending on the overall behavior, composition and processes of the MD system [112]. Generally, at temperatures in the range 0-1500 K, ReaxFF can run with time steps of up to 0.5 fs and retain reasonable energy conservation. Therefore, in our calculations, *0.25 ps* and *0.5 ps* were chosen for the investigated processes at high (about 1200 K) and low (about 300 K) temperatures, respectively.

As mentioned in the beginning of this chapter, when setting up a molecular dynamics simulation, not only must we decide on a suitable time step and starting conditions, but we must also choose a suitable interaction potential for the chosen Si as well as Si/O systems.

2.3.7 Interaction potentials for Si and Si/O

In a molecular dynamics simulation, atoms dynamically interact with each other. These interactions generate forces that act upon the atoms, which move under the action of these instantaneous forces. As mentioned before, forces are derived as the negative gradients of the potential energy U of a system of N atoms with respect to the atomic positions. Generally, the interaction potential of N atoms consists of many terms related to individual atoms, pairs, triplets, quadruplets and so on:

$$U(\boldsymbol{r}_1, \dots, \boldsymbol{r}_N) = \sum_i \varphi_1(\boldsymbol{r}_i) + \sum_i \sum_{j>i} \varphi_2(\boldsymbol{r}_i, \boldsymbol{r}_j) + \sum_i \sum_{j>i} \sum_{k>j>i} \varphi_3(\boldsymbol{r}_i, \boldsymbol{r}_j, \boldsymbol{r}_k) + \cdots \qquad (2.16)$$

where the first sum is the one-body term, representing the effect of an external field on the system. The second sum accounts for pairwise interactions, the third for three-body contributions, etc. Based on this expansion, interatomic potentials can be classified into two classes: pair potentials (in which only φ_2 is present) and many-body potentials (in which φ_3 and higher terms are also included).

Determination of a suitable potential function is extremely important for a molecular dynamics simulation, as all observed system properties and processes are directly related to this function. The choice of the interatomic potential depends on the area of intended application. There are, however, no “good” or “bad” potentials, only appropriate or inappropriate potentials for a given problem. When choosing a potential, one should consider three basic characteristics: *accuracy* (i.e., reproduce properties of interest as accurately as possible), *transferability* (i.e., can be used to study a variety of properties for which it was not fit) and *computational speed* (i.e., calculations are fast with simple potentials).

Although many potential functions have been presented until now, I here only discuss potentials developed for Si and its oxide. Silicon, as a solid covalent material with directional bonds, cannot be properly described by a pair-potential. Indeed, standard pairwise force-fields may perhaps be suitable for modelling the dynamics of covalently bonded molecules in solution, but these are, in general, unsuitable for bulk crystals in which we may want to describe large deviations from equilibrium. Therefore, many-body potentials are commonly chosen for bulk systems. Frequently used potentials for silicon include the angular-dependent Stillinger-Weber (SW) potential, the bond-order Tersoff potential and the Environment-Dependent Interatomic Potential (EDIP). The *SW potentials* widely used for Si because it more accurately describes elastic properties, phonon dispersion relations, melting point, yield strength and thermal expansion coefficients [119, 120]. However, it has certain serious limitations or transferability. For instance, it is difficult to extend it to an element such as carbon that can have equilibrium configuration. On the other hand, Watanabe and co-workers [121] have also developed SW-based potential for SiO_2 system. However, the stresses in the oxide simulated by this potential is larger from experiment. The *Tersoff potential* also particularly used for Si system including simple and diamond cubic Si, as well as Si_2 dimers [122, 123].The behavior of the potential so parameterized was tested by comparing it to results from a number of ab initio simulations, mainly of lattice defect structures. However, the Tersoff potential does not properly reproduce the force of $Si|SiO_2$ systems at low temperature (e.g., 300 K). The *EDIP* [124] combines the approaches used in the SW and Tersoff potentials. The highly involved parameterization of this potential results in good transferability to certain types of silicon lattice defect structures [125]. This force field much better describes the silicon systems, however, it also has some aforementioned disadvantages as SW and Tersoff potentials have. Moreover, several potentials have been developed and implemented for only silica (SiO_2) structures as well [e.g, 126, 127]. Indeed, while all aforementioned potentials are very often used, they only describe either Si or SiO_2.

A recently proposed generic potential is the reactive force field "*ReaxFF*", developed by A. van Duin [128], which has successfully been applied to both Si and SiO_2 systems [129]. This potental shows a high accuracy, sometimes comparable to DFT, good transferibility (i.e., applicable to a wide range of chemical environments) and high computational speed comparing with quantum calculations. Therefore, all simulations presented in this work were carried out using this potential. Our choice for ReaxFF is based on the fact that it has been parameterized to describe deformations and strains including bond breaking and formation and its ability to accurately describe the expansion of the Si crystal during the oxide formation process.

2.4 ReaxFF potential

2.4.1 Background

ReaxFF is a classical force field with parameters optimized against both experimental and quantum mechanical (QM) data for reaction energies, reaction barriers and configuration energies as well as geometrical and structural data. ReaxFF accurately simulates bond breaking and bond formation processes, commonly approaching QM accuracy. Thus, ReaxFF serves as a link between QM and empirical (unreactive) force fields [130]**.** The main difference between traditional unreactive force fields and ReaxFF is that in ReaxFF the connectivity is determined by bond orders calculated from interatomic distances that are updated every MD step. This allows for bonds to break and form during the simulation [131]. Therefore, in this work, all investigations were carried out using this reactive potential instead of a non-reactive potential.

ReaxFF is capable of describing both covalent and ionic bonds, as well as the entire range of intermediate interactions, and has until now been successfully applied to describe nearly half of the periodic table of the elements and their compounds, including metals (e.g., Cu, Al, Mg, Ni, Pt, etc) and metal-catalyzed reactions [132-134], metal oxides [135], metal hydrides [136], metalloids (e.g., Si) [137] and their oxides (SiO_2) [138-140] together with silica-water interfaces [141], non-metals (C, O, H, N), hydrocarbons [128, 131], as well as organic [142, 143] and complex molecules [144].

2.4.2 Potential functions

Overall system energy. The total system energy is divided into several partial energy contributions. I here briefly introduce the most important energy terms. The total energy of the system is given by *equation 2.17*:

$$E_{system} = E_{bond} + E_{over} + E_{under} + E_{lp} + E_{val} + E_{pen} + E_{tors} + E_{conj} + E_{vdWaals} + E_{Coulomb} \tag{2.17}$$

These partial contributions include bond energies E_{bond}, over-coordination penalty energies E_{over}, under-coordination energies E_{under}, lone-pair energies E_{lp}, valence angle energies E_{val}, energy penalty for handling atoms with two double bonds E_{pen}, torsion angle energies E_{tors}, conjugated bonds energies E_{conj} and terms to handle non-bonded interactions, i.e., van der Waals $E_{vdWaals}$ and Coulomb $E_{Coulomb}$ interactions. All terms except the last two are bond-order dependent, i.e. will contribute more or less to a given bond depending on the local environment of each atom.

Bond order. ReaxFF calculates chemical bonds directly from the instantaneous interatomic distances $\boldsymbol{r}_{ij}$, which are updated in every time step. The total bond is partitioned into contributions from sigma-bonds (single bond), pi-bonds (double bonds) and double pi-bonds (triple bonds):

$$BO'_{ij} = BO'^{\sigma}_{ij} + BO'^{\pi}_{ij} + BO'^{\pi\pi}_{ij} = exp\left[p_{bo,1}\left(\frac{r_{ij}}{r_0^{\sigma}}\right)^{p_{bo,2}}\right] + exp\left[p_{bo,3}\left(\frac{r_{ij}}{r_0^{\pi}}\right)^{p_{bo,4}}\right] + exp\left[p_{bo,5}\left(\frac{r_{ij}}{r_0^{\pi\pi}}\right)^{p_{bo,6}}\right] \tag{2.18}$$

The obtained bond orders *BO'* are corrected for overcoordination [128] as follows:

$$BO_{ij} = BO'_{ij} \cdot f_1(\Delta'_i, \Delta'_j) \cdot f_4(\Delta'_i, BO'_{ij}) \cdot f_5(\Delta'_j, BO'_{ij}) \tag{2.19}$$

where Δ'_i is the deviation of atom *i* from its optimal coordination number, $f_1(\Delta'_i, \Delta'_j)$ enforces an over-coordination correction and $f_4(\Delta'_i, BO'_{ij})$, together with $f_5(\Delta'_j, BO'_{ij})$ account for a 1-3 bond order correction.

Bond energy. The bond energy is determined solely from corrected bond orders *BO:*

$$E_{bond} = -D_e^{\sigma} \cdot BO_{ij}^{\sigma} \cdot exp\left[p_{be,1}\left(1 - \left(BO_{ij}^{\sigma}\right)^{p_{be,2}}\right)\right] - D_e^{\pi} \cdot BO_{ij}^{\pi} - D_e^{\pi\pi} \cdot BO_{ij}^{\pi\pi} \tag{2.20}$$

Equation 2.20 ensures that the energy and force associated with a bond smoothly go to zero as the bond breaks.

Lone pair energy. This energy term accounts for unpaired electrons of an atom using the following equation:

$$E_{lp} = \frac{p_{lp} \cdot \Delta_i^{lp}}{1 + exp\left(-75 \cdot \Delta_i^{lp}\right)} \tag{2.21}$$

where $\Delta_i^{lp} = n_{opt}^{lp} - n_i^{lp}$ corresponds to the number of unpaired electrons. This energy is important for describing atoms with defective bonds. Lone electron pairs on heteroatoms such as oxygen and nitrogen can affect dramatically the response of these atoms to over- and undercoordination.

Overcoordination energy. For an overcoordinated atom, the following equation imposes an energy penalty on the system:

$$E_{over} = \frac{\alpha}{\Delta_i^{lpcorr} + Val_i} \cdot \Delta_i^{lpcorr} \cdot \left[\frac{1}{1 + exp(\lambda_6) \cdot \Delta_i^{lpcorr}}\right] \tag{2.22}$$

where

$$\alpha = \sum_{j=1}^{nbond} p_{be,3} BO_{ij} \tag{2.22a}$$

$$\Delta_i^{lpcorr} = \beta - \Delta_i^{lp} \cdot \frac{1}{1 + \lambda_6 \cdot exp(\lambda_{32} \cdot \gamma)} \tag{2.22b}$$

$$\beta = \sum_{j=1}^{nbond} BO_{ij} - Val_i \tag{2.22c}$$

$$\gamma = \sum_{j=1}^{neighbors(j)} \left(\Delta_j - \Delta_j^{lp}\right) BO_{ij}^{\pi} \tag{2.22d}$$

Here, *Val_i* is the number of bonding electrons of the atom, which binds to other atoms.

Undercoordination energy. If the bond between atoms *i* and *j* is a π-bond, the energy due to the resonant π-electrons between these atomic centers is determined by the following equation (undercoordination energy):

$$E_{under} = -p_{under} \cdot \frac{1 - exp\left(\lambda_7 \cdot \Delta_i^{lpcorr}\right)}{1 + exp\left(-\lambda_8 \cdot \Delta_i^{lpcorr}\right)} \cdot f_6(i, \lambda_9, \lambda_{10}) \tag{2.23}$$

where

$$f_6(i, \lambda_9, \lambda_{10}) = \left(1 + \lambda_9 \cdot exp\left(\lambda_9 \cdot \sum_{j \in neighbors(i)} \left(\Delta_j - \Delta_j^{lp}\right) \cdot \left(BO_{ij}^{\pi} + BO_{ij}^{\pi\pi}\right)\right)\right)^{-1} \quad (2.24a)$$

Valence angle energy. The energy associated with vibration around the optimum valence angle between atoms *i*, *j* and *k* is calculated as follows:

$$E_{val} = f_7(BO_{ij}) \cdot f_7(BO_{jk}) \cdot f_8(\Delta_j) \cdot \left\{k_a - k_a \cdot exp\left[-k_b(\Theta_0 - \Theta_{ijk})^2\right]\right\} \quad (2.24)$$

where

$$f_7(BO) = 1 - \exp\left(-\lambda_{11} BO^{\lambda_{12}}\right) \quad (2.24a)$$

$$f_8(\Delta_j) = \frac{2 + \exp\left(-\lambda_{13} \cdot \Delta_j\right)}{1 + exp\left(-\lambda_{13} \cdot \Delta_j\right) + \left(p_{v,1} \cdot \Delta_j\right)} \cdot \left[\lambda_{14} - (\lambda_{14} - 1) \cdot \frac{2 + \exp\left(\lambda_{15} \cdot \Delta_j\right)}{1 + \exp\left(\lambda_{15} \cdot \Delta_j\right) + \exp\left(-p_{v,2} \cdot \Delta_j\right)}\right] \quad (2.24b)$$

$$\Theta_0 = \pi - \Theta_{0,0}\{1 - exp[-\lambda_{18}(2 - SBO2)]\} \quad (2.24c)$$

$$\begin{aligned} &SBO2 = 0 \ if \ SBO \leq 0 \\ &SBO2 = SBO^{\lambda_{17}} \ if \ 0 < SBO < 1 \\ &SBO2 = 2 - (2 - SBO)^{\lambda_{17}} \ if \ 1 < SBO < 2 \\ &SBO2 = 2 \ if \ SBO > 2 \end{aligned}$$

$$SBO = 1 - \left[\prod_{n=1}^{neighbors(j)} \exp\left(-BO_{jn}^{8}\right)\right] \left(\Delta_j - \lambda_{34}\Delta_j^{lp} + \sum_{n=1}^{neighbors(j)} BO_{jn,\pi}\right) \quad (2.24d)$$

The equilibrium angle Θ_0 for Θ_{ijk} depends on the sum of π-bond orders (*SBO*) around the central atom *j*. Here, *SBO*=0, 1 and 2 means the equilibrium angle will be around 109.47^0 for sp^3 hybridization, 120^0 for sp^2 hybridization and 180^0 for sp hybridization, respectively. It is important to note that the energy contribution from valence angle terms goes to zero as the bond orders in the valence angle goes to zero.

Penalty energy. To describe systems with two double bonds sharing an atom in a valence angle, an additional energy penalty is imposed for such systems:

$$E_{pen} = \lambda_{19} \cdot f_9(\Delta_j) \cdot exp\left[-\lambda_{20} \cdot (BO_{ij} - 2)^2\right] \cdot exp\left[\lambda_{20} \cdot (BO_{jk} - 2)^2\right] \qquad (2.25)$$

where

$$f_9\left(\Delta_j\right) = \frac{2+\exp\,(-\lambda_{21}\cdot\Delta_j)}{1+exp\left(-\lambda_{21}\cdot\Delta_j\right)+exp(\lambda_{22}\cdot\Delta_j)} \qquad (2.25a)$$

Torsion angle energy. The energy associated with a torsion angle ω_{ijkl} (i.e., the middle bond of three bonds formed by four atoms maintaining a certain angle) is computed as

$$E_{tors} = f_{10}(BO_{ij}, BO_{jk}, BO_{kl}) \cdot sin\Theta_{ijk} \cdot sin\Theta_{jkl} \cdot \left[\frac{1}{2}V_2 \cdot exp\left\{p_t\left(BO_{jk} - 3 + f_{11}\left(\Delta_j, \Delta_k\right)\right)^2\right\} \cdot \left(1 - cos2\omega_{ijkl}\right) + \frac{1}{2}V_3 \cdot \left(1 + cos3\omega_{ijkl}\right)\right] \qquad (2.26)$$

where

$$f_{10}\left(BO_{ij}, BO_{jk}, BO_{kl}\right) = \left[1 - exp\left(-\lambda_{23} \cdot BO_{ij}\right)\right] \cdot \left[1 - exp(-\lambda_{23} \cdot BO_{jk})\right] \cdot \left[1 - exp(-\lambda_{23} \cdot BO_{kl})\right] \qquad (2.26a)$$

$$f_{11}\left(\Delta_j, \Delta_k\right) = \frac{2+exp\,(-\lambda_{24}\cdot(\Delta_j+\Delta_k))}{1+ex\,p[-\lambda_{24}\cdot(\Delta_j+\Delta_k)]+ex\,p[-\lambda_{25}\cdot(\Delta_j+\Delta_k)]} \qquad (2.26b)$$

As in the valence energy term, the torsional contribution from a four-body structure should vanish as any of its bonds dissociates.

Conjugation energy. A conjugated system is a system of connected pi-orbitals with delocalized electrons. In general, the overall energy of the system may be lowered in this case, and thus the system stability increases. The contribution of the conjugation effects to the system energy is described as follows:

$$E_{conj} = f_{12}\left(BO_{ij}, BO_{jk}, BO_{kl}\right) \cdot \lambda_{26} \cdot [1 + (cos^2\omega_{ijkl} - 1)] \cdot sin\Theta_{ijk} \cdot sin\Theta_{jkl} \qquad (2.27)$$

where

$$f_{12}\left(BO_{ij}, BO_{jk}, BO_{kl}\right) = exp\left[-\lambda_{27} \cdot (BO_{ij} - 1.5)^2\right] \cdot exp\left[-\lambda_{27} \cdot (BO_{jk} - 1.5)^2\right] \cdot exp[-\lambda_{27} \cdot (BO_{kl} - 1.5)^2] \quad (2.27a)$$

As shown in the equation, the conjugation energy has a maximal contribution to the total system energy when successive bonds have bond-order values of 1.5.

Taper correction [145] is employed by ReaxFF to avoid energy discontinuities when atoms move in and out of the non-bonded cutoff radius. Each energy and derivative of the non-bonded interactions is multiplied by a Taper-term, which is taken from a distance-dependent 7th order polynomial:

$$Tap(r_{ij}) = \sum_{m=0}^{7} Tap_m \cdot r_{ij}^m \quad (2.28)$$

where

$$\begin{aligned} Tap_0 &= 1 \\ Tap_1 &= 0 \\ Tap_2 &= 0 \\ Tap_3 &= 0 \\ Tap_4 &= -35 \cdot r_{cut}^{-4} \\ Tap_5 &= 84 \cdot r_{cut}^{-5} \\ Tap_6 &= -70 \cdot r_{cut}^{-6} \\ Tap_7 &= 20 \cdot r_{cut}^{-7} \end{aligned} \quad (2.28a)$$

Here, r_{cut} is the non-bonded cutoff radius, which is typically set to 10 Å in ReaxFF.

Van der Waals interactions. In addition to valence interactions which depend on overlap, non-bonded van der Waals interactions are also included. The net interaction is the sum of the repulsive interactions at short interatomic distances due to Pauli principle orthogonalization and attractive interactions at long distances due to dispersion. To account for these non-bonded interactions, ReaxFF uses a distance-corrected Morse potential including Taper terms:

$$E_{vdWaals} = Tap(r_{ij}) \cdot D_{ij} \cdot \left\{exp\left[\alpha_{ij} \cdot (1 - \frac{f_{13}(r_{ij})}{r_{vdW}})\right] - 2 \cdot exp\left[0.5\alpha_{ij} \cdot (1 - \frac{f_{13}(r_{ij})}{r_{vdW}})\right]\right\} \quad (2.29)$$

where

$$f_{13}(r_{ij}) = [r_{ij}^{\lambda_{29}} + \left(\frac{1}{\gamma_\omega}\right)^{\lambda_{28}}]^{1/\lambda_{28}} \quad (2.29a)$$

Coulomb interactions. Like van der Waals interactions, Coulomb interactions need to be computed between all atom pairs:

$$E_{Coulomb} = C \cdot Tap(r_{ij}) \cdot \frac{q_i \cdot q_j}{\left[r_{ij}^3 + (1/\gamma_{ij})^3\right]^{1/3}} \quad (2.30)$$

There are no long-range electrostatic interactions in ReaxFF. Thus, all Coulomb interactions are confined to the outer cutoff radius r_{cut} = 10 Å as mentioned above. Atomic charges are calculated using the Electron Equilibration Method (EEM) [146]. EEM parameters are typically optimized against Mulliken charge distributions obtained from DFT calculations.

In practice, some energies terms, i.e., conjugation, penalty and torsion energies, are almost zero and virtually negligible in ReaxFF applied to Si/O. Therefore, these energy contributions could be removed from force field for the silicon and silicon oxide system.

2.4.3 Force field parameterization, validation and application

Parameters for interatomic potentials are usually obtained by optimization against a set of data obtained from QM and/or from empirical data. For the parameters of the Si/O Reax force field ($\text{ReaxFF}_{\text{SiO}}$) as used in this work, optimization was carried using a single-parameter search optimization method to minimize the sum of squares error function

$$error = \sum_{i=1}^{n} \left[\frac{\left(\lambda_i^{QM} - \lambda_i^{ReaxFF}\right)}{\sigma}\right]^2 \quad (2.31)$$

where λ^{QM} is the QM value, λ^{ReaxFF} is the ReaxFF calculated value, and σ is the accuracy specified in the training set (see *e.g.*, [131]). Note that ReaxFF does not include the concept of multiple spin states and is parametrized to reproduce the energy corresponding to the lowest energy spin state.

In this work, I used the force field parameters employed by Buehler et al [137], which is a modified version of the original force field for Si/O/H parameters described by van Duin and co-workers [129]. The original force field was trained extensively against both Si and SiO_2 phases, including bond dissociation, angle bending, under/overcoordination, key reactions (including transition states), charges and condensed phase data (i.e., equations of states, heats of formation, etc.). The validation of the $ReaxFF_{SiO}$ results have been presented by the developers comparing ReaxFF results with DFT and experiment. They demonstrated that the potential correctly describes the equation of states of α-Si, β-Si and cubic Si as well as α-crystobalite, coesite, and stishovite SiO_2. For these systems, cohesive energy, condensed phase stability and densities are fairly close to the quantum chemistry data and experiment. Furthermore, Fogarty and co-workers [141] presented the potential validation for the amorhous silica (*a*-SiO_2) system as well. They reported that the silica density in $ReaxFF_{SiO}$ is fairly close to experimental data, while somewhat lower than classical MD results. They also demonstrated that Si-O, Si-Si, and O-O distances as well as Si-O-Si and O-Si-O bond angles are also close to both experiment and classical MD results. The Si/O force field has previously successfully been applied for the study of self-assembly of silica nanocages [138], crack propogations in Si [137], silica-water interactions [141], etc.

However, while the force field was extensively trained against Si and SiO_2 phases, Si suboxide components were not taken into account. Nevertheless, a force field evaluation against suboxide stabilities and oxygen migration barriers is warranted to validate the results obtained in this work. Wherever comparison with experiment or ab-initio data is available, the current force field reproduces these data faithfully [139, 140]. A detailed description of the force field [137] can be found in *Appendix 1*.

2.4.3 Pros and cons of the potential

Accuracy. As mentioned before, ReaxFF is typically fitted very extensively to quantum mechanical (QM) data, and is often found to approach QM accuracy. Results obtained using ReaxFF are fairly close to the DFT data.

Transferability. The concept of ReaxFF is to provide a generic description of interatomic interactions. Each element is described by just one atom type, allowing good transferability of the force field to new systems and avoiding complicated atom type modifications during chemical reactions. The force field currently describes ten of elements and their components.

Computational speed. ReaxFF is several orders of magnitude faster than quantum mechanical calculations. However, ReaxFF is 20-100 times more time consuming than simple empirical force fields such as CHARMM [147], DREIDING, or covalent type Tersoff potentials [122].

System size. ReaxFF allows for reactive MD-simulations on systems containing more than 1000 atoms. The low computational cost of ReaxFF (compared to QM) makes the method suitable for simulating reaction dynamics for relatively large systems. However, the number is may not enough describing certain systems and processes. Therefore, parallel ReaxFF (GRASP/Reax, USC/reax, Purdue/Reax, incorporation into LAMMPS ongoing, F-ReaxFF, etc.) implementations been realized, allowing reactive simulations on more than a million atoms [148] and even up to a billion atoms [149].

Parameterization. In comparison with any other interatomic potential, ReaxFF can be considered as very accurate. On the other hand, it is also relatively complex because of the many required terms, for which many aforementioned parameters need to be fitted via *ab-initio* calculations.

2.5 Reax code – reactive MD code

For the simulation of the Si oxidation process, I use the original, non-commercial Reax code developed by Prof. A.C.T. van Duin. The original version of the code is written in Fortran 77. The flow chart of the Reax program is presented in figure 2.2.

The code is basically divided in six parts: reac.f, poten.f, ffopt.f, vibra.f, blas.f and shanno.f. The general MD routine is contained in *reac.f*. In *poten.f*, the actual potential energy contributions are calculated. Force field optimization is done in *ffopt.f*. BLAS (Basic Linear Algebra Subprograms) routines are provided in the *blas.f*. *Vibra.f* is included in the code for calculating vibrational frequencies. Furthermore, both the conjugate gradient and the steepest descent energy minimization methods are also included in the code and contained in *shanno.f*. Some details of the minimization metod are discussed in *chapter 2.6*. Program parameters are defined in *cbka.blk*.

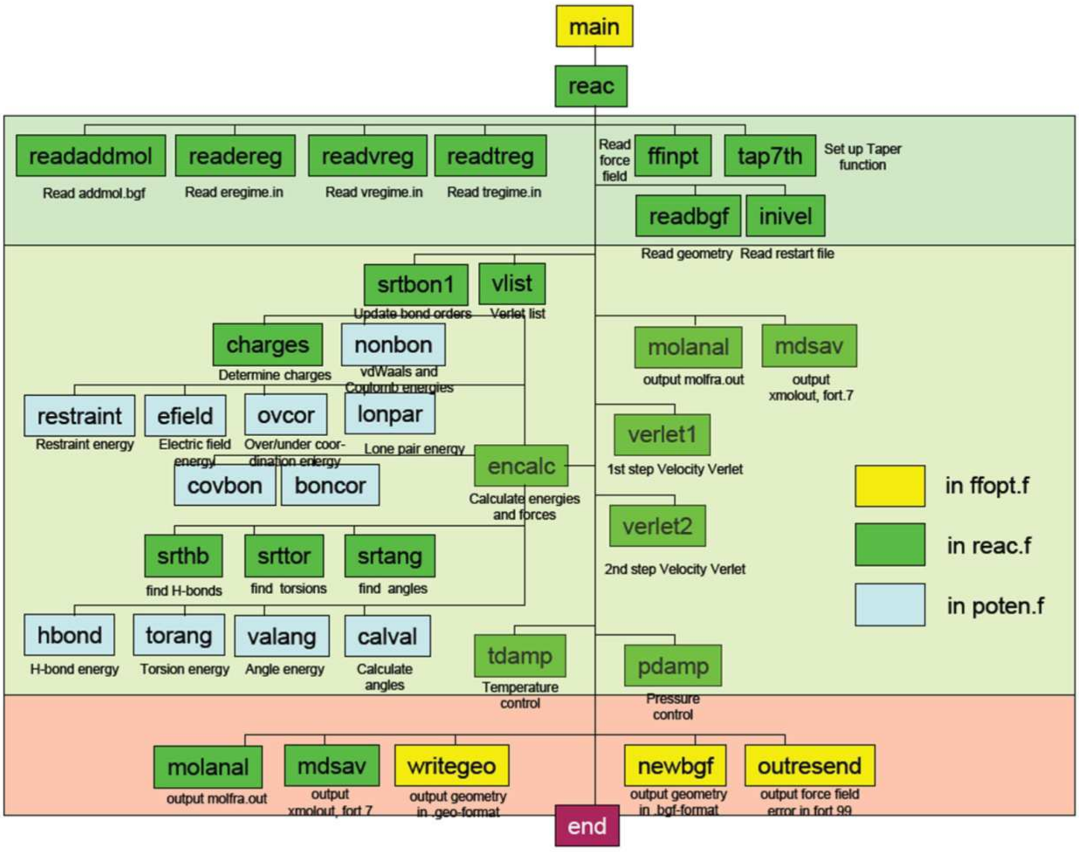

Figure 2.2. *Flow-chart of the Reax code. The figure was presented by A.C.T van Duin in the training session at NASA AMES (August 2006).*

2.6 Energy minimization methods

Many minimization algorithms have been developed to find the minimum energy of a system. Especially derivative minimization methods are successfully used for the energy minimization. The derivative methods can be classified as zero-order methods, which do not use any derivatives, first-order methods, which use first derivatives (i.e., the gradients) and second-order methods, which use both first and second derivatives. The basic criterium is follows: at a minimum point in the energy landscape, the first derivatives of the energy function E (x_1, x_2 , …, x_i) should be zero, while the second derivatives are all positive, that is:

$$\frac{\partial E}{\partial x_i} = 0 \qquad \frac{\partial^2 E}{\partial x_i^2} > 0 \tag{2.32}$$

Derivatives may be obtained either analytically or numerically. As shown in figure 2.3, there are two type special points, i.e., energy minima and the saddle point between two minima, where the first derivative of energy function is zero with respect to all coordinates.

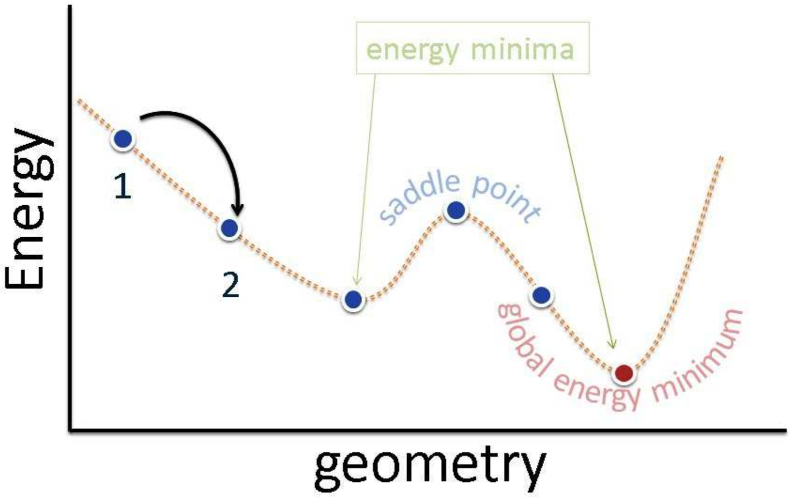

Figure 2.3 *A schematic one-dimensional energy surface. The process of energy minimization changes the geometry of the system in a step-wise fashion until a minimum is reached.*

Minimization methods move the system energy closer and closer to the minimum point by gradually changing the geomery of the system. This process is called geometry optimization. The optimization is basically done using an iterative formula as follows:

$$x_{new} = x_{old} + correction \tag{2.33}$$

In the equation, x_{new} refers to the 3N coordinates specification of the geometry at the next step (for example, moving from step 1 to 2 in the figure), x_{old} refers to the system geometry at the current step, and *correction* is some adjustment made to the geometry. In all these methods, a numerical test is applied to the new geometry (x_{new}) to decide if a minimum is reached. For example, the slope may be tested to see if it is zero within some numerical tolerance. If the criterion is not met, then the formula is applied again to make another change in the geometry. For example, in the *Newton-Raphson (NR) method*, the aforementioned equation for updating the geometry is

$$x_{new} = x_{old} - \frac{E\prime(x_{old})}{E"(x_{old})} \tag{2.34}$$

Note that the correction term depends on both the first derivative (also called the slope or gradient) of the potential energy surface at the current geometry and also on the second derivative (also called the curvature). Therefore, the method is very expensive per step, although it usually requires the fewest steps to reach the minimum.

An algorithm based on *the steepest descent (SD) method* is used to find nearest local minima nearby a given initial point. In this method, the second derivative of the function is assumed to be constant and therefore the method is much faster per step than the NR method. The equation for the method is written as:

$$x_{new} = x_{old} - \gamma E'(x_{old}) \tag{2.35}$$

where γ is a constant. Due to the approximation, however, this method is not highly efficient and many steps are required for finding the energy minimum.

Another alternative is *the conjugate gradient (CG) method*. In this method, the gradients of the current geometry are first computed. The direction of the largest gradient is determined. The geometry is minimized along this one direction (this is called a line search). Then, a direction orthogonal to the first one is selected (a “conjugate” direction). The geometry is subsequently minimized along this direction. This continues until the geometry is optimized in all directions.

Chapter 3

Goal & Scope of this Thesis

In this thesis, I aim to reach two goals. The *first goal* is a better understanding of the Si oxidation mechanisms, and comparing with already existing oxidation models. The general silicon oxidation model (Deal-Grove mechanism) and its extensions (Massoud, Kao etc) have successfully elucidated various aspects of the oxidation mechanism under different conditions. These models, however, do not entirely describe the oxidation processes in my systems. For example, the Deal-Grove model clearly fails to describe the ultrathin oxide growth and therefore Massoud's extension has been introduced. However, few studies address ultrathin oxides with a thickness less than 2 nm. On the other hand, Kao and co-workers developed their model for only wet oxidation of Si-NW in the micrometer scale. In MOSFET technology, however, dry oxidation plays a significant role for getting ultrathin gate oxides.

The *second goal* is the analysis of the obtained nanostructures. Both the hyperthemal Si|SiO_2 interface and SiO_2 covered small Si-NWs have been poorly studied. Basic understanding of such structures is an important issue for nanoelectronic technology.

This work is divided into two parts: (1) hyperthermal oxidaton of Si(100) surfaces, discussed in chapters 4-7, and (2) thermal oxidation of small Si nanowires, discussed in chapters 8-9.

In *chapter 4*, the effect of single-impacts in low-energy (thermal – 100 eV) bombardment of a Si(100){2x1} surface by atomic and molecular oxygen is investigated. Penetration probability distributions, as well as defect formation distributions, are presented as a function of the impact energy for both species. It is found that at low impact energy, defects are created chemically due to the chemisorption process in the top layers of the surface, while at high impact energy, additional defects are created by knock-on displacement of Si and oxygen implantation.

The possibility of tuning the structure of ultrathin oxide on a crystalline Si surface is discussed in *chapter 5*. The growth mechanism of ultrathin silica (SiO_2) layers during hyperthermal oxidation is studied at room temperature. Oxidation of Si(100){2x1} surfaces by both atomic (O) and molecular oxygen

(O_2) is investigated in the energy range 1-5 eV. The oxidation mechanism at room temperature, which differs from thermal oxidation, is also discussed. The results show that control over the oxide thickness is possible by choosing the energy and type of oxygen species (O, O_2).

Chapter 6 is devoted to the hyperthermal Si|SiO_2 interface as a continuation of the discussions in chapter 5. In this chapter, the interface morphology and interfacial stresses during hyperthermal oxidation at room temperature are carefully studied. Interface thickness and roughness, as well as the bond-length and bond-angle distributions in the interface are also discussed and compared with other models developed for the interfaces induced by traditional thermal oxidation. Furthermore, the formation of a compressive interfacial stress during oxidation is observed.

General oxide growth mechanisms in hyperthermal oxidation are studied in *chapter 7*. Therefore, in this chapter, the growth mechanism of ultrathin silica (SiO_2) layers on the Si(100){2x1} surface during hyperthermal oxidation (impact energies of O and O_2 in the range of 1 to 5 eV) is investigated as a function of temperature in the range 100 – 1300 K. Two different growth mechanisms are found, corresponding to low temperature and high temperature oxidation. Also, the initial step of the Si oxidation process is analyzed in detail.

The second part of this work, described in *chapters 8* and *9*, is devoted to small *c*-Si|SiO_x|*a*-SiO_2 nanowires, which are envisaged to be used in Si-NW field-effect transistors. In these chapters, the occurrence of two temperature-dependent oxidation mechanisms of ultra-small diameter Si-NWs with initial diameters in the range of 1-3 nm is demonstrated. In chapter 8, two different oxidation mechanisms are discussed and compared with the Kao model: a self-limiting process that occurs at lower temperature than a specific transition temperature, resulting in a Si core | ultrathin SiO_2 silica shell nanowire, and a complete oxidation process that takes place above the transition temperature, resulting in the formation of an ultrathin SiO_2 silica nanowire. The transition temperature is found to linearly decrease with the nanowire curvature.

Finally, in *chapter 9*, it is demonstrated that control over the Si-core radius and the SiO_x ($x \leq 2$) oxide shell is possible by tuning the growth temperature and the initial Si-NW diameter. Stress calculations were also performed to study the oxidation behavior of these ultra-small nanowires. Specifically, the interfacial stress is found to be responsible for the self-limiting oxidation, depending on both the initial Si-NW radius and the oxide growth temperature.

Part II

RESULTS AND DISCUSSIONS

Hyperthermal oxidation of Si surfaces

Chapter 4

Hyperthermal oxygen interacting with Si surfaces: adsorption, implantation and damage creation

4.1 Introduction

The reaction behavior of oxygen during the initial stage of Si(100) thermal oxidation has been carefully investigated both experimentally [60, 150-156] and theoretically [157, 158]. It is generally accepted that the adsorption probability of thermal oxygen atoms at room temperature is much higher than that of molecular oxygen [150-153, 159-161]. Namely, molecular adsorption has a rather low probability, in the order of 0.0002 – 0.2, which decreases with increasing incident energy in the thermal energy regime due to the trapping ability of the surface [154, 155]. At thermal energy, molecular oxygen frequently scatters, while in the hyperthermal energy regime, dissociative scattering, atom abstraction and charge transfer are often observed [29, 51, 161]. Thus, the oxidation character of hyperthermal oxygen species becomes significantly changes with increasing impact energy. Thus, while various theoretical and experimental studies are devoted to investigate the initial oxidation process of Si, the probabilities for penetration, desorption and implantation during this stage have not yet been investigated in full detail [60, 61]. On the other hand, mechanisms of adsorption and desorption have previously been analyzed by first-principles calculations [157, 158, 162]. Due to computational limits, however, these calculations cannot probe e.g. implantation probability distributions or defect formation at higher impact energies. Therefore in this chapter, I investigate the impact behaviour of both atomic and molecular oxygen as a function of impact energy on a pristine Si(100){2x1} surface near room temperature. This work was published in the Journal of Physical Chemistry C [163].

4.2 Computational details

In this work, MD simulations are used to trace the impact behaviour of oxygen on the silicon surface. The Reactive Force Field ($ReaxFF_{SiO}$) potential is employed for describing interaction of Si and O atoms [129].

In our all simulations related to hyperthermal Si oxidation (*chapters 4-7*), a {2x1} reconstructed Si(100) surface is chosen, with dimensions 21.7 Å x 21.7 Å x 27.1 Å. A side view and top view of the resulting structure are shown in figure 4.1. The chosen rectangular Si bulk contains 640 atoms. In the (x,y) plane of the system, 20 atomic layers are positioned at distances of about 1.3 Å from each other in the z direction. Thus, the number of Si atoms per layer is 640/20 = 32 atoms. Periodic boundary conditions are applied to the (x,y) plane, to mimic a laterally infinite surface. Prior to oxygen impact, the Si(100){2x1} surface was treated as follows: First, the surface is equilibrated at 333 K using the Berendsen heat bath (NVT dynamics). Then, the obtained structure is relaxed in the microcanonical ensemble for 5 ps. The radial distribution function of the resulting structure shows peaks at 2.32, 3.77, and 4.46 Å, which is in good correspondence with the experimental values of 2.35, 3.84, and 4.50 Å [164].

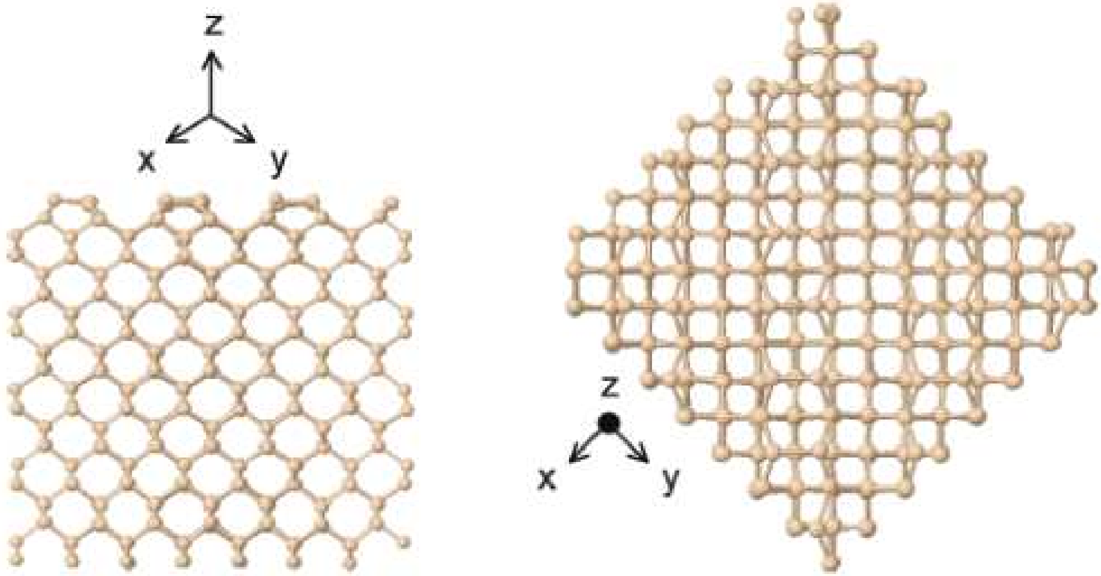

Figure 4.1 *Side view and top view of the Si(100){2x1} substrate.*

Oxygen impacts are performed using the following procedure: the incident particle (oxygen atom or oxygen molecule) is positioned at 5 Å above the highest Si-atom of the crystal, perpendicular to the surface, while its location in the surface plane is chosen randomly. In the case of molecular oxygen, the O_2 molecule is rotated randomly prior to impact. Depending on the oxygen source, the impinging particle is either launched randomly at the surface, in the thermal case, or directed normal to the surface to describe the laser detonation for the hyperthermal impacts [46, 47]. All impacts are non-consecutive, i.e., each impact occurs on a pristine Si-surface, and monitored for 3 ps. The impinging particle was given a kinetic energy equal to 0.028 eV (here below referred to as thermal), 1, 5, 10, 31.6, 50 and 100 eV and each case is repeated 1000 times to gather statistically valid results.

4.3 Results and discussion

4.3.1 Oxygen penetration probability distributions

In figure 4.2, the penetration probability distributions are shown for atomic and molecular oxygen as a function of the impacting energy on the Si(100){2x1} surface at 333 K. Interestingly, the chemisorption process of O_2 is found, in all cases, to be dissociative, which implies that, even in the case of the impact of molecular oxygen, the O radicals penetrate the surface. In the low energy regimes (thermal and 1 eV), the deposition behaviour is very similar for the atomic and the molecular forms: after impact, most of the oxygen atoms are located in the uppermost Si-layer and the first subsurface layer (note that in the case of the {2x1} reconstruction of Si(100), the atoms belonging to the first and about half of the atoms of the second subsurface layer are not covered by the surface atoms). The oxygen atoms are found to migrate from the topmost layer to a back-bond centre (after dissociation in the case of O_2), in good agreement with previous reports based on first-principles simulations [157]. Most atoms cannot move deeper into the bulk due to the associated activation energy barrier, which is in the order of 1 eV [153, 157].

In the hyperthermal energy regime, on the other hand, this energy barrier (estimated to be about 1.0 eV and 2.4 eV [157]) can be surmounted and the incoming atoms can penetrate deeper than the first or second subsurface layers (located at about 1.1 Å and 2.4 Å below the surface, respectively), as illustrated by the calculated surface depth reached by the oxygen atoms as a function of the kinetic energy provided (*Table 4.1*). Note that the change in maximum penetration depth as a function of incident energy is smaller for the molecular impacts than for the atomic oxygen one due to the immediate break-up upon collision of the molecules. Indeed, as the molecules are given the same initial kinetic energy as the atoms (in our atomic impact models), the individual atoms obtained after dissociation have less momentum and hence a lower velocity than the ones generated in the atomic impacts, and will therefore not penetrate as deep in the surface as the oxygen atoms issued from the atomic bombardment.

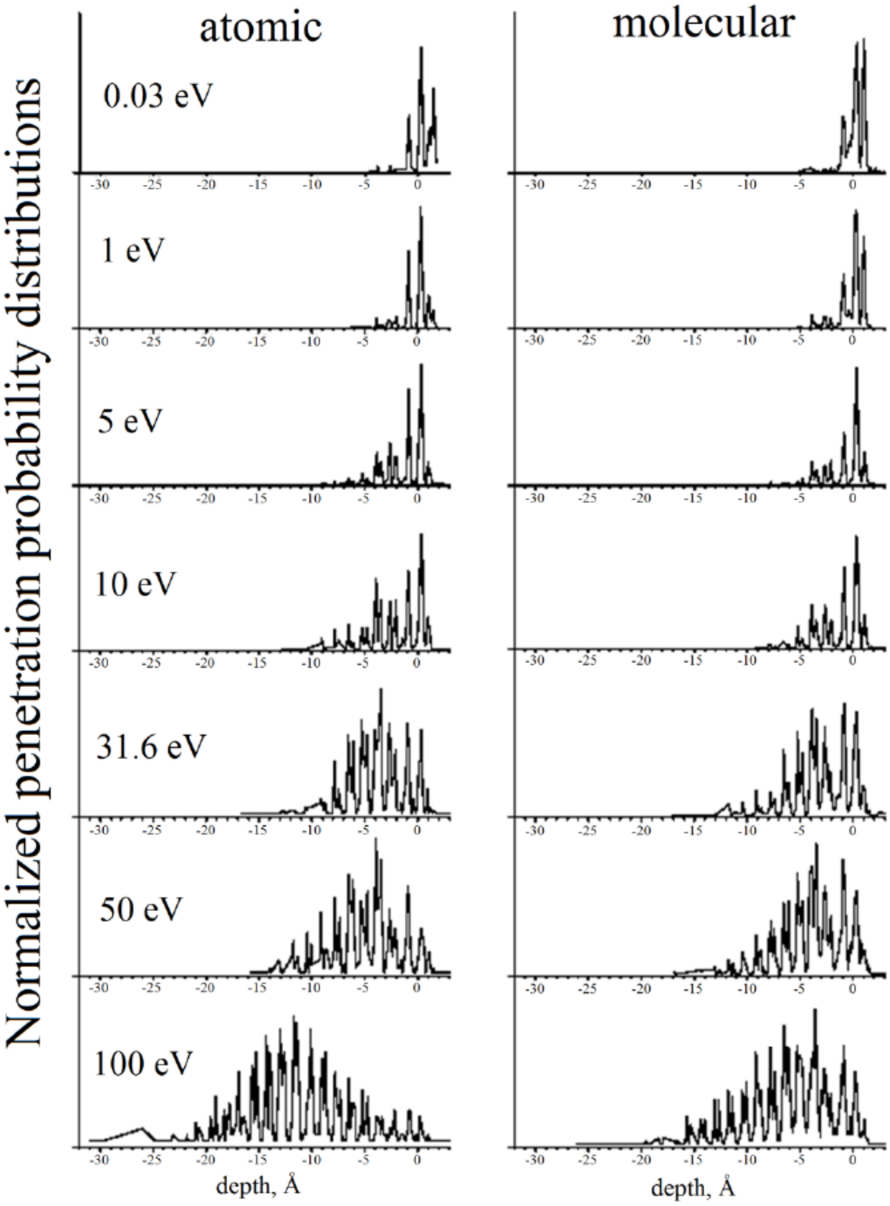

Figure 4.2 *Calculated normalized penetration probability distributions of oxygen atoms, after the impact of atomic or molecular oxygen on Si(100){2x1}.*

Table 4.1 *Maximum depth reached by the hyperthermal oxygen atoms after impact (by atomic or molecular oxygen), for different incident energies.*

Incident energy (eV)	Maximum depth (Å) (O impacts)	Maximum depth (Å) (O_2 impacts)
5.0	9.0	8.0
10.0	9.5	9.0
31.6	13.0	12.0
50.0	14.0	14.5
100.0	26.0	19.5

The analysis of the penetration probability distributions reveals that the implanted oxygen atoms preferentially reside in or close to the silicon layer planes rather than in between the silicon sheets, as illustrated in figure 4.3 for the atomic oxygen impacts at 5 eV. Indeed, while at thermal energy, the atom reacts with the surface and resides on the uppermost and in the first subsurface layer, the hyperthermal ones can penetrate deeper as they can surmount the corresponding energy barriers [46].

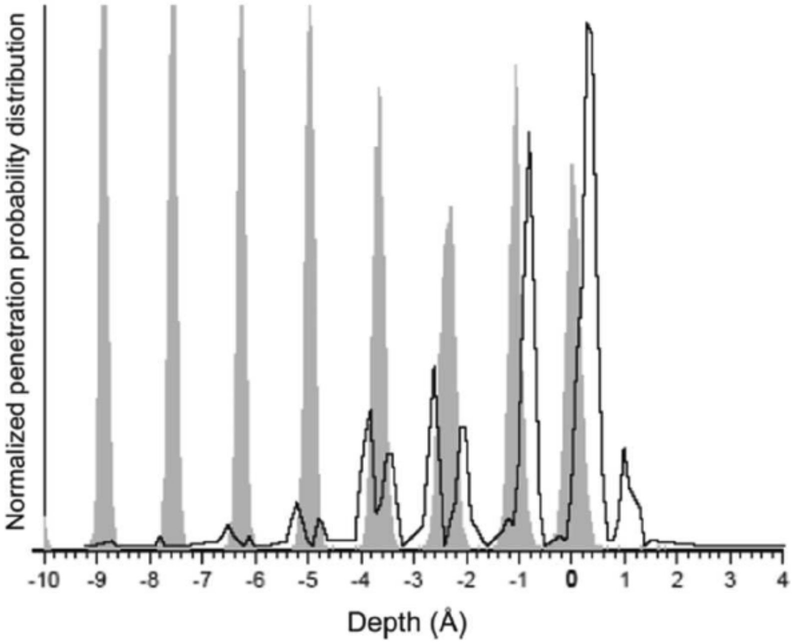

Figure 4.3 *Calculated normalized penetration probability distribution of atomic oxygen with 5 eV impact energy in Si(100){2x1} (black line). The grey peaks indicate the positions of the silicon layers. The top four Si layers are broader than the bulk layers due to the surface reconstruction. The depth = 0 Å position corresponds to the location of the surface dimer.*

As can be seen in figure 4.3, the atoms that are located at the topmost layer or in the first subsurface layer, are only found on the topside of these layers. In contrast, oxygen atoms residing deeper in the crystal are found on both sides of the silicon layers. This behaviour is strongly bound to the structure of the silicon surface. Indeed, the distributions show that the oxygen atoms have a low probability of being located under a reconstructed dimer on the terrace of the Si(100){2x1} surface, as indicated by the absence of oxygen peaks at the left hand side of the first two Si peaks at the surface, which is consistent with the fact that the chemisorbed atoms in the top layer and in the first subsurface layer cannot migrate between atoms of the silicon dimer [153].

4.3.2 Impact - induced damage

Perhaps of even greater importance for material scientists than the actual penetration depth of the oxygen atoms is the damage that they induce in the Si-crystal due to their impact. In an effort to quantify this event, the energy-dependent damage in terms of the average number of created *displaced* or *missing atoms* (MA) per impact (figure 4.4) was computed [165]. For each atom *i* at position r_i, the sum $\sum_j (\boldsymbol{r_i} - \boldsymbol{r_j})$ of the vectors from *i* to all nearest neighbors *j* is calculated. If this sum is zero or very small, atom *i* is in a (near) perfect symmetrical environment, and is considered to signal the absence of a point defect near *i*. However, if the magnitude of the sum is larger than a critical reference value, a MA is attributed to the position as:

$$\boldsymbol{r_{MA}} = \boldsymbol{r_i} - \sum_j (\boldsymbol{r_i} - \boldsymbol{r_j}) \tag{4.1}$$

We use a value of 1.88 Å for the reference value, which is 80% of the nearest - neighbor distance in silicon. This allows us accounting for some structural or thermal disorders as compared to a perfect vacancy.

Both in the atomic and in the molecular case, the average number of MA's per impact steeply increases as from 31.6 eV (figure 4.4). Note that a few MAs are already created at 10 eV in the case of atomic impacts. At 31.6 eV, about 1 MA is created per impact, while this value increases to more than 2 at 100 eV.

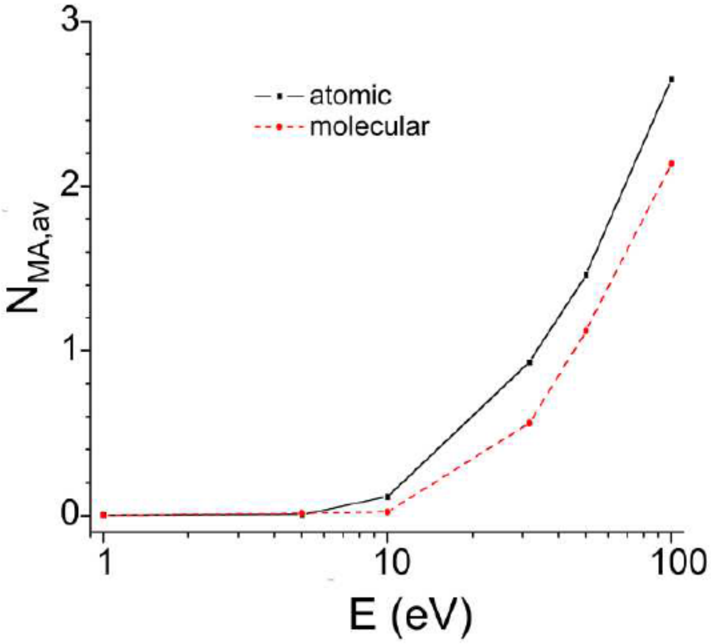

Figure 4.4 *Calculated average number of missing atoms created in the Si-crystal per impact as a function of impact energy for atomic and molecular impacts.*

Two distinct generation mechanisms of defects are observed in our calculations: the first one occurs through a simple knock-on displacement: when the impinging oxygen atom has sufficient kinetic energy, it can displace a Si-atom from its lattice location due to the collision, thereby creating a vacancy-interstitial pair (a Frenkel pair) [166]. Note that the oxygen atom sets itself interstitially in this process. This event is only observed at high impact energy, i.e., above 10 eV, which is consistent with the experimentally observed energy window of 10-30 eV for the displacement of Si [164, 167-169], as well as to the Frenkel pair energy threshold calculated by DFT for the [100] direction in Si (20 eV) [170].

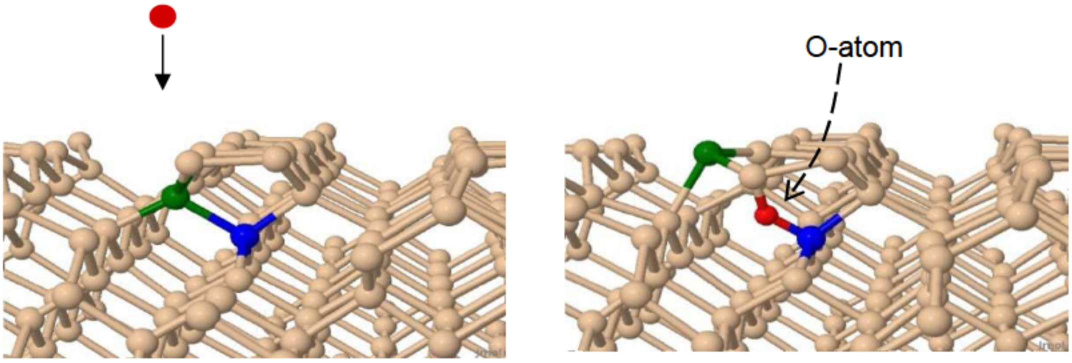

Figure 4.5 *Mechanism of defect creation by O atom chemisorption at low impact energy below 10 eV.*

In the second mechanism, the oxygen atom binds itself to two Si ones, forming a Si-O-Si bond. In some cases, a Si-atom (the upper one as seen from the surface) is pushed towards the surface, and is displaced from its equilibrium lattice location (see figure 4.5) and also creates a MA at that site.

In figure 4.6, the distribution of the position of the impact induced defects, or the location of the created vacancy, is depicted for different incoming energies, for both atomic and molecular impacts. Again, two energy regimes can be discerned: below and above 10 eV. Up to 10 eV, the impinging atom does not have enough energy to easily create a defect in the bulk of the structure. As a consequence, the created defects in this energy regime are all confined to the top layers of the crystal, especially in the first and second atomic layers. The incoming atom(s) will insert themselves into the Si-Si bond, thereby displacing the Si-atoms. This leads in a few cases to the creation of an atomic vacancy. Note, however, that the probability of this event to occur is small and ranges from 0.002 at 1 eV to 0.112 at 10 eV (see figure 4.6). In this regime, the energy is too low to displace Si-atoms from their lattice positions, and knock-on displacements of Si-atoms do not take place. Hence, the interaction is limited to the chemisorption process.

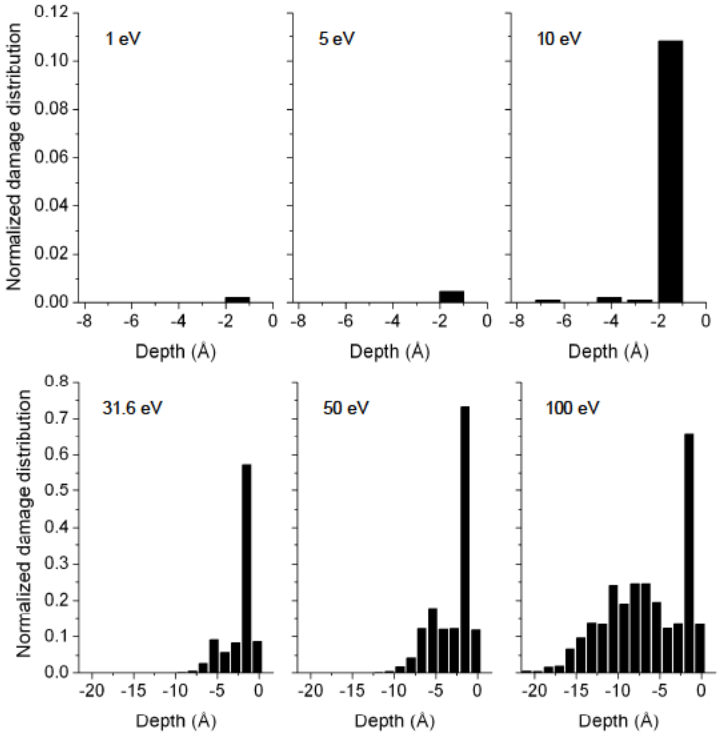

***Figure 4.6** Distributions of the calculated damages, as a function of depth in the surface, for the different impact energies investigated (using atomic oxygen).*

At higher impact energies, the knock-on displacement of Si occurs through both primary and secondary knock-on mechanisms. The resulting defect distributions are shown in figures 4.6 and 4.7. In figure 4.6, besides the sharp peak around -2 Å, also a secondary broad distribution is observed around -5 to -10 Å for the atomic impacts. For the molecular impacts, depicted in figure 4.7, the secondary distribution is visible until about -6 Å for the 31.6 eV case and until about –10 Å for the 100 eV case. Indeed, the initial impact, which usually displaces one or more Si-atoms in the top layers and which contributes to the peak at around -2 Å, slows down the impinging atom and subsequently sets it in an interstitial position into a Si-Si bond, creating a second defect in the underlying layer.

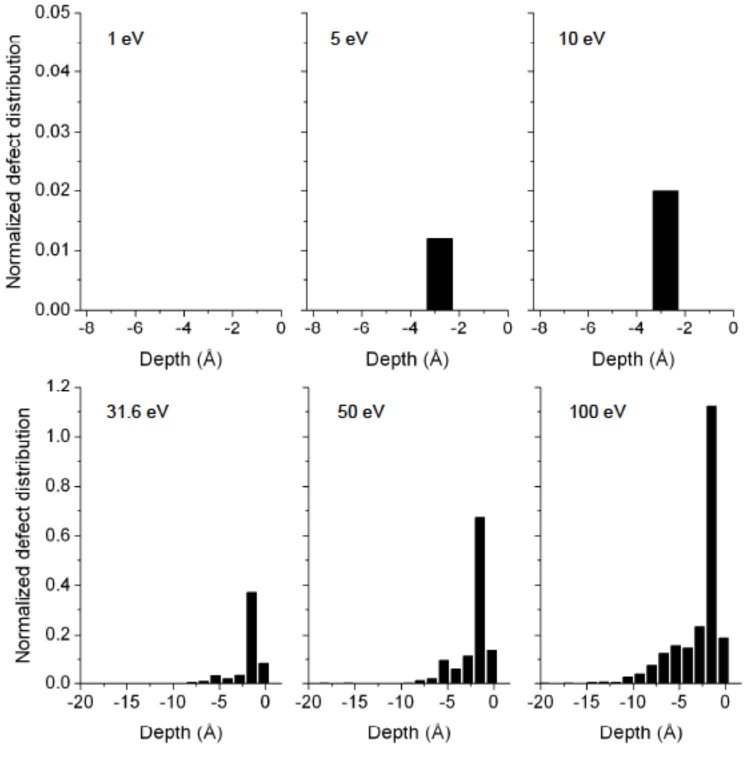

Figure 4.7 *Distributions of the calculated damages, as a function of depth in the surface, for the different impact energies investigated (using molecular oxygen).*

Further, the impinging O-atom(s) also transfer a substantial amount of energy to the Si-atom in the collision. Indeed, the maximum energy that can be transferred in the O-Si collision, is given by $T_{max}=E_0(4m_1m_2)/(m_1+m_2)^2$, corresponding to about 92.5% of the initial impact energy (or less). Therefore, secondary knock-on displacements can occur if the initial impact energy is sufficiently high, due to Si-Si collision cascades in the bulk of the structure. In this energy range, the total defect formation probability (composed of primary and secondary knock-on displacements) ranges from 0.92 (atomic case) and 0.56 (molecular case) at 31.6 eV impact energy to 2.65 (atomic case) and 2.14 (molecular case) at 100 eV impact energy.

Note that in the implantation process, the final location of the created defects and the final location of the implanted atom(s) are often found to be separated from each other by a considerable distance. This is illustrated in figure 4.8, showing the impact of a 100 eV oxygen atom. The position of the oxygen atom (colored red) is shown every 6.25 fs; the positions of the silicon atoms are the final positions at the end of the trajectory. The darkness of the silicon atoms indicates the deviation of their final positions from their original positions, prior to the impact.

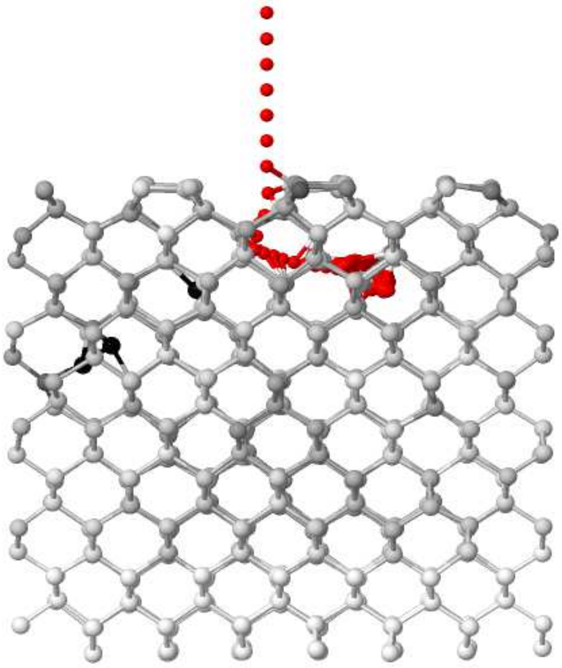

Figure 4.8 *Illustration of the spatial separation between the location of the impact induced defect (black Si-atoms, left side in the figure), and the implantation position of the O-atom (red atom, right side in the figure). The positions of the Si-atoms are plotted once, for the final configuration; the time interval between the consecutive positions of the impinging O-atom is 6.25 fs. The impact energy is 100 eV.*

In the process, the oxygen atom displaces a silicon atom of the fourth Si-layer from its lattice position (towards the left side in the figure). As explained above, the impinging O-atom transfers a considerable amount of energy in the O-Si collision to this Si-atom, which can therefore displace another Si-atom. This Si-atom in turn becomes an interstitial in the lattice (colored blue in the movies). Meanwhile, the O-atom is deflected from the Si-atom nearly horizontally and travels through the lattice (to the right side in the figure) until it has lost most of its kinetic energy. The distance between the implanted O-atom and the created defect in the final configuration is about 15 Å in this case.

4.4 Conclusions

The probability of penetration of O_2 and single oxygen atoms generated through thermal and hyperthermal sources and the associated impact induced damage in a Si(100){2x1} surface was investigated. It is found that at low impact energies (i.e., lower or equal to 1.0 eV), the oxygen atoms remain confined to the surface layers, and that the damage to the bulk is very limited and purely induced by the chemisorption process. At higher energies, the O atoms can penetrate in the crystal to a depth of up to 20 Å. At these higher energies, the damages are much more pronounced, and primary and secondary knock-on displacements of Si are observed. This results in two distributions in the spatially resolved defect distributions.

.

Chapter 5

Controlling the thickness of ultrathin SiO_2 layers by hyperthermal Si oxidation at room temperature

5.1 Introduction

Silicon dioxide (SiO_2) films can nowadays successfully be grown on crystal silicon, with a thickness of a few monolayers by hyperthermal oxygen [40, 62, 171]. Although several experimental works extensively investigated hyperthermal oxidation of the Si (100) surface at room temperature, oxidation mechanisms have not been clearly described yet. Therefore, an investigation of the growth process at the atomic-scale (i.e., oxidation kinetics and dynamics, transport phenomena during oxidation, etc.) of ultrathin silicon dioxide is of prime importance [20, 62,].

As mentioned before, the most generally adopted model for silicon oxidation, the Deal-Grove model [22], does not accurately describe the kinetics of the silicon oxidation for thin layers (< 100 Å) [60-62]. Furthermore, the mechanism clearly fails when describing the oxidation kinetics of ultrathin films (~20 Å) at room temperature [20, 62]. The Massoud extension of this model [172] reported data for the oxidation rate for layers between about 20 Å and 500 Å in detail. However, there is little or no experimental data extending continuously from 20 Å downward [29]. Furhermore, this model cannot describe the onset of hyperthermal oxidation. In another extension of the Deal-Grove model, Cerofolini et al. [173] presented a model for the oxidation kinetics in air at room temperature, based on the Elovich equation [174], which is generally applied to chemisorption kinetics [175, 176]. They properly elucidated the mechanisms governing formation and growth of the substoichiometric and stoichiometric oxides. Unfortunately, the kinetic model fails in two situations for describing the hyperthermal oxidation: (a) there is no solution of the equation for the formation of substoichiometric oxides in the case $\theta(0) = 0$, that is, when there is no pre-existing oxide layer on the Si surface prior to oxidation; and (b) there are no suitable parameters for describing the direct oxidation, i.e., energetic oxygen species directly oxidizing the Si-subsurface layers.

The growth mechanism of silicon dioxide in the initial state of hyperthermal oxidation has not yet been properly analyzed, and investigations at the atomic scale are required. Therefore, I carried out reactive molecular dynamics (MD) calculations for clarifying the formation and growth behaviour of SiO_2 on a Si(100){2x1} reconstructed surface at room temperature during oxidation by oxygen species (O, O_2) with hyperthermal energies (1- 5 eV), and the resulting silica thickness. The results presented in this chapter were published in the Journal of Physical Chemistry C [139].

5.2 Computational details

In these simulations, a Si(100){2x1} reconstructed surface is chosen, with dimensions 21.7 Å x 21.7 Å x 27.1 Å. Based on the mass centre position of Si layer planes [177], the average thickness of each layer is calculated to be 1.296 Å, corresponding to the thickness of one half oxide layer (one oxide layer thickness is 2.6 Å [51]). Periodic boundary conditions are applied to the (x,y) plane, to mimic a laterally infinite surface (see figure 4.1). Prior to the impact simulations, the box is equilibrated at 300 K using the Berendsen heat bath [113]. The obtained structure is subsequently relaxed in the microcanonical ensemble for 10 ps.

Oxygen impacts are performed as follows. The incident particle (oxygen atom or oxygen molecule) is positioned at a z position of 10 Å above the uppermost Si atom of the crystal. The {x, y} coordinates of the incident particles are chosen randomly. In the case of molecular oxygen, the O_2 molecule is rotated randomly prior to impact. The impinging particle is directed normal to the surface, corresponding to laser detonation experiments [47, 178]. Every impact is followed for 3 ps. Three series of simulations were carried out for kinetic energies of the impinging oxygen species (O, O_2) of 1, 3 and 5 eV.

5.3 Results and discussion

5.3.1 Growth process

Two-stage hyperthermal oxidation. A general evolution of the growth process is presented in figure 5.1. Figure 5.1a shows the evolution of the oxygen content of the Si lattice as a function of O fluence in monolayers (ML) for both atomic and molecular impact cases with initial kinetic energies of 1, 3, and 5 eV.

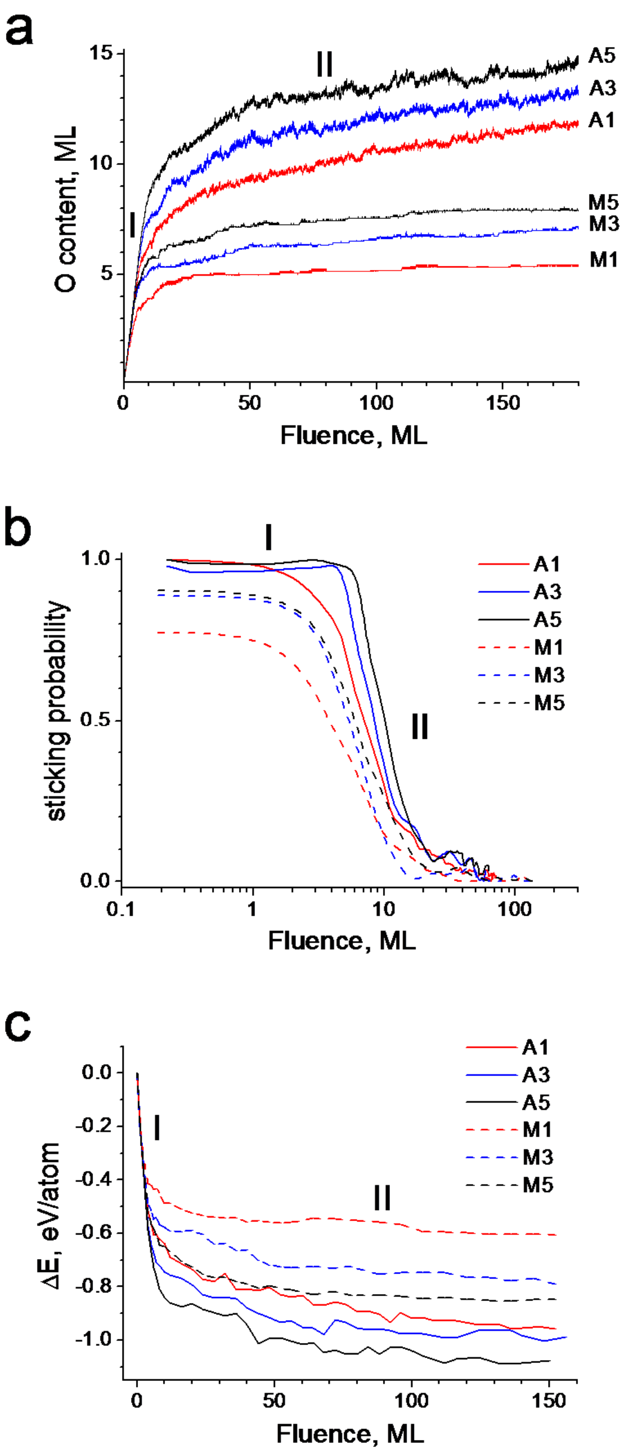

Figure 5.1 *Oxidation stages (I and II) during hyperthermal oxidation (1-5 eV) on the {2x1} reconstructed Si(100) surface at room temperature: (a) oxygen coverage on the silicon surface, (b) adsorption behaviour of incident oxygen species, and (c) variation of total energy of the* SiO_2*/Si system as a function of fluence, for both atomic (A1-1eV, A3-3eV, A5-5eV) and molecular (M1-1eV, M3-3eV, M5-5eV) oxygen beams.*

In our calculations one ML corresponds to 32 atoms. It can be seen in the figure that the oxidation process can be divided into two stages: (I) the initial fast oxidation stage and (II) the subsequent slow oxidation stage. This corresponds to previous experimental studies [48, 61]. In the first stage, the oxygen content rapidly increases due to the high adsorption probability of the oxygen species on the pure silicon surface. In this stage, the silicon surface and subsurface layers are directly oxidized by hyperthermal oxygen species [47, 51, 179]. Consequently, the oxygen sticking probability is in this stage not a function of the oxygen fluence (figure 5.1b), and the oxygen content grows linearly. The duration of the first stage strongly depends on incident energy and type of oxygen species. The results indicate that the first stage continues for 2.6, 5.0 and 6.2 ML of oxygen fluence in the atomic case with 1, 3 and 5 eV, respectively. In the molecular case, the duration of stage I is shorter due to the lower adsorption probability, and lasts for about 1.6, 2.4 and 2.6 ML, respectively, for initial kinetic energies of 1, 3 and 5 eV.

In the beginning of the second stage, the sticking probability of the incident oxygen species decreases rapidly due to the presence of the previously adsorbed oxygen atoms, which appear on the topmost layer of the newly formed silica layer. As a result, most of the new impacting oxygen atoms do not link to the surface atoms during this stage. This leads to a gradual saturation of the oxygen content. In the molecular impact case, the saturation occurs much faster than in the atomic case. While the oxygenated silicon thickness quickly increases in the first stage, the main effect of the second stage is structural change. Figure 5.1c presents the energy gain of the $SiO_2|Si$ interface due to oxidation. In the first stage, the energy curve drops (i.e., becomes more negative) much more quickly than in the second stage. The energy plot indicates that oxygenated silicon is energetically more stable than pure silicon. As shown in figure 5.1c, the total energy of the oxygenated silicon bulk strongly depends on energy and type of incident oxygen species, that is, the system appears to become more stable upon atomic impacts than upon molecular impacts, and also with increasing energy of the impacting species. Indeed, the energy gain depends on the extent of the Si-O bonding, which is analyzed below.

Growth mechanism of ultrathin silica (SiO_2) layers. In figure 5.2, the SiO_2 growth process on a {2x1} reconstructed Si (100) surface by both oxygen atoms and molecules with incident energy of 5 eV is presented. The oxidation progress is shown by molecular structure representations and suboxide histograms. Here, grey, green and red bars describe the density distribution per depth of pure Si, oxygenated Si (i.e., SiO_x) species and ultrathin silica (i.e., SiO_2) layers, respectively. z=0.0 Å corresponds to the topmost layer of the original pristine Si lattice.

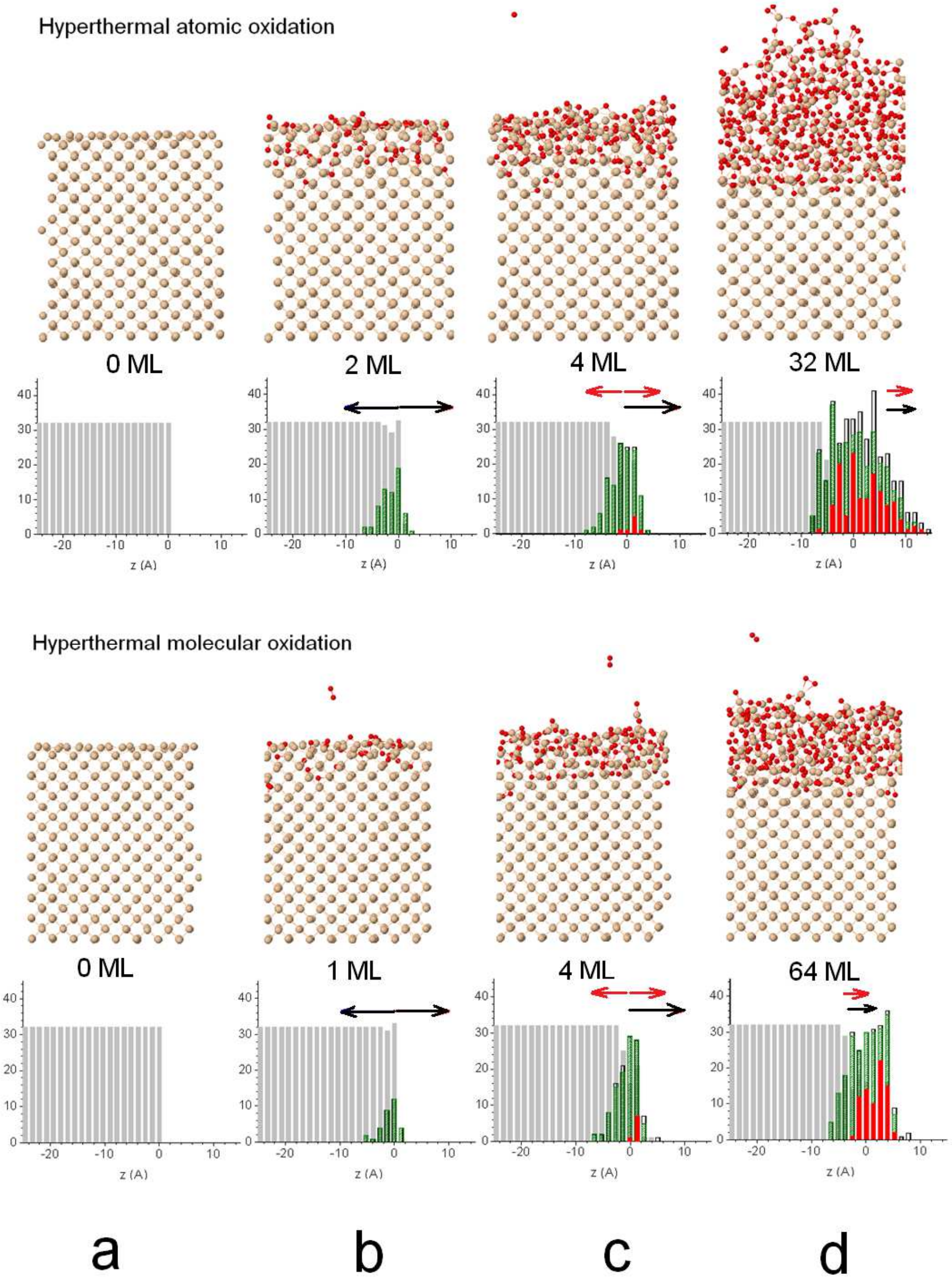

Figure 5.2 *Growth behaviour of ultrathin silica layers induced by 5 eV atomic and molecular oxygen at room temperature. The occurrence of pure Si,* SiO_x *and* SiO_2 *is indicated in the histograms by light grey bars, green bars and red bars, respectively. Black and red arrows indicate the growth direction of the oxidized and silica layers, respectively.*

We can distinguish two steps in the growth mechanism of silica layers at room temperature. In the first step, the oxidized layers grow simultaneously inward and outward, normal to the surface (see figure 5.2b in both the atomic and molecular impact case; the black arrows indicate the growth direction of oxidized layers). However, due to the associated activation energy barrier of the Si subsurface layers, which is on the order of 1 eV [153, 180], the inward growth is interrupted quickly and atoms cannot penetrate in the crystal any further. This indicates the end of the initial growth step. Consequently, during the entire oxidation process, the penetrated oxygen atoms can move only up to the limit depth. The limit of the oxidized depth is equal to the maximum penetration depth of the oxygen atoms and it determines the maximum number of silicon atoms, which may contribute to the formation of the oxygenated silicon layers. The results show that the limit depth is nearly constant during the second oxidation stage and it depends on both kinetic energy and type of incident oxygen species. The maximum penetration depth was found to be 8, 9 and 10 Å during the atomic oxidation with kinetic energies 1, 3 and 5 eV, respectively. In the molecular oxidation case, the limit depths were slightly less than in the atomic case and the values were equal to 4, 6.9, and 7 Å for kinetic energies of 1, 3, and 5 eV, respectively. The limit depths are very close to the values of our previous calculations [163].

When the second growth step starts, an “incipient” silica layer appears (figure 5.2c in both the atomic and molecular impact case). The results demonstrate that silica also grows in two directions during the second step (the red arrows indicate the growth direction of silica in figure 2 c, d). Inward growth of silica continues up to the interface area, which is located between silica (SiO_2) and crystalline Si. When the oxygen content is completely saturated, only the outward silica growth continues (see figure 5.2d). Indeed, in the molecular case, the maximum silica thickness is nearly constant during the second oxidation stage. Furthermore, in this case silica formation is almost completed at the beginning of the second stage and the silica layer is thinner due to fast saturation of the oxygen content and the low limit depth of penetrated oxygen atoms. The maximum thickness is reached when also the outward growth of the silica stops (not shown in figure 5.2).

Si suboxide components in the initial oxidation stage. As was mentioned in the first section, a direct insertion of oxygen atoms into the Si subsurface layers is found during the initial stage, for hyperthermal oxidation at room temperature, which has not been observed in thermal oxidation. On the other hand, in the hyperthermal energy regime, incident atoms can surmount the energy barriers of the first or even second subsurface layers [163], which are estimated to be about 1.0 and 2.4 eV, respectively [180]. Such oxidation behaviour was also studied by ellipsometry and synchrotron radiation photoemission spectroscopy [47, 51, 179]. The temporal evolution of the formation and growth of the oxygenated silicon in the initial oxidation stage can easily be understood by observing the variation of the silicon suboxide components. Generally, the components Si^{1+}, Si^{2+} , Si^{3+} and Si^{4+} are supposed to arise from interfacial silicon atoms, which bind to one, two, three and four nearest-neighbor oxygen atoms, respectively, that is, this corresponds to Si_2O, SiO, Si_2O_3 and SiO_2, respectively.

Figure 5.3a shows the variation of the relative concentrations of Si suboxide species in order to elucidate the oxidation behaviour in the initial stage. In this stage, an adsorbed oxygen atom can bind to surface atoms in different configurations. Previous studies [21, 180, 181] demonstrated back-bond (B), dimer-bridge (D), on-dimer (D1) and on-top (T) structures on the initial Si (100) structure (see pictures in figure 5.3b). It was argued that the B or D bonds are energetically most favorable [21, 180-182]. In our case, each of these Si-O bond configurations, except the D structure, are found during the initial oxidation stage. As can be seen in figure 5.3a, the Si^{1+} peak (α) initially dominates. Indeed, in the earliest stage, the adsorbed oxygen atoms bind according to one of the bond configurations as shown in figure 5.3b. The D configuration is found as soon as the first subsurface layer becomes oxidized. The Si^{2+} peak (β) indicates the appearance of two bonds, that is, BB, BD, BT or BD1, of which BB and BD1 dominate. The appearance of mainly BBD, BBD1 and BDT bonds is represented by the Si^{3+} peak (γ). In figure 5.3a, it is shown both in the atomic and molecular oxidation case that Si^{1+}, Si^{2+} and Si^{3+} suboxide species consecutively dominate in the initial oxidation stage. All of these three Si suboxide species are found in the first few tens of impacts. Indeed, incident oxygen can penetrate deeper than the Si topmost surface and directly oxidizes the Si subsurface layers, that is, the uppermost (no barrier energy [180]) and first subsurface layers (barrier energy about 1 eV [180]). When the silica layer appears, the Si^{4+} curve increases continuously and the other suboxide components significantly decrease, as is clear from figure 5.3a. Note that the yellow curve in both the atomic and molecular case denotes the sum of Si^{1+},

Si^{2+}, Si^{3+} and Si^{5+}, whereas the blue curve gives the Si^{4+} contribution; the sum of these two curves is equal to 1.

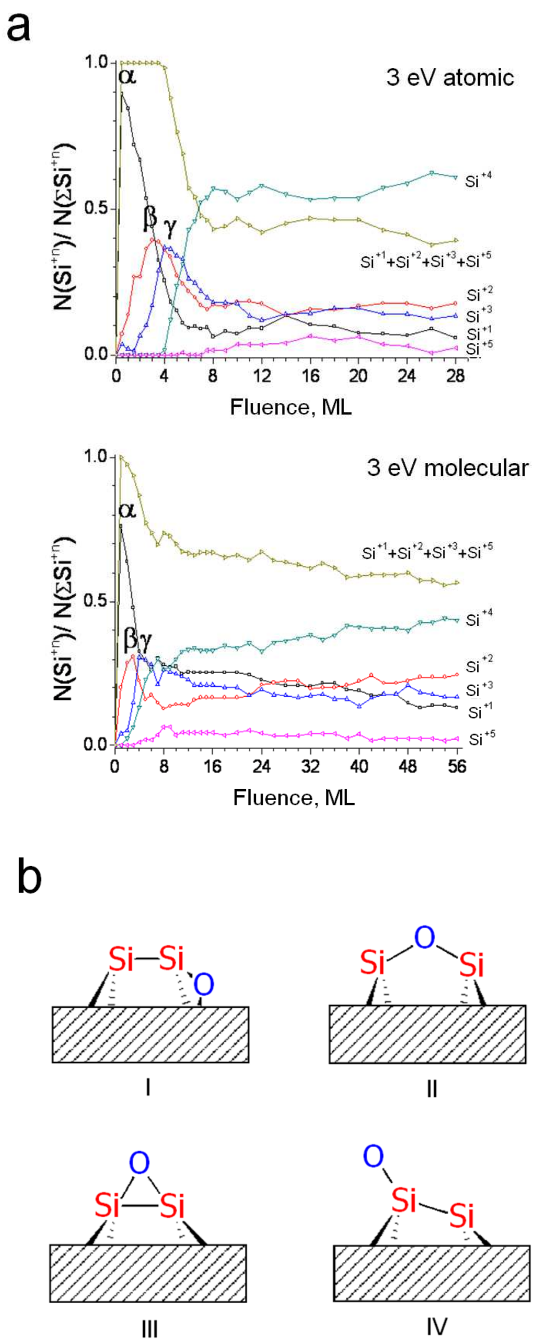

Figure 5.3 *(a) Relative numbers of silicon suboxide components as a function of atomic and molecular oxygen fluence. (b) Possible bond configurations of an oxygen atom with a Si(100){2x1} surface in the initial silicon oxidation: (I) back-bond (B), (II) dimer-bridge (D), (III) on-dimer (D1), and (IV) on-top (T) structures.*

This behaviour allows us to assess when the SiO_2 growth starts, that is, after about 4ML in the atomic case and after about 2 ML in the molecular case. Note that our calculations also some five-fold suboxide species are detected in the silica bulk during the oxidation process, although in very low concentration, which is due to residual uncorrected overbinding in the potential.

Charge distribution of the Si|SiO$_x$|SiO$_2$ system. Calculation of the charge distribution facilitates to identify two regions of the oxidized silicon: transition (SiO$_x$) and silica (SiO$_2$).

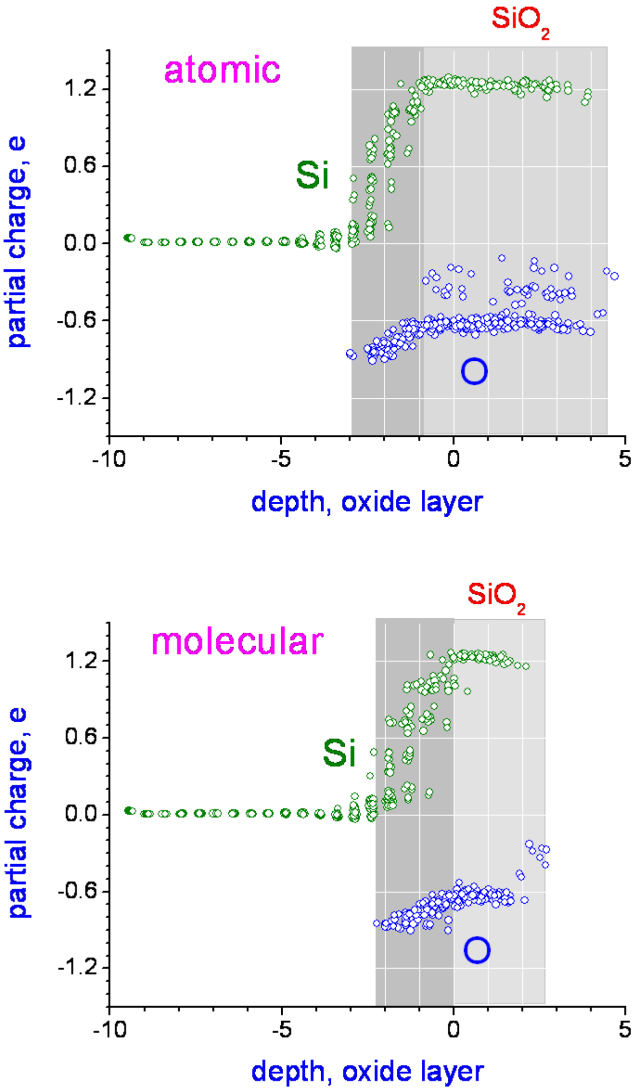

Figure 5.4 *Charge distributions of Si and O in the Si(100)|SiO$_x$|SiO$_2$ system, for (a) atomic and (b) molecular oxidation, for a kinetic energy of 3 eV. The oxidized Si (i.e., SiO$_x$) transition layer and the silica (SiO$_2$) bulk can clearly be identified by the dark grey and lighter grey regions, respectively.*

In figure 5.4, partial charge distributions of Si and O in the SiO$_2$|SiO$_x$|Si structure are shown for oxidation by atomic and molecular oxygen, for energy of

3 eV. In the transition region (coloured dark grey), the partial charges of Si and O atoms range approximately from 0 to +1.2e and from -0.9e to -0.6e, respectively. On the other hand, the average partial charges are about +1.2e and -0.6e in the SiO_2 region (coloured light grey) for Si and O atoms, respectively. Indeed, analysis of the obtained oxygenated silicon bulk during the oxidation process by the partial charge distribution clearly shows that the bulk is split up in two regions: a transition layer and silicon dioxide (or pure silica), which is consistent with experimental and theoretical studies [61, 183, 184].

The charges of the oxygen atoms are distributed in the range of -0.3e and -0.6e in the case of atomic oxidation because of peroxyl and threefold oxygen bond configurations in the silica region (see below). Furthermore, also some Si-Si bonds (i.e., oxygen vacancies) [185]) are found in the SiO_2 region in the molecular oxidation case. Previous DFT calculations [184] suggested that such a distribution in the silica region is induced by oxygen-deficient defects. Moreover, due to intrinsic defects (i.e., an incorrect coordination of a Si or O atom, or a Si-Si or an O-O bond), the total charge of the oxygenated silicon area is locally not zero. We believe that some O-O peroxyl bridge and threefold oxygen bond configurations [185, 186] in SiO_2 disorder the charge distribution of the oxygen atoms. In addition, oxygen atoms, which are distributed in the top oxide layer, strongly affect the incident oxygen species during oxidation. This effect may accelerate the saturation of the oxygen content in the molecular case. Finally, note that the calculated charges are determined from the EEM method, fitted to Mulliken charges. As Mulliken charges are heavily dependent on the basis set used, the exact values should not be taken too literally. Nevertheless, the obtained values are in reasonable agreement with experimental values for quartz and coesite [187].

Variation of the SiO_x (transition layers) thickness. In the previous section, the partial charge distribution also indicates that all Si suboxide components are found in the oxygenated silicon region. The silicon suboxide species allow analysis of the transition area as well. In the transition or non-stoichiometric oxide region, located between the crystalline silicon and the silicon dioxide (silica) layer, all three Si suboxide species (Si^{1+}, Si^{2+} and Si^{3+}) are found. Our calculations predict that the oxygen density is somewhat higher in the transition region than in the pure silica bulk, as is also experimentally found [61] through the analysis of the oxygenated silicon bulk as grown by thermal oxidation. Both the temporal variation of the silicon sub-oxide components and the partial charge distribution predict that the transition area is thinner than the SiO_2 bulk.

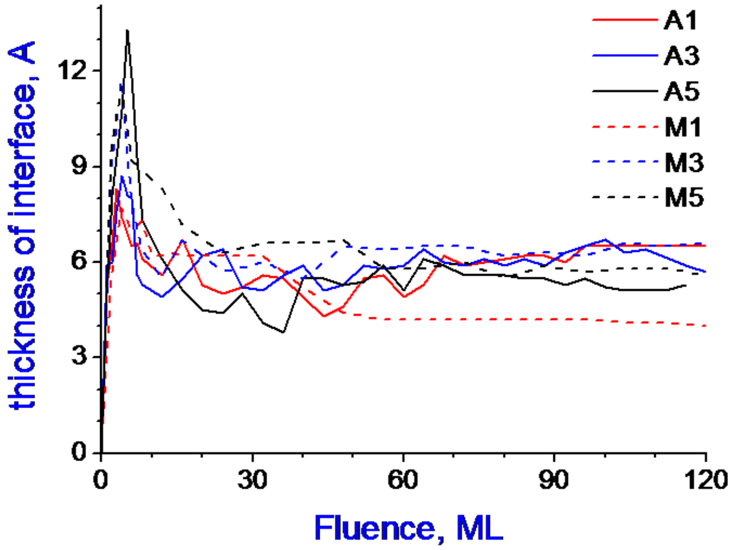

Figure 5.5 *Variation of the interface thickness during hyperthermal oxidation, as a function of the oxygen fluence, for both atomic and molecular impacts of 1, 3 and 5 eV.*

In figure 5.5, the variation in thickness of the transition layer, also called interface, during hyperthermal oxidation by oxygen species is shown. For both atomic and molecular oxidation, the thickness of the transition area increases with increasing thickness of the oxygenated silica during the initial oxidation stage. In the second stage, the thicknesses of the transition area slightly decrease again and become about 5 Å. This value corresponds to the lower limit of several experimental measurements [60, 61, 188], in which the thickness of the transition region ranges from 5 to 50 Å. Moreover, this value seems to be rather independent from the energy and type (atomic/molecular) of the impacting species.

Evolution of the ultrathin SiO_2 thickness. Figure 5.6 shows the temporal evolution (or evolution as a function of oxygen fluence) of the thickness of the pure silica layer during hyperthermal oxidation. As mentioned above, the silica appears when a few ML of oxygen is incorporated during the initial oxidation stage. In the initial oxidation stage, the silica layer grows rapidly. Our results predict that the increase in the silica thickness consists of two stages: a linear and a nonlinear stage.

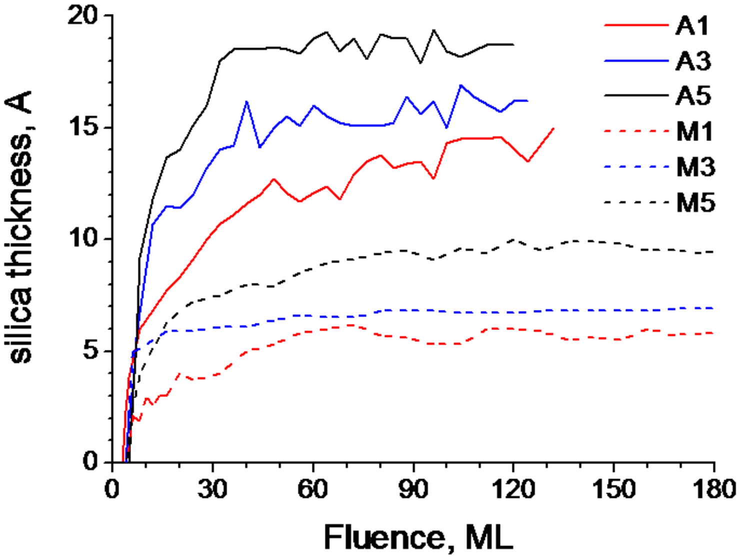

Figure 5.6 *Variation of the SiO_2 thickness as a function of the oxygen fluence, for both atomic and molecular impacts of 1, 3 and 5 eV.*

A linear increase in the silica thickness is observed during the initial oxidation stage. This linearity was also found by using ellipsometry and synchrotron radiation photoemission spectroscopy [47], in which the limits of the linear growth for 1.8, 2.7, 3.8 and 5.0 eV were 3.0, 6.2, 6.2 and 7.0 Å, respectively. Our calculations show that the limits of linear growth during hyperthermal oxidation with oxygen atoms for incident energies of 1, 3, and 5 eV are about 2.0, 6.0, and 9.0 Å, respectively, which differs only slightly from the experimental result. This linearity was also observed in the molecular case, although only during a relatively shorter time.

In the molecular oxidation case, the thickness quickly becomes constant at the start of the second oxidation stage due to the next-to-complete saturation of the oxygen content. However, the silica thickness slightly oscillates around an average thickness value due to the consecutive hyperthermal oxygen impacts and increasing stress of the Si(100)|SiO_2 system, due to which, the topmost silica layer is significantly damaged after each atomic impact.

Analysis of the fluctuations induced by molecular oxygen with an energy of 3 eV shows that the average value of the thickness is about 6.3 Å. This is close to the experimental value of 6 Å [51], which was obtained by using supersonic O_2 molecular beams at room temperature. Our results predict that, in the molecular oxidation cases with energies of 1 and 5 eV, the average values of the silica thickness are about 5 and 9 Å, respectively.

In the atomic case, the minimum thickness of the final silica configuration was not less than 5.5 oxide layers (~14 Å) for the 1 eV impacts, and it increases with higher impact energy, to about 15 Å at 3eV, and 18.5 Å at 5eV. This value is also close to the experimental value of 17.5 Å, which was obtained at 493 K by oxygen atoms with kinetic energy of 4.6 eV [48]. However, this oxidation was performed on a H-terminated Si(001) surface using a relatively low oxygen fluence. The thickness obtained at 5 eV is also in close agreement with other experimental results [179].

Analysis of the thickness variations assumes that the change in silica thickness as a function of incident energy is smaller for the molecular oxidation than for the atomic one due to the immediate breakup upon collision of the molecules. Indeed, as the molecules are given the same initial kinetic energy as the atoms, the individual atoms obtained after dissociation have less momentum and hence a lower velocity. Therefore, oxygen molecules do not penetrate as deep in the surface as the oxygen atoms. However, hyperthermal O_2 molecules are found to be more effectively than oxygen atom for controlling the ultrathin oxide thickness at room temperature.

5.3.2 Analysis of the obtained films

Roughness of transition region between Si and SiO_2. The roughness of the SiO_2|Si interface is a crucial parameter for ultrathin films. Indeed, careful analysis of the interface roughness at the atomic scale is quite important for MOSFET technology, for example. Therefore, we analyzed the interface between ultrathin SiO_2 and crystalline Si. As mentioned in above, the thickness of all interfaces (or transition layers, which consist of Si^{1+}, Si^{2+} and Si^{3+} suboxide components) is almost constant and is limited to about 5 Å during the second oxidation stage. In figure 5.7, six interfaces, obtained after 150 ML of oxygen fluence during both atomic and molecular oxidation with 1, 3 and 5 eV, are shown. As can be seen, the interface with the crystalline Si is very sharp. Clearly, the interface is sharper in the structures obtained by 1 eV atomic and molecular oxidation than other structures. The root-mean-square surface roughness of the interface is low. Moreover, analysis of the surface indicates that some small protrusions exist in the ultrathin nonstoichiometric oxide region, which is presented also in the Irene's interface model for the thermal oxidation case [188]. In *chapter 6*, a more detailed analysis of the interface, including stress calculations, is presented.

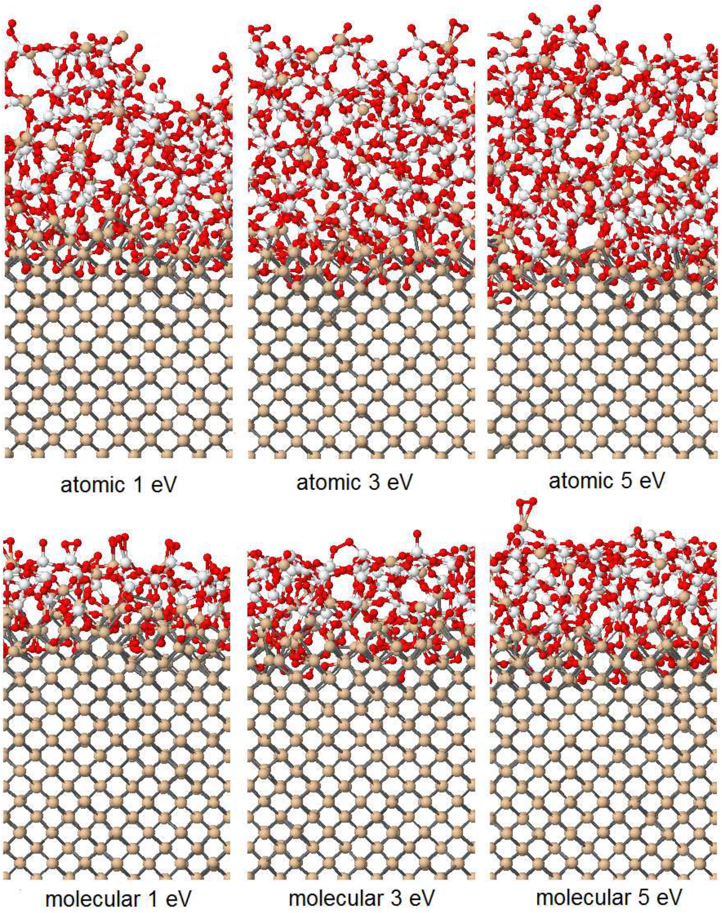

Figure 5.7 *$SiO_2|Si$ interfaces (dark grey regions) obtained by both atomic and molecular oxidation with 1, 3 and 5 eV. White and grey silicon atoms indicate ultrathin SiO_2 and crystalline Si, respectively.*

Analysis by means of mass and charge distributions. As was mentioned above, the oxidized silicon layer can be divided into two parts: a near-interface region ("transition layer") and a pure silica region. Furthermore, the pure silica region can also be divided in bulk and surface parts [61]. In figure 5.8, the oxygenated silicon layer is schematically represented by both the mass and charge distributions. In the mass distribution graph, the resolution of the analyzed layer thickness is 2.592 Å, which corresponds to the thickness of one oxide layer. The oxygenated silicon layer is divided into three parts by means of the obtained mass and partial charge distributions, that is, interface, silica bulk and silica surface (indicated by II, III and IV, respectively, in figure 5.8; region I is the pure Si region).

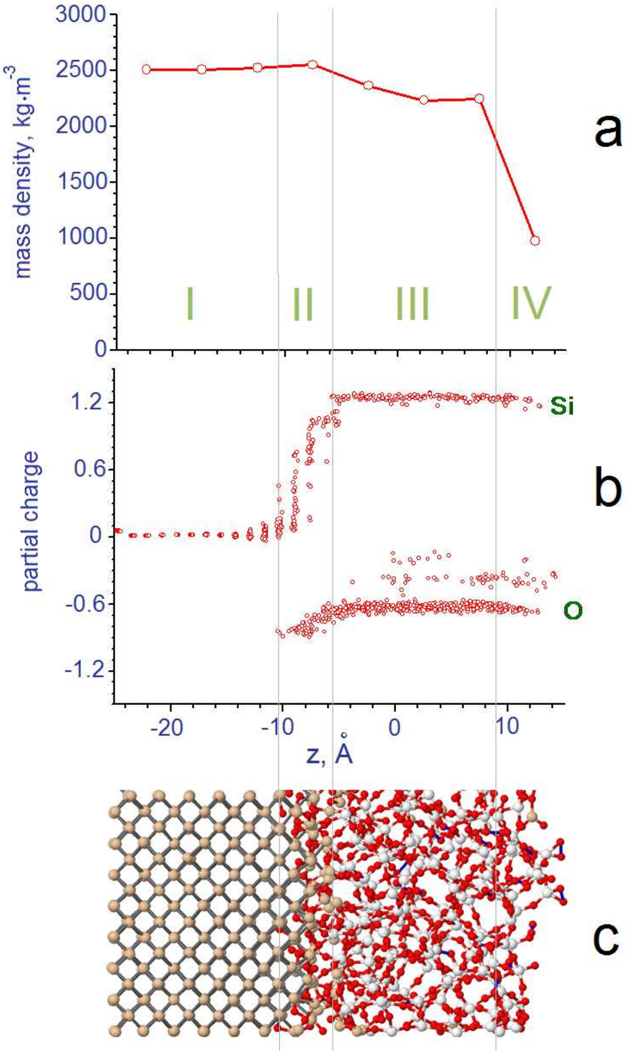

Figure 5.8 *(a) Calculated mass density distribution and (b) partial charge distribution of the pure Si and oxygenated Si layer. (c) Schematic representation of the oxygenated silicon structure. The different regions are clearly indicated in (b): (I) pure Si; (II) interface; (III) SiO_2 bulk; and (IV) SiO_2 surface.*

Gusev at al. [61] clearly showed the presence of these three parts in their relatively thicker oxide films (~ 50 Å), as obtained by thermal oxidation at 1020-1170 K. They also explained that these regions overlap in ultrathin oxide films (~ 20 Å) during the oxidation process. Such an overlapping was also found in our obtained oxide films. The mass distribution shows that relatively high density area corresponds to the interface region, where most of the intermediate Si suboxide components (Si^{1+}, Si^{2+}, Si^{3+}) reside. Indeed, because the entering oxygen atoms are stopped by the silicon barrier energy, the interface is enriched in oxygen, which is translated into the mass distribution by two silica regions. Due to the relatively high energy, the silica surface contains many small craters (e.g., see atomic 1 eV in the figure 5.7). Therefore, the mass density of the surface silica (region IV) is lower than that of the silica bulk (region III).

In *Table 5.1*, the thickness of the various regions, that is, interface, bulk silica and surface silica, as estimated from the mass and partial charge distributions (cf. figure 5.8) is presented for both the atomic and molecular impacts, at the three different impacting energies investigated. It can be seen from the table that the thickness is a nearly a linear function of the kinetic energy of the impinging oxygen species. The thickness of the layer obtained by atomic oxygen is almost twice the value obtained for molecular oxygen. Indeed, these observations suggest that the thickness of the layer can be controlled by the choice of the impinging species and the impinging energy.

Table 5.1 *Final thickness of the oxygenated silicon, split up into interface, bulk silica and surface silica regions, for both atomic and molecular impacts at the three different energies investigated, as estimated from the mass and partial charge distributions (cf. Figure 5.8).*

Incident oxygen species	incident energy, eV	thickness of oxygenated silicon, Å				
		Interface	silica (SiO_2)			Total
			bulk	surface	total	
atom	1.0	5.5	9.9	5.3	15.2	20.7
	3.0	5.6	11.9	5.0	16.9	22.5
	5.0	5.8	13.5	5.2	18.7	24.5
molecule	1.0	4.8	2.9	2.3	5.2	10.0
	3.0	5.2	4.9	1.4	6.3	11.5
	5.0	5.6	7.0	2.1	9.1	14.7

Analysis by means of the radial distribution function (RDF). Figure 5.9a shows the total RDF of the obtained bulk silica structures for the atomic and molecular oxidation with kinetic energies of 1, 3 and 5 eV. The Si-O, O-O and Si-Si bonds (β, γ and δ peaks, respectively, in figure 5.9a), are found to be 1.61, 2.51 and 3.15 Å, respectively, at all cases investigated, that is, both atomic and molecular impacts, at the three different impact energies. These values agree with both experimental values and other MD calculations [141, 189, 190] and indicate that the obtained structure is amorphous.

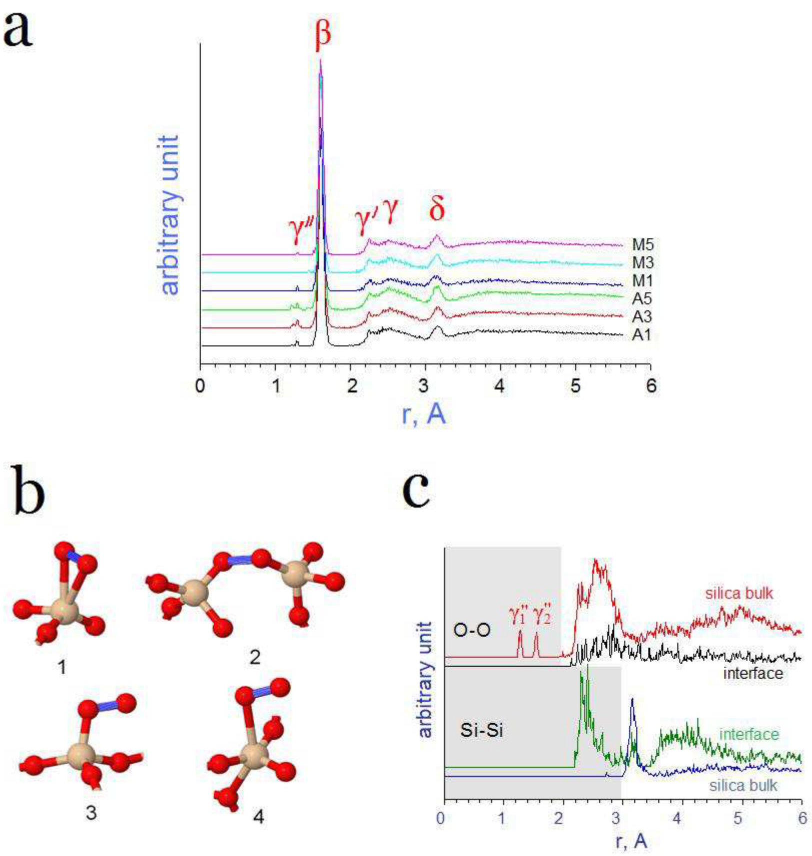

Figure 5.9 *(a)Total radial distribution functions (RDFs) of the SiO_2 bulk silica structures, for the atomic and molecular impacts at the three different impact energies investigated, (b) some oxygen peroxyl bridge bonds in silica and (c) RDFs of O-O and Si-Si in both bulk silica and interface.*

Some unexpected O-O nonbonded neighbors (γ' peak) are found with distance 2.25 Å, close to the γ peak. We believe this peak is caused by stresses near the interface. Also, the γ' peak depends on the silica thickness, that is, an increasing in the ultrathin silica thickness significantly decreases such O-O in tetrahedral silicon structure. Furthermore, a γ'' peak indicates that the silica film contains also O-O peroxyl bonds, both in the bulk as well as at the surface. In our structures, two types of peroxyl bonds are found (indicated as 1 and 2 in figure 5.9b), which correspond to the $\gamma_1^{''}$ and $\gamma_2^{''}$ peaks in figure 5.9c. The existence of peroxyl bridges and three-fold bond configurations in amorphous SiO_2 has already been suggested on the basis of some experimental and first-principles calculations [185, 186, 191]. Indeed, it was suggested that the peroxyl bridge configuration is energetically more stable than the three-fold oxygen bond (O^{3-}) configuration, in which oxygen is linked to three silicon atoms. Our results also show that such peroxyl bonds occur more in the silica induced by atomic oxidation than by molecular oxidation, although their contributions to the total RDF is small. Indeed, most peroxyl oxygen atoms do not originate from one oxygen molecule but rather appear in the silica bulk after impact. The appearance of the peroxyl bridge bonds reduces the silica mass density. This explains the slightly lower mass density of the obtained silica bulk during atomic oxidation compared to the silica obtained by molecular oxidation. Indeed, such peroxyl bonds were almost absent in the molecular oxidation case.

Moreover, due to diffusion, the peroxyl bridges in silica may temporarily link to silicon atoms, increasing the number of metastable overcoordinated silicon atoms as indicated by 3 and 4 in figure 5.9b. Some first-principles calculations [62, 191] predicted that oxygen molecules or peroxyl bonds can also diffuse without linking to Si, and that the diffusivity depends on the ring size, which appears during silica formation. Furthermore, it is shown in figure 5.9c that O-O bonds with bond distances less than 2.0 Å are not found in the interface. Indeed, the peroxyl oxygen atoms only exist in the silica bulk and they break when they enter the interface region. Also Si-Si bonds (oxygen vacancies) [185] are found in both the interface and silica regions, albeit in very low concentration. Our results are in agreement with both experimental and first-principle calculations, indicating that the existence of the oxygen vacancy and diffusion of the peroxyl bridge bonds could play a role in the oxidation of the interface region during the formation of ultrathin silica films.

Analysis by means of angle distribution. In agreement with the assessment established based on the RDF data, the angle distribution in the bulk silica structures indicates an amorphous structure. Figure 5.10a presents O-Si-O angle distributions in the silica region.

In this distribution, most angles are distributed around 110^o in the atomic oxidation case and this value corresponds to the tetrahedral silicon structure (this angle in α-quartz is the tetrahedral angle of 109°). However, the peak slightly shifts to 90^o in the molecular case due to either stress near the interface or oxygen peroxyl bonds. Amorphous silica structure is characterized by the Si-O-Si angles. For comparison, the Si-O-Si angle in α-quartz is 144°. In the case of amorphous silica, slightly differing mean values of the Si-O-Si angle distribution were reported. Mozzi and Warren [190] reported on the vitreous (amorphous) silica structure, which is obtained by oxidation of thermal O_2, citing Si-O-Si angles widely distributed in the range 120° - 180°, while a peak in this distribution was found at 144°.

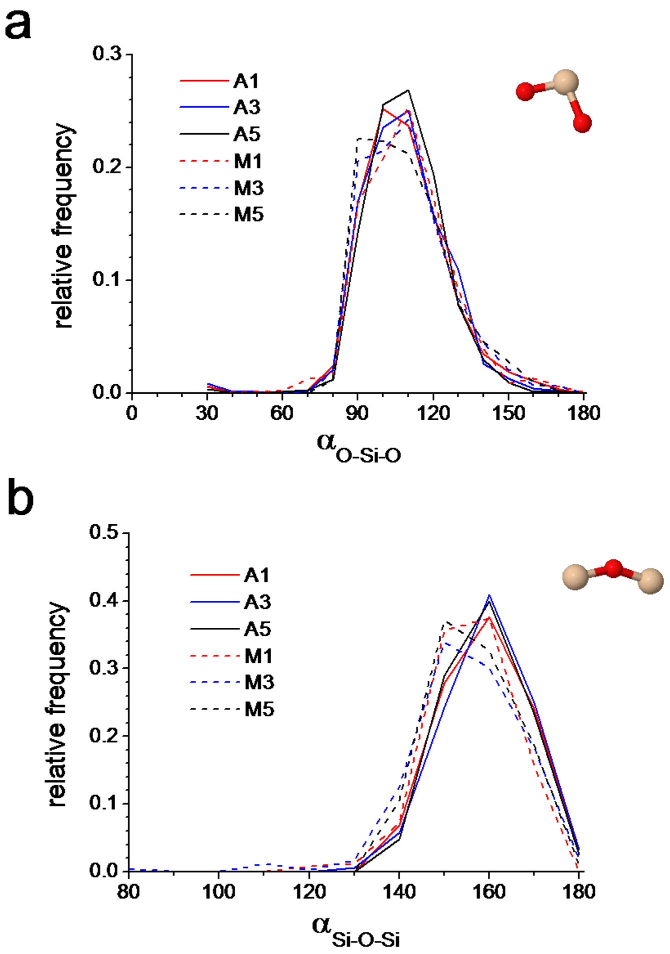

Figure 5.10 *Distribution of (a) the O-Si-O and (b) the Si-O-Si angles in the SiO_2 bulk silica structures, for the atomic and molecular impacts at the three different impact energies investigated.*

Furthermore, Watanabe et al. [192] investigated thermal growth by large-scale molecular dynamics and they concluded that the Si-O-Si bond angle in ultrathin SiO_2 film is reduced from 144° toward a narrower angle in the range 130° - 140°. Moreover, Mauri et al. [193] found a slightly higher mean value (i.e., 151°±11°) and a relatively narrow distribution (120° - 170°), in the Si-O-Si angular distribution of vitreous silica. However, in our case, corresponding to hyperthermal oxidation, two peaks in the Si-O-Si angle distribution were found around 145° and 160°, as illustrated in figure 5.10b. The first peak is in good agreement with results [190] of thermal O_2 oxidation. However, the second peak of the Si-O-Si distribution is slightly shifted to higher values, especially in the atomic oxidation case. Indeed, peroxyl oxygen bonds significantly affect the structures. As mentioned above, a relatively high number of oxygen peroxyl bridge bonds are found to be formed during the atomic oxidation process. Furthermore, about 3% the Si-O-Si angles near 110° are found, which indicates that some oxygen atoms have three silicon neighbors. Indeed, the contribution of oxygen peroxyl bridge (O-O) bonds, threefold coordinated oxygen (O^{3-}) atoms and fivefold coordinated silicon (Si^{5+}) atoms in the silica, widens the range of both the O-Si-O and Si-O-Si angle distributions, respectively. Although some intrinsic defects are found in the silica, the overall spread in the angle distribution confirms the amorphous character of the SiO_2 structure.

5.4 Conclusions

The growth behaviour of ultrathin silica during the hyperthermal oxidation process (with kinetic energies in the range 1-5 eV) at room temperature is investigated by reactive molecular dynamics.

The results show that hyperthermal oxidation consists of an initial fast and a subsequent slow oxidation stage. In the initial oxidation stage, incident oxygen species can penetrate deeper than the Si topmost surface and directly oxidize Si subsurface layers, in contrast to thermal oxidation. The oxygen atoms cannot move deeper into the bulk due to the associated activation energy barrier. The limit depth of the penetrating O species is deeper in the atomic oxygen case compared to the molecular one.

The oxygenated silicon structure is analyzed by division into three regions, that is, silica bulk, a transition layer, and the surface. The oxygenated silicon is energetically more stable than pure silicon. In all cases, the thickness of the transition layer is about 5 Å and surface roughness of the interface is low. A linear growth of the silica thickness in the earlier oxidation stage was observed. The silica thickness of the layers grown by molecular oxygen with an energy of 3 eV and atomic oxygen with 5 eV become about 6 Å and 19 Å, respectively, in agreement with experimental data. Therefore, it is concluded that the silica thickness can be controlled by controlling the initial kinetic energy of incident oxygen at room temperature.

The radial distribution function (RDF) indicates that the silica bulk contains some intrinsic defects (i.e., incorrect coordination of Si or O atoms, oxygen vacancies) and oxygen peroxyl linkages, both in the bulk as well as at the surface. Diffusion of peroxyl oxygen bridges could play a role in the oxidation during the formation of ultrathin silica films. The overall spread of the angle distribution confirms the amorphous character of the SiO_2 (a-SiO_2) structure.

Finally, it can be concluded that the control of the ultrathin a-SiO_2 thickness is possible by a hyperthermal oxidation of silicon surfaces at room temperature. This control over the obtained silica layer thickness is of great importance for technological applications as discussed in the introduction part of this thesis.

Chapter 6

On the *c*-Si|*a*-SiO_2 interface in hyperthermal Si oxidation at room temperature

6.1 Introduction

As gate insulator films in metal-oxide-semiconductor (MOS) devices are becoming as thin as a few nanometers or less, atomic scale understanding of the interface geometry as well as the electronic structure becomes increasingly important, specifically in relation to the required properties, such as high reliability, high resistivity, excellent dielectric strength, low interface defect density, and large band gap [2, 10]. The Si|SiO_2 interface obtained by traditional thermal Si oxidation [194] is therefore a very important interface, both from an economical as well as a technological viewpoint [195]. This interface has been investigated in detail through the years and various models have been put forward [188, 194-202]. Although the physics and chemistry of the Si|SiO_2 interface as formed in traditional thermal oxidation has already been intensively studied [2, 195, 197, 203], we still do not have a basic understanding of the interface obtained in hyperthermal Si oxidation [40]. Nevertheless, interest in hyperthermal oxidation of Si-surfaces as an alternative to thermal oxidation has been rapidly increasing and this process can be envisaged for semiconductor applications as well [43, 46-52, 139, 163, 178]. As mentioned above, the reaction of hyperthermal oxygen species (O, O_2; i.e., with energies of 1-5 eV) with Si surfaces at low temperature has unique properties compared to ordinary high temperature thermal oxidation. To be precise, using hyperthermal oxidation, ultrathin oxide films can be formed even at room temperature [40, 47-51, 139]. Furthermore, the possibility to accurately control [40, 50, 139] the oxide thickness at low temperatures (i.e., less than 500 K [204]) potentially provides new opportunities in the development of integrated nanoelectronic technologies.

Atomic scale investigations could elucidate several fundamental aspects of the hyperthermal oxidation of Si at low temperatures. Although several works [172, 173], which can be considered as modifications of the Deal-Grove model

[22], describe thermal oxidation kinetics well even at low temperatures, they fail to describe the formation of ultrathin oxide with a thickness lower than 2 nm [29], as also discussed in *chapters 5* and *7*. In the hyperthermal oxidation process, the nature of the self-limiting oxidation behavior at low temperature is still unclear. Several aspects can affect the Si|SiO_2 interface quality in such oxidation regime and distinguish it from thermal oxidation. Therefore, a set of questions regarding the interface remains open: How does the interface affect the growth process? What is a chemical composition of the transition layer compared to nonstoichiometric oxide layers as obtained in thermal oxidation? Indeed, investigation of the oxidation or of the defect formation processes near the Si|SiO_2 interface is also important to clarify various phenomena, such as the generation of defects and the interface degradation due to interfacial stresses.

This work is therefore focused on the *c*-Si(100)|*a*-SiO_2 interface as formed in hyperthermal Si oxidation. Reactive molecular dynamics (MD) calculations were carried out using the ReaxFF [128] potential in order to investigate the quality and oxide-limiting behavior of the interface on the atomic scale during the oxidation of the (2x1) reconstructed Si(100) surface, which is the most important surface facet for MOS devices fabrication at room temperature. The results presented in this chapter were published in the Journal of Physical Chemistry C [205].

6.2 Computational details

For the simulations, a Si(100){2x1} reconstructed surface is chosen (see figure 4.1). In our calculations, 1 monolayer (ML) corresponds to 32 atoms, which is equal to the number of Si atoms per layer. Prior to the oxidation process, the (2x1) reconstructed Si (100) surface is prepared as follows. First, the surface is equilibrated at 300 K using the Berendsen heat bath (NVT dynamics) [177] for 20 ps with a damping constant of 0.1 ps. Next, the obtained structure is relaxed in the microcanonical ensemble (NVE dynamics) for 10 ps.

Energetic oxygen impacts are subsequently performed as follows. The incident particle (oxygen atom or oxygen molecule) is positioned at a z-position of 10 Å above the uppermost Si-atom of the crystal. The {x, y} coordinates of the incident particle are chosen randomly. In the case of molecular oxygen, the O_2 molecule is rotated randomly prior to impact. The impinging particle is directed normal to the surface, corresponding to laser detonation experiments

[47, 178]. Every impact is followed for 3 ps in the microcanonical ensemble. The initial kinetic energies of the oxygen species (O, O_2) were set to 5 eV. At the end of each impact, the excess energy is allowed to dissipate and the temperature is allowed to decrease to 300 K prior to the next impact.

After oxidation, Cauchy atomic stresses [113] were calculated as the virial stress for structures obtained by O and O_2 oxidation, as well as for the pristine Si crystal. For all stress calculations, the structures were first equilibrated at 0.01 K using NpT dynamics, to remove the kinetic energy part from the stress calculation, and subsequently the total energy was minimized using the steepest descent and conjugate gradient techniques. The local stress is calculated by dividing the oxidized and non-oxidized structures into small rectangular boxes [206]. The tensor has 6 components for each atom and is stored as a 6-element vector in rectangular Cartesian coordinates: normal - σ_{xx}, σ_{yy}, σ_{zz}, and shear - σ_{yz}, σ_{zx}, σ_{xy}. The stress components in all directions are averaged per unit thickness of 1.296 Å, corresponding to the distance between two neighbor layers in the *c*-Si (100) along the z-axis or equal to half of the thickness of the oxide layer [51]. The local tensor of each i atom is defined as

$$\sigma_i = \begin{bmatrix} \sigma_{ixx} & \sigma_{ixy} & \sigma_{ixz} \\ \sigma_{iyx} & \sigma_{iyy} & \sigma_{iyz} \\ \sigma_{izx} & \sigma_{izy} & \sigma_{izz} \end{bmatrix} = -\frac{1}{2\Omega}\sum_{k=1}^{N} \vec{F}_{ik} \times \vec{r}_{ik} \qquad (6.1)$$

where Ω is volume of the rectangular box, $\vec{F}_{ik}$ is the vector of the force acting on atom *i* due to atom *j*, which are separated from each other by the vector $\vec{r}_{ik}$. *N* is the total number of neighbors of atom *i*. The local stress in each box is calculated by averaging the atomic stresses of the atoms included in the rectangular box.

6.3 Results and discussion

6.3.1 Partially oxidized and transition oxide layers

Corresponding to experimental [40, 48] and MD studies (see *chapter 5*), the oxidation process in hyperthermal Si oxidation at room temperature can be divided in two stages: (I) the initial fast (or direct) oxidation stage and (II) the subsequent slow oxidation stage. In figure 6.1, two representative oxygenated Si structures are shown for both stages, corresponding to the atomic oxidation with initial incident energy of 5 eV.

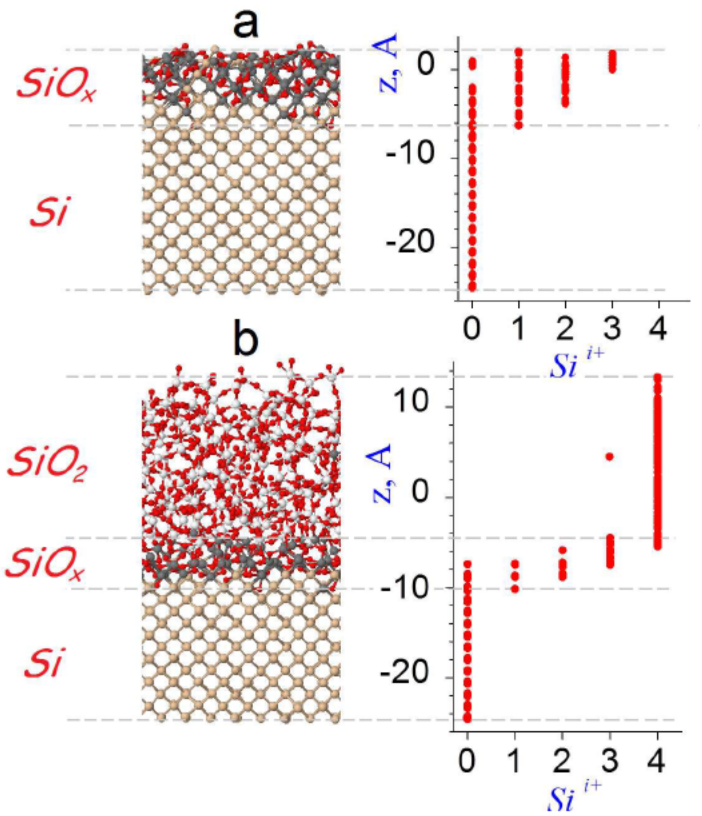

Figure 6.1 *Oxidized Si structures induced by hyperthermal (5 eV) oxygen impacts in the first (a) and second (b) oxidation stage, respectively. Here, the light grey, grey and white Si atoms are components of silicon (Si), non-stoichiometric oxide layers (SiO_x, $0<x<2$) and silica (SiO_2) regions, respectively. The oxygen atoms are colored in red. Every structure is analyzed by means of the Si-(sub) oxide (Si^{i+}) components. 0 Å corresponds to the top-most layer of the original pristine Si lattice.*

The oxide growth process and the chemical structure of the obtained oxide can be easily analyzed by means of the Si-(sub) oxide components [47-51, 139]. The Si^{1+}, Si^{2+}, Si^{3+} and Si^{4+} components arise from interfacial silicon atoms, which bind to one, two, three and four nearest-neighbor oxygen atoms, respectively, and thus correspond to Si_2O, SiO, Si_2O_3 and SiO_2, respectively [181]. The notation used corresponds to formal charge states and not to the actual atomic charges. The nomenclature "SiO_2" is used for fully oxidized silicon (i.e., silica). The term "SiO_x" is used to indicate the partially oxidized or non-stoichiometric oxide region ($0 < x < 2$), instead of Si_2O, SiO and Si_2O_3. As this work is devoted to the understanding of the Si|SiO_2 interface, we focus on the non-stoichiometric oxide (SiO_x) region as formed during hyperthermal oxidation. It was found that the non-stoichiometric oxide layers mostly consist of three Si suboxide species (i.e., Si^{+1}, Si^{+2} and Si^{+3}), albeit some Si^{4+} atoms, which is the unique component of amorphous stoichiometric oxide (a-SiO_2), can also be found in low concentration [186].

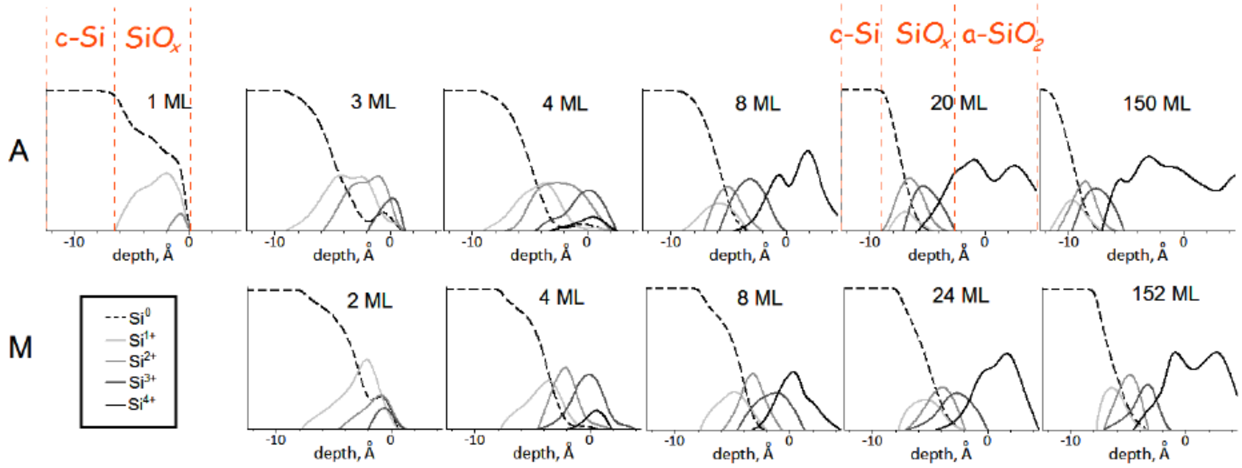

Figure 6.2 *Distribution of Si-(sub)oxide components during atomic (A) and molecular (M) oxidation using 5 eV impacts. Here,* Si^{1+} *(light grey),* Si^{2+} *(grey) and* Si^{3+} *(dark grey) species are components of the* SiO_x *region. Most* Si^0 *(black dash) and* Si^{4+} *(black solid) atoms are located in the c-Si and a-*SiO_2 *regions, respectively. 0 Å corresponds to the top-most layer of the original pristine Si lattice. Note that 1 ML corresponds to 32 atoms.*

Figure 6.2 shows the spatial distribution of the Si-oxide components in the oxygenated Si region during both atomic (A) and molecular (M) oxidation at an impact energy of 5 eV. As mentioned before, 1 ML (monolayer) corresponds to 32 atoms. In the first stage, the oxygen content increases rapidly due to the high adsorption probability of the oxygen species on the pure silicon surface [139]. As shown in the figure, the Si^{1+} component dominates in the first three MLs of oxygen fluence for both oxidation cases. This is due to the direct oxidation of the silicon surface and sub-surface layers by hyperthermal oxygen atoms [47, 51, 139, 179, 204]. In this stage, penetrating oxygen atoms can directly oxidize up to the second sub-surface layer [46, 51, 204] at room temperature. This is a marked difference with thermal oxidation at the same temperature [172, 173]. Due to relatively high impact energy, the chemisorption of O_2 molecules is found to be dissociative in all cases [163]. Therefore, in both oxidation cases (O as well as O_2), the only penetrating particle is an O-atom. Our previous results [139, 163, 204] also showed that the final penetration depth per impact is found to be determined in the first ps, and essentially remains constant afterwards, thereby validating our impingement rate of 1 impact every 3 ps. At low temperatures, however, the deposited oxygen atoms cannot move deeper into the crystal due to the high energy barrier [180]. As a result, the Si^{1+} gradually converts to Si^{2+} and Si^{3+} [47-51, 139] forming a non-stoichiometric oxide layer which consist of oxygen atoms with relatively high oxidation states. Consequently, the oxygenated Si region (i.e., partially oxidized layers) consists of three sub-oxide components, which are consecutively dominating in the SiO_x oxide formation process [139]. Namely, the entire oxygenated Si region is non-stoichiometric in this stage, while some initial silica molecules (SiO_2) appear on the oxygenated Si surface after 4 ML. Consequently, in the period from 4 ML to 8 ML, the surface becomes fully covered by one silica layer.

When the second oxidation stage starts, a SiO_2 monolayer completely covers the SiO_x surface. Therefore, in stage II, the oxygenated Si is divided into a stoichiometric (SiO_2) oxide region and a non-stoichiometric (SiO_x) oxide one. This non-stoichiometric oxide region therefore forms a transition layer between crystalline silicon (*c*-Si) and amorphous silica (*a*-SiO_2) [40, 47-51, 139, 204]. We refer to the non-stoichiometric oxide region as a "partially oxidized layer" (figure 6.1a) in stage I and as the "*c*-Si|*a*-SiO_2 interface" or "transition oxide layer" (figure 6.1b) in stage II. Thus, as shown in figure 6.2, the "partially oxidized layer" (A, 1 ML) becomes the "transition oxide layer" (A, 20 ML), which corresponds to *c*-Si|*a*-SiO_2 interface after about 8 ML for both atomic and molecular oxidation. This value constitutes the transition between the first and second oxidation stages.

In stage II, all Si oxide components are found in the transition oxide layers as shown in the figure. In the transition layers, the spatial distribution of the suboxide species indicates that Si^{1+}, Si^{2+} and Si^{3+} species are concentrated in a region of 4.5 Å, 5.0 Å and 5.5 Å between the non-oxidized Si layer and the *a*-SiO_2, respectively. The Si^{2+} species are localized between Si^{1+} and Si^{3+} states in the transition oxide region. The interval of the distribution peaks is about 1.0 Å.

The percentages of Si-oxide components in the SiO_x and SiO_2 regions are 45% and 55%, respectively, in molecular oxidation in the second stage. In the atomic oxidation case, they are 26% and 74%, respectively. However, Tagawa and co-workers [40] reported that the oxide formed by 5 eV O atoms at room temperature consisted mainly of Si^{4+} with only 6% suboxide components, based on an analysis of X-ray photoelectron spectroscopy (XPS), which plots the number of detected electrons versus their binding energy. This difference can be explained by considering that this percentage of Si-oxide components depends on the oxide thickness, which in turn, also strongly depends on the fluence of the energetic oxygen species even, at the same temperatures [23]. It has been reported that the oxide thickness decreases from 4.5 nm to 1.75 nm when the oxygen fluence is reduced from $1\cdot10^{19}$ to $1\cdot10^{17}$ O atoms$\cdot$cm^{-2}, at almost the same conditions [14, 16] as for the hyperthermal oxidation process. In our calculations, the O fluence is $2.1\cdot10^{17}$ O atoms$\cdot$cm^{-2} and the obtained oxide thickness is 1.85 nm for the atomic oxidation. This is fairly close to the experimental oxide thickness of 1.75 nm obtained using a fluence of $1\cdot10^{17}$ O atoms$\cdot$cm^{-2}, as determined from XPS measurements [48]. Further, our simulations show that the percentage of Si-oxide components in the partial (SiO_x) and fully oxidized Si (SiO_2) regions is almost constant during the relatively long second oxidation stage.

An important quantity is the number of Si atoms displaying an intermediate oxidation state (per unit area), which is denoted by $N_{\mathrm{SiO}x}$. In the second stage, after 20 ML of O fluence, the total density in the interface is about 5.5 MLs or $3.7\cdot10^{15}$ atoms$\cdot$cm^{-2}, which is somewhat larger than the experimental estimates for the thermal oxidation [199, 207, 208]. However, we point out that the distribution character of suboxide species in the transition region, as shown in figure 6.2, agrees with the XPS and photoemission spectroscopy (i.e., PES – measurement of the energy of photoelectrons emitted from target) reports [199, 208]. In figure 6.3, the distribution of the Si-suboxide species versus the oxidation progression is shown.

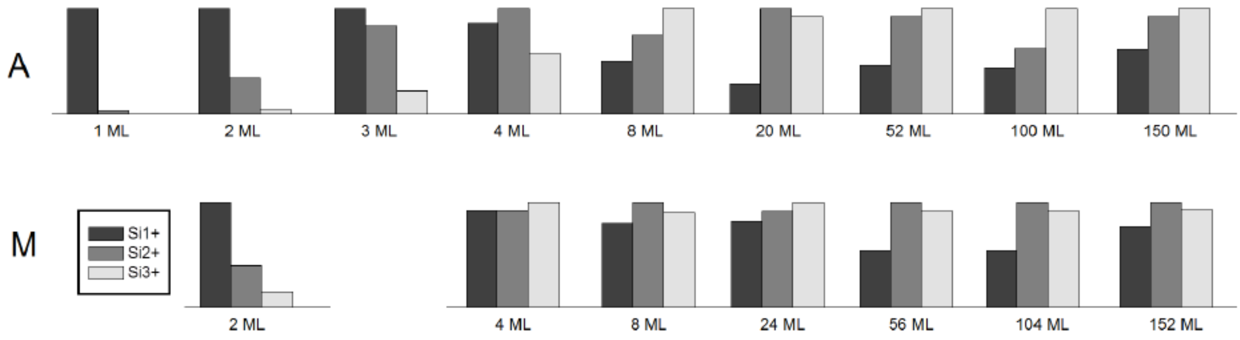

Figure 6.3 *Distribution of the Si-suboxide species, i.e.,* Si^{1+} *(black),* Si^{2+} *(grey) and* Si^{3+} *(light grey) in the non-stoichiometric oxide region, i.e., the partially oxidized layers (0-8 ML) and transition oxide layers (8-152 ML) during atomic(A) and molecular(M) oxidation at an impact energy of 5 eV.*

With respect to the nominal population ratio of Si^{1+}, Si^{2+}, and Si^{3+} species in the SiO_x oxide region in the first stage, it is found that the density of the intermediate oxidation states evolves as $N(Si^{1+}) > N(Si^{2+}) > N(Si^{3+})$ for both the atomic and molecular oxidation (figure 6.3). However, this distribution changes in this case. The intensity distribution of intermediate oxidation states in the second stage is $N(Si^{1+}) < N(Si^{2+}) \leq N(Si^{3+})$ for the atomic oxidation, suggesting that this is a universal property of the $Si|SiO_2$ interface during a thermal oxidation process [199]. On the other hand, in the molecular case, the distribution is $N(Si^{1+}) < N(Si^{3+}) \leq N(Si^{2+})$. Indeed, the number of the Si^{2+} components is greater than the number of Si^{3+} components in the last 100 MLs. Therefore, the oxygen deficiency is somewhat larger in the interface induced during molecular oxidation. Furthermore, our calculations show that the silicon density in the transition region is slightly higher than in the a-SiO_2 region, while the oxygen density is lower, corresponding to experimental evidence obtained by Gusev et al. [61].

6.3.2 Thickness evolution of the non-stoichiometric oxide region

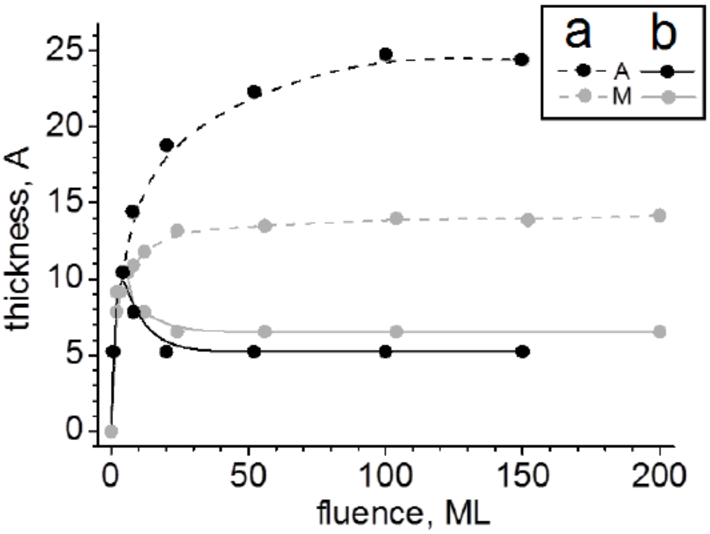

Figure 6.4 *Thickness of (a) the oxygenated Si and (b) its non-stoichiometric oxide layers as a function of the oxygen fluence, for both atomic (A) and molecular (M) impacts of 5 eV.*

Figure 6.4 illustrates the evolution of the thickness of the oxygenated Si and its non-stoichiometric oxide layers for oxidation by both atomic (A) and molecular (M) oxygen, at an impact energy of 5 eV. The thickness is calculated based on the distribution of the Si-suboxide species as shown in figure 6.2 and its resolution is 1.296 Å, which corresponds to the thickness of one half oxide layer (OL) [51].

In stage I, the thickness of the oxygenated Si region (a) and its non-stoichiometric oxide layers (b) rapidly increases up to 11.7 Å (4.5 OLs) for both atomic and molecular oxidation, as shown in the figure. At the beginning of stage II, the thickness of the non-stoichiometric oxide region starts decreasing due to partial conversion of this region to silica, reducing the thickness of the transition oxide layers (or a *c*-Si|*a*-SiO_2 interface) to 5.3 Å (2.0 OLs) for atomic oxidation, and to 6.5 Å (2.5 OLs) for molecular oxidation. These *c*-Si|*a*-SiO_2 interface thicknesses correspond to the lower limit of several experimental measurements [209] and ab-initio results [210], in which the one of the non-stoichiometric oxide was reported to range from 4 Å to 50 Å in thermal Si oxidation. However, due to the immediate breakup upon impact of the O_2 molecules, the change in the oxygenated silicon thickness as a function of the incident energy is smaller for the molecular oxidation than for the atomic oxidation process, and the final thickness is equal to 24.7 Å in the atomic oxidation case, and to 14.3 Å in the molecular oxidation one. Indeed, as the impinging molecules are given the same initial kinetic energy as the impinging atoms, the individual atoms obtained after molecule dissociation have less momentum and hence a lower velocity. As a result, oxygen molecules do not penetrate as deep in the surface as the oxygen atoms [163].

Although the thickness of the ultrathin interface remains constant and almost the same for both atomic and molecular oxidation, the morphology of the interface structure might be different. This is discussed in the next sections.

6.3.3 Morphological analysis of the *c*-Si|*a*-SiO_2 interface

Roughness. The morphology of the transition oxide region (or the *c*-Si|*a*-SiO_2 interface) is characterized in terms of its root-mean-square (RMS) roughness. Figure 6.5 presents the variation of the RMS roughness versus the oxygen fluence for both atomic and molecular oxidation using 5 eV impacts. The RMS roughness δ [211] is obtained as

$$\delta = \sqrt{\langle (h - \bar{h})^2 \rangle} \tag{6.2}$$

where h is the top z-coordinate of a Si atom which has no O neighbors in the c-Si|a-SiO$_2$ interface, and $\overline{h}$ is the average over all h values. Prior to oxidation, the roughness of the (2x1) reconstructed Si (100) surface is 1.03 Å.

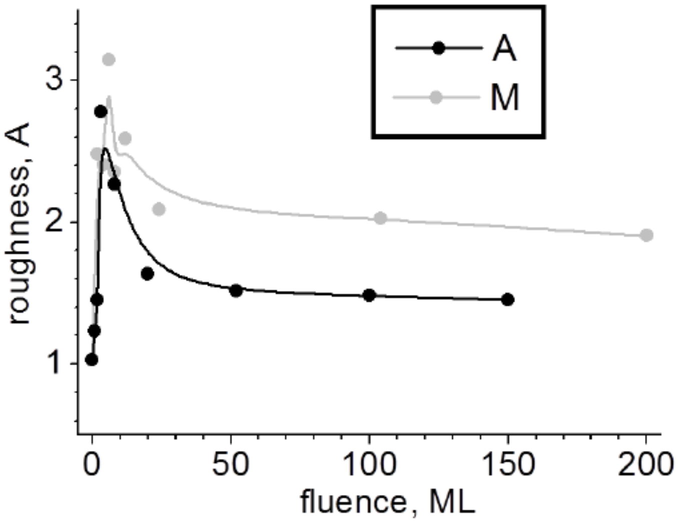

Figure 6.5 *Root-mean-square (RMS) roughness of the c-Si|a-SiO$_2$ interface versus the oxygen fluence, for both atomic (A) and molecular (M) impacts of 5 eV.*

The figure demonstrates a roughening of the initially smooth surface in the first oxidation stage and subsequently a smoothening of the rough surface during the second stage, as was previously also proposed by Irene [188]. In stage I, the surface roughness linearly increases up to approximately 3 Å in both oxidation cases. In this stage, some surface restructuring occurs, resulting in higher Si oxidation states. In the second stage, the c-Si|a-SiO$_2$ interface roughness decreases again due to the appearance of a stoichiometric oxide layer on top of the SiO$_x$ region. In atomic oxidation, the roughness of the interface is constant at about 1.5 Å, which is close to the RMS value (~1.3 Å) of the c-Si|a-SiO$_2$ interface as obtained in thermal oxidation [212]. Molecular oxidation, on the other hand, enhances the surface roughness: The average value is somewhat larger (~2.1 Å) than in the atomic oxidation case and the interface is therefore less abrupt. In addition, such behavior is also experimentally observed in thermal oxidation: In typical industrial oxides, the roughness of the Si|SiO$_2$ interface increases with decreasing oxide layer thickness [213]. Furthermore, stresses in the interface region may change the interface roughness as well, which is discussed in the last section. Discussion of the interface morphology is continued in the next section.

Bond-length and bond-angle distributions. The bond-length and bond-angle distributions for the interface structures as generated during the oxidation are shown in figure 6.6. During the second oxidation stage, the bond-length distributions are very similar in both atomic and molecular oxidation (see figure 6.6a). Indeed, the peaks of the Si-O and Si-Si bond length distributions correspond to 1.58 Å and 2.35 Å in the atomic case, respectively, and to 1.59 Å and 2.4 Å in the molecular case. These values are fairly close to the results reported in interface models [200, 202]. However, it is also observed an unusual tail in the Si-Si bond-length distribution in the range 2.5 – 2.9 Å, which has not been reported in the thermal models. Although O-O peroxyl-bridge bonds are not found in this structure [139], the interface is not free from coordination defects. For instance, some threefold oxygen atoms (O^{3-}) are found in the interface, albeit in very low concentration.

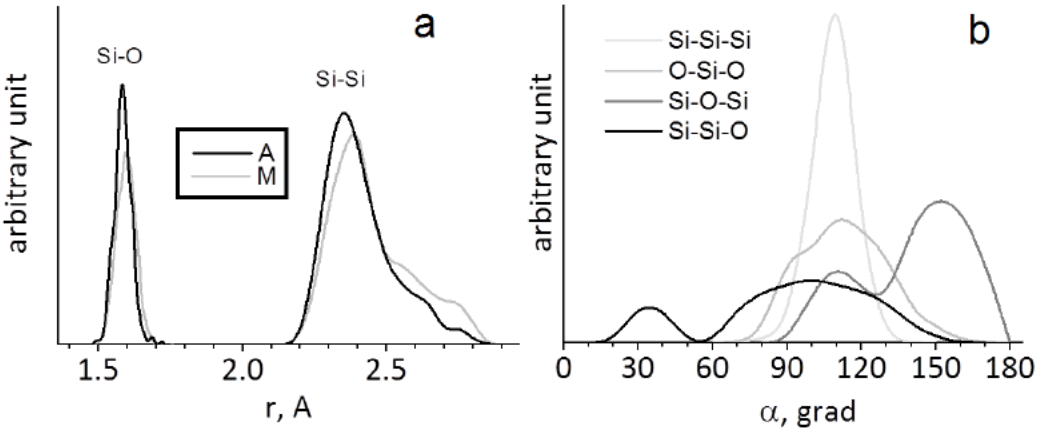

Figure 6.6 *(a) Bond-length and (b) bond-angle distributions in the c-Si|a-SiO$_2$ interface during atomic (A) and molecular (M) oxidation with impact energy of 5 eV after 150 MLs of oxygen fluence.*

In figure 6.6b, the Si-Si-Si, O-Si-O, Si-O-Si and Si-Si-O bond-angle distributions in the second oxidation stage (after 150 ML) for only the atomic oxidation case are shown. It's found that these distributions are almost the same for the molecular oxidation case and therefore only the picture for the atomic oxidation case is shown. The bond angle is about 110° for both the Si-Si-Si and O-Si-O angle distributions, which is fairly close to the experimental value, while the O-Si-O distribution is somewhat wider in our structures (i.e., 75°-165°) than the distribution usually cited for amorphous silica (i.e., 109°±10°) [141, 190, 193]. Also, two main peaks are observed for both the Si-O-Si and Si-Si-O cases. The peaks are located at about 103˚ and 152˚ for the Si-O-Si angle distribution and at 38˚ and 100˚ for the Si-Si-O angle distribution.

For the vitreous (amorphous) silica structure as generated by thermal O_2 oxidation, Mozzi and Warren [190] obtained a wide distribution of Si-O-Si angles varying between 120° and 180°, with a main peak found at 144°. However, Da Silva et al. [214] suggested that the most probable Si-O-Si bond angle of vitreous silica is 152° instead of 144°. Mauri et al. [193] also found a slightly higher mean value of 151°±11° and a relatively narrow distribution (120° - 170°) in the Si-O-Si angular distribution of vitreous silica. In our model, a second peak in the Si-O-Si angle distribution is in the range of 120°-180°, peaking at about 152°. These values are in good agreement with the results of Silva et al. [214] and Mauri et al. [193] and indicate that some part of the transition region is similar to *a*-SiO_2.

Although the interface morphology is close to interface models proposed for thermal oxidation, some unexpected SiO (defect) structures are found in our interface model induced by hyperthermal oxidation, which is discussed in the next section.

“Si epoxide linkages”. The first peak of the Si-O-Si and Si-Si-O bond angle distributions indicates that some defects, i.e., Si-O-Si triangular configurations (indicated by blue circles in figure 6.7a) exist in the interface.

Stefanov et al. [215] also observed such three-membered Si-O-Si rings in high temperature annealing of the water-exposed Si (100)-{2x1} surface using infrared absorption spectroscopy and density functional cluster calculations to identify the intermediate oxide structures. They termed this unexpected defect “Si epoxide linkage” and denoted it by SiØSi, by reference to the analogous structure in carbon chemistry. They demonstrated that this structure is the thermodynamically favored product and should be preferentially formed at silica interfaces. In our calculations, the Si-Si bond-length of this configuration is in the range 2.5-2.9 Å (see figure 6.6a), which is somewhat longer than the Si-Si bond-length of 2.16 Å suggested by Stefanov et al. [215]. Figure 6.7b shows that the concentration of these triangular structures significantly increases in the initial oxidation stage. In this stage, the entire oxygenated Si region is non-stoichiometric and the Si epoxide linkages can be found in this entire region. However, these epoxide structures are only found in the interface when the silica formation begins. Therefore, their concentration remains constant during the second oxidation stage.

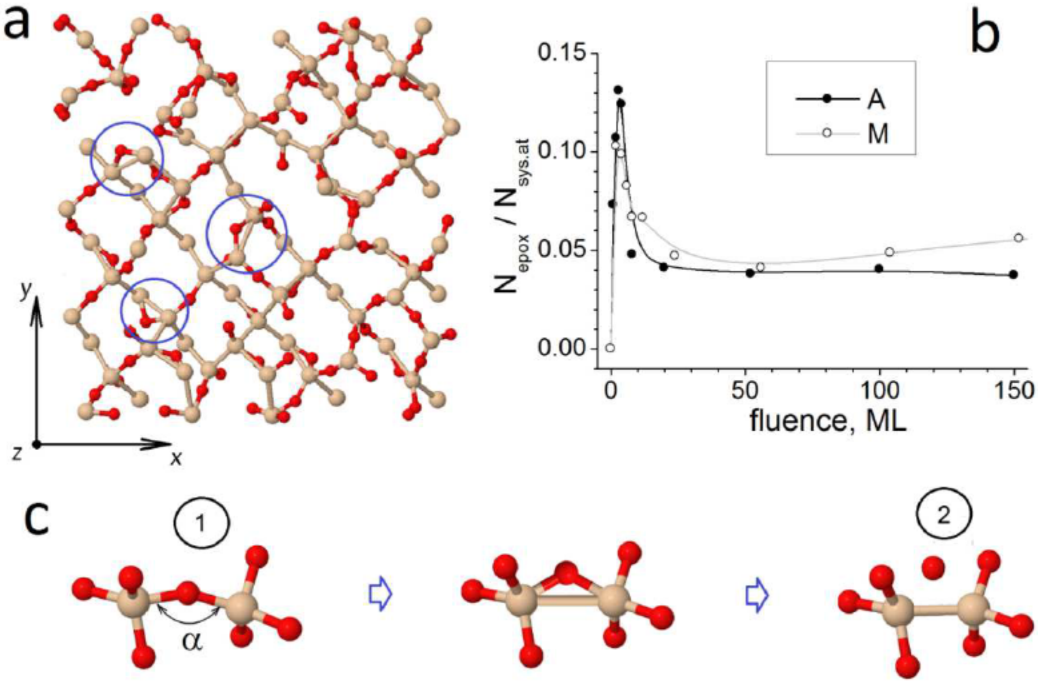

Figure 6.7 *(a) Top view of the Si|SiO*$_2$ *interface and some Si-O-Si triangular configurations (or "Si epoxide linkages") in the interface (in blue circles). (b) Evolution of the Si epoxide concentration during oxidation. (c) Physical stress-enhanced bond breaking mechanism, proposed by Yang et al. [216].*

Formation of such structures may also be explained by a physical stress-enhanced bond breaking mechanism as proposed by Yang and Saraswat [216], which is schematically represented in figure 6.7c: For the oxide breakdown to occur, the Si-O-Si bonds in SiO_2 (panel 1) break and are replaced by the Si-Si bonds, ultimately pushing away the O-atom (panel 2). It was proposed that the Si-O-Si (α) angle decreases when the stress increases. They concluded that this mechanism is strongly dependent on the physical stress in the thin oxide films. This conclusion was also in agreement with the previous Fourier transform infrared spectroscopy results of Tagawa et al. [40], which revealed that smaller Si-O-Si bond angles exist in oxide films as created by hyperthermal atomic oxygen, compared to the Si-O-Si angles in alpha-quartz, implying that compressive stresses exist in the SiO_2 film. We propose that the SiØSi structures (figure 6.7a) in our *c*-Si|*a*-SiO_2 interface may constitute a transition state between two states (panels 1 and 2 in figure 6.7c) in the bond breaking mechanism due to interfacial stresses [217]. It is also known that a high stress is associated with low temperature oxidation while a low stress is associated with high temperature oxidation [40, 216, 217]. Therefore, the interfacial stresses may significantly enhance the concentration of Si-O-Si triangular structures in our interface as obtained at room temperature. This behaviour will be explained by the stress calculation, as presented in section 6. Hence, the study of the interfacial stress gives useful information on the interface properties in hyperthermal oxidation at low temperatures [40].

6.3.4 Interfacial stresses during oxidation

The interfacial stress, which can be thought as a combination of chemical and mechanical (physical) stresses [217], plays an important role in the reliability of gate oxides with its ultrathin interface [215]. The chemical stress at the interface is associated with Si atoms which have an intermediate oxidation state between *0* (in Si) and *4+* (in SiO_2). Mechanical stress appears from the mismatch of unit cells and local bonding mismatch in the bulk construction between the Si and SiO_2 parts. Mechanical stress causes the deformation of bonds and bond angles at the interface. Korkin et al. [218] suggested that the chemical and the mechanical stress make comparable contributions to the total Si|SiO_2 interface stress.

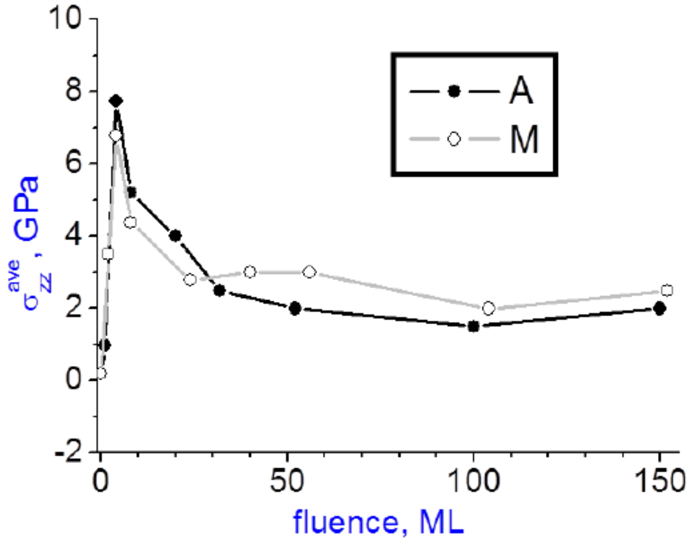

Figure 6.8 *Evolution of the in-plane (x-y plane) averaged stress along the z-axis in the c-Si|a-SiO_2 interface during atomic (A) and molecular (M) oxidation with 5 eV impacts.*

As mentioned in section of computational details, it was calculated stresses as the symmetric per-atom stress tensor for each Si atom in the *c*-Si, SiO_x and *a*-SiO_2 regions using the approach proposed in reference [219]. The calculations show that all stress components in the non-oxidized *c*-Si (100) {2x1} surface are very small and compressive, i.e., σ_{xx} ~ 0.1 GPa, σ_{yy} ~ 0.1 GPa and σ_{zz} ~ 0.2 GPa. We believe that the oxidation reaction rate coefficient is not lowered by the stress in the initial oxidation stage as suggested Kao and co-workers [82]. Consequently, the initial oxidation rate depends more strongly on the stress-free initial reaction rate coefficient rather than on stress and temperature. In the *c*-Si|*a*-SiO_2 interface, as formed during the oxidation, however, σ_{xx} and σ_{yy} are somewhat higher than the σ_{zz}, and are in the range 6 – 8.5 GPa. The applied periodic boundary conditions (PBC) in x and y directions, increases the mechanical stress in those directions [177, 82]. We suggest that the inward oxide growth [204] depends on the σ_{zz} rather than σ_{xx} and σ_{yy} stresses.

Figure 6.8 shows the evolution of stress along the z-axis (σ_{zz}) versus the oxygen fluence for both atomic and molecular oxidation. Note that positive and negative values correspond to compressive and tensile stresses, respectively. In the first oxidation stage, the σ_{zz} stress significantly increases due to the quick expansion of the *c*-Si. In this stage, the $Si^{1+} \rightarrow Si^{2+} \rightarrow Si^{3+}$ conversion occurs relatively fast as mentioned in the previous sections, and it leads to an increase in both the chemical as well as the mechanical stresses. As a result, the average value of the σ_{zz} stress increases up to 8 GPa in the partially oxidized Si layers. In the second oxidation stage, however, the average stress value at the *c*-Si|*a*-SiO_2 interface decreases to about 2.0 and 2.5 GPa for atomic and molecular oxidation, respectively, and subsequently remains almost constant. These obtained stress values are in good agreement with experimental data, in which the Si|SiO_2 interface was investigated using high-resolution transmission electron microscopy (HRTEM) analysis and a compressive stress was found of approximately 2 GPa [220]. While this value is not very high, it is strong enough for significantly reducing the oxygen diffusivity in the Si|SiO_2 interface during the second oxidation stage. Such a self-limiting effect, which increases with decreasing growth temperature [40], was previously also observed in Si nanowire oxidation [83, 84, 140, 217, 221]. This effect may also significantly influence the flat interface thickness and roughness, which were discussed in previous sections. Due to both the high impact energy and the compressive interfacial stresses, the resulting interface thickness is different in atomic and molecular oxidation.

In summary, the formation and properties of the Si|SiO_2 interface in hyperthermal oxidation was investigated, in comparison with existing thermal models. Although no attempt was made to determine the statistical variation in the obtained results, the general conclusions are found to correspond to experimental results. As reported in several experimental studies [40, 47-51], the interface plays a significant role in controlling the hyperthermal oxide thickness. The high reactivity of hyperthermal oxygen reduces the mobility of atomic oxygen at the Si|SiO_2 interface at the low (room) oxidation temperature and leads to micro roughness, sub-oxides, and a high stress at the interface. In these low temperature experiments, the hyperthermal oxygen species (atoms and molecules) (with energies in the range of 1-10 eV) were generated by laser-detonation source developed by Physical Science Inc. [53]. These experimental outcomes corroborate our conclusions.

6.4 Conclusions

The *c*-Si|*a*-SiO_2 interface as obtained by hyperthermal oxidation of Si(100) {2x1} surfaces by oxygen atoms and molecules was studied using reactive molecular dynamics simulations.

The formation of the non-stoichiometric oxide region was analyzed, and two oxidation regimes were found: First a fast oxidation stage lasting for about 8 monolayers (MLs) of oxygen fluence (“stage I”), followed by a subsequent slow oxidation stage (“stage II”). Distribution of Si-suboxide components show that the oxygen deficiency is somewhat higher in the interface induced by molecular oxidation compared to atomic oxidation. The distribution of the suboxide species in the transition region agrees with several interface models. Calculations show that the thickness of the oxygenated Si region rapidly increases up to 11.7 Å in the initial oxidation stage. The thickness of the non-stoichiometric oxide region decreases again in the second oxidation stage due to a partial conversion to silica. The interface reaches a constant thickness of about 6.0 Å, which corresponds to the lower limit in experimental results. It is also observed that molecular oxidation increases the surface roughness. A root-mean-square (RMS) roughness value of about 2.1 Å was found, whereas it was about

1.5 Å in the atomic oxidation case. This indicates that the interface is less abrupt in the molecular oxidation case. The Si-Si-Si and O-Si-O angle distributions show a peak at 110˚, which is close to the experimental value. However, the Si-O-Si and Si-Si-O bond-angle distributions indicate some defects, e.g., Si-O-Si triangular configurations (or “Si epoxide linkages”) exist in the *c*-Si|*a*-SiO_2 interface, which can be explained by a physical stress-enhanced bond breaking mechanism. Finally, the interfacial stresses during oxidation were also investigated. In the interface, a compressive stress of about 2 GPa was found, which is in agreement with experimental evidence.

Chapter 7

Effect of growth temperature in hyperthermal Si oxidation

7.1 Introduction

Reaction and diffusion of oxygen atoms and molecules during thermal oxidation have been previously analyzed both by experimental and theoretical means [21, 153, 155, 181, 203, 222-225]. However, for hyperthermal oxidation, such studies are still rare. Although numerous studies have elucidated the overall oxidation behavior [47-51], various aspects, such as direct oxidation or the effect of the growth temperature, are still poorly understood. Also, there are still many open questions regarding the growth mechanism in the initial oxidation stage as a function of temperature, which is significantly different from the mechanism in the thermal oxidation case.

According to the generally adopted Deal–Grove model [22] for thermal wet and dry oxidation, silicon oxide films grow via diffusion of oxidants, i. e., oxygen atoms or molecules to the $SiO_2|Si$ interface and by reaction of these oxygen species with silicon at the interface. As discussed in the previous chapters, it is well known that the model and its extentions [172, 173] clearly fail to describe the oxidation kinetics of ultrathin films (< 20 Å) [20, 61] in hyperthermal oxidation in two situations:

(a) there is no solution of the equation for the formation of substoichiometric oxides in the case $\theta(0) = 0$, that is, when there is no pre-existing oxide layer on the Si surface prior to oxidation; and

(b) there are no suitable parameters for describing the direct oxidation, i.e., energetic oxygen species directly oxidizing the Si-subsurface layers.

Such thin layers can, however, be obtained by hyperthermal oxidation of Si at room temperature [139]. Some other models, such as the so-called reactive layer model [226], have also been presented. According to this model, silicon atoms diffuse through the thin reactive layer and react with oxygen on top of this layer, forming the SiO_2 phase. Unfortunately, little experimental evidence has been reported to support this idea [61]. The atomistic mechanism of Si emitting from the Si|SiO_2 interface was reported [227], which was in fairly good agreement with experimental results corresponding to layer-by-layer Si oxidation theory [153]. However, oxide growth mechanism is not described well by this theory [173]. Furthermore, the outward diffusion of Si has not been investigated yet for hyperthermal oxidation.

Indeed, the growth mechanism of silicon dioxide in the initial stage of hyperthermal oxidation has not yet been properly analyzed and investigations at the atomic scale may further elucidate the growth mechanism. Although our study in *chapter 5* is devoted to understanding the oxidation process of the Si(100) surface by energetic oxygen species (i.e., O atoms and O_2 molecules with initial energies from 1 to 5 eV) at room temperature on the atomic scale, the oxide formation and growth mechanism at higher temperatures in hyperthermal oxidation is still unclear. Therefore, reactive molecular dynamics (MD) calculations were also carried out in order to investigate the growth mechanism of new oxide layers during hyperthermal oxidation (i.e., initial kinetic energies in the range 1-5 eV) of the (2x1) reconstructed Si(100) surface in a wide temperature range (100-1300 K). The results presented in this chapter were published in the Journal of Physical Chemistry C [204].

7.2 Computational details

As before, the 2x1 reconstructed Si(100) surface was chosen as the initial structure (see figure 4.1). Prior to oxygen bombardment, eight Si(100){2x1} surfaces were prepared as follows. First, the surfaces are equilibrated at 100 K, 300 K, 500 K, 700 K, 900 K, 1100 K, 1200 K, and 1300 K using the Berendsen heat bath (NVT dynamics) [113] for 20 ps with a damping constant of 0.1 ps. Then, the obtained structures are relaxed in the microcanonical ensemble (NVE dynamics) for 10 ps. Periodic boundary conditions are applied to the (x,y) plane, to mimic a laterally infinite surface during the simulation. Energetic oxygen impacts are performed as follows. The incident particle (oxygen atom or oxygen molecule) is positioned at a z position of 10 Å above the uppermost Si atom of the crystal. The {x, y} coordinates of the incident particles are chosen randomly. In the case of molecular oxygen, the O_2 molecule is rotated randomly prior to impact. The impinging particle is directed normal to the surface, corresponding to laser detonation experiments [47, 178]. Every impact is followed for 3 ps. The initial kinetic energies of the oxygen species (O, O_2) were set to 1 eV, 3 eV and

5 eV. In total, 48 different cases were investigated for the oxidation process, i.e., 3 different impact energies for both atomic and molecular oxygen at the 8 different growth temperatures, as mentioned above. Each case was run for 1024 consecutive impacts, corresponding to a growth thickness of 32 monolayers (ML).

7.3 Results and discussion

7.3.1 Hyperthermal Oxidation Process at Various Growth Temperatures

Figure 7.1 shows the distribution of the formed oxygenated silicon layers for various growth temperatures after 32 monolayers (ML) of oxygen impacts, both for molecular (M) and atomic (A) oxygen impacts at 1 eV and 5 eV. In our calculations, 1 ML equals 32 atoms. The grey and red atoms represent silicon and oxygen atoms, respectively. As can been seen in the figure, the oxidized silicon can be divided in two parts: an interface region and pure silica. Our previous results on hyperthermal oxidation at room temperature showed that also the silica (SiO_2) region (yellow region in figure 7.1) can be divided in two sections: a surface region and a bulk region. The interface region, which is located between the crystalline Si and the SiO_2 bulk, (i.e., dark grey region in figure 7.1) consists of Si^{1+}, Si^{2+} and Si^{3+} suboxide components. Generally, the Si^{1+}, Si^{2+} , Si^{3+} and Si^{4+} components are supposed to arise from interfacial silicon atoms, which bind to one, two, three and four nearest-neighbor oxygen atoms, respectively [21, 181]. Silicon atoms that connect to four oxygen atoms (Si^{4+}) are the unique members of the silicon dioxide SiO_2 phase, although some overcoordinated and undercoordinated Si atoms can be found in this region as well.

Figure 7.1 clearly shows how the growth temperature, the incident oxygen species and its initial kinetic energy affect the oxygenated silicon thickness. The change in oxygenated silicon thickness as a function of incident energy is smaller in the case of molecular oxidation than for atomic oxidation, due to the immediate breakup upon collision of the molecules. Indeed, as the molecules are given the same initial kinetic energy as the atoms, the individual atoms obtained after dissociation have less momentum and hence a lower velocity. Therefore, oxygen molecules do not penetrate as deep in the surface as the oxygen atoms.

Furthermore, in all cases, the growth temperature significantly affects the interface thickness, rather than the thickness of the SiO_2 (silica layer). Note that the interface thickness is limited in all cases up to 700 K due to the activation energy barrier associated with the penetration of successive Si layers by the impinging oxygen species.

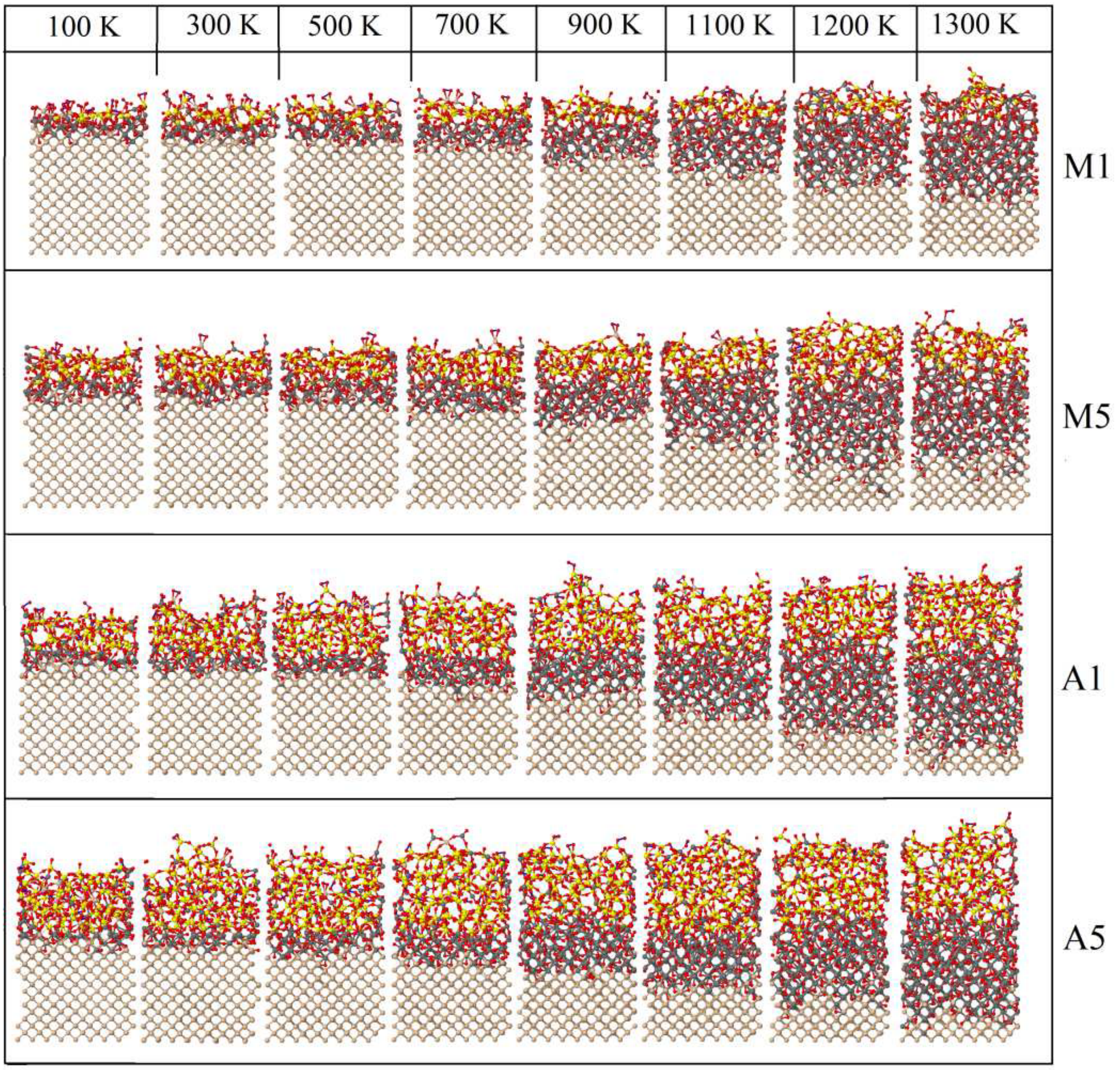

Figure 7.1 *Illustration of the temperature effect on the oxidation of silicon after 32 monolayers (ML) of oxygen impacts, by oxygen molecules at* E_0*=1 eV (M1) and* E_0*=5 eV (M5) and by oxygen atoms at:* E_0*=1 eV (A1) and* E_0*=5 eV (A5). Note that 1 ML corresponds to 32 atoms. Here, the Si crystal (*Si^0*), interface (*Si^{1+}*,* Si^{2+}*,* Si^{3+}*), silica (*Si^{4+}*) and oxygen atoms are colored light grey, dark grey, yellow and red, respectively.*

However, above this temperature, the interface atoms can surmount this energy barrier, which results in a higher diffusivity. Therefore, the temperature of 700 K can be regarded as the transition temperature between the two different growth mechanisms during hyperthermal oxidation, as will be explained in *section 7.3.3*. This result is in close agreement with experimental evidence for thermal oxidation. Indeed, it was found that the interstitial neutral oxygen atoms and molecules become mobile above 200 °C (~500 K) and 400 °C (~700 K), respectively [224].

For a given incident species, the thickness of the oxide layer depends on two factors, namely, the incident energy and the growth temperature. Our results indicate that at temperatures below 700 K, both the final thickness of the silica layer and the growth mechanism depend mostly on the incident energy. Indeed, the oxygenated silicon and ultrathin silica thickness can be easily controlled by the particle impact energy at low temperature. At higher temperatures, the thickness and the growth mechanism strongly depend on the growth temperature as well. Indeed, in this case, the mobility of the penetrated oxygen atoms increases significantly. As mentioned above, in hyperthermal oxidation, all incident molecules dissociate to individual atoms due to the (relatively) high impact energy. Therefore, the mobility of the molecules in the oxygenated silicon cannot be analyzed.

Analysis of the interface region, which is located between the silica (SiO_2) and crystalline Si phases, by means of the number of suboxide components (Si^{1+}, Si^{2+} and Si^{3+}) after oxidation by 32 ML of oxygen atoms (see figure 7.2a) clearly shows the two types of interfaces, i.e., at temperatures below and above the transition temperature of 700 K. Below the transition temperature (i.e., 100 - 500 K), a very thin interface is formed of about 5 Å (cf. figure 7.1). In this interface, the number of these suboxide components is less than 1 ML, as is clear from figure 7.2a. Above this transition temperature (i.e., 900 – 1300 K), however, their number drastically increases with increasing growth temperature. This means that mobile oxygen atoms continue to penetrate deeper into the silicon. Especially the number of the Si^{1+} species dominates in the interface region due to the high diffusivity of the oxygen atoms.

In figure 7.2b, the appearance of silica and its growth behavior at different temperatures is presented by means of the number of Si^{4+} components, expressed in number of ML, plotted after different values of ML impacts, as indicated by the legend. At temperatures below 700 K, the first silica layer appears after 4 ML, whereas above this temperature, no silica layer is observed yet. Subsequently, after 8 ML, the number of Si^{4+} components is much higher at low temperature than at high temperature, indicating that the initial growth of the silica layer occurs much faster at low than at high temperature. However, after 32 ML, the number of Si^{4+} components is almost the same at all temperatures. This indicates that the silica layer now grows faster at higher temperature, but its nucleation started later. The rapid growth of the silica layers can be understood from the growth mechanism as will be outlined below.

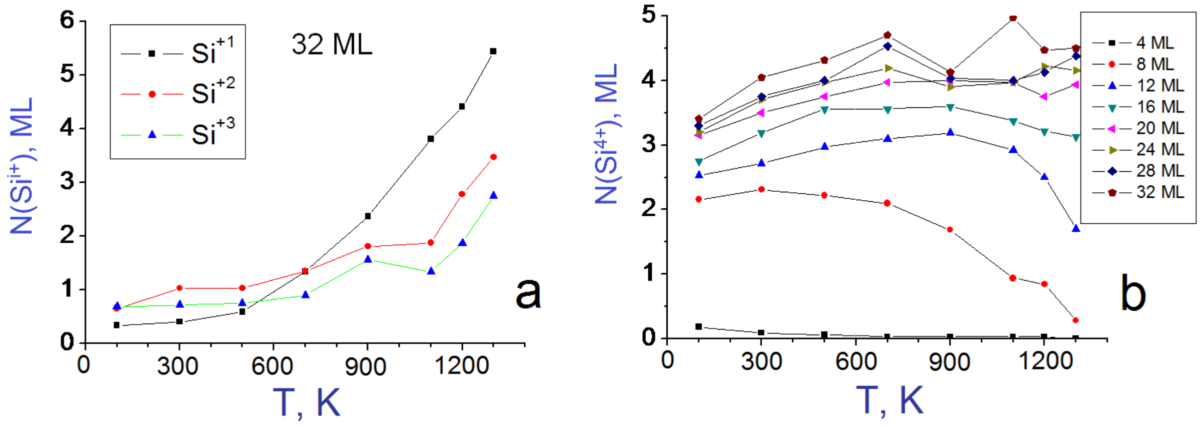

Figure 7.2 *(a) Analysis of the interface region by the total number of Si^{1+}, $Si^{2+}$and Si^{3+} suboxide components (expressed in ML) as obtained after 32 ML of atomic oxygen impacts for a kinetic energy E_0=5 eV, as a function of oxidation temperature. (b) Total number of Si^{4+}, expressed in ML, in the interface region, as a function of oxidation temperature, after a specific number of impacts, expressed in ML as defined in the legend.*

Indeed, in the traditional thermal oxidation regime, the onset of silicon oxidation is characterized by an incubation period, i.e., the oxide thickness remains constant during this period, and is equal to the initial native-oxide thickness. The duration of this incubation period decreases with increasing temperature [179]. However, our results presented in figure 7.2 show that the mechanism is different in the case of hyperthermal oxidation. Therefore, in the following section, the onset of the hyperthermal Si oxidation process is studied in more detail.

7.3.2 Onset of hyperthermal Si oxidation

In the hyperthermal oxidation process, the results show that the initial oxidation stage can be divided in a first direct oxidation stage and a second relatively slow one. These two stages are governed by the initial kinetic energy of the impacting species and the growth temperature, respectively. The oxidation onset is characterized by direct insertion of incident oxygen species in the Si crystal. Indeed, direct insertion of oxygen atoms into the Si subsurface layers occurs during the initial oxidation stage in the hyperthermal oxidation process, which is not observed in thermal oxidation. This is explained as follows. In the hyperthermal energy regime, the incident atoms having kinetic energies in the range E_0=1.0-5.0 eV, in our case, can surmount the energy barriers of the first and second subsurface layers [46-48], which are estimated to be about 1.0 and 2.4 eV, respectively [180]. In other words, oxygen species can be incorporated directly in the silicon substrate. Such oxidation behavior near room temperature was also studied by ellipsometry and synchrotron radiation photoemission spectroscopy [47, 51, 228]. Formation and growth of the oxygenated silicon during this direct oxidation stage can be easily understood by observing the variation of the silicon suboxide components.

As stated in the beginning of this section, the initial oxidation stage can be divided in a first direct oxidation stage and a second relatively slow oxidation stage. The end of the first direct oxidation stage is indicated by the vertical dashed line as shown in figure 7.3. At this moment, Si^{2+} is also found (figure 7.3b) and its density continues to increase slightly in the second oxidation stage. At low temperatures, the O atoms cannot penetrate deeper into the crystal at the end of the direct oxidation stage, and the Si^{1+} gradually converts to Si^{2+} and Si^{3+}. This conversion from Si^{1+} to Si^{2+} and Si^{3+} characterizes the second oxidation stage. The Si^{3+} component appears only in this oxidation stage and two groups of curves (indicated by α and β in figure 7.3c) are found. Note that in the lower temperature range (i.e., curves indicated by α), the density of Si^{3+} suboxide species increases slightly faster than at higher temperatures (i.e., curves indicated by β). This means that at low temperature, the consecutive $Si^{1+} \rightarrow Si^{2+} \rightarrow Si^{3+} \rightarrow Si^{4+}$ conversion, i.e., the appearance of a new silica layer, occurs much faster than at high temperatures. Indeed, the penetrated O atoms cannot move deeper into the crystal due to the energy barrier and the Si-Si bonds convert relatively fast to Si-O bonds in the oxygenated silicon region. As a result, the formed silica layer is found to be thicker at low temperature at the same oxidation stage (see figure 7.2b).

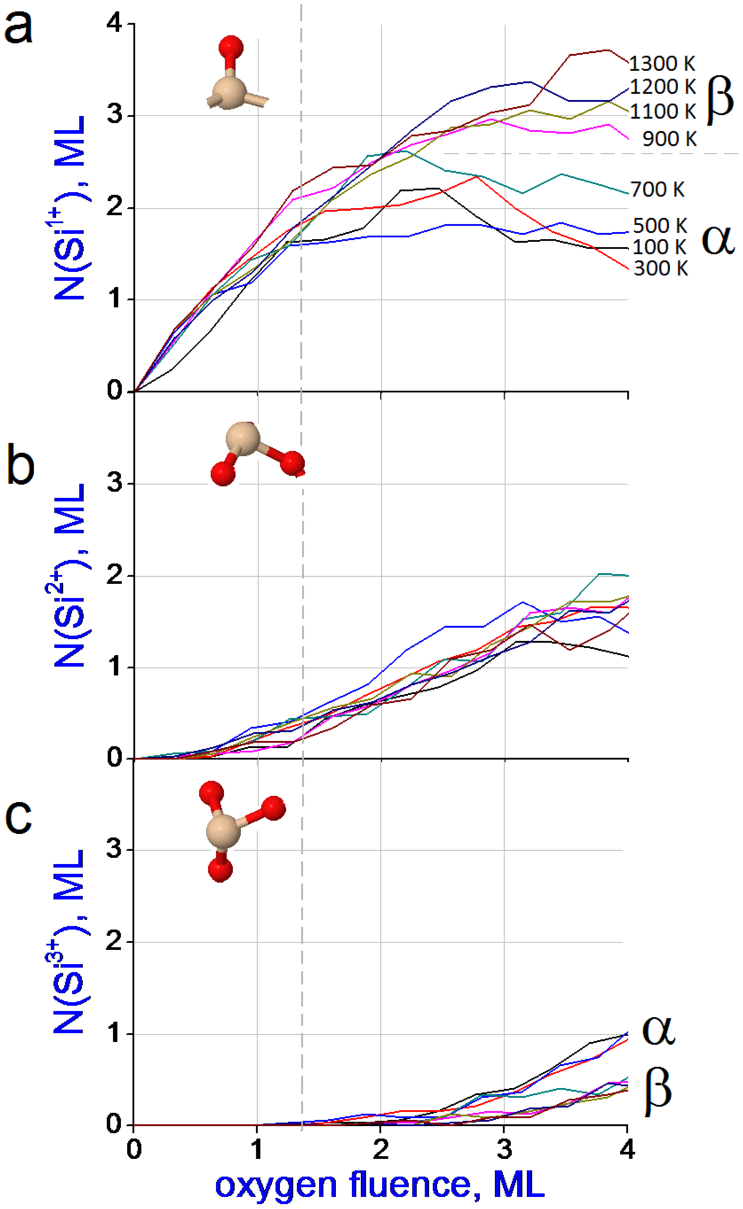

Figure 7.3 *Analysis of the initial oxidation stage (i.e., up to 4 ML impacts) by means of the Si suboxide components: Si^{1+}, Si^{2+} and Si^{3+} are silicon atoms, which bind to one, two and three nearest-neighbor oxygen atoms, respectively. Here, α and β indicate the two groups of curves related to the low (100-500 K) and high (900-1300 K) temperature cases, respectively.*

Furthermore, during the conversion, the most stable Si-O bonds appear near the surface, which can significantly affect the sticking rate of the incident oxygen species. In all impact cases, the density of the penetrated O atoms drastically decreases after the initial oxidation stage. This, of course, affects the thickness of the oxygenated silicon. At higher growth temperatures, however, oxygen atoms can penetrate deeper due to their higher diffusivity. As a result, the conversion of the Si^{1+} to Si^{2+} and Si^{3+} is slower. Therefore, the second group of curves (see figure 7.3c) in Si^{3+} changes less than the first group of curves. Indeed, the relatively slow conversion of the Si suboxide components is caused by the diffusion of the interstitial oxygen atoms, allowing the oxygen to penetrate deeper into the silicon bulk due to the easy surmounting of the energy barrier in this higher temperature range. Also, because the conversion is slower, the interface region becomes much thicker at high temperature than at low temperature, as was indeed clear from figure 7.1.

Finally, when one complete silica layer is formed, the initial oxidation period, which consists of a direct oxidation stage and a relatively slow one as mentioned above, ends. This corresponds to the addition of 4 ML of oxygen atoms. Because of the energy barriers, the penetrated atoms lose their kinetic energy rapidly and further inward oxygen displacement is prevented (below the transition temperature region) or controlled by the growth temperature (above the transition temperature region). Therefore, we believe that the threshold temperature (see figure 7.3a, dashed horizontal line) is an important factor in controlling the formation of the oxygenated silicon.

To conclude, the initial oxidation stage is indicative of some notable differences between the hyperthermal oxidation and traditional thermal oxidation, i.e., instead of an incubation period [179], direct oxidation is observed with a specific duration that depends on the energy of the incident species. As this can change the growth mechanism of the oxide layer in the initial oxidation stage, the hyperthermal oxide growth mechanism is analyzed in the next section.

7.3.3 Oxide Growth Mechanisms

As mentioned above, the silicon oxidation behavior is significantly different below and above the transition temperature. Here, the growth mechanism of the oxide layers is analyzed in both cases. In figure 7.4, the SiO_2 growth process on a {2x1} reconstructed Si(100) surface by oxygen atoms with an incident energy of 5 eV at 300 and 1300 K is presented. The oxidation progress is shown by suboxide histograms. Here, grey, green and red bars describe the density distribution per depth of pure Si, oxygenated Si (i.e., SiO_x) species (with $x < 2$) and ultrathin silica (i.e., SiO_2) layers, respectively. The z=0 Å position corresponds to the topmost layer of the original pristine Si lattice. Our calculations are based on the mass center position of Si layer planes [177] and show that the average thickness of each layer is equal to 1.296 Å, corresponding to the thickness of one half oxide layer (i.e., the thickness of one oxide layer is 2.6 Å [51]). The growth mechanism was analyzed by comparing four specific stages (denoted as I, II, III, IV in figure 7.4) during the growth process at 300 and 1300 K.

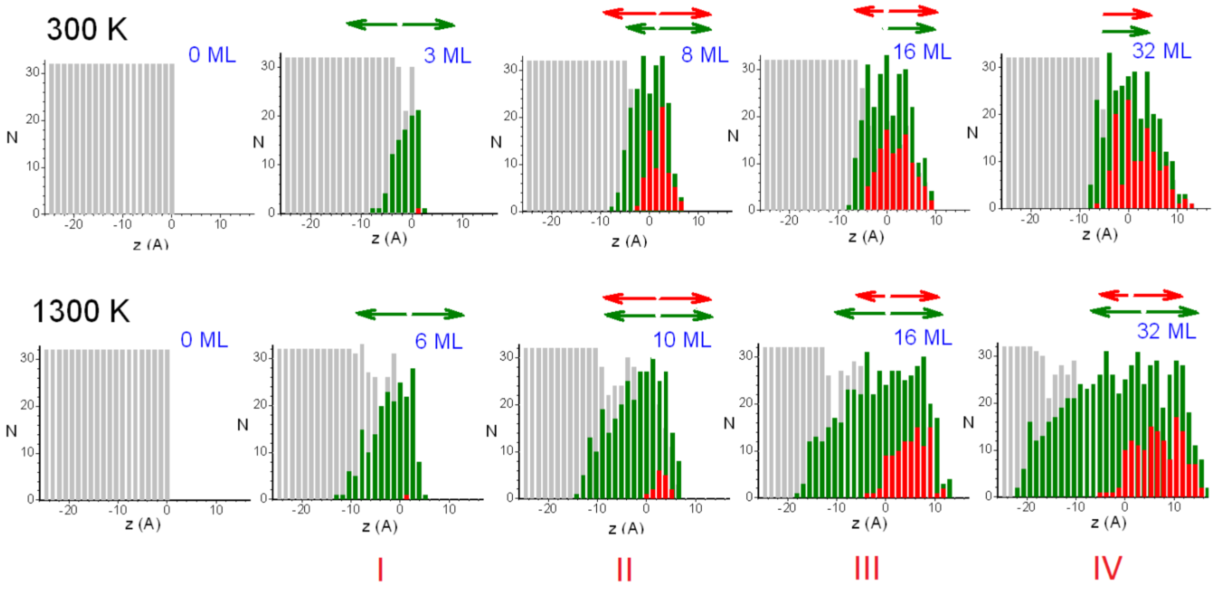

Figure 7.4 *Growth behavior of oxidized silicon and ultrathin silica layers induced by 5 eV atomic oxygen at temperatures of 300 K and 1300 K. The occurrence of pure Si, SiO_x ($x < 2$) and SiO_2 phases is indicated in the histograms by light grey bars, green bars and red bars, respectively. Green and red arrows indicate the growth direction of the oxidized silicon and silica layers, respectively.*

In stage I, for both cases, the oxidized layers grow simultaneously inward and outward, normal to the surface; note that the green arrows indicate the growth direction of oxidized layers in figure 7.4. In this stage, the number of the Si^{1+} component increases significantly, as was clear from Figure 7.3a. This corresponds to the initial oxidation stage, which was discussed in section 2. The appearance of an incipient silica layer indicates the end of stage I.

Stage II is indicated by the appearance and growth of the silica layer. At this stage, not only the oxidized layers but also the silica grows in two directions, i.e., inward and outward, at both temperatures (the red arrows indicate the growth direction of silica in figure 7.4). Because of the relatively high activation energy barrier, however, the inward growth rate of the oxidized layer drops at low temperature. In that case, as mentioned in section 2, the $Si^{1+} \rightarrow Si^{2+} \rightarrow Si^{3+} \rightarrow Si^{4+}$ conversion is fast, and a new silica layer quickly forms and grows faster than at high temperature. As a result, the thickness of ultrathin SiO_2 obtained at low temperature is slightly higher than at high temperature, as was obvious from Figure 7.2b.

In stage III, the inward growth at low temperature is slowed down, especially for the oxidized layer but also for the silica layer, and the O atoms cannot penetrate in the crystal any further due to the associated activation energy barrier of the Si subsurface layers, which is in the order of 1 and 2.4 eV for the first and second Si subsurface layers, respectively [153, 180]. However, at higher temperature, interstitial neutral oxygen atoms are still sufficiently mobile to surmount the activation energy barrier. In reference [224], a threshold temperature of 500 K for this process was suggested. Therefore, at higher temperature, both the inward and outward growth of the substoichiometric (SiO_x) and the stoichiometric (SiO_2) oxide layers still continues. However, the inward growth of the silica layer slows down, in a similar way as at low temperature.

In stage IV, i.e., the final stage, the inward growth becomes negligible at low temperature. Therefore, in this stage, only the outward growth of the oxidized silicon and silica phases continues. Our earlier study on the growth mechanism at room temperature [139] showed that, during the entire oxidation process (150 ML), the penetrated oxygen atoms can move only up to a certain limit depth, which is about ten Angströms from the top of the surface of the pristine crystalline Si. The limit of the oxidized depth is equal to the maximum penetration depth of the oxygen atoms and it determines the maximum number of silicon atoms that may contribute to the formation of the oxygenated silicon layers. The limit depth is found to be nearly constant after stage IV and it depends on both kinetic energy and type of incident oxygen species. The maximum penetration depth was found to be 5 and 9 Å for the atomic oxidation case with kinetic energies of 1 and 5 eV, respectively. In the case of oxidation by molecular oxygen, the limit depths were slightly lower than in the atomic case and the values were equal to 4 and 8 Å for kinetic energies of 1 and 5 eV, respectively. The limit depths are also close to the values of our previous calculations [163].

At high temperature, however, both the oxidized silicon and silica layers continue to grow in both directions (i.e., inward and outward), although the inward silica growth rate drops. In that case, the interface, which consists of the Si^{1+}, Si^{2+} and Si^{3+} species, is significantly thicker than at low temperature, as was also observed in figure 7.1. The oxide thickness attains its maximum value when also the outward growth of the silica stops (not shown in figure 7.4).

Study of the outward and inward displacement of silicon and oxygen species in the oxide growth process also allows a further understanding of the growth mechanism. In figure 7.5 the evolution of the Si and O layers is shown as a function of oxygen fluence, during the oxidation at 300 and 1300 K. As mentioned above, $z = 0$ Å corresponds to the topmost layer of the original pristine Si lattice in both cases. In figure 7.5a, each line corresponds to the average z coordinate of the Si atoms (belonging to the pristine substrate layer) as a function of the oxidation progress, expressed in number of added ML of oxygen. The simulated Si crystal consists of 20 layers, with an initial interlayer separation of about 1.3 Å.

The results are interpeted as follows. At the very beginning of the oxidation process, the lines indicate that the upper surface and subsurface layers remain in place. In this short period (direct oxidation stage), some oxygen atoms can penetrate up to the limit depth of about 9 Å in the low temperature (300 K) case [163]. During the growth process, the top layers expand and the distance between the layers doubles relative to the initial separation (see light grey lines in figure 7.5a), corresponding to one oxide layer [51]. By comparing both temperatures, it can be seen that the thickness of the formed silica layer is almost the same in both cases for the same oxidation time, but a thicker oxygenated silicon layer is obtained at high temperature (as was also obvious from Figure 7.1). The silica structure obtained at higher temperatures contains some Si-Si bonds, i.e., undercoordinated Si atoms, which are explained by the relatively slow conversion of the Si suboxide components. Therefore, the distance between the lines (layers) is different from the interlayer distance at lower temperature. Furthermore, we did not observe the outward displacement of any Si atom that is not connected to oxygen atoms. As mentioned in the introduction, according to the reactive layer model [226], silicon atoms should diffuse through the thin reactive layer and react with oxygen on top of this layer, forming the SiO_2 phase, which is not the case in our simulations. Therefore, this model cannot describe the growth behavior in hyperthermal oxidation.

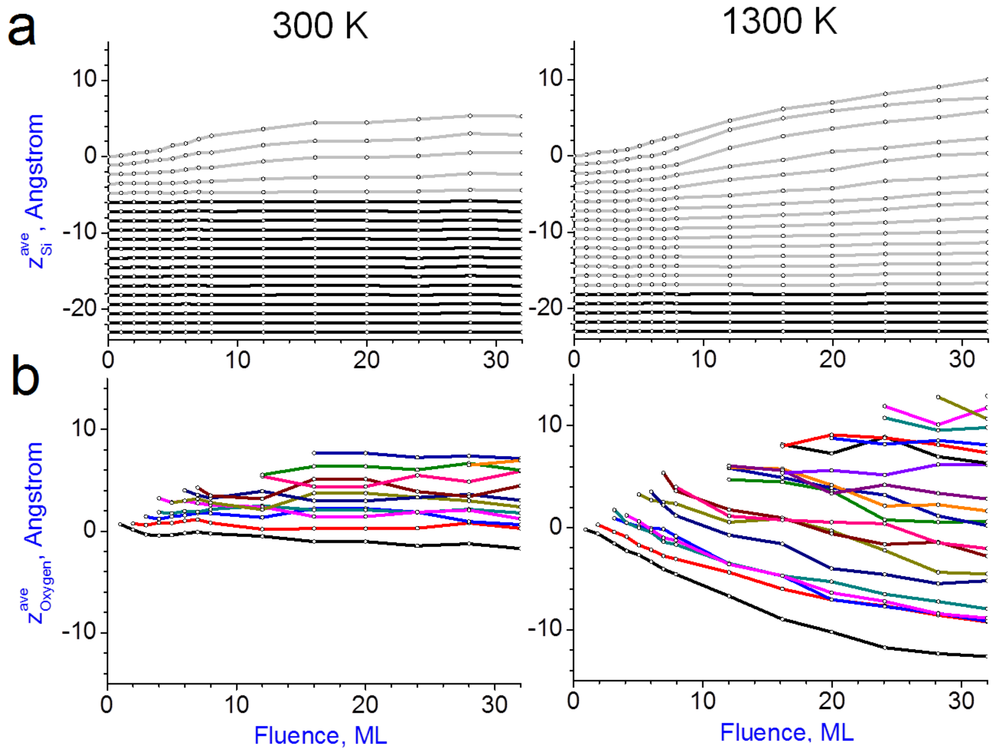

Figure 7.5 *Evolution of (a) the growth of oxygenated Si layers, as shown by the average z-coordinate of the silicon atoms per atomic layer, and (b) the inward diffusion depth of penetrated oxygen during hyperthermal oxidation by oxygen atoms of 5 eV, at temperatures of 300 K and 1300 K, respectively. Here, z = 0 Å corresponds to the top-most layer of the original pristine Si lattice. The black curves in (a) indicate the pure Si layers, whereas the grey curves indicate the Si atoms in the oxidized layers. The curves with different colors in (b) just represent different oxygen layers, but have no further specific meaning.*

In figure 7.5b, each line corresponds to the average z coordinate of 32 penetrated oxygen atoms during oxidation. Positive z values indicate oxygen atoms adsorbed on top of the Si surface, whereas negative z values represent penetrated oxygen atoms due to inward diffusion during the oxidation process. Note that, due to the increasing activation energy, inward oxygen diffusion is observed only at temperatures above the transition temperature. At low temperature, inward oxygen growth is inhibited by the associated energy barrier. Indeed, in hyperthermal oxidation in this temperature region, the kinetic energy of the incident oxygen atoms is the dominant factor, rather than the growth temperature. In contrast, in the oxidation process at high temperature, oxygen atoms are continuously being displaced due to their high diffusivity. However, we did not observe the oxidation by oxygen diffusion through oxidized layers. Hence, also the Deal-Grove model [22] does not describe the hyperthermal oxidation mechanism as observed in our simulations.

Hence, our growth mechanism predicts that, when the temperature is below the transition temperature (i.e., $T < T_{transition}$), the oxide thickness depends on the kinetic energy of the incident oxygen species. However, in the case $T > T_{transition}$, the oxide thickness depends on both the incident energy and the growth temperature. Note that these predictions are not observed nor expected in the traditional thermal oxidation process.

7.3.4 Analysis of the oxygenated Si structure during oxidation

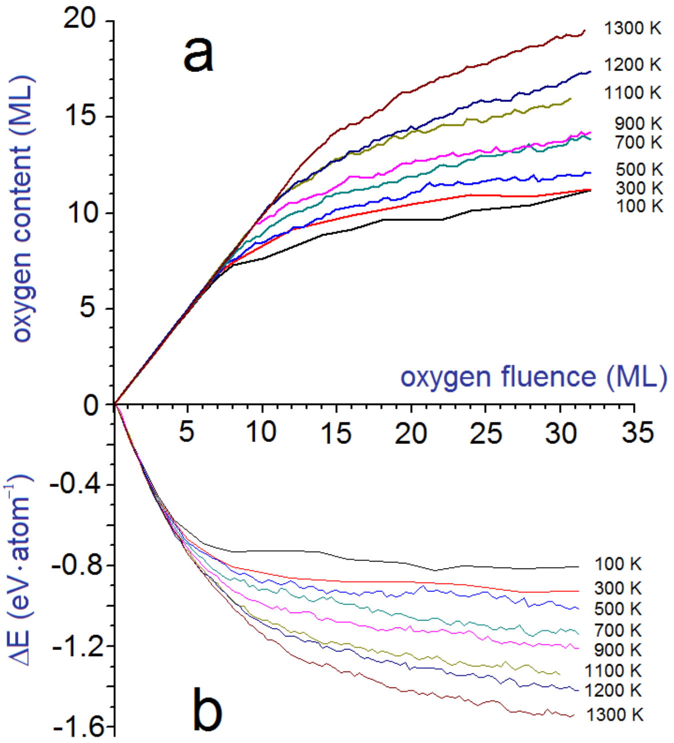

Figure 7.6 *Oxygen content during hyperthermal oxidation of the 2x1 reconstructed Si(100) surface at various temperatures (a) and variation of the total energy of the oxygenated system (b) as a function of fluence, for an atomic oxygen beam with 5 eV kinetic energy.*

Figure 7.6 shows the oxygen content and the energy gain of the oxygenated + nonoxygenated system as a function of the oxygen atom fluence at 5 eV. As can be seen in figure 7.6b from the calculated system energy gain, the oxygenated silicon is energetically more stable than pure silicon. This stabilization occurs due to the formation of the Si-O bonds. Moreover, the total energy of the oxygenated silicon bulk strongly depends on the temperature, i.e., the system appears to become more stable with increasing growth temperature at this impact energy. It was found that the energy gain depends also on the incident energy and type of the oxygen species, i.e., the energy gain is higher in atomic oxidation and for higher initial impact energy.

Our previous results [139] predicted that the silica thickness also strongly depends on the type and initial energy of the incident oxygen species at room temperature. As mentioned above, it was found that the ultrathin silica films formed by this hyperthermal oxidation process can be divided in a pure silica bulk region and a silica surface region during oxidation. The roughness of the silica surface is rather high and its mass density is lower than that of the pure silica bulk. Such a rough surface is found at all temperatures (see also figure 7.1). Indeed, the surface roughness is also related to the incident energy rather than to the growth temperature.

In figure 7.7, both the total and partial O-O radial distribution functions (RDFs) are shown for the structures grown by 3 eV atomic impacts, for all temperatures. Very similar RDFs are obtained for impact energies of 1 and 5 eV (not shown). In figure 7.7a, analysis of the silica structure by means of the RDF shows that the Si-O (α peak), O-O (β peak) and Si-Si (γ peak) bonds are located at 1.6 Å, 2.5 Å and 3.2 Å, respectively. These values agree with both experimental values and other MD calculations [141, 189, 190]. Moreover, only the α peak is sharp, whereas the other peaks are rather weak, indicating that the obtained structures are amorphous. However, at low temperature, some unexpected O-O nonbonded neighbors (β_2 peak) are found with a distance of 2.25 Å, close to the β peak. We believe that this peak is caused by stress near the interface. The β_2 peak also depends on the growth temperature, i.e., increasing the growth temperature significantly decreases these O-O interactions in the tetrahedral silicon structure. Also, some unexpected peaks in the RDF analysis indicate some intrinsic defects, i.e., peroxyl bridges ($see\ \beta_1^{'}\ and\ \beta_1^{''}$ in figure 7.7b), three-fold oxygen, as well as over- and undercoordinated silicon atoms can be found in the silica structure during oxidation. The existence of peroxyl bridges and three-fold bond configurations in amorphous SiO_2 has already been suggested on the basis of some experimental and first-principles calculations [51, 185, 191, 224]. Indeed, it was suggested that the peroxyl bridge configuration is energetically stable. Our results also show that such peroxyl linkages occur more in the silica induced by atomic oxidation than by molecular oxidation at temperatures below the transition temperature, although their number is small. The results also show that the total number of oxygen peroxyl bridges significantly decreases with increasing growth temperature.

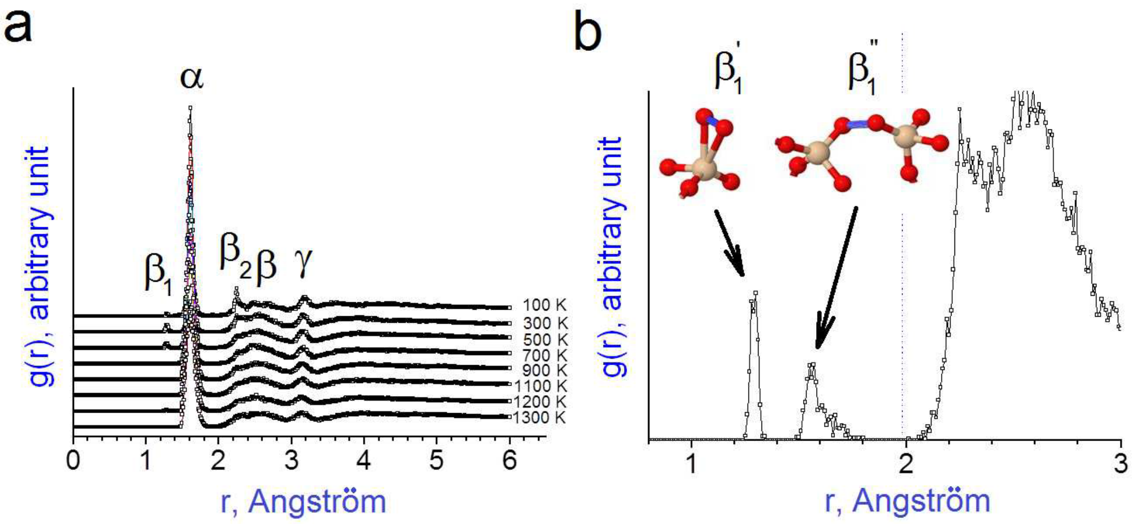

Figure 7.7 *(a) Total radial distribution functions (RDFs) of the SiO_2 bulk silica structures during hyperthermal oxidation, for an atomic oxygen beam with 3 eV kinetic energy at different growth temperatures, and (b) partial distribution function of the O-O distance at 300 K, showing also two types of oxygen peroxyl bridge bond in silica. The symbols α, β, β_1 (β'_1, β''_1), β_2 and γ denote Si-O, O-O, O peroxyl (first type at 1.3 Å and second type at 1.6 Å), and non-bonded O-O and Si-Si bonds, respectively.*

Finally, the ability to accurately control the growth of ultrathin *a*-SiO_2 and its interface thickness increases with decreasing growth temperature. As demonstrated in the previous sections, the interface thickness strongly depends on the growth temperature, due to the increasing mobility and diffusivity of the penetrated oxygen atoms at higher temperatures. We therefore believe that the transition temperature is one of the key factors in controlling the thickness of the ultrathin silica with an abrupt interface. Indeed, the thickness of the ultrathin silica is most easily controlled by the incident energy and type of the incident oxygen species at temperatures below the transition temperature (i.e., at temperatures below 500 - 700 K) [139].

7.4 Conclusions

The temperature dependence of hyperthermal oxidation of Si(100){2x1} surfaces by oxygen atoms and molecules was analyzed by reactive molecular dynamics simulations. A transition temperature of about 700 K was found: below this temperature, the oxide thickness only depends on the impact energy of the impinging species. Above this temperature, the oxide thickness depends on both the impact energy and the surface temperature. More specifically, the oxide thickness increases with increasing temperature. This is caused by the enhanced diffusivity of the oxygen atoms with increasing temperature as well as the activation barrier for oxygen penetration in the silicon crystal. Furthermore, the initial oxidation stage in hyperthermal oxidation shows some notable differences from the traditional thermal oxidation: instead of an incubation period, an initial stage of direct oxidation with a specific duration is observed. This changes the growth mechanism of the oxide layer in the initial oxidation stage. Two growth mechanisms of the bulk silica and interface region were found, corresponding to temperatures below and above the transition temperature. Where possible, we validated our results with experimental and ab-initio data, and good agreement was obtained. These results are of importance for the fabrication of silica-based devices in the micro- and nanoelectronics industry and open up a new route for silica growth by hyperthermal oxidation.

Thermal oxidation of small Si-NWs

Chapter 8

Self-limiting oxidation of small Si nanowires

8.1 Introduction

As mentioned in *section 1.4.3*, small-diameter (< 10 nm) Si-NWs are potentially very attractive because of the quantization of the electronic structure [65, 66]. This requires a fundamental understanding of the oxidation mechanism of such small Si-NWs, which may be significantly different from existing mechanisms for micrometer sized Si-NWs [22, 82]. Since the Deal-Grove model [22] only considers the oxidation of planar bulk silicon, some modifications need to be applied for describing two dimensional (cylindrical) structures, as outlined in detail for wet oxidation by Kao and co-workers [82] (see *section 1.4.4*). The mechanism of the initial oxide growth and also dry oxidation, however, cannot be properly explained with this model [229]. Furthermore, this microscale model fails for the nanoscale regime, in which stresses depend also on the crystallographic facets of small Si-NWs. Until now, self-limiting oxidation of small diameter Si-NWs has not yet been properly investigated. As mentioned in *sections 1.4.2* and *1.4.3*, self-limiting oxidation of Si nanowires and spheres is of considerable concern, for instance for the design of metal-oxide-semiconductor (MOS) devices [66, 67, 82] as well as photovoltaic cells [69]. Various modeling efforts and analyses regarding this effect can also be found elsewhere [67, 83-85, 88, 89, 229]. However, all conclusions were related to Si-NWs with diameters above 3 nm and higher temperatures, i.e., starting from 600°C.

Because of these problems, careful studies are needed to unravel the oxidation mechanisms of small diameter (< 3 nm) Si NWs at the atomic scale. This chapter is therefore concerned with the oxidation behavior of such small diameter NWs as a function of the oxidation temperature. I report here on the oxidation process and structure analysis of oxygenated Si-NWs with initial diameter of 2 nm at temperatures of 300 and 1273 K, studied by means of reactive molecular dynamics simulations using the ReaxFF potential. The results presented in this chapter were published in Chemistry of Materials [140].

8.2 Computational details

Si(100) nanowires with diameter of 2 nm and of 1 nm length are considered. In figure 8.1a, the ideal Si(100) nanowire structure at 0 K is shown. A periodic boundary condition is applied along the z-direction, which corresponds to the axial direction of the nanowire, in order to mimic an infinitely long nanowire. The nanowire is terminated by four {110}-type and four {001}-type facets (denoted by 1 and 2, respectively in figure 1). The angle between two {110} or two {001}-type facets is 90°, whereas the one between the {110} and {001} facets is 135°.

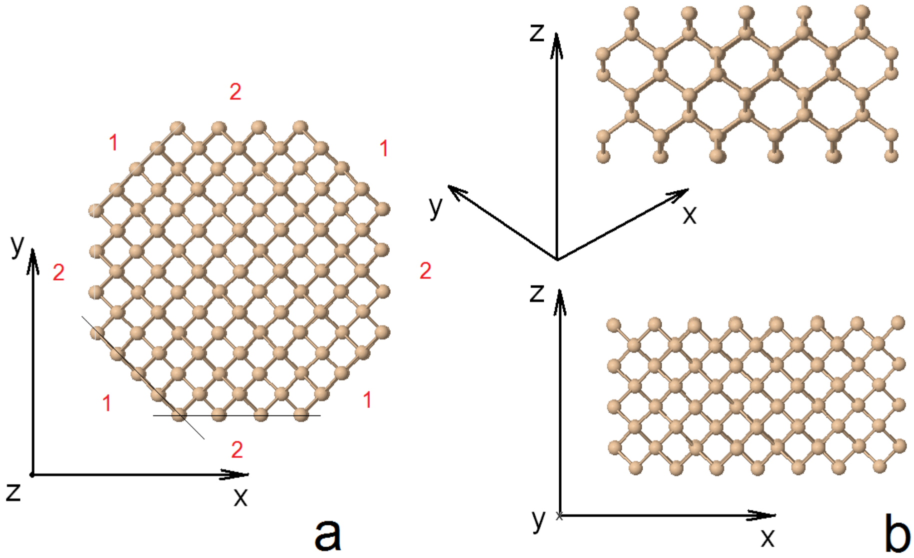

Figure 8.1 *Ideal structure of Si nanowires (Si-NWs) with 2 nm diameter: (a) top and (b) side view. Here, 1 and 2 indicate {110} and {001}-type facets, respectively.*

Prior to oxidation, the octagon-shaped Si(100) NWs are equilibrated at 300 and 1273 K using the Berendsen thermostat and barostat (NpT ensemble) [113] for 40 ps with temperature and pressure damping constants of 0.1 ps and 5.0 ps, respectively. The obtained structures are subsequently relaxed in the microcanonical NVE ensemble for 20 ps. After thermalization, the structure as obtained at low temperature (300 K) almost keeps the same shape, displaying both facets, similar to the ideal sample (see figure 8.2a). It was suggested that such faceting affects the surface reaction coefficient and subsequently the oxidation rate as well [82, 84, 88, 94]. At high temperature (1273 K), however, the shape of the NW structure becomes circular (see figure 8.2b).

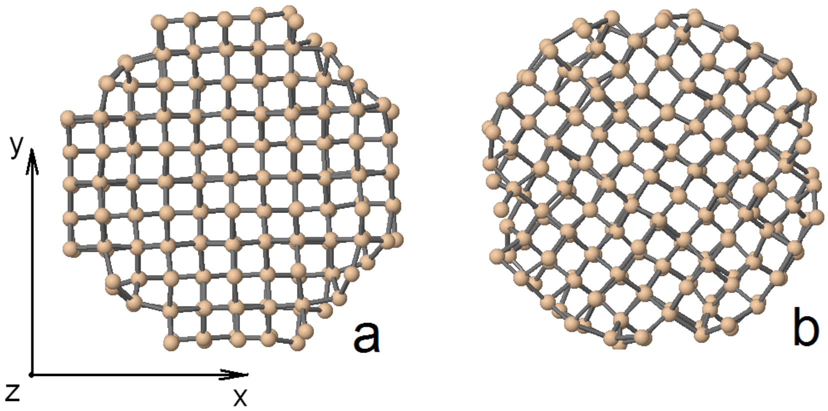

Figure 8.2 *Initial structures after thermalization at (a) 300 K and (b) 1273 K, respectively.*

Both obtained structures are analyzed by the radial distribution function (RDF). The RDF shows that the first, second, third and fourth neighbors of Si atoms are located at 0.23, 0.38, 0.44 and 0.53 nm, respectively. The Si-Si-Si peak in the angle distribution corresponds to about 110°. These parameters are close to the experimental values for Si(100) NWs [65].

Oxygen impacts are performed as follows. Each incident oxygen molecule is positioned at 1 nm above the uppermost atom of the nanowire in the (x,y) plane. The z coordinates of the incident particles are chosen randomly. The O_2 molecule is rotated randomly prior to impact. Every impact is followed for 10 ps, after which the next impact starts. The initial velocity vector of the incident molecule is randomized and its magnitude is set to the root-mean-square velocity corresponding to the oxidation temperature. During the impacts, NpT dynamics are applied to mimic dissipation of the heat of reaction and to allow for a volume expansion due to the oxidation process. In total, 2240 and 1456 consecutive impacts were performed at 300 and 1273 K, respectively.

8.3 Results and discussion

8.3.1 Oxidation and oxide growth process

The thermalized Si-NWs are oxidized by O_2 molecules at 300 and 1273 K. Figure 8.3 presents general information on the oxidation and the (sub)oxide growth process on Si-NWs with diameter of 2 nm, at low (300 K) and high (1273 K) temperature. The figure shows the evolution of the oxygen content (right axis), oxide shell thickness, radii of the Si-core and total oxygenated Si-NW (left axis) as a function of the O_2 fluence in monolayers (ML) for both temperatures. In these calculations, one ML corresponds to 56 atoms. At 300 K (figure 8.3a), the oxide growth process saturates after 60 ML, resulting in an oxide thickness of 1 nm. At the same time, the Si-core radius drops from 1 to 0.5 nm, and consequently, the total Si-NW radius increases to 1.5 nm. The oxygen content after saturation is about 4.5 ML. At 1273 K (figure 8.3b), however, the Si-NW is completely oxidized after 40 ML.

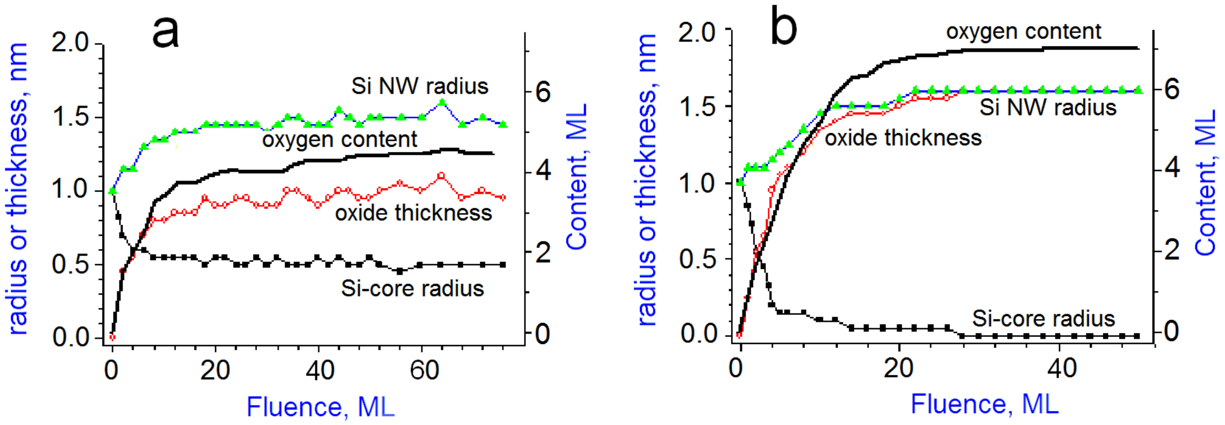

Figure 8.3 *Evolution of the oxide shell and Si-core thickness, and total Si NW radius (left axis), as well as oxygen content (right axis) during oxidation of a Si-NW with initial diameter of 2 nm at (a) 300 K and (b) 1273K.*

At both temperatures, the oxidation appears to change from a linear to a logarithmic function of time. Such dry oxidation behavior corresponds roughly to the Kao model for the wet oxidation of Si-NW in µm scale, applying the following equation to describe the kinetics of the process at the $Si|SiO_2$ interface:

$$\frac{\partial x}{\partial t} = \frac{1}{N}\frac{C^*}{\frac{1}{k_S}+\frac{1a}{hb}+\frac{1}{D}a\log\left(\frac{b}{a}\right)} \tag{8.1}$$

where N is the number of oxidants required to form a cubic unit of oxide, a is the NW core radius, b is the total NW radius (Si core + SiO_2 shell), and $x = b - a$ is the oxide thickness. It is assumed that the oxide growth rate is determined by the surface reaction rate coefficient k_s at the $SiO_2|Si$ interface, the surface mass transfer constant h of the oxidant, the diffusivity D of the oxidant in SiO_2, and the solid solubility C^* of the oxidant in SiO_2. See more details in *section 1.4.4.*

However, this equation should be altered for oxidation of the pure Si NW, i.e., in the initial oxidation stage. In this stage, the $(1/D)\cdot a\cdot log(b/a)$ term is omitted as a and b are initially equal to 1.0 nm. Generally, the $1/D$ and $1/h$ terms are included for oxidation of Si with a pre-existing oxide layer (i.e., $b > a$) and they should be ignored in the initial oxidation stage. The parameter C^*, which equals the oxygen flux (or oxygen fluence) is constant in this stage. As a result, the oxidation rate depends only on the surface reaction coefficient in the initial oxidation stage. As suggested in [82, 139] for planar oxidation, the growth rate is determined by the surface reaction rate coefficient k_s for thinner oxides, i.e., $x_o \approx 0$. The k_s parameter depends on the initial surface reaction rate coefficient (k_{so}), the normal stress (σ) and the surface temperature (T) [82]. However, in the initial oxidation stage, the surface reaction coefficient strongly depends on k_{so} rather than on the stress and oxidation temperature. We calculated stresses as the symmetric per-atom stress tensor for each atom in the Si-NW using the approach proposed in reference [219]. The tensor has 6 components for each atom and is stored as a 6-element vector in rectangular Cartesian coordinates: σ_{xx}, σ_{yy}, σ_{zz}, σ_{yz}, σ_{zx}, σ_{xy} and correspondingly in cylindrical coordinates σ_{rr}, $\sigma_{\theta\theta}$, σ_{zz}, $\sigma_{\theta z}$, σ_{zr}, $\sigma_{r\theta}$. The stress components in all directions are averaged per unit radius of 0.232 nm, which corresponds to the distance between first Si-Si neighbors in the crystalline Si-NW. The calculations show that the radial (normal, σ_{rr}) and tangential ($\sigma_{\theta\theta}$) stresses on a nonoxidized Si-NW surface are compressive and relatively small, i.e., $\sigma_{rr} \sim 0.2$ GPa and $\sigma_{\theta\theta} \sim 0.03$ GPa. Kao et al. [82] suggested that σ_{rr} and $\sigma_{\theta\theta}$ components are almost zero in a pure cylindrical Si. Although the axial stress is somewhat higher ($\sigma_{zz} \sim 0.3$ GPa), due to the periodic boundary in the z-direction, we believe that the reaction rate coefficient is not significantly lowered by the stress in the initial oxidation stage. As a result, the initial oxidation rate depends more strongly on the stress-free initial reaction rate coefficient rather than on stress and temperature. Therefore, as shown in figure 8.3, the oxide thickness quickly increases during the initial oxidation stage, due to the initial reaction rate, which depends on the surface crystallographic orientation, the number of dangling bonds on the nanowire surface, and the surface energy barrier. Note that the sticking behavior also depends on the spin-state, i.e., singlet or triplet state of an incident O_2 molecule [21, 203], which is not taken into account in our calculations. *ReaxFF* does not include the concept of multiple *spin states* and is parameterized to reproduce the energy corresponding to the lowest energy spin state. Therefore, in our simulations, the spin state corresponding to the lowest-energy path is assumed at all times.

The time evolution of the formation and growth of the oxygenated silicon in the initial stage of planar surface oxidation can easily be understood by observing the variation of the silicon suboxide components, i.e., Si^{1+}, Si^{2+} , Si^{3+} and Si^{4+}, which bind to one, two, three and four nearest-neighbor oxygen atoms, respectively [21]. The notation used corresponds to formal charge states and not to actual atomic charges. As shown in figure 8.4, all four Si suboxide species are found in Si-NW oxidation as well. Also some overcoordinated silicon atoms, i.e., five-fold suboxide (Si^{5+}) species are detected on the silica surface, although in low concentration. Initially, only Si^{1+} and Si^{2+} are formed. As the oxidation progresses, these are transformed into Si^{3+} and subsequently into Si^{4+}. The Si^{1+}, Si^{2+}, and Si^{3+} fractions consecutively dominate in the initial oxidation stage (see figure 8.4). Usually, such an oxidation behavior is also observed in the oxidation of planar Si [139, 173]. When a stoichiometric oxide layer appears, the fraction of Si^{4+} components increases continuously and the one of the other suboxide components decreases. It is only in the final oxidized wire step, at high temperature, that all Si atoms are converted in the Si^{4+} oxidation state (figure 8.4b). On the other hand, at low temperature, all Si-suboxide components can be found in the final structure, as is illustrated from Figure 8.4a.

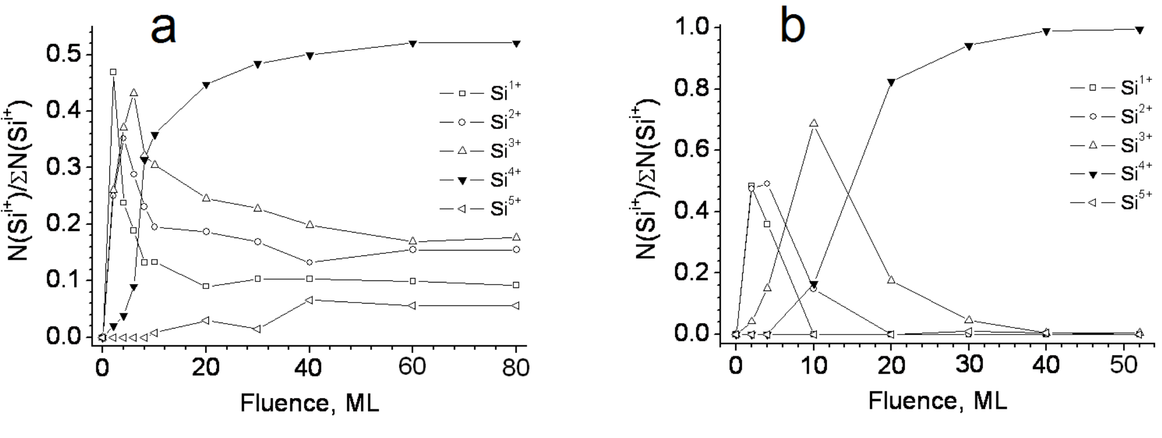

Figure 8.4 *Variation of the fraction of Si-suboxide components during oxidation at (a) 300 K and (b) 1273 K.*

The oxidation is continued until the oxygen content saturates. At high temperature, the saturation occurs faster (see figures 8.3 and 8.4) because of the relatively high diffusivity and mobility of the oxidant, i.e., the oxide thickness also depends on the diffusion coefficient D (see *equation 8.1*). Therefore, the Si-core radius (a) goes to zero during thermal dry oxidation at high temperature (see figure 8.3a). This indicates that the Si-NW completely converts to a SiO_2-NW, as is also shown in figure 8.4b, where the Si^{4+} fraction becomes equal to 1. At low temperature, however, the Si-core radius shrinks down to about 0.5 nm after which, it remains constant. It has been suggested [73, 82-84] that compressive stresses at the $Si|SiO_2$ interface significantly slow down the reaction rate. Furthermore, a compressive pressure in SiO_2 reduces the oxidant diffusion and concentration. The oxidation is therefore self-limiting. Note that this behavior is not unique to Si-NWs, but is also observed in the hyperthermal oxidation of planar Si surfaces with the formation of a thin oxide surface layer at room temperature [137, 139]. While the current work is dedicated to a morphological analysis of the obtained structures, a detailed analysis regarding the stress and pressure evolutions during the oxidation process are presented in the next chapter.

8.3.2 Analysis of the Obtained Structures

At the end of the oxidation process, two different structures, i.e., silicon-silica ($Si|SiO_x|SiO_2$) and pure silica (SiO_2) are obtained at 300 and 1273 K, respectively, as shown in figure 8.5a. As mentioned in the previous section, the formation of such a structure at low temperature can be explained by self-limiting oxidation [73, 82]. In contrast to the oxidation at low temperature, the Si-NW is completely oxidized at high temperature (1273 K), in agreement with the experimental observations reported by Büttner and Zacharias [229]. They found that 925°C (~1200 K) is a sufficient temperature for complete oxidation of a Si-NW with an initial radius of 15 nm or less. Since the molecular volume of SiO_2 (45 $Å^3$) is larger than the atomic one of Si (20 $Å^3$), the newly formed oxide continuously pushes the ‘old’ oxide outwards, in order to accommodate the volume expansion [73, 229]. As a result, the final diameters of both structures are found to be 2.9 and 3.1 nm at 300 and 1273 K, respectively, at the end of the oxidation process. This corresponds to an expansion by a factor of 2.1 and 2.4 relative to the initial dimensions of the Si-NWs. Note that the expansion coefficient of 2.4 as obtained at a high temperature treatment is larger than the ideal expansion one obtained for Si-to-SiO_2 (2.25) [82, 83, 88, 94, 229], since in the current oxidation process, a low density amorphous SiO_2 phase is formed rather than the high density quartz one.

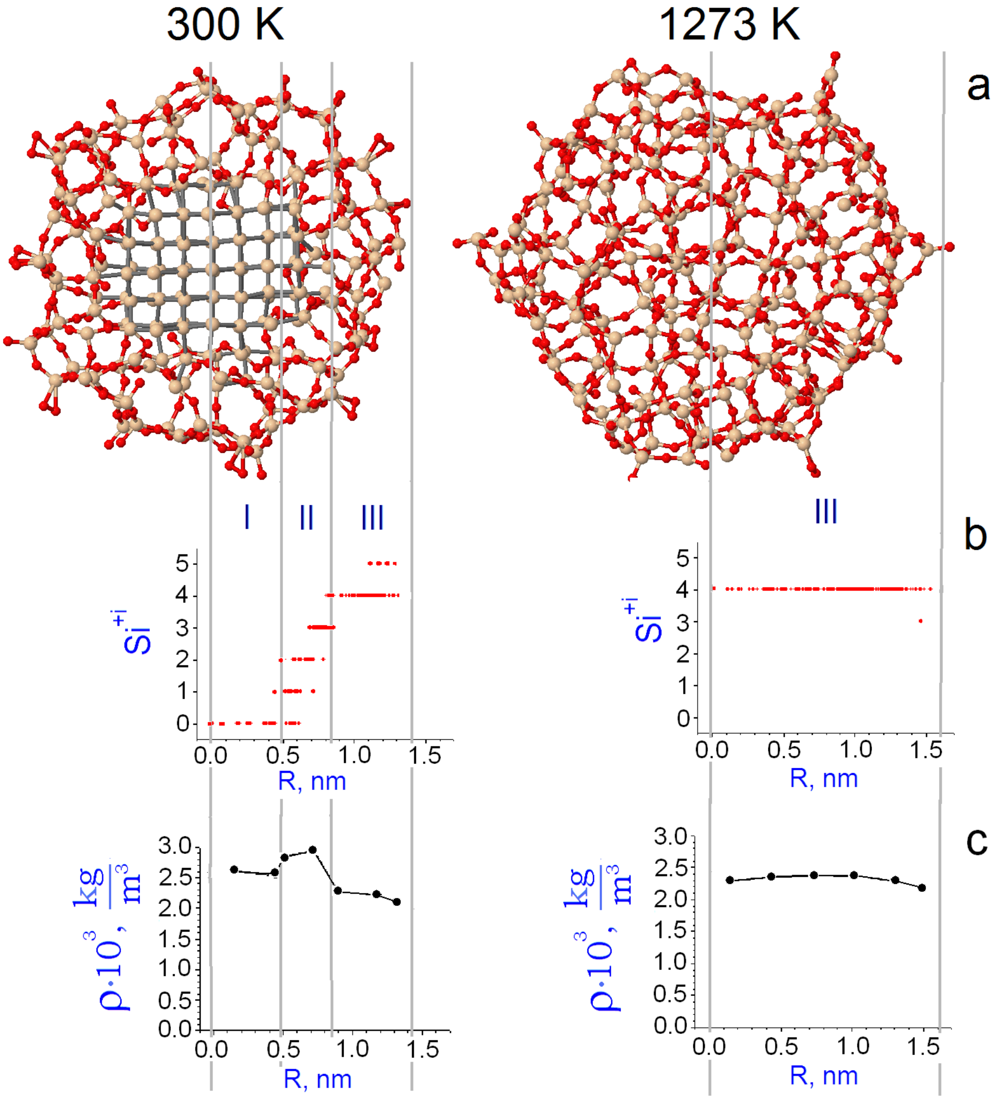

Figure 8.5 *Analysis of (a) post-oxidation structures obtained at 300 and 1273 K by (b) their Si-suboxide components and (c) their mass density distribution.*

As shown in figure 8.5b, both obtained structures are analyzed by the distribution in their suboxide components. The distribution of the Si-suboxide components in the oxidized Si-NW at 300 K shows that the final structure contains three regions, i.e., region I corresponds to a Si-core region (containing only Si^0), region II to a $Si|SiO_2$ interface (existing of Si^{1+}, Si^{2+}, Si^{3+}) and region III to an ultrathin SiO_2 shell (consisting of Si^{4+}). At high temperature, the distribution of Si^{4+} indicates that the Si structure completely converts to silica

(SiO_2).As can be seen in figure 8.5c, the mass density of the structure obtained at high temperature is around 2250 kg/m^3, which is close to the value for amorphous silica [141]. The surface density is however slightly lower. In the structure obtained at low temperature, the mass density of the Si-core is about 2550 kg/m^3. Since the experimental silicon density is about 2330 kg/m^3 at room temperature, the silicon density in our calculations is slightly too high in the low temperature regime. Indeed, differences with the experiment of this order are virtually inevitable in force field generated structures. In the Si|SiO_2 interface, where most of the intermediate Si-suboxide components (Si^{1+}, Si^{2+}, Si^{3+}) reside, a relatively high mass density is found. As a matter of fact, the entering oxygen atoms are stopped by the silicon energy barrier (cf. the planar oxidation case [139, 163, 180]) such that the interface region is enriched in oxygen. Finally, in the SiO_2 shell at low temperature, the mass density was found to be slightly lower than the mass density of the silica obtained at high temperature due to the occurrence of a small number of O-O peroxyl bridges [185].

Both structures are also analyzed by means of their radial distribution functions (RDF), as shown in figure 8.6a. For the model formed at high temperature, three peaks are found. These three peaks correspond to the Si-O bond, nonbonded O-O and Si-Si neighbor distances, located at 0.16, 0.25 and 0.32 nm, respectively. These values agree with both experimental and other MD reports [141, 189, 190], and indicate that the obtained structure is indeed amorphous silica. However, at low temperature, the number of peaks increases up to six due to the occurrence of the three different aforementioned regions in the obtained structure, i.e., the crystalline Si-core, the Si|SiO_2 interface and the ultrathin SiO_2 layer. The first peak, located at 0.13 nm, indicates that the silica surface contains a number of O-O peroxyl bonds [185], which also play a role in the appearance of Si^{5+} on the oxygenated Si-NW surface. A similar effect was also suggested by DFT calculations analyzing various defects during planar Si oxidation [186, 223]. The formation of an intermediate structure in which the extra oxygen atom is attached to the shared Si atom and acts as its fifth neighbor was proposed. The process then becomes a three-step mechanism. It begins with the formation of a peroxyl bridge, then evolves into a fivefold Si configuration, and finally leads to the formation of a new peroxyl bridge connected to another Si atom. The appearance of the peroxyl bridge bonds reduces the silica mass density as mentioned above, which explains the slightly lower mass density of the silica obtained at low temperature (see figure 8.5c). The second peak, located at about 0.16 nm, corresponds to Si-O bonds in the silica. This bond length is close to the Si-O one in the high temperature silica, although the peak is narrower due to the thermal widening at high temperature. The third and sixth peaks correspond to the Si-Si first (0.23 nm) and second (0.38 nm) nearest-neighbors, respectively, in the Si-core. Other near-neighbor interactions almost completely disappeared due to the oxidation. Finally, the fourth and fifth peaks of the RDF are related to O-O (0.25 nm) and Si-Si (0.32 nm) non-bonded interactions, respectively, in the ultrathin silica. The RDF analyses indicate that the obtained silica structures are amorphous at both temperatures.

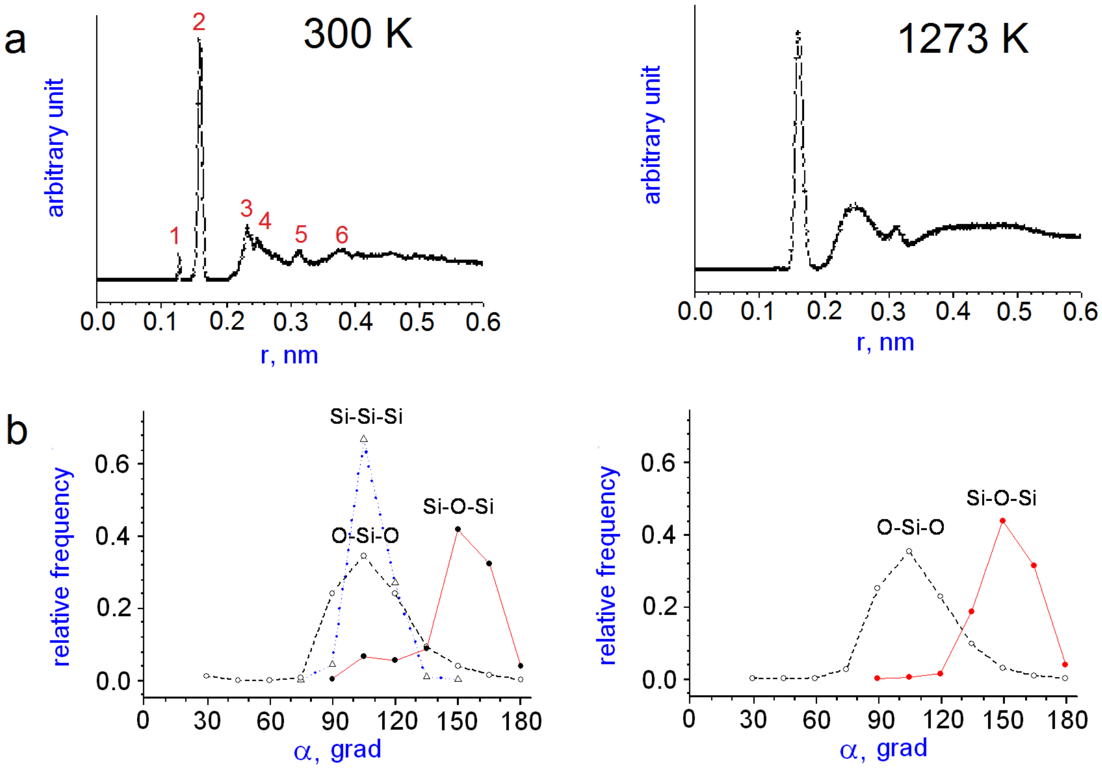

Figure 8.6 *Analysis of the obtained Si-core and SiO_2 structures by means of (a) radial distribution function and (b) angle distribution at 300 and 1273 K.*

Figure 8.6b shows the angle distributions in both structures. The Si-Si-Si angle distribution characterizes the non-oxygenated Si, and is therefore only present in the structure obtained at low temperature (due to the presence of the Si-core). The peak in the Si-Si-Si distribution is about 110°, which is close to the peak of the pure Si-NW one, as mentioned above. The oxygenated Si region is characterized by the Si-O-Si and O-Si-O angles. For both structures, most O-Si-O angles are distributed around 110° which corresponds to the tetrahedral silicon and silica structures. In α-quartz, this angle is the tetrahedral angle of 109.5°. The peaks are slightly wider in our structures (i.e., 75°-165°) than the O-Si-O angle distribution usually cited for amorphous silica (i.e., 109°±10°) [141, 190, 193]. Also, for the structure obtained at low temperature, an additional feature is found around 30°, which corresponds to the O-Si-O angle formed by some intrinsic defects, i.e., oxygen peroxyl bonds on the silica surface.

The amorphous silica structure is further characterized by the Si-O-Si angles, i.e., both by its peak position and the distribution range of this angle. For comparison, the Si-O-Si angle in α-quartz is 144°. In the case of amorphous silica, slightly differing mean values of the Si-O-Si angle distribution have previously been reported. Mozzi and Warren [190] obtained for the vitreous (amorphous) silica structure, which is generated by thermal O_2 oxidation, a wide distribution of Si-O-Si angles varying between 120° and 180°, with a main peak found at 144°. Watanabe et al. [192] investigated the thermal growth process using large-scale molecular dynamics and concluded that the Si-O-Si bond angle present in ultrathin SiO_2 film is reduced from 144° towards 130° to 140°. However, Da Silva et al. [214] suggested that the most probable Si-O-Si bond angle of vitreous silica is 152° instead of 144°. Mauri et al. [193] also found a slightly higher mean value of 151°±11° and a relatively narrow distribution (120° - 170°) in the Si-O-Si angular distribution of vitreous silica. In our high temperature model, the Si-O-Si angle distribution is in the range of 120°-180°, peaking at ~150°. These values are in fairly good agreement with the results obtained from thermal O_2 oxidation of a flat Si surface [214], and in very good agreement with the DFT results of Mauri et al. [193]. However, in the structure obtained at low temperature, the total Si-O-Si distribution is somewhat wider (90°-180°), with a peak located at about 150°. The lower angle part of this distribution is due to the strain build-up near the interface, which corresponds to a distribution in the range of 90° - 125°. At low temperature, the overall spread in the RDF, angle and mass density distributions confirms that the obtained structure consists of a crystalline Si region, an ultrathin $Si|SiO_2$ interface and an amorphous SiO_2 shell, although some intrinsic defects, i.e., some oxygen peroxyl bridge bonds, are found in the silica region. Therefore, all Si-suboxide components (Si^{i+}, $i \leq 4$) can be found in the structure obtained at low temperature. Also, some overcoordinated Si atoms (Si^{5+}) exist on the surface of this structure as mentioned before. At high temperature, the crystalline Si-NW converts completely to an amorphous silica (a-SiO_2) nanowire.

8.4 Conclusions

Thermal oxidation of Si-NWs with a diameter of 2 nm was studied at two different temperatures (300 and 1273 K) by reactive MD simulations. The oxidation mechanism was found to be temperature dependent. After oxidation, two types of nanostructures were obtained: ultrathin SiO_2 silica (i.e., dielectric) nanowire at high temperature, and a Si core | ultrathin SiO_2 silica shell (i.e., semiconductor + dielectric) nanowire at low temperature. The Si-core radius and the SiO_x ($x < 2.0$) oxide shell can be accurately controlled in the nanoscale regime by controlling the oxidation temperature. The obtained structures were analyzed by the radial distribution function, their mass density and their angle distributions. The overall analyses show that both ultrathin silica structures are amorphous, albeit some intrinsic defects were found in the structure formed at room temperature.

Chapter 9

Size control of SiO_2-coated small Si nanowires

9.1 Introduction

The oxidation of ultra-small Si-NWs (< 3 nm) has until now hardly been studied. Various characteristics and processes, including dry oxidation mechanisms of small Si-NWs at different temperatures, self-limiting behavior of the oxidation, as well as the effects of size and temperature on the oxidation process have not been properly studied yet. Furthermore, the understanding of the stress dependence and the non-conservative nature of the oxidation process is useful for controlling non-planar oxidation nanoscale integrated processes. Because the oxide should expand more to accommodate the volume expansion in thinner Si-NWs, the self-limiting oxidation, as described in chapter 8, is more significant in Si-NWs with smaller diameters. According to the Kao model [82], compressive stresses normal to the $Si|SiO_2$ interface reduce the interfacial reaction rate compared to a planar Si surface, whereas tensile stresses generated within the oxide shell reduce the effective oxide viscosity and enhance the oxygen diffusivity and solubility [93]. However, such stress behavior may change in the oxidation of Si-NWs at the nanoscale, as the shape of nanowire changes accordingly from circular to polygonal with increasing curvature. Therefore, in that case, stress results may disagree with the conclusions for Si-NW oxidation at the micro-scale due to this “curvature effect” [230].

In this chapter, the oxidation of ultra-small Si-NWs is studied in order to unravel these aforementioned effects during and after oxidation at the atomic scale. Specifically, the ability to control the Si-core radius and oxide sheath thickness by dry thermal oxidation of (100) Si-NWs with initial diameters 1.0 - 3.0 nm in the temperature range of 300 K - 1200 K is discussed. The results presented in this chapter were published in Nanoscale [231].

9.2 Computational details

In figure 9.1a, ideal (0 K) and thermalized (300 K and 1200 K) structures of the Si (100) nanowires (Si-NWs) with a diameter range of 1 to 3 nm are shown. In figure 9.1b, the top view of the {110} and {001} facets in the 2.5-nm diameter Si-NW is illustrated. In our calculations, the nanowire diameter d_0 corresponds to the averaged distance between the center of mass of the wire and the positions of the surface atoms in the radial direction in the (x,y) plane. A periodic boundary condition is applied along the z-axis, which corresponds to a unit cell length of 1 nm, to mimic an infinitely long nanowire. In reality, however, Si-NW have finite lengths, and longer than 1 nm. In order to test the "length effect" a number of test calculations have been performed for 1 nm diameter Si-NWs having different lengths (1nm, 5nm and 10nm). The results showed that the oxidation mechanism is identical in all cases although the shapes are slightly different. Thus, the 1 nm length Si-NW is chosen for keeping the computational time to a minimum.

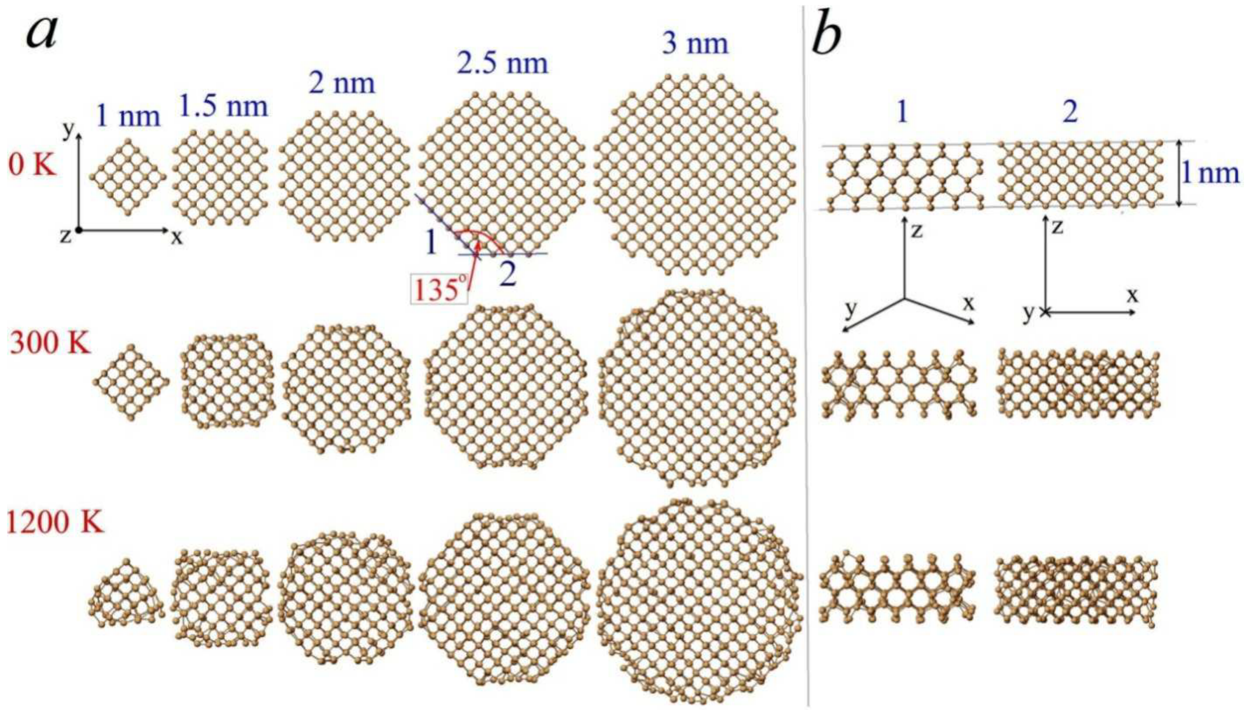

Figure 9.1 *(a) Ideal (0 K) and thermalized (300 K and 1200 K) structures of Si nanowires (Si-NWs) with a diameter (d_0) range of 1-3 nm. The indices 1 and 2 indicate the {110} and {001}-type facets, respectively, which terminate the nanowires. (b) Top view of the facets in the SiNW with d_0 = 2.5 nm at 0 K, 300 K and 1200 K, respectively.*

Prior to oxidation, the ideal Si(100) NWs are equilibrated at 10 temperatures ranging from 300 K – 1200 K in steps of 100 K during 40 ps, using the isothermal-isobaric ensemble (i.e., NpT dynamics) [113] with temperature and pressure coupling parameters of 0.1 ps and 5.0 ps, respectively. The NpT ensemble is employed to ensure the generation of a zero-pressure structure at the desired temperature. To verify that the resulting structure is effectively relaxed at the desired temperature, the obtained structures are subsequently relaxed in the microcanonical NVE ensemble for another 20 ps.

The structures at low temperatures (300 K – 700 K) display both {110} and {001} facets, similar to the ideal samples as shown in figure 9.1a. It was suggested that the faceting affects the surface reaction coefficient and subsequently the oxidation rate as well [82, 84, 88, 94]. However, the shape of the NW structure at high temperatures (800 - 1200 K) becomes more circular (see figure 9.1a). Si-Si bond-lengths and Si-Si-Si bond angles in all structures are close to the experimental values for small Si(100) NWs [65].

Oxygen impacts are performed as follows. Each incident oxygen molecule ($r_{O\text{-}O}$ = 0.121 nm) is randomly positioned at 1 nm above the uppermost atom of the nanowire in the (x, y) plane. The O_2 molecule is rotated randomly prior to impact. Every impact is followed for 10 ps, after which the next impact starts. The initial velocity vector of the incident molecule is randomized and its magnitude is set to the root-mean-square velocity corresponding to the oxidation temperature. During the impacts, NpT dynamics are applied to allow for a volume expansion due to the oxidation process, as mentioned above.

Stress calculation details. During and after oxidation, Cauchy atomic stresses were calculated as the virial stress for pristine Si and the oxide sheathed Si nanowires [219]. The local stress is calculated by dividing the nanowire structure into small rectangular boxes [206]. The stress tensor has 6 components for each atom and is stored as a 6-elements vector in rectangular Cartesian coordinates (x,y,z): σ_{xx}, σ_{yy}, σ_{zz}, σ_{yz}, σ_{zx}, σ_{xy}. More details can be seen in *section 6.2*. Then, the stresses in Cartesian coordinates are transformed into cylindrical coordinates (r,θ,z) as σ_{rr}, $\sigma_{\theta\theta}$, σ_{zz}, $\sigma_{\theta z}$, σ_{zr}, $\sigma_{r\theta}$ as follows [232]:

$$\begin{aligned} \sigma_{rr} &= \sigma_{xx}cos^2\theta + \sigma_{yy}sin^2\theta + \sigma_{xy}sin2\theta \\ \sigma_{\theta\theta} &= \sigma_{xx}sin^2\theta + \sigma_{yy}cos^2\theta - \sigma_{xy}sin2\theta \\ \sigma_{zz} &= \sigma_{zz} \\ \sigma_{\theta z} &= \sigma_{yz}cos\theta - \sigma_{zx}sin\theta \end{aligned} \tag{9.1}$$

$$\sigma_{zr} = \sigma_{yz} sin\theta + \sigma_{zx} cos\theta$$
$$\sigma_{r\theta} = (\sigma_{yy} - \sigma_{xx}) sin\theta cos\theta + \sigma_{xy} cos2\theta$$

where $cos\theta = \frac{x}{r}$, $sin\theta = \frac{y}{r}$, $z=z$. The local stress in each box is calculated by averaging the atom stresses of the atoms included in the box. For all stress calculations, the structures were first equilibrated at 0.01 K using NpT dynamics, to remove the kinetic energy part from the stress calculation, and subsequently the total energy was minimized using the steepest descent and conjugate gradient techniques [112].

9.3 Results and discussion

9.3.1 Temperature dependent oxidation mechanism

Temperature dependent oxidation mechanism in dry oxidation for all chosen nanowires is similar. Therefore, the oxide growth process is presented only for Si-NWs with initial diameters of 2 nm. The dry oxidation behavior of a 2 nm diameter (ultra)small Si-NWs is illustrated in figure 9.2, showing the oxide formation and growth process of the nanowire as a function of the O_2 fluence in monolayers (ML) at (a) low (300 K) and (b) high (1200 K) temperature. The time evolution of the formation and growth of the oxygenated silicon are studied by observing the variation of the silicon sub-oxide components (Si^{i+}, $i \leq 4$) in order to easily compare with experiment (i.e., the Si-2p photoemission spectra [51]) to validate our results.

Prior to oxidation, only Si^0 components are found, i.e., Si-O bonds do not exist in the Si-NW (figure 9.2, initial structures). When the oxidation process starts, only Si^{1+} and Si^{2+} are initially formed. As the oxidation progresses, these are transformed into Si^{3+} and subsequently into Si^{4+}. Note that the notation used corresponds to the formal charge states and not to the actual atomic charges. Our calculations show that the Si^{1+}, Si^{2+}, and Si^{3+} fractions consecutively dominate in the initial oxidation stage. In this stage, the oxygenated Si-NW consists of crystalline silicon (*c*-Si) and a non-stoichiometric oxide (SiO_x, $x<2$) region. After a fluence of 2ML (figure 9.2), the Si^{4+} suboxide species are also found on the oxidized Si-NW at low temperature, but not yet at high temperature. This means that the consecutive $Si^{1+} \rightarrow Si^{2+} \rightarrow Si^{3+} \rightarrow Si^{4+}$ conversion (i.e., the appearance of a new silica layer), occurs much faster at low temperature than at high temperature. Indeed, at low temperature, the penetrated O atoms or molecules cannot move deeper into the nanowire due to the associated energy barrier and the Si-Si bonds convert relatively fast to Si-O bonds in the oxygenated silicon (SiO_x) region. When a stoichiometric (SiO_2) oxide layer appears, the fraction of Si^{4+} components increases continuously and the fractions of the other suboxide components therefore decrease, as is clear from figure 9.2. This indicates the end of the initial oxidation stage. Our simulations show that this stage ends earlier at low temperature than at high temperature.

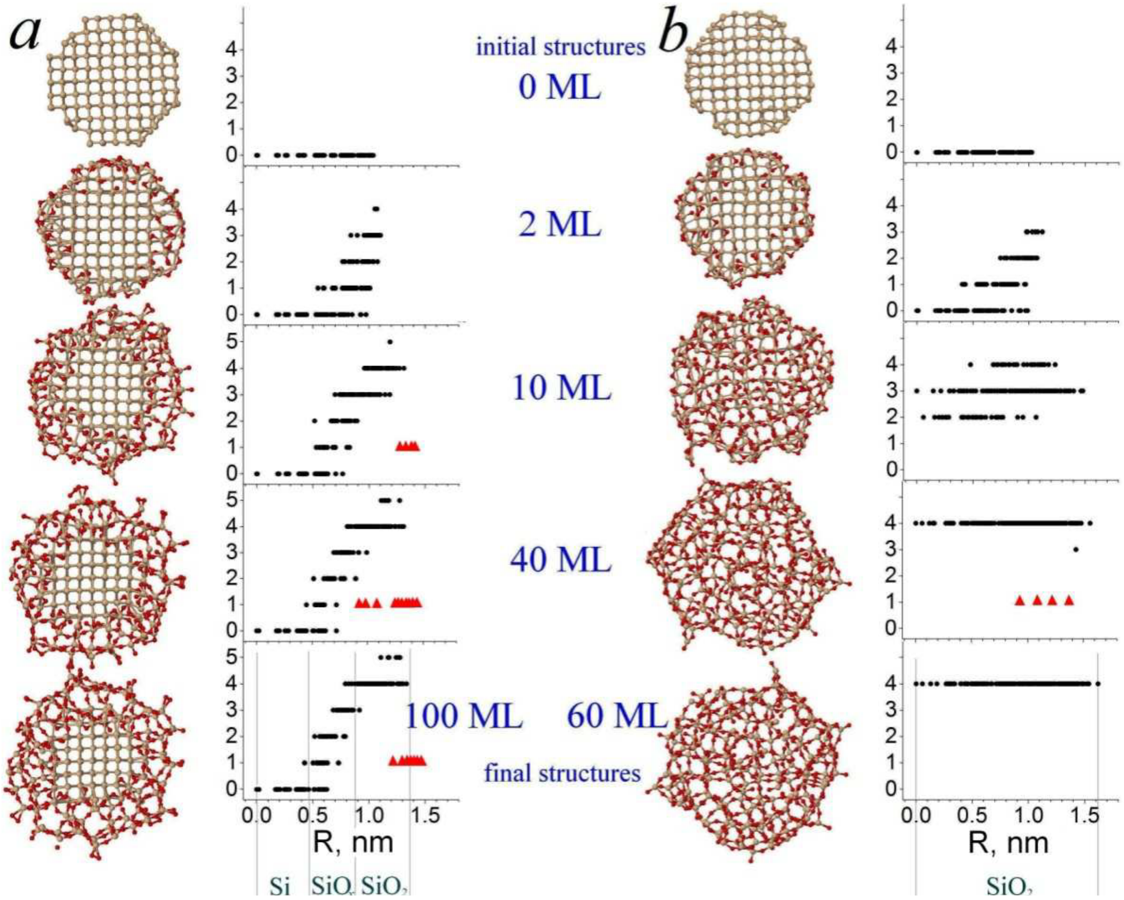

Figure 9.2 *Oxide formation and growth as a function of the* O_2 *fluence in the 2 nm Si-NW at (a) low (300 K) and (b) high (1200K) temperatures, respectively. 1 ML corresponds to 28* O_2*. Each structure is analyzed by the radial distribution of the Si-(sub)oxide components (black circles) and the O-O peroxyl bridges (red triangles). R is the radial distance from the centre of the Si-NW (i.e., R=0) to the nanowire atoms in the (x,y) plane. Here, Si,* SiO_x*, (x>2) and* SiO_2 *correspond to the crystalline silicon (or Si-core), non-stoichiometric oxide and amorphous silica regions, respectively*

In the stage between 2 ML and 10 ML, the oxide growth process at low temperature is almost entirely stopped due to the energy barrier, interfacial stresses and lowered diffusivity of the penetrated oxygen species. This also leads to the appearance of some overcoordinated silicon (Si^{5+}) species in the SiO_2 region [140, 186], albeit in low concentration (see figure 9.2a). The silica contains a number of O-O peroxyl bonds as well (see figure 9.2, red triangles) [185], which also play a role in the appearance of Si^{5+} in the oxygenated Si-NW. A similar effect was also suggested by DFT calculations analyzing various defects during planar Si oxidation [139, 173, 186, 223].

Starting from 10 ML, the number of peroxyl linkages and five-fold silicon species increases and they spread in the whole silica region. This indicates that Si-NW oxidation is only continued by diffusing oxygen species. Therefore, the duration of this process is much longer than the initial oxidation stage. Indeed, the oxidation rate not only depends on the surface reaction coefficient, but also on the transfer and diffusion coefficients. Such oxidation behavior is also explained in depth by Kao and co-workers in their micro-scale model [82]. Furthermore, distribution of the O-O peroxyl bridges in the Si-NW at low temperature indicated that oxidation might be gradually continued in the slow oxidation stage (see 10 and 40 ML in figure 9.1a). Such oxidation behaviour was not reported in wet oxidation of Si-NWs [82]. Similar oxidation behaviour is also observed at high temperature (40 ML, figure 9.1b), albeit its contribution is small compared with the low temperature case. The oxidation is continued until the oxygen content saturates. Although the oxide growth continues, the Si-core radius remains constant at low temperature after 40 ML. At high temperature, some oxygen species penetrate into the Si-NW center already at 10 ML. In the final oxidized nanowire (figure 9.2b, 100 ML), all Si atoms are in the Si^{4+} oxidation state and all O-O peroxyl bridges disappear. On the other hand, at low temperature, all Si-suboxide components (including some Si^{5+}) can be found in the final structure after 100 ML, as is illustrated in figure 9.2a. However, such intermediate structures, i.e., overcoordinated Si atoms and peroxyl linkages, are only found on the silica surface, and not in the whole silica region, indicating that the oxide growth by diffusing oxygen species has entirely stopped.

Finally, at the end of the oxidation process, two different structures are obtained (figure 9.2, final structures). As discussed in previous chapter, the overall spread in the radial distribution function (RDF), angle and mass density distributions confirms that the initially crystalline silicon (*c*-Si) nanowire converts to either a silicon-silica (c-Si|SiO$_x$|a-SiO$_2$) nanowire at low temperature (300 K) or an amorphous silica (a-SiO$_2$) nanowire at high temperature (1200 K). This was also reported in our previous work, as well as in literature [140, 229]. The formation of the structure obtained at low temperature can be explained by self-limiting oxidation [82, 221], as will be further explained below.

9.3.2 Ultra-small c-Si|SiO$_x$|a-SiO$_2$ nanowires

As mentioned in previous section, and illustrated in figure 9.3, two types of nanostructures are ultimately obtained, i.e., c-Si|SiO$_x$|a-SiO$_2$ (typical at low temperatures) and a-SiO$_2$ nanowires (typical at the higher temperatures). Only the 1 nm diameter Si-NW (not shown in figure 9.3) completely converts to the a-SiO$_2$ nanowire at all temperatures. In figure 9.3a, all finally obtained core shell c-Si|SiO$_x$|a-SiO$_2$ structures are shown. At temperatures above 800 K, all obtained structures are fully amorphous and are therefore not shown.

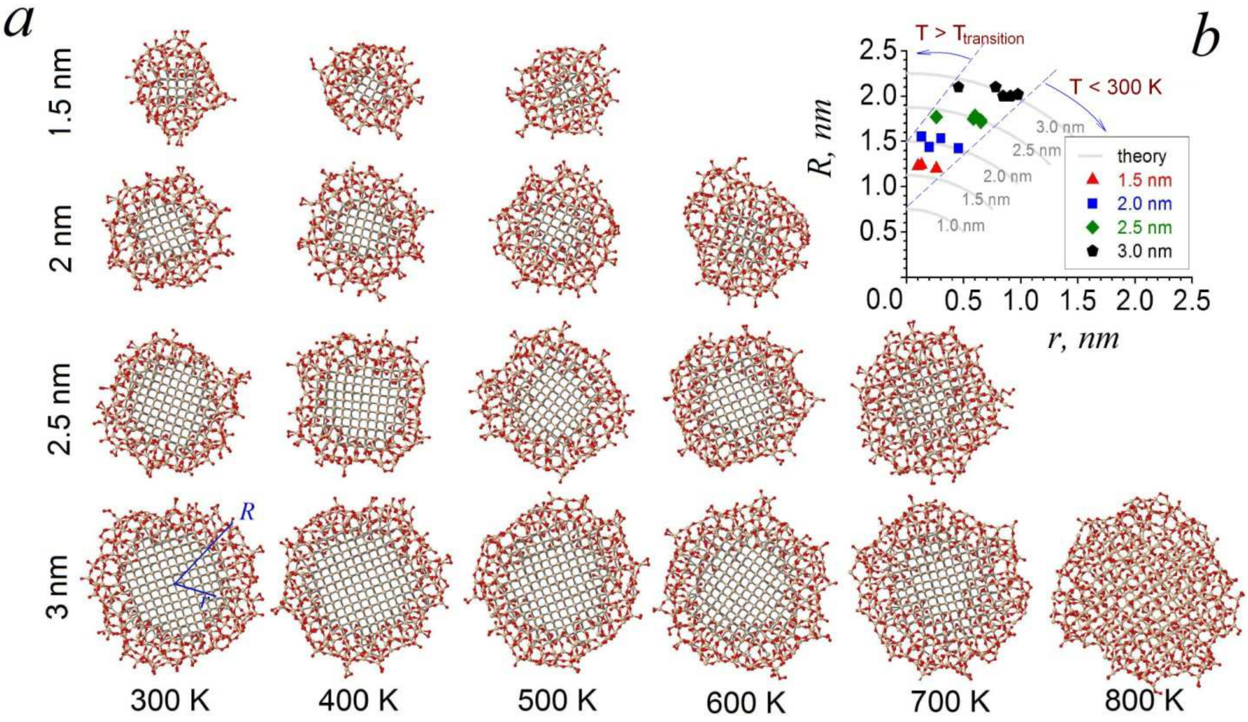

Figure 9.3 *(a) The c-Si|SiO$_x$|a-SiO$_2$ nanowires with initial diameter in the range 1.5 – 3 nm after oxidation at T=300-800 K. (b) Final radii of Si-core (r) and Si-NW (R), compared with theoretical calculations derived from equation (3).*

The figure illustrates that both the Si-core radius (r) as well as the Si-NW radius (R) depend on the d_0 diameter and inversely depend on the oxidation (or oxide growth) temperature T, i.e., $r\ (or\ R) \sim \frac{d_0}{T}$. We found that the maximum radius of the Si-core is about 0.26 nm, 0.46 nm, 0.65 nm and 0.91 nm for 1.5, 2, 2.5 and 3 nm diameter Si-NWs, respectively, at 300 K. Due to the increasing diffusivity and mobility of the penetrated oxygen atoms, the core radius drops with rising temperature. While the growth temperature increases, the Si-core radius decreases to zero ($r \to 0$) and consequently the nanowire converts to a pure SiO_x ($x \leq 2$) nanowire at a certain "transition temperature" (T_{trans}). Thus, for a given nanowire diameter, T_{trans} is the temperature above which amorphous a-SiO_2 is obtained, and below which core shell c-Si|SiO_x|a-SiO_2 nanowires are obtained. From figure 9.3a it can be seen that T_{trans} is roughly equal to 500 K, 600 K, 700 K and 800 K for Si-NWs with diameter 1.5 nm, 2 nm, 2.5 nm and 3 nm, respectively. This clearly demonstrates that control over the Si-core radius is possible by selecting the appropriate initial diameter of the Si-NW and the growth temperature.

On the other hand, the contribution of long timescale diffusion to *equation 8.1* cannot be accurately accounted for in MD simulations. As a result, the partially oxidized structure may finally become fully oxidized, provided a sufficiently long oxidation time (in the range $1 \cdot 10^3$ to $1 \cdot 10^5$ s depending on the experimental conditions in planar surface oxidation [173]) is permitted at 300 K. However, the final radii of the c-Si|SiO_x|a-SiO_2 nanowires, as obtained in our MD calculations, can be compared with a theoretical derivation, to which also most experimentalists compare their results [67, 88, 229]:

$$\pi(R^2 - r^2)L - \pi(R_0^2 - r_0^2)L = \frac{\Omega_{SiO_2}}{\Omega_{Si}}\pi(r_0^2 - r^2)L \qquad (9.2)$$

where r_0, r and R_0, R are the initial and final radii of Si-core and oxidized Si-NW, respectively; L is the Si-NW length; Ω_{SiO2} is the molecular volume of SiO_2 (~ 45 Å^3) and Ω_{Si} is the atomic volume of Si (20 Å^3). Prior to oxidation, initially $r_0 = R_0$. From (3), the following formula including this initial condition can be obtained:

$$R = \sqrt{2.25 r_0^2 - 1.25 r^2} \qquad (9.3)$$

The relation between the final Si-NW (R) and Si-core (r) radii for partially oxidized structures in self-limiting oxidation with initial diameters ($d_0=2r_0$) from 1 to 3 nm can be calculated by means of this formula. The results are presented in figure 9.3b (grey curves). It can be seen in the figure that most of our MD results are fairly close to this theoretical calculation. Furthermore, this indicates that at low temperature, the oxidation process does not strongly depend on the diffusion coefficient and is only a function of the surface reaction rate, which depends on the normal stress rather than on the temperature. Especially, in the cases above 2 nm diameter, this effect clearly appears: at all temperatures below the transition temperature, the diamonds (d_0=2.5 nm) or pentagons (d_0=3 nm) are close to each other, close to the lower dotted line, indicating that the oxidation hardly changes between these temperatures. Increasing the temperature to above the transition temperature, however, results in a strong increase in the oxidation, as indicated by the data points lying close to the upper dotted line. Note that this effect is not observed in the Si-NWs with higher curvature (d_0<2.5 nm).

Indeed, it was previously suggested that compressive stresses at the Si|SiO_2 interface significantly slow down the reaction rate [82-84, 221], and furthermore, that a compressive pressure in SiO_2 can reduce the oxidant diffusion and transport [83].

9.3.3 Pre-oxidation stresses

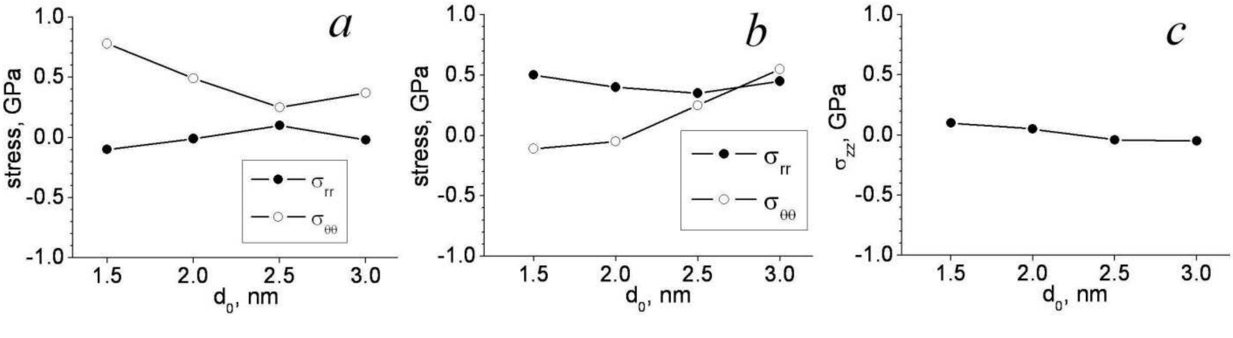

Figure 9.4 *Calculated radial (σ_{rr}) and tangential ($\sigma_{\theta\theta}$) stresses for (a) the {110} and (b) {001}-facets of the Si-NWs with initial diameters (d_0) from 1.5 to 3 nm) at 300 K, respectively. (c) The axial stress (σ_{rr}) versus the nanowire curvature.*

Before oxidation, the initial (radial σ_{rr}, tangential $\sigma_{\theta\theta}$ and axial σ_{zz}) stresses in the Si-NW structure are analyzed as shown in figure 9.4. The compressive stress is presented as a positive value, and the tensile stress as a negative value. The calculations show that the radial and tangential stresses on the non-oxidized Si-NW surface strongly depend on the crystal facets (see figure 9.1) for sub-3 nm diameter nanowires. The stress profiles for {110}-type facets are shown in figure 9.4a. In this figure, the radial σ_{rr} stresses are small and tensile on the surfaces of the 1.5 nm, 2nm and 3 nm diameter Si-NWs, with values ranging from -0.1 GPa (1.5 nm) to 0.1 GPa (2.5 nm) and again to -0.02 GPa (3 nm). In contrast, the tangential $\sigma_{\theta\theta}$ stresses on the surface are somewhat higher than σ_{rr} and compressive instead of tensile. As shown in figure 9.4a, their maximum values decrease from 0.78 GPa (1.5 nm) to 0.25 GPa (2.5 nm) and increase again to 0.37 GPa on the 3 nm diameter Si-NW. These trends may be explained by the changing nanowire shape types, i.e., the shape of the 3-nm Si (100) nanowire is unlike the octagon-shaped 1.5 nm, 2 nm and 2.5 nm diameter nanowires. Therefore, the stress behavior changes on the 3 nm nanowire because of extra “bumps” on the {110}-facets (see figure 9.1a). Regarding the {001}-facets (figure 9.4b), the radial stresses are compressive and somewhat higher than the stresses on the {110}-facets. Note that the σ_{rr} and $\sigma_{\theta\theta}$ stress profiles for the {001}-type facets change opposite to the corresponding stresses for the {110}-facets. As shown in figure 9.4b, the σ_{rr} stresses decrease with increasing nanowire diameters from 1.5 nm to 2.5 nm, which corresponds to previous theoretical suggestions [82]. However, the stress somewhat increases again for the 3 nm nanowire due to the changing nanowire shape. Their values actually fluctuate in the range of 0.4 ± 0.1 GPa. While the tangential $\sigma_{\theta\theta}$ stresses are tensile for 1.5 nm (-0.11 GPa) and 2 nm (-0.05 GPa) Si-NW, their values are compressive for 2.5 nm (0.25 GPa) and 3 nm (0.55 GPa). Because of the crystallographic orientation, the radial and tangential stress behavior strongly depends on the precise structure of the small Si-NW surface [65]. However, such behavior is only found at the surface and first subsurface layers of the Si-NW. From the second (radial) subsurface layer these stresses are fairly close to zero. Furthermore, the axial stresses σ_{zz} i.e., the stress along the z-axis, is also very small, and fluctuates around zero as shown in figure 9.4c, albeit a periodic boundary is applied in this direction [177].

The calculations show that although all initial σ_{rr}, $\sigma_{\theta\theta}$ and σ_{zz} stresses change depending on the crystal orientation and nanowire curvature, their values are relatively small and consequently their contributions for reducing the Si-O reaction rate are negligible. The obtained stress values are fairly close to theoretically suggested values (i.e., close to zero), and the average values of the σ_{rr} and $\sigma_{\theta\theta}$ stresses are compressive in the pure cylindrical Si-NWs [82]. As mentioned before, such surface stresses cannot affect the oxygen reaction and penetration into the Si-NW crystal. It is also suggested that the inward oxide growth [204] depends on the σ_{rr} rather than $\sigma_{\theta\theta}$ and σ_{zz} stresses [82], which will discussed in the next sections.

9.3.4 Stress evolutions during oxidation

In Si-NW oxidation, two key factors can be discerned: (1) Oxygen diffusion in the SiO_x ($x \leq 2$) oxide region, characterized by the diffusion constant D; and (2) reaction with the Si-core, characterized by the reaction rate constant k_s [82]. These two parameters also strongly depend on the hydrostatic pressure p (i.e., the obtained oxide can be considered as a fluid with high viscosity [82]) and the normal stress σ_{rr} at a given temperature, respectively. According to the theory of fluid mechanics, the pressure is equal to the average total σ_{rr} on a control volume in the fluid and it is found as $p = -\frac{1}{2}(\sigma_{rr} + \sigma_{\theta\theta})$ [233].

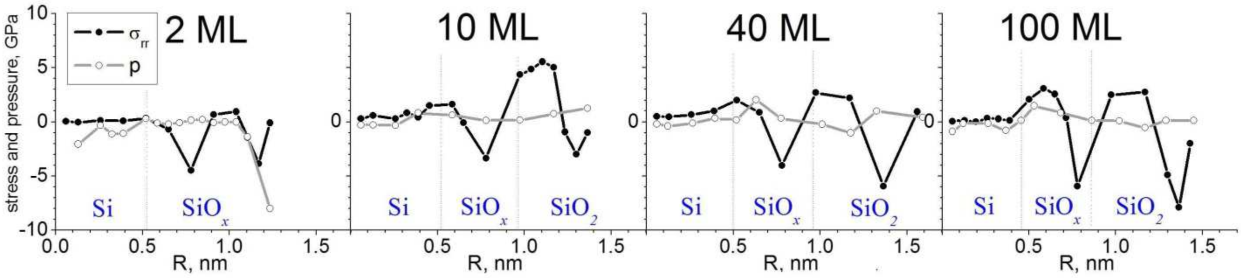

Figure 9.5 *Normal (σ_{rr}) stress and hydrostatic pressure (p) as a function of the oxidation time for the Si-NW with d_0=2 nm at 300 K. Here, Si, SiO_x, (x>2) and SiO_2 correspond to the crystalline silicon (or Si-core), non-stoichiometric oxide and amorphous silica regions, respectively.*

Figure 9.5 presents the normal stress and (hydrostatic) pressure evolution during oxidation for a Si NW with d_0 = 2 nm at 300 K. The compressive stress (or pressure) is presented as a positive value, and the tensile stress (or pressure) as a negative value. Our calculations show that in the initial oxidation stage (0-2 ML), σ_{rr} and p are tensile on average and fluctuate around zero GPa. This permits oxygen to react easily with the Si-crystal after diffusing through the SiO_x region. As a result, the oxidation rate rapidly increases in this oxidation stage. Because of the increasing reaction rate, the stress in the Si-core initially increases slightly. In this period, the oxygen atom or molecule penetrates deeper into the crystal, depending on the energy barrier of the Si surface and sub-surfaces. Consequently, the consecutive $Si^{1+} \rightarrow Si^{2+} \rightarrow Si^{3+} \rightarrow Si^{4+}$ conversion leads to a gradual expansion of the Si crystal. Specifically, when the oxide layer becomes continuous, the volume expansion resulting from oxidation of the silicon is restrained by the silicon. This is similar to the compressive stress resulting from epitaxial growth of a film with a lattice parameter larger than the substrate [229]. When a stoichiometric (SiO_2) oxide layer appears (after 2 ML), the oxygen diffusivity significantly decreases due to compressive σ_{rr} and p and the reaction rate is drastically reduced. It is also theoretically suggested that a compressive p reduces the solubility of the oxygen molecule in SiO_2 as it raises the potential energy of the molecule in its interstitial site, whereas a tensile p increases its solubility for the opposite reason [83]. Indeed, such compressive p and σ_{rr} may also significantly reduce the oxidant transport in the oxide region.

When the slow oxidation stage starts (2-10 ML), the nanowire can be divided into three parts (see figure 9.2): a crystalline Si-core (*c*-Si), a partially oxidized Si region (SiO_x, $x<2$) and a fully oxidized Si or silica (SiO_2) region. It is clear from figure 9.5 that the σ_{rr} is tensile in the SiO_x ($x<2$) oxide and at the SiO_2 surface, whereas it is compressive in the SiO_2 bulk and at the c-Si|SiO_x interface in the slow oxidation stage (i.e., ~10 ML). In the interface, the compressive normal stress gradually increases from 1.6 GPa to 2.0 GPa and 3.0 GPa after 10 ML, 40 ML and 100 ML, respectively. Finally, the Si-core stress decreases again while the interfacial stress is constant at about 3 GPa as shown in figure 9.5 (100 ML). Some classical continuum analysis concluded that such compressive stress in the silicon core significantly slows down the oxidation [82, 83, 85].

9.3.5 Interfacial stresses

The self-limiting behavior of the Si-NW oxidation strongly depends on the aforementioned “interfacial stresses” [83-85, 204], which correspond to the stresses in the outer Si shell and the oxide shell near the Si|SiO_x interface. The interfacial stresses, which can also be thought of as a combination of chemical and mechanical (physical) stresses [218], plays an important role in the reliability of gate oxides with its ultrathin interface [216].

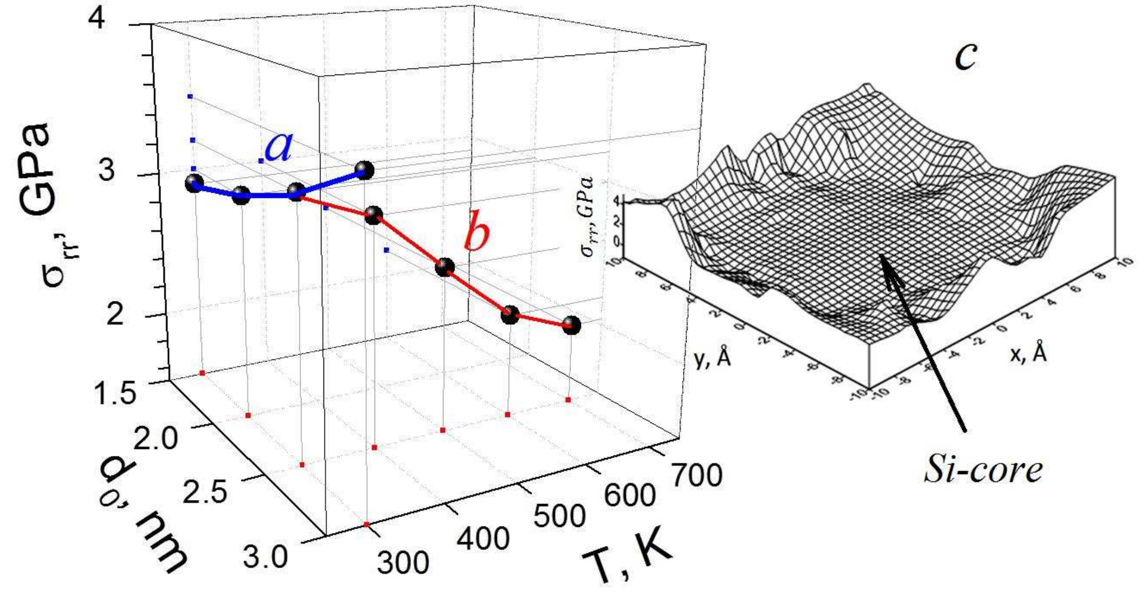

Figure 9.6 *Averaged radial (normal) σ_{rr} stresses in the Si|SiO$_2$ interface of the final oxidized Si-NW structure as a function of (a) the curvature and (b) oxide growth temperature. (c) The interfacial σ_{rr} stress on the x-y plane for a Si-NW with d_0=3 nm at 300 K. The (0, 0) position corresponds to the Si-NW center.*

Figure 9.6 shows the interfacial stress as a function of the initial Si-NW diameter and the oxidation temperature. Our calculations predict that when the temperature increases the stress decreases. As shown in figure 9.6b, the average values of the residual stresses in the interface are 3.2 GPa, 3.0 GPa, 2.6 GPa, 2.2 GPa, 2.04 GPa at 300 K, 400 K, 500 K, 600 K and 700 K, respectively for the 2.5 nm Si-NW. Such temperature dependent behavior of the interfacial stress is consistent with previous theoretical work of Si-NW oxidation [82]. The same authors also proposed that the stress is higher for smaller radii and they explained that the deformation of a small structure requires more rearrangement. However, our nanowires are all very small and the obtained results are in contrast to this theoretical suggestion. Indeed, our calculations predict that the 1.5 nm diameter Si-NW exhibits a somewhat smaller compressive stress than the other nanowires (figure 9.6a). To be exact, the averaged interfacial stress of the NWs at 300 K is calculated to be 2.9 GPa, 3.0 GPa, 3.2 GPa, and 3.5 GPa for the NWs with 1.5 nm, 2 nm, 2.5 nm and 3 nm diameter, respectively. This phenomenon of a residual compressive stress decreasing with rising curvature (hence, smaller diameter) was also reported by Kim et al. [230]. Following these authors, the non-oxidized Si-core of smaller Si-NWs (in the sub-10 nm diameter regime) deforms more to compensate for the volume expansion of the surface oxide layer, resulting in a smaller compressive stress. Furthermore, we also suggest that crystal orientation effects may play a role to develop this phenomenon.

The distribution of interfacial stresses around the Si-core in the (x,y) plane is also presented in figure 9.6c. As shown in the figure, the compressive interfacial stresses at room temperature are significantly higher than the stresses of its Si-core. Such compressive stresses significantly reduce the oxygen reaction with Si near the planar Si|SiO_2 interface, which was investigated using high-resolution transmission electron microscopy (HRTEM) analysis [220]. Indeed, these residual stresses are relatively high at low temperature (e.g., 300 K) in ultra-small Si-NWs and therefore their effect is significant in self-limiting oxidation [140, 221]. Thus, it is observed from our calculations that accurate control of the interfacial stress by choosing a suitable temperature and Si-NW diameter can lead to accurate control over the Si-core radius at the nanoscale.

9.4 Conclusions

Oxidation of ultra-small Si nanowires with initial diameters in the range 1 nm to 3 nm was studied using reactive molecular dynamics. Attention was focussed on the temperature-dependent mechanism for dry oxidation of small Si-NW at low (300 K) and high (1200 K) temperature. The oxidation mechanism is discussed in comparison to wet oxidation of micrometer sized Si-NW and other mechanisms of planar Si oxidation. In the oxidation mechanism, diffusion of O-O bridge linkages is also discussed. Although their contribution is small, they may play a role in a diffusion-dependent oxidation process.

At the end of two temperature-dependent oxidation mechanisms two types of structures are found: At low temperatures, *c*-Si|SiO_x|*a*-SiO_2 nanowires are formed, while *a*-SiO_2 nanowires are created at higher temperatures. The transition temperature between both regimes was found to increase with the NW diameter. Indeed, for the 1.5 nm, 2 nm, 2.5 nm and 3 nm diameter Si-NWs, the transition temperature was found to be about 500 K, 600 K, 700 K and 800 K, respectively. The final radii of the *c*-Si|SiO_x|*a*-SiO_2 nanowires are close to the theoretically suggested radii. The calculations predict for the partially oxidized *c*-Si|SiO$_x$|*a*-SiO$_2$ nanowires that the Si-core (*c*-Si) and the total nanowire radius depend on the initial Si-NW diameter and inversely depend on the oxidation temperature.

Stress calculations were also performed to study the oxidation behavior of these ultra-small nanowires. It is found that a compressive pressure and stress may significantly reduce the oxidant transport in the oxide region and its reaction with the Si-core. Stresses in the interface were also analyzed. Specifically, when the temperature increases, the interfacial stresses decrease. This is consistent with previous theoretical work. However, it is also found that the compressive interfacial stresses decrease with increasing curvature for the 1-3 nm Si-NWs investigated, which is in contrast to the theoretical suggestions for Si-NW at the micro-scale.

Generally, it can be concluded from our simulations that an accurate control over the interfacial stress by choosing a suitable oxidation temperature and a Si-NW diameter can lead to a precise control over the Si-core radius at the nanoscale regime.

PART III

SUMMARY - SAMENVATTING

General summary and conclusions

An important issue in the fabrication of microelectronics and photovoltaic devices (e.g., MOSFETs, solar cells, optical fibers etc.) is the growth of (ultra)thin silica (SiO_2) layers on crystalline Si. It is known that such ultrathin (~2 nm) SiO_2 growth is difficult if not impossible by a thermal process at low temperature, due to low sticking ability of incidence oxygen species. However, thermal oxidation at high temperature does not offer the possibility to obtain ultrathin and high-*k* dielectric SiO_2. Furthermore, the control of the oxide thickness is very difficult at high temperature because of high oxygen diffusivity. Recently, however, it has been shown that such ultrathin oxide can be grown and tuned even at low temperature (including room temperature), by hyperthermal oxidation or when performed on non-planar Si surfaces (e.g., Si nanowires or spheres).

In this work, I have therefore studied two main topics: (1) hyperthermal Si oxidation and (2) thermal oxidation of Si nanowires. These investigations were carried out by applying molecular dynamics calculations using the ReaxFF (Reactive Force Field) potential, developed by Prof. A. C. T van Duin and co-workers.

1. Hyperthermal oxidation of planar Si surfaces. Although various theoretical and experimental studies have been carried out to investigate the silicon oxidation process even at room temperature, hyperthermal silica growth in general and the initial stages in particular have not yet been investigated in full detail. A number of related studies has therefore been carried out to elucidate this oxidation process.

First of all, I have investigated the interaction of thermal and hyperthermal O and O_2 with a Si(100){2x1} surface. All my investigations, the Si(100) surface is chosen as this is the most important surface facet for metal-oxide-semiconductor device fabrication. This oxidation process is also of importance for spacecrafts traveling through the low-Earth orbital, in which the dominant components are hyperthermal oxygen species (i.e., O, O_2^+, O_3, etc.), which can seriously damage the spacecraft surface. The simulations demonstrate that at low impact energies (<10 eV), the impinging oxygen atoms remain confined to the surface layers, and that the damage to the bulk is very limited and purely induced by the chemisorption process. At higher energies up to 100 eV, the O atoms can penetrate in the crystal up to 20 Å. The oxygen atoms cannot move deeper into the bulk due to the associated activation energy barrier. The limit depth of the penetrating O species is deeper for atomic oxygen compared to molecular oxygen. At these higher energies, the damage is much more pronounced, and primary and secondary knock-on displacements of Si are observed. This results in two distributions in the spatially resolved defect distributions. Furthermore, the results show that the low energies (1-5 eV) are more suitable for the Si oxidation.

Understanding the appearance of an ultrathin silica layer ultimately requires atomic level information. While numerous studies have elucidated the overall oxidation behavior, various aspects, such as direct oxidation or the effect of the growth temperature, are still poorly understood. Also, there are still many open questions regarding the oxide growth mechanism in this oxidation process, which is significantly different from the mechanism in the thermal oxidation case.

Therefore, reactive molecular dynamics calculations were carried out in order to investigate the growth mechanism of new oxide layers during hyperthermal oxidation (i.e., initial kinetic energies in the range 1-5 eV) of the Si(100){2x1} surface in a wide temperature range (100 K -1300 K). The results show that, in the initial oxidation stage, incident oxygen species can penetrate deeper than the Si top-most surface and can directly oxidize Si subsurface layers, in contrast to thermal oxidation. The temperature dependence of hyperthermal Si oxidation was analyzed and a transition temperature of about 700 K was found: below this temperature, the oxide thickness only depends on the impact energy of the impinging species. Above this temperature, the oxide thickness depends on the impact energy, type of oxidant and the surface temperature.

The initial stage of the oxide growth mechanism was also compared with two different thermal models, i.e., the Deal-Grove and “reactive layer” mechanisms. The hyperthermal Si oxidation mechanism is found to be significantly different both mechanisms due to direct oxidation.

The oxygenated silicon structure was analyzed by division into three regions, i.e., amorphous silica (*a*-SiO_2), a transition layer (or Si|SiO_2 interface), and the crystalline silicon (*c*-Si). The partial charge and mass density distributions in these structures show that the silica can reach a thickness of about 2 nm in a hyperthermal oxidation process induced by oxygen atoms and molecules with incident energies 1-5 eV at room temperature. It is therefore concluded that control over the ultrathin *a*-SiO_2 thickness is possible by hyperthermal oxidation of silicon surfaces at temperatures lower than certain transition temperature (e.g., at room temperature).

The radial distribution function (RDF) indicates that the silica bulk contains a number of intrinsic defects (i.e., incorrect coordination of Si or O atoms, oxygen vacancies) and oxygen peroxyl linkages, both in the bulk as well as at the surface. Diffusion of peroxyl oxygen bridges could play a role in the oxidation during the formation of ultrathin silica films. The overall spread of the angle distribution confirms the amorphous character of the SiO_2 (*a*-SiO_2) structure. Also, the Si-O-Si and Si-Si-O bond-angle distributions indicate some defects, e.g., Si-O-Si triangular configurations (or "Si epoxide linkages") exist in the *c*-Si|*a*-SiO_2 interface, which can be explained by a physical stress-enhanced bond breaking mechanism.

A comparison with several interface models developed for the traditional thermal oxidation was also performed. The thickness of the interface formed at low temperature was found to be about 0.5 nm, which is fairly close to experimental data. It was also found that interfacial stresses (~ 2 GPa) during hyperthermal oxidation at room temperature significantly slow down the inward silica growth.

2. Thermal oxidation of Si nanowires. Oxidation of nano-structured silicon is expected to be a key process to fabricate Si-based electronic devices in near-future technology. Specifically, core-shell silicon nanowires (Si-NWs) have being envisaged to be used as nanowire field-effect transistors and photovoltaic devices. In these nanodevices, control over the ultrathin oxide shell thickness is highly important. Usually, such small Si-NWs can be obtained by oxidizing large diameter Si-NWs and removing the oxide shell. Although electronic devices are continually shrinking in size, the formation of ultra-small diameter Si-NWs has not yet been investigated at the atomic-scale.

In this work, the formation of core shell Si-NWs by dry thermal oxidation of (100) Si nanowires with initial diameters from 1.0 nm to 3.0 nm and in the temperature range 300 K - 1273 K was investigated by reactive molecular dynamics simulations. The dry oxidation kinetics is analyzed in comparison with other existing models. Two temperature-dependent oxidation mechanisms are found, resulting in two types of structures: a self-limiting process that occurs at low temperature, resulting in a Si core | ultrathin SiO_2 silica shell (i.e., semiconductor + dielectric) or c-Si|SiO_x|a-SiO_2 nanowire, and a complete oxidation process that takes place at a higher temperature, resulting in the formation of an ultrathin SiO_2 silica (i.e., dielectric) nanowire. The transition temperature between both regimes was found to increase with the NW diameter. The presented calculations predict for the partially oxidized c-Si|SiO_x|a-SiO_2 nanowires that the Si-core (c-Si) and the total nanowire radius depend on the initial Si-NW diameter and inversely depend on the oxidation temperature. The final radii of the c-Si|SiO_x|a-SiO_2 nanowires are close to the theoretically suggested radii.

Stress calculations were also performed to study the oxidation behavior of these ultra-small nanowires. It is found that a compressive pressure and stress may significantly reduce the oxidant transport in the oxide region and its reaction with the Si-core. Specifically, when the temperature increases, the interfacial stresses decrease. This is consistent with previous theoretical work. However, it was also found that the compressive interfacial stresses decrease with increasing curvature for the 1-3 nm Si-NWs investigated, which is in contrast to the theoretical suggestions for Si-NW at the micro-scale. Generally, it can be concluded that an accurate control over the interfacial stress by choosing a suitable oxidation temperature and Si-NW diameter can lead to a precise control over the Si-core radius at the nanoscale.

In conclusion, in this work, various important issues have been resolved and several mechanisms have been elucidated in both hyperthermal Si oxidation and thermal Si-NW oxidation. The results give useful information for the fabrication of silica-based devices in the nanoelectronics industry.

Samenvatting en conclusies

De groei van dunne SiO_2 lagen op kristallijn Si is tegenwoordig een erg belangrijk onderwerp in de fabricage van microelectronica en fotovoltaische toestellen (bv. MOSFETs, zonnecellen, optische fibers, enz.). Het is bekend dat oxidatie bij lage temperatuur zeer moeilijk is, wegens de erg lage reactiecoëfficiënt van de invallende zuurstofdeeltjes. Anderzijds laat oxidatie bij hoge temperatuur niet toe om ultradunne, hoge-*k* diëlectrische SiO_2 lagen te vormen. Bovendien is een accurate controle over de dikte van de gevormde SiO_2 laag moeilijk bij hoge temperatuur omwille van de hoge O-diffusiviteit.

Het is echter aangetoond dat dergelijke dunne lagen wel gevormd kunnen worden bij lage temperaturen, en zelfs bij kamertemperatuur, door gebruik te maken van hyperthermische oxidatie. Dit hyperthermische oxidatieproces kan bovendien toegepast worden op zowel vlakke Si-oppervlakken als op Si-nanodraden. In deze thesis is deze hyperthermische oxidatie onderzocht, in het bijzonder met het oog op de oxidatiekinetiek en dynamica op atomaire schaal. Hierbij werd gebruik gemaakt van moleculaire dynamica (MD) simulaties, gebaseerd op de zogenaamde ReaxFF potentiaal voor het Si/O systeem, ontwikkeld door Prof. A. C. T. van Duin (PennState). Dergelijke reactieve MD simulaties zijn bijzonder geschikt om chemische reacties in (relatief) grote atomaire en moleculaire systemen te bestuderen.

Het onderzoek voorgesteld in deze thesis is dan ook gefocust op twee onderwerpen: (1) hyperthermische oxidatie van vlakke silicium oppervlakken, en (2) thermische oxidatie van Si-nanodraden.

1. ***Hyperthermische oxidatie van vlakke Si-oppervlakken.*** Hoewel reeds een aantal theoretische en experimentele studies zijn uitgevoerd met betrekking tot de oxidatie van Si(100) oppervlakken bij kamertemperatuur, is de hyperthermische groei van een silicalaag en in het bijzonder de eerste stadia daarvan nog niet in detail onderzocht. In alle studies uitgevoerd in dit werk is het Si(100) oppervlak onderzocht, vermits dit het belangrijkste oppervlakte facet is voor metaaloxide halfgeleider componenten. Daarenboven zijn deze studies ook relevant voor ruimtevaartuigen die in de zogenaamde “low-Earth orbital” bewegen, waarin de belangrijkste deeltjes de hyperthermische zuurstofdeeltjes

(zoals O, O_2, O_2^+, O_3, …) zijn. Deze deeltjes kunnen door botsingen immers het buitenoppervlak van het ruimtevaartuig beschadigen.

In een eerste studie werd daarom onderzocht hoe O en O_2 deeltjes interageren met een Si(100){2x1} oppervlak, in functie van hun energie. Bij lage invallende energie (< 10 eV), blijven de zuurstofdeeltjes beperkt tot de bovenste oppervlaktelagen, en is de schade aan de bulk erg beperkt en volledig geïnduceerd door chemisorptie. Bij hogere energieën, tot 100 eV, kunnen de O atomen dieper in het kristal penetreren, tot op een diepte van 20 Å. De zuurstofatomen kunnen echter niet verder in het kristal dringen ten gevolge van de geassocieerde energiebarrière. De maximale diepte die de zuurstofatomen kunnen bereiken is groter in het geval van atomaire impacts dan in het geval van moleculaire impacts. Bij deze hogere energieën, is de schade veel groter en primaire en secundaire “knock-on” verplaatsingen van Si-atomen worden waargenomen. Dit resulteert in twee distributies in de ruimtelijk geresolveerde defect distributies. De resultaten tonen ook aan dat de lage impactenergieën (1 – 5 eV) het meest geschikt zijn voor gecontroleerde Si-oxidatie.

Een fundamenteel begrip van de vorming van ultradunne silica lagen vereist uiteindelijk inzicht op atomaire schaal. Onderzoek van processen op atomaire schaal geven bovendien inzicht in de initiële groeistadia. Hoewel reeds een aantal onderzoeken uitgevoerd zijn met betrekking tot het oxidatieproces op kamertemperatuur, blijven verschillende aspecten, zoals directe oxidatie of de invloed van de temperatuur op het oxidatieproces, vooralsnog niet goed begrepen. Ook zijn er nog steeds open vragen met betrekking tot het hyperthermische groeimechanisme, dat significant verschilt van het thermische proces.

Daarom zijn reactieve MD simulaties uitgevoerd om het groeimechanisme van Si-oxide lagen op Si(100){2x1} oppervlakken te bestuderen onder hyperthermische condities. In deze simulaties hebben de invallende zuurstofdeeltjes een energie in het gebied 1 – 5 eV, en is de temperatuur gevarieerd in het gebied 100 K – 1300K. De resultaten tonen aan dat in de initiële groeifase, de invallende zuurstofdeeltjes dieper in het kristal kunnen dringen dan in thermische oxidatie, dwz., dieper kunnen doordringen dan de bovenste oppervlaktelagen. De temperatuursafhankelijkheid van de hyperthermische oxidatie werd onderzocht en een transitietemperatuur van 700 K werd vastgesteld: onder deze temperatuur, blijkt de dikte van de oxidelaag enkel afhankelijk te zijn van de impactenergie van de invallende deeltjes. Boven deze temperatuur echter, is de dikte van het resulterende oxidelaagje afhankelijk van de impactenergie, het type van invallend deeltje alsook van de substraattemperatuur.

De initiële fase werd vergeleken met twee verschillende thermische modellen, nl. het Deal-Grove model en het "reactieve laag model". De resultaten behaald in dit werk tonen aan dat hyperthermische oxidatie niet beschreven kan worden door deze modellen, ten gevolge van het voorkomen van directe oxidatie.

De geoxigeneerde siliciumstructuur is geanalyzeerd door een verdeling in drie gebieden: een amorfe silica (a-SiO_2) laag, een transitielaag ($Si|SiO_2$ interface), en het kristallijne silicium (c-Si). Distributies in partiële ladingen en massadichtheid van deze structuren tonen aan dat de silicalaag tot 2 nm dik kan worden in het hyperthermische proces, waarbij de invallende O atomen en O_2 moleculen een energie van 1 – 5 eV hebben bij kamertemperatuur. Hieruit kan geconcludeerd worden dat controle over de ultradunne a-SiO_2 dikte mogelijk is door gebruik te maken van hyperthermische oxidatie van siliciumoppervlakken bij een temperatuur lager dan de transitietemperatuur.

Radiale distributiefuncties (RDF) tonen aan dat de silica bulk intrinsieke defecten bevat (dwz., incorrecte coördinatie van Si- of O-atomen en O-vacatures), alsook zuurstof peroxylbruggen. Deze peroxylbruggen komen zowel in de bulk als aan het oppervlak voor. Diffusie van deze zuurstof peroxylbruggen kunnen een belangrijke rol spelen bij de oxidatie ter vorming van ultradunne silica lagen.

Naast RDFs werden ook de hoekdistributiefuncties ("angular distribution functions", ADF) berekend. De spreiding in deze distributies toont aan dat het gevormde SiO_2 amorf is. De Si-O-Si en Si-Si-O distributies tonen bovendien defecten aan, zoals het voorkomen van Si-O-Si driehoeksconfiguraties ("Si epoxide bruggen"). Deze epoxiden komen voor in de c-$Si|a$-SiO_2 interface, en kunnen verklaard worden aan de hand van het stress-geïnduceerd breken van bindingen. Omwille van het belang hiervan, werd ook de morfologie van de c-$Si|a$-SiO_2 interface bij lage temperatuur nauwkeurig onderzocht. Bovendien werd een vergelijking met verschillende interface modellen, zoals ontwikkeld voor traditionele thermische oxidatie, doorgevoerd. De dikte van de interface bij lage temperatuur bedraagt ongeveer 0.5 nm, hetgeen in redelijke overeenstemming is met experimentele gegevens. Tenslotte werd ook aangetoond dat de stress in de interface (~ 2 GPa) tijdens de hyperthermische oxidatie de inwaartse groei van silica bij kamertemperatuur sterk vertraagt.

2.***Thermische oxidatie van Si-nanodraden.*** Dunne "core-shell" silicium nanodraden bieden perspectief om gebruikt te worden als nanodraad veldeffect transistoren en fotovoltaische componenten. Ook in deze nanocomponenten is controle over de precieze dikte van de oxide laag van groot belang.

Gewoonlijk worden dunne Si-nanodraden bekomen door een dikke Si-nanodraad thermisch te oxideren, en vervolgens het oxide te verwijderen. Dit leidt echter niet altijd tot nauwkeurige controle over de oxide laag. Ondanks de continue miniaturizatie van elektronische componenten en het nut van Si-nanodraden, is de vorming van ultradunne Si-nanodraden nog niet onderzocht op atomaire schaal.

Specifiek werd in deze thesis de vorming van core-shell Si-nanodraden door droge thermische oxidatie van Si(100) Si-nanodraden onderzocht bij een temperatuur in het gebied 300 K – 1273 K. Deze Si-nanodraden hadden initieel een diameter tussen 1.0 en 3.0 nm. In het bijzonder werd de oxidatiekinetiek onderzocht en vergeken met bestaande modellen.

Twee temperatuursafhankelijke oxidatiemechanismen werden gevonden, resulterend in twee types van structuren: enerzijds een zelf-limiterend proces dat plaatsvindt bij lage temperatuur, en dat leidt tot de vorming van een Si core | ultradunne SiO_2 oxide shell (dwz., een halfgeleider + isolator structuur) of c-Si|SiO_x|a-SiO_2 nanodraad, en anderzijds een volledig oxidatieproces dat plaatsvindt bij hogere temperatuur, en dat leidt tot de vorming van een ultradunne SiO_2 silica (dwz., isolator structuur) nanodraad. De simulaties tonen aan dat de transitietemperatuur tussen beide regimes toeneemt met toenemende nanodraad diameter. Bovendien werd gevonden dat voor de partieel geoxideerde c-Si|SiO_x|a-SiO_2 nanodraden de Si-kern en de totale nanodraad diameter evenredig zijn met de initiële diameter en omgekeerd evenredig zijn met de oxidatietemperatuur. De uiteindelijke straal van de gevormde c-Si|SiO_x|a-SiO_2 nanodraden komt goed overeen met de theoretisch voorspelde waarde.

Om het oxidatiegedrag van deze ultradunne draden verder te bestuderen, werden ook stress berekeningen uitgevoerd. Deze simulaties tonen aan dat het optreden van een compressieve stress het transport van het oxidans in de oxide regio en de reactie met de Si-kern sterk kan vertragen. De interface stress daalt met toenemende temperatuur, hetgeen consistent is met eerder theoretisch werk.

De berekeningen tonen echter ook aan dat de compressieve interface stress ook daalt met toenemende curvatuur van de onderzochtte draden, hetgeen in tegenspraak is met de theoretische bevindingen voor oxidatie op microschaal. Uit de uitgevoerde berekeningen kan geconcludeerd worden dat een accurate controle van de interface stress bekomen kan worden door controle van de oxidatie temperatuur en de diameter van de Si-nanodraad. Dit leidt op zijn beurt tot een accurate controle van de diameter van de Si-kern in het nanoschaal regime.

Appendix A. Force field parameters for Si-O system (Buehler et al., 2006-2007)

```
Reactive MD-force field, Buehler PRL 2006, 2007
 39       ! Number of general parameters
   50.0000 !Overcoordination parameter
    5.5469 !Overcoordination parameter
   21.2839 !Valency angle conjugation parameter
    3.0000 !Triple bond stabilisation parameter
    6.5000 !Triple bond stabilisation parameter
    1.0000 !Not used
    1.0159 !Undercoordination parameter
    9.0000 !Triple bond stabilisation parameter
    8.0878 !Undercoordination parameter
   13.0238 !Undercoordination parameter
  -13.8107 !Triple bond stabilization energy
    0.0000 !Lower Taper-radius
   10.0000 !Upper Taper-radius
    2.8793 !Not used
   33.8667 !Valency undercoordination
   25.6125 !Valency angle/lone pair parameter
    1.0563 !Valency angle
    2.0384 !Valency angle parameter
    6.1431 !Not used
    6.9290 !Double bond/angle parameter
    0.3989 !Double bond/angle parameter: overcoord
    3.9954 !Double bond/angle parameter: overcoord
   -2.4837 !Not used
    4.7747 !Torsion/BO parameter
   10.0000 !Torsion overcoordination
    2.3276 !Torsion overcoordination
   -1.2327 !Conjugation 0 (not used)
    2.1645 !Conjugation
    1.5591 !vdWaals shielding
    0.1000 !Cutoff for bond order (*100)
    2.8921 !Valency angle conjugation parameter
    1.6356 !Overcoordination parameter
    5.6937 !Overcoordination parameter
    2.5067 !Valency/lone pair parameter
    0.5000 !Not used
   20.0000 !Not used
    5.0000 !Molecular energy (not used)
    0.0000 !Molecular energy (not used)
    1.6052 !Valency angle conjugation parameter
  7    ! Nr of atoms; cov.r; valency;a.m;Rvdw;Evdw;gammaEEM;cov.r2;#
            alfa;gammavdW;valency;Eunder;Eover;chiEEM;etaEEM;n.u.
            cov r3;Elp;Heat inc.;n.u.;n.u.;n.u.;n.u.
            ov/un;val1;n.u.;val3,vval4
 C    1.3931   4.0000  12.0000   2.0430   0.0715   0.8712   1.2481   4.0000
     10.5900   1.9058   4.0000  38.2875  75.7665   5.7254   6.9235   0.0000
      1.2520   0.0000 206.7910   5.3452  24.6774  12.1341   0.8563   0.0000
    -10.8644   2.4601   1.0564   6.2998   2.9663   0.0000   0.0000   0.0000
 H    0.6555   1.0000   1.0080   1.6558   0.0228   0.7625  -0.1000   1.0000
     10.0764   4.1572   1.0000   0.0000 116.3988   3.8196   9.8832   1.0000
     -0.1000   0.0000  54.9848   4.0736   2.6883   1.0000   1.0698   0.0000
    -12.5850   2.7466   1.0338   6.2998   2.8793   0.0000   0.0000   0.0000
 O    1.1534   2.0000  15.9990   1.7195   0.1292   0.7819   0.9660   6.0000
     10.2695   4.0190   4.0000  32.8323 116.0768   8.5000   7.3000   2.0000
      0.9800   6.8930  -1.1912   2.7851   2.1946   1.0000   0.9745   0.0000
     -6.7189   2.6656   1.0493   6.2998   2.9225   0.0000   0.0000   0.0000
 N    1.2360   3.0000  14.0000   1.9333   0.1373   0.8596   1.1602   5.0000
     10.0725   8.0467   4.0000  34.5504 100.0000   6.8418   6.3404   2.0000
      1.0365  14.7406 138.0808   2.5032   2.7335   2.6432   0.9745   0.0000
```

```
    -15.0000   2.6491   1.0183   6.2998   2.8793   0.0000   0.0000   0.0000
 S    1.9405   2.0000  32.0600   2.0677   0.2099   1.0336   1.5479   6.0000
      9.9575   4.9055   4.0000  52.9998 112.1416   6.5000   8.2545   2.0000
      1.4601   9.7177 201.5221   5.7487  23.2859  12.7147   0.9745   0.0000
    -11.0000   2.7466   1.0338   6.2998   2.8793   0.0000   0.0000   0.0000
 Si   2.0175   4.0000  28.0600   2.0473   0.1835   0.6587   0.9641   4.0000
     12.3588   1.2523   4.0000  21.7115 139.9309   2.4081   6.4081   0.0000
     -1.0000   0.0000 128.2031   8.7895  23.9298   0.8381   0.8563   0.0000
     -4.7525   2.1607   1.0338   6.2998   2.5791   0.0000   0.0000   0.0000
 X   -0.1000   2.0000   1.0080   2.0000   0.0000   1.0000  -0.1000   6.0000
     10.0000   2.5000   4.0000   0.0000   0.0000   8.5000   1.5000   0.0000
     -0.1000   0.0000 127.6226   8.7410  13.3640   0.6690   0.9745   0.0000
    -11.0000   2.7466   1.0338   6.2998   2.8793   0.0000   0.0000   0.0000
 18      ! Nr of bonds; Edis1;LPpen;n.u.;pbe1;pbo5;13corr;pbo6
                         pbe2;pbo3;pbo4;n.u.;pbo1;pbo2;ovcorr
  1  1 150.2857 102.1226  73.9998   0.1094  -0.5558   1.0000  17.2117   0.5000
         0.2455  -0.2256   9.4807   1.0000  -0.1005   6.0387   1.0000
  1  2 167.9626   0.0000   0.0000  -0.4259   0.0000   1.0000   6.0000   0.5000
        18.9231   1.0000   0.0000   1.0000  -0.0102   8.2763   0.0000
  2  2 166.5174   0.0000   0.0000  -0.3599   0.0000   1.0000   6.0000   0.6500
        10.6518   1.0000   0.0000   1.0000  -0.0177   5.3255   0.0000
  1  3 172.8767 109.3662  93.2629   0.5518  -0.2029   1.0000  19.7207   0.5000
         0.4387  -0.2871   9.2845   1.0000  -0.1406   5.6488   1.0000
  3  3  81.4891  30.2266 202.3398   0.7334  -0.0688   1.0000  10.4340   0.7000
         1.2986  -0.1057   5.7341   1.0000  -0.1770   5.0269   1.0000
  1  4 170.0282 132.5726  69.9149   0.2278  -0.1754   1.0000  30.0000   0.6500
         0.2304  -0.3072   8.6708   1.0000  -0.1771   4.9068   1.0000
  3  4 147.4287 109.4565  61.7111   0.9507  -0.1616   1.0000  21.7802   0.7500
         0.7441  -0.3665   7.2396   1.0000  -0.2439   4.8277   1.0000
  4  4 154.5270 128.3844 139.6322   0.2171  -0.1418   1.0000  13.1260   0.7500
         0.3601  -0.1310  10.7257   1.0000  -0.0869   5.3302   1.0000
  2  3 217.6778   0.0000   0.0000  -0.7049   0.0000   1.0000   6.0000   0.4031
         4.9325   1.0000   0.0000   1.0000  -0.0668   4.4019   0.0000
  2  4 212.4218   0.0000   0.0000  -0.5681   0.0000   1.0000   6.0000   0.6000
         9.7582   1.0000   0.0000   1.0000  -0.0307   6.0744   0.0000
  1  5 128.9942  74.5848  55.2528   0.1035  -0.5211   1.0000  18.9617   0.6000
         0.2949  -0.2398   8.1175   1.0000  -0.1029   5.6731   1.0000
  2  5 151.5159   0.0000   0.0000  -0.4721   0.0000   1.0000   6.0000   0.6000
         9.4366   1.0000   0.0000   1.0000  -0.0290   7.0050   0.0000
  3  5   0.0000   0.0000   0.0000   0.5563  -0.4038   1.0000  49.5611   0.6000
         0.4259  -0.4577  12.7569   1.0000  -0.1100   7.1145   1.0000
  4  5   0.0000   0.0000   0.0000   0.4438  -0.2034   1.0000  40.3399   0.6000
         0.3296  -0.3153   9.1227   1.0000  -0.1805   5.6864   1.0000
  5  5  96.1871  93.7006  68.6860   0.0955  -0.4781   1.0000  17.8574   0.6000
         0.2723  -0.2373   9.7875   1.0000  -0.0950   6.4757   1.0000
  6  6  78.0276  54.0531  30.0000   0.5398  -0.3000   1.0000  16.0000   0.0476
         0.2865  -0.8055   7.1248   1.0000  -0.0681   8.6957   0.0000
  2  6 192.0767   0.0000   0.0000  -0.5621   0.0000   1.0000   6.0000   0.3529
        22.1879   1.0000   0.0000   1.0000  -0.0377   7.2563   0.0000
  3  6 252.6471  53.4022  43.3991  -0.7699  -0.3000   1.0000  36.0000   0.6262
         8.4871  -0.8398  26.9303   1.0000  -0.0982   7.8659   1.0000
  3    ! Nr of off-diagonal terms; Ediss;Ro;gamma;rsigma;rpi;rpi2
  2  6   0.0503   1.5421  13.5806   1.3054  -1.0000  -1.0000
  3  6   0.1481   2.0087  11.4016   1.6805   1.4330  -1.0000
  2  3   0.0427   1.7283  10.2714   0.9397  -1.0000  -1.0000
 61    ! Nr of angles;at1;at2;at3;Thetao,o;ka;kb;pv1;pv2;val(bo)
  1  1  1  75.3892  20.0233   2.1017   2.4996   0.0031  35.9933   1.0400
  1  1  2  71.5185  11.6939   6.5331   0.0000   0.0000   0.0000   1.0400
  2  1  2  72.0977   8.3496   2.2003   0.0000   0.2000   0.0000   1.0400
  1  2  2   0.0000   0.0000   6.0000   0.0000   0.0000   0.0000   1.0400
  1  2  1   0.0000  28.5244   6.0000   0.0000   0.0000   0.0000   1.0400
  2  2  2   0.0000  27.9213   5.8635   0.0000   0.0000   0.0000   1.0400
  1  1  3  74.0268  28.8967   1.2260   0.0000   4.6228   0.0000   1.0400
  3  1  3  80.2138  52.6408   1.3212   0.0000   4.6228 -35.0000   1.0400
  1  1  4  66.4599  51.9415   0.7082   0.0000   4.6228   0.0000   1.0400
```

```
  3  1  4  74.1764  40.5898   1.6351   0.0000   4.6228   0.0000   1.0400
  4  1  4  67.4646   7.7402   2.9526   0.0000   4.6228   0.0000   1.0400
  2  1  3  79.3704  19.7034   2.5917   0.0000   0.0000   0.0000   1.0400
  2  1  4  72.6759  13.4161   5.9166   0.0000   0.0000   0.0000   1.0400
  1  2  4   0.0000   0.0019   6.3000   0.0000   0.0000   0.0000   1.0400
  1  3  1  76.4435  43.0224   0.6138   0.0000   0.4897   0.0000   1.0400
  1  3  3  81.4803  53.9823   0.8786   0.0000   0.4897   0.0000   1.0400
  1  3  4  89.4608  53.6036   0.7017   0.0000   0.4897   0.0000   1.0400
  3  3  3  78.4963  61.0192   1.0093 -38.4200   0.4897   0.0000   1.0400
  3  3  4  79.0601  38.7432   2.1471   0.0000   0.4897   0.0000   1.0400
  4  3  4  74.5183  54.0833   1.9745   0.0000   0.4897   0.0000   1.0400
  1  3  2  82.1464  36.8788   1.3932   0.0000   0.0000   0.0000   1.0400
  2  3  3  89.4640  10.1026   4.7764   0.0000   0.0000   0.0000   1.0400
  2  3  4  87.0795  48.4138   1.4565   0.0000   0.0000   0.0000   1.0400
  2  3  2  81.7479  15.4269   4.2247   0.0000   0.0000   0.0000   1.0400
  1  4  1  70.5355  19.5076   1.2344   0.0000   2.7993   0.0000   1.0400
  1  4  3  77.6934  20.6976   1.4669   0.0000   2.7993   0.0000   1.0400
  1  4  4  78.1599  13.8502   1.8371   0.0000   2.7993   0.0000   1.0400
  3  4  3  74.8323  35.2858   1.4738 -21.5494   2.7993   0.0000   1.0400
  3  4  4  77.6183  29.5041   1.2928  -2.0087   2.7993   0.0000   1.0400
  4  4  4  75.2419  20.4666   3.1280   0.0000   2.7993   0.0000   1.0400
  1  4  2  81.6606  49.2031   0.6194   0.0000   0.0000   0.0000   1.0400
  2  4  3  88.7810  66.7825   0.9625   0.0000   0.0000   0.0000   1.0400
  2  4  4  89.4242  36.9752   1.1820   0.0000   0.0000   0.0000   1.0400
  2  4  2  85.3507  23.0120   2.3616   0.0000   0.0000   0.0000   1.0400
  1  2  3   0.0000   0.0019   6.0000   0.0000   0.0000   0.0000   1.0400
  1  2  4   0.0000   0.0019   6.0000   0.0000   0.0000   0.0000   1.0400
  1  2  5   0.0000   0.0019   6.0000   0.0000   0.0000   0.0000   1.0400
  3  2  3   0.0000   0.0019   6.0000   0.0000   0.0000   0.0000   1.0400
  3  2  4   0.0000   0.0019   6.0000   0.0000   0.0000   0.0000   1.0400
  4  2  4   0.0000   0.0019   6.0000   0.0000   0.0000   0.0000   1.0400
  2  2  3   0.0000   0.0019   6.0000   0.0000   0.0000   0.0000   1.0400
  2  2  4   0.0000   0.0019   6.0000   0.0000   0.0000   0.0000   1.0400
  1  1  5  74.9397  25.0560   1.8787   0.1463   0.0559   0.0000   1.0400
  1  5  1  86.9521  36.9951   2.0903   0.1463   0.0559   0.0000   1.0400
  2  1  5  74.9397  25.0560   1.8787   0.0000   0.0000   0.0000   1.0400
  1  5  2  86.1791  36.9951   2.0903   0.0000   0.0000   0.0000   1.0400
  1  5  5  85.3644  36.9951   2.0903   0.1463   0.0559   0.0000   1.0400
  2  5  2  93.1959  36.9951   2.0903   0.0000   0.0000   0.0000   1.0400
  2  5  5  84.3331  36.9951   2.0903   0.0000   0.0000   0.0000   1.0400
  6  6  6  71.0490  32.4076   1.2648   0.0000   0.0133   0.0000   1.2899
  2  6  6  71.9021  14.1096   1.6768   0.0000   1.6264   0.0000   1.0400
  2  6  2  77.2257  16.0297   2.1560   0.0000   2.8421   0.0000   1.0400
  3  6  6  59.5932  16.1656   0.5837   0.0000   3.5470   0.0000   1.0400
  2  6  3  68.0560  21.3156   4.5715   0.0000   0.5983   0.0000   1.0400
  3  6  3  78.2491  11.8348   0.1760   0.0000   0.4141   0.0000   1.0400
  6  3  6  39.8239   1.2281   0.2412   0.0000   3.7260   0.0000   1.0400
  2  3  6  81.6231   7.6711   4.5986   0.0000   1.4086   0.0000   1.0400
  3  3  6  85.4020  18.1749   1.2713   0.0000   2.6177   0.0000   1.0400
  2  2  6   0.0000  47.1300   6.0000   0.0000   1.6371   0.0000   1.0400
  6  2  6   0.0000  31.5209   6.0000   0.0000   1.6371   0.0000   1.0400
  3  2  6   0.0000  31.0427   4.5625   0.0000   1.6371   0.0000   1.0400
 20    ! Nr of torsions;at1;at2;at3;at4;;V1;V2;V3;V2(BO);vconj;n.u;n
  1  1  1  1   0.0000  25.1267   0.2722  -4.6251  -1.2327   0.0000   0.0000
  1  1  1  2   0.0000  15.9983   0.4583  -4.0203  -1.2327   0.0000   0.0000
  2  1  1  2   0.0000  50.0880   0.3349  -5.3444  -1.2327   0.0000   0.0000
  0  1  2  0   0.0000   0.0000   0.0000   0.0000  -1.2327   0.0000   0.0000
  0  2  2  0   0.0000   0.0000   0.0000   0.0000  -1.2327   0.0000   0.0000
  0  1  3  0   1.2595 112.3590   0.6986  -4.0480  -1.2327   0.0000   0.0000
  0  2  3  0   0.0000   0.1000   0.0200  -2.5415  -1.2327   0.0000   0.0000
  0  3  3  0   2.6089  -1.7346  -0.1083  -4.7170  -1.2327   0.0000   0.0000
  0  1  4  0  -2.7302 104.9719   0.3292  -4.6130  -1.2327   0.0000   0.0000
  0  2  4  0   0.0000   0.1000   0.0200  -2.5415  -1.2327   0.0000   0.0000
  0  3  4  0   0.4947  36.1724   0.1127  -5.7235  -1.2327   0.0000   0.0000
  0  4  4  0  -2.7105  91.7450   1.9165  -3.4903  -1.2327   0.0000   0.0000
```

```
 0  1  1  0   0.0000  12.4562   0.0000  -3.6133  -1.2327   0.0000   0.0000
 4  1  4  4  -6.0000  48.9253   0.1230  -5.0000  -1.2327   0.0000   0.0000
 0  1  5  0   3.3423  30.3435   0.0365  -2.7171  -1.2327   0.0000   0.0000
 0  5  5  0  -0.0555 -42.7738   0.1515  -2.2056  -1.2327   0.0000   0.0000
 0  2  5  0   0.0000   0.0000   0.0000   0.0000  -1.2327   0.0000   0.0000
 2  6  6  2   0.0000   0.0000   0.0640  -2.4426   0.0000   0.0000   0.0000
 2  6  6  6   0.0000   0.0000   0.1587  -2.4426   0.0000   0.0000   0.0000
 0  2  6  0   0.0000   0.0000   0.1200  -2.4847   0.0000   0.0000   0.0000
 9    ! Nr of hydrogen bonds;at1;at2;at3;Rhb;Dehb;vhb1
 3  2  3   2.1047  -5.2340   3.6501   1.8988
 3  2  4   1.3705 -12.4623   3.6501   1.8988
 4  2  3   1.5780  -5.5050   3.6501   1.8988
 4  2  4   1.6506  -4.9753   3.6501   1.8988
 3  2  5   2.2982  -4.2337   3.6501   1.8988
 4  2  5   2.2237  -4.9119   3.6501   1.8988
 5  2  3   2.3781  -2.9505   3.6501   1.8988
 5  2  4   2.3400  -4.4265   3.6501   1.8988
 5  2  5   2.4461  -2.0000   3.6501   1.8988
```

List of publications

Publications related to this thesis, published

1. E.C. Neyts, **U. Khalilov**, G. Pourtois, A.C.T. van Duin, *Hyperthermal Oxygen Interacting with Silicon Surfaces: Adsorption, Implantation, and Damage Creation* J. Phys. Chem. C, *2011, 115(11), 4818–4823*.

2. **U. Khalilov**, E.C. Neyts, G. Pourtois, A.C.T. van Duin, *Can We Control the Thickness of Ultrathin Silica Layers by Hyperthermal Silicon Oxidation at Room Temperature?* J. Phys. Chem. C, *2011, 115(50), 24839–24848*.

3. **U. Khalilov**, G. Pourtois, A.C.T. van Duin, E.C. Neyts, *Hyperthermal Oxidation of Si(100)2x1 Surfaces: Effect of Growth Temperature* J. Phys. Chem. C, *2012, 116, 8649–8656*.

4. **U. Khalilov**, G. Pourtois, A.C.T. van Duin, E.C. Neyts, *Self-Limiting Oxidation in Small-Diameter Si Nanowires* Chem. Mater., *2012, 24, 2141–2147*. **Selected as cover picture for the journal.**

5. **U. Khalilov**, G. Pourtois, A.C.T. van Duin, E.C. Neyts, *On the c-Si|a-*SiO_2 *Interface in Hyperthermal Si oxidation at Room Temperature* J. Phys. Chem. C, *2012, 116, 21856–21863*.

6. **U. Khalilov**, G. Pourtois, A. Bogaerts, A.C.T. van Duin, E.C. Neyts, *Reactive Molecular Dynamics simulations on* SiO_2*-coated ultra-small Si-nanowires* Nanoscale, *2013, 5, 719-725*.

Publications related to this thesis, in preparation

7. **U. Khalilov**, G. Pourtois, A.C.T. van Duin, E.C. Neyts, *Plasma-assisted oxidation of small Si nanowires: reactive MD study*, in preparation.

8. **U. Khalilov**, G. Pourtois, A.C.T. van Duin, E.C. Neyts, *Hyperthermal oxygen interacting with native Si oxide: reactive MD study*, submitted to Chemistry of Materials.

Publications not related to this thesis

1. M. Yusupov, E.C. Neyts, **U. Khalilov**, R. Snoeckx, A.C.T. van Duin, A. Bogaerts, *Atomic-scale simulations of reactive oxygen plasma species interacting with bacterial cell walls* New J. Phys., *2012, 14, 093043*.

2. A. Dzhurakhalov, **U. Khalilov**, D. Husanova, *Investigation of small metal cluster interactions with atomic chains at grazing incidence* Poverkhnost (Russian journal "Surface"), 2006, 7, 25-29.

3. N. Turaev, **U. Khalilov**, G. Rakhimova, *Cluster formation mechanism in atomic sputtering process* Uzbek Journal of Physics, 2002, 4, 102-106.

4. **U. Khalilov**, G. Rakhimova, N. Turaev, *About one mechanism of formation of clusters at sputtering of single crystals* Uzbek Journal of Physics, 2002, 5, 65-69.

Contributions to conferences

1. **Khalilov U.**, Pourtois G., van Duin A. C. T. and Neyts E. C. Reactive MD Study of Hyperthermal Si-Oxidation Mechanisms in Ultrathin a-SiO_2 Films *Poster presentation at the 25th International Conference on Atomic Collisions in Solids (ICACS 25)* October 21-25, 2012, Kyoto, Japan.

2. **Khalilov U.**, Pourtois G., van Duin A. C. T. and Neyts E. C. Wet and plasma-assisted oxidation of small Si nanowires at room temperature: reactive molecular dynamics study *Poster presentation at the International Conference on Plasma Surface Engineering (PSE 13)* September 10-14, 2012, Garmisch-Partenkirchen, Germany.

3. **Khalilov U.**, Pourtois G., van Duin A. C. T. and Neyts E. C. Reactive MD study of small Si nanowire oxidation: Control of Si-core radius *Poster presentation at the Computer Simulations of Radiation Effects in Solids (COSIRES 2012)* June 24-29, 2012, Santa Fe, NM, United States.

4. **Khalilov U.**, Pourtois G., van Duin A. C. T. and Neyts E. C. Reactive MD study of hyperthermal Si oxidation: Effect of growth temperature *Poster presentation at the Computer Simulations of Radiation Effects in Solids (COSIRES 2012)* June 24-29, 2012, Santa Fe, NM, United States.

5. **Khalilov U.**, Neyts E. C., Pourtois G., van Duin A. C. T. Self-limiting hyperthermal Si oxidation: a reactive MD study *Poster presentation at the Computer Simulations of Radiation Effects in Solids (COSIRES 2012)* **Student poster award: runner-up.** June 24-29, 2012, Santa Fe, NM, United States.

6. **Khalilov U.**, Neyts E. C., Pourtois G., van Duin A. C. T. Controlling the Si-core / SiO_2 oxide shell thickness during oxidation of Si nanowires with diameter up to 3 nm *Poster presentation at the Workshop on Graphene and Carbon Nanotubes* September 23, 2011, Leuven, Belgium.

7. A.A. Dzhurakhalov, S.E. Rahmatov, M.S. Yusupov, **U. Khalilov** Sputtering processes of CuAu(100) and Cu_3Au(100) surfaces at low energy ion bombardment // *Abstracts of 16th International Conference on Ion Beam Modification of Materials (IBMM'08),* August 31 – September 5, 2008, Dresden, Germany.

8. A.A. Dzhurakhalov, **U. Khalilov,** D.Kh Husanova. MD simulation of atom and cluster scattering at grazing incidence // *Abstracts of Conference on Computational Physics (CCP2007)*, Brussels, Belgium, September 5-8, 2007, P.119.

9. N.Yu. Turaev, A.A. Dzhurakhalov, **U. Khalilov** Peculiarities of ion-single crystal surface interaction processes at grazing incidence.// *Proceedings of International conference on Ion-Surface Interactions (ISI 2007)*, Moscow, Russia, August 24-28, 2007, P.4

10. A.A. Dzhurakhalov, G.R.Rahimova, **U. Khalilov**, D.Kh. Husanova Investigation of process of interaction small metal clusters with atoms chain at grazing incidence // *Abstract of International conference on Ion-Surface Interactions (ISI 2005)*, August 25, 2005, Moscow, Russia.

11. A.A. Dzhurakhalov, **U. Khalilov**, D.Kh. Husanova Simulation by molecular dynamics method of interaction's process small cluster with surface of single crystal // *Abstract of 34th International conference on the physics of interaction charged particles with crystals*, May 31 - June 2, 2004, Moscow, Russia.

12. **U. Khalilov**, D.Kh. Husanova, A.A. Dzhurakhalov. MD simulation of low-energy small cluster bombardment of crystal surfaces at grazing incidence, // *Abstracts of E-MRS 2004 Spring Meeting,* May 24-28, 2004, Strasbourg, France.

13. A.A. Dzhurakhalov, D.Kh. Husanova, **U. Khalilov** BCA and MD simulations of particle surface interaction processes at grazing incidence // *Abstracts of International Conference on Condensed Matter and Materials Physics(CMMP'04)*, Warwick, UK, April 4-7, 2004, P.13

14. **Khalilov U.**, Rakhimova G.R., Turaev N.Yu. About one mechanism of formation of clusters at sputtering of single crystals // *Abstracts of 13th Int. Conf. on Ion Beam Modification of Materials (IBMM2002)*. Kobe, Japan, September 1-6, 2002, P.10.

Bibliography

[1] Siffert, P.; Krimmel, E. *Silicon: Evolution and Future of a Technology,* Spring-Verlag Berlin Heidelberg, **2004**.

[2] Gibson, J. M.; Lanzerotti, M. Y. *Nature* **1989**, 340, 128-131.

[3] Achuthan, M. K.; Bhat, K. N. *Fundamentals of Semiconductor Devices,* New Delhi, India, **2007**.

[4] Hurle, D. T. J. *Handbook of Crystal Growth*, Elsevier Science, Amsterdam, **1994**.

[5] Schlier, R. E.; Farnsworth, H. E. *J. Chem. Phys*., **1959,** 30, 917.

[6] Zhu, Z.; Shima, N.; Tsukada, M. *Phys. Rev.B,* **1989,** 40, 11868-11879.

[7] Chadi, D. J. *Phys. Rev. Lett.*, 1979, 43, 43–47.

[8] Ramstad, A.; Brocks, G.; Kelly, P. *J. Phys. Rev. B,* **1995**, 51, 14504-14523.

[9] Tang, S.; Freeman, A. J.; Delley, B. *J. Phys. Rev. B,* **1992**, 45, 1776-1783.

[10] Green, M. L.; Gusev, E. P.; Degraeve, R.; Garfunkel, E. L. *J. Appl. Phys*., **2001**, 90.

[11] http://heraeus-quarzglas.com/en/home/Home.aspx

[12] Shabal, Y. J. *Fundamental aspects of Si oxidation*, Spring-Verlag Berlin Heidelberg, **2001**.

[13] Cady, W. G. *Physical Review A*, **1921**, 17, 531-533.

[14] Bartenev, G. *Journal of Non-Crystalline Solids* ,**1968**, 1, 69.

[15] Garfunkel, E. ; Gusev, E. P.; Vul, A.; *Fundamental Aspects of Ultrathin Dielectrics on Si-based Devices,* Kluwer Academic Publishers, Dordrecht, **1998**.

[16] Nalwa, H.S. *Silicon-Based Materials and Devices*, vol. 1 Academic, New York, **2001**.

[17] Popovich, M. *High Performance Power Distribution Networks with On-Chip Decoupling Capacitors for Nanoscale Integrated Circuits*, University of Rochester, New York, **2007**.

[18] Engstrom, J. R.; Bonser, D. J.; Nelson, M. M.; Engel, T. *Surf. Sci.,***1991**, 256, 317-343.

[19] Engstrom, J. R.; Bonser, D. J.; Engel, T.*Surf. Sci.*, **1992**, 268, 238-264.

[20] Bongiorno, A. *Simulation of atomistic processes during silicon oxidation*, PhD thesis, Lausanne, EPFL **2003**.

[21] Choi, C. H.; Liu, D.; Evans, J. W.; Gordon, M. S. *J. Am. Chem. Soc.*, **2002**, 124, 8730-8740.

[22] Deal, B. E.; Grove, A. S. *J. Appl. Phys*., 1965, 36, 3770–3778.

[23] Massoud, H. Z.; Plummer, J. D.; Irene, E. A. *J. Electrochem. Soc,*. **1985**, 132, 2685.

[24] Massoud, H. Z. ; Plummer, J. D.; Irene, E. A. *J. Electrochem. Soc.*, **1985**, 132, 2693.

[25] Cui, H.; Sun, Y.; Yang, G. Z.; Yang, G. W.; Wang, C. X. *Appl. Phys. Lett*., **2009**, 94, 083108.

[26] van der Meulen, Y. J. *J. Electrochem. Soc.*, **1972**, 119, 530-534.

[27] Hu, S. M. *Appl. Phys. Lett.*, **1983**, 42, 872-874.

[28] Han, C.-J.; Helms, C. R. *J. Electrochem. Soc.,***1987**, 134, 1297.

[29] Enta, Y.; Mun, B. S.; Rossi, M.; Ross, P. N.; Hussain, Z., Jr.; Fadley, C. S.; Lee, K.; Kim, S. *Appl. Phys. Lett.* **2008**, 92, 012110.

[30] Cheng, Y.; Hu, Ch. *MOSFET modeling & BSIM3 user's guide*., Springer, **1999**.

[31] Kahng, D.; Atalla, M. *US patents* 3206670 & 3102230, **1960**.

[32] Baumvol, I. J. R. *Surface Science Reports*, **1999**, 36, 1-166.

[33] Sasaki, H.; Ono, M.; Yoshitomi, T.; Ohguro, T.; Nakamura, S.; Saito, M.; Iwai, H. *Electron Devices, IEEE Transactions*, **1996**, 43, 1233-1242.

[34] Robertson, J. *Eur. Phys. J. Appl. Phys*., **2004**, 28, 265-291.

[35] Stoneham, A.M. *Journal of Non-Crystalline Solids*, **2002**, 303, 114–122.
[36] Morita, M.; Ohmi, T.; Hasegawa, E.; Kawakami, M.; Ohwada, M. *J. Appl. Phys.* **1990**, 68, 1272.
[37] Massoud, H. Z.; Poindexter, E. H.; Helms, C. R. *The Physics and Chemistry of* SiO_2 *and the Si|*SiO_2 *Interface*, The Electrochemical Society, Pennington, **1996**.
[38] Pasquarello, A.; Hybertsen, M. S.; Car, R. *Nature*, **1998**, 396, 58.
[39] Schulz, M.; *Nature*, **1999**, 399 729-730.
[40] Tagawa, M.; Ema, T.; Kinoshita, H.; Ohmae, N.; Umeno, M.; Minton, T. K. *Jpn. J. Appl. Phys.*, **1998**, 37, L1455-1457.
[41] Jacobs, D. C. *Annu. Rev. Phys. Chem.*, **2002**, 53, 379–407.
[42] Amirav, A.; Cardillo, M. J.; Trevor, P. L.; Lim, C.; Tully, J. C. *J. Chem. Phys*., **1987**, 87, 1796.
[43] Okada; M. *J. Phys.: Condens. Matter*, **2010**, 22, 263003.
[44] Rabalais, J. W.; Marton, D. *Nucl. Inst. Meth. in Phys. Res.B*, **1992**, 67, 287-295.
[45] Rabalais, J. W. *Low-Energy Ion Surface Interactions*, Wiley, New York, **1994**.
[46] Kisa, M.; Minton, T. K.; Yang, J. C. *J. Appl. Phys.*, **2005**, 97, 23520.
[47] Tagawa, M.; Yokota, K.; Tsumamoto, S.; Sogo, C.; Yoshigoe, A.; Teraoka, Y. *Appl. Phys. Lett.*, **2007**, 91, 033504.
[48] Tagawa, M.; Yokota, K.; Ohmae, N.; Kinoshita, H.; Umeno, M. *Jpn. J.Appl. Phys., Part 1*, **2001**, 40, 6152.
[49] Tagawa, M.; Sogo, C.; Yokota, K.; Yoshigoe, A.; Teraoka, Y.; Shimura, T. *Appl. Phys. Lett.*, **2006**, 88, 133512.
[50] Teraoka, Y.; Yoshigoe, A., *Surf. Sci.* **2002**, 507-510, 797-802.
[51] Yoshigoe, A.; Teraoka, Y. *Surf. Sci.* **2003**, 532-535, 690-697.
[52] Tzvetkov, T.; Qin, X.; Jacobs, D. C. *Phys. Rev. B*, **2003**, 67, 075418.
[53] Caledonia, G. E.; Krech, R. H.; Green, B. D. *AIAA Journal*, **1987**, 25, 59.
[54] Caledonia, G. E.; Krech, R. H.; Green, B. D.; Pirri, A. N. *Source of High Flux Energetic Atoms*, Physical Sciences, Inc., US Patent No, 4894511, **1990**.
[55] Yokota, K.; Tagawa, M.; Kitamura, A.; Matsumoto, K.; Yoshigoe, A.; Teraoka Y. *Appl. Surf. Sci.*,**2009**, 255, 6710-6714.
[56] Kinoshita, H. *Rev. Sci. Inst*., **2008**, 79, 073109.
[57] Troya, D.; Schatz, G. C.; Garton, D. J.; Brunsvold, A. L.; Minton, T. K. *J. Chem. Phys*., **2004**, 120, 731.
[58] Kinoshita, H.; Tagawa, M.; Umeno, M.; Ohmae, N. *Surf. Sci.*, **1999**, 440, 49.
[59] Kisa, M. *Silicon oxidation by atomic and molecular oxygen*, Master Thesis, University of Belgrade, **1998**.
[60] Gusev, E. P.; Lu, H. C.; Gustafsson, T.; Garfunkel, E. *App. Surf. Sci.*, **1996**, *104/105*, 329-334.
[61] Gusev, E. P.; Lu, H. C.; Gustafsson, T.; Garfunkel, E. *Phys. Rev. B*, **1995**, *52*, 1759-1775.
[62] Pasquarello, A.; Stoneham, A. M. *J. Phys.: Condens. Matter*, **2005**,17, V1-V5.
[63] Hayden, O.; Agarwal, R.; Lu, W. *Nanotoday*, **2008**, 3, 5−6.
[64] Bandaru, P. R.; Pichanusakorn, P. *Semicond. Sci. Technol.*, **2010**, 25, 024003.
[65] Ma, D. D. D.; Lee, C. S.; Au, F. C. K.; Tong, S. Y.; Lee, S. T. *Science*, **2003**, 299, 1874.
[66] Trivedi, K.; Yuk, H.; Floresca, H. C.; Kim, M. J.; Hu, W. *Nano Lett.*, **2011**, 11, 1412−1417.
[67] Liu, B.; Wang, Y.; Ho, T.; Lew, K.-K.; Eichfeld, S. M.; Redwing, J. M.; Mayer, T. S.;Mohney, S. E. *J. Vac. Sci. Technol.* A, **2008**, 26.

[68] Peng, K.-Q.; Lee, S.-T. *Adv. Mater.*, **2011**, 23, 198-215.
[69] Konagai, M. *Jpn. J.Appl. Phys.*, **2011**, 50, 030001.
[70] Wanekaya, A. K.; Chen, W.; Myung, N. V.; Mulchandani, A. *Electroanalysis*, **2006**, 18, 533-550.
[71] Chen, K.-I.; Li, B.-R.; Chen, Y.-T. *Nano Today*, **2011**, 6, 131-154.
[72] Schmidt, V.; Wittemann, J. V.; Senz, S.; Go□sele, U. *Adv. Mater.*, **2009**, 21, 2681−2702.
[73] Liu, H. I.; Biegelsen, D. K.; Ponce, F. A.; Johnson, N. M.; Pease, R. F.W. *J. Vac. Sci. Technol.* B, **1993**, 11, 2532.
[74] Wagner, R. S.; Ellis, W. C. *Appl. Phys. Lett.*, **1964**, 4, 89.
[75] Lee, S. T.; Wang, N.; Zhang, Y. F.; Tang, Y. H. *MRS Bull.*, **1999**, 24, 36.
[76] Kolb, F. M.; Hofmeister, H.; Scholz, R.; Zacharias, M.; Gösele, U.; Ma, D. D.; Lee, S. T. J. *Electrochem. Soc.*, **2004**, 151, G472.
[77] Cui, Y.; Zhong, Z.; Wang, D.; Wang, W. U.; Lieber, C. M. *Nano Lett.*, **2003**, 3, 2.
[78] Li Z, Chen Y, Li X, Kamins T I, Nauka K, Williams R S, *Nano Lett.*, **2004**, 4, 245.
[79] Patolsky, F.; Zheng, G. F.; Lieber, C.M. *Nat. Protoc*., **2006**, 1, 1711.
[80] Duan, X.; Niu, C.; Sahi, V.; Chen, J.; Parce, S.; Empedocles, S.; Goldman, J. L. *Nature*, **2003**, 425, 274.
[81] van de Walle, C. G.; Northrup, J. E. *Phys. Rev. Lett*., **1993**, 70, 1117-1119.
[82] Kao, D.–B.; McVittie, J. P.; Nix, W. D.; Saraswat, C. K. *IEEE Tran. Elec. Dev.*, **1988**, 35, 25-37.
[83] Dalla Torre, J.; Bocquet, J.-L.; Limoge, Y.; Crocombette, J.-P.; Adam, E.; Martin, G. *J. Appl. Phys.*, **2002**, 92, 2.
[84] Fazzini, P.-F.; Bonafos, C.; Claverie, A.; Hubert, A.; Ernst, T.; Respaud, M. *J. Appl. Phys,*. **2011**, 110, 033524.
[85] Chen, Y. *Modeling of the Self-Limiting Oxidation for Nanofabrication of Si* in: Technical Proceedings of the Third International Conference on Modeling and Simulation of Microsystem; San Diego, CA, March 27-29, **2000**.
[86] Goldberger, J.; Hochbaum, A. I.; Fan, R.; Yang, P. *Nano Lett.*, **2006**, 6, 2006.
[87] Büttner, C. C.; Zacharias, M. *Appl. Phys. Lett*., **2006**, 89, 263106.
[88] Shir, D.; Liu, B. Z.; Mohammad, A. M.; Lew, K. K.; Mohney S. E. *J. Vac. Sci. Technol. B,* **2006**, 24.
[89] Bondi, R. J.; Lee, S.; Hwang, G. S. *ACS Nano*, **2011**, 5, 1713-1723.
[90] Judge, J. S. *J. Electrochem. Soc.*, **1971**, 118, 1772-1775.
[91] van der Heide, P. A. M.; Baan Hofman, M. J.; Ronde, H. J. *J. Vac. Sci. Technol.*, **1989**, A7, 1719-1723.
[92] Magyar, J.; Sklyarov, A.; Mikaylichenko, K.; Yakovlev, V. *Appl. Surf. Sci.,* **2003**, 207, 306–313.
[93] Krylyuk, S.; Davydov, A. V.; Levin, I.; Motayed, A.; Vaudin, M. D. *Appl. Phys. Lett.*, **2009**, 94, 063113.
[94] Liu, J. L.; Lu, Y.; Shi, Y.; Gu, S. L.; Jiang, R. L.; Wang, F. ; Bu, H. M.; Zheng, R. L. *J. Phys. Stat. Sol.*, **1998**, 168, 441.
[95] http://hal.inria.fr/docs/00/64/36/17/PDF/understanding_self_limited_oxidation_effect.pdf
[96] Jorgensen, W. L.; Tirado-Rives, J. *J. Phys. Chem.*, **1996**, 100, 14508.
[97] Sickafus, K.E.; Kotomin, E.A. *Radiation Effects in Solids*, Spring, NATO Publishing Unit, Dordrecht, The Netherlands, **2005**.
[98] Alder, B. J.; Wainwright, T. E.; *J. Chem. Phys*., **1957**, 27, 1207-1208.
[99] Car, R.; Parrinello, M. *Phys. Rev. Lett.*, **1985**, 55, 2471.
[100] Schrödinger, E. *Ann. Physik* , **1926**, 79, 361–377.

[101] Born, M.; Oppenheimer, R. *Ann. Physik*, **1927**, 84, 457.

[102] Neyts, E. *Mathematical Simulation of the Deposition of Diamond-like carbon (DLC) films*. PhD thesis, University of Antwerp, Antwerp, **2006**.

[103] Verlet, L. *Physical Review*, **1967**, 159, 98–103.

[104] Fincham, D., Heyes, D. M *CCP5 Quarterly*, 1982, 6, 4-10.

[105] Hockney, R. M. *Meth. Com. Phys.*,**1970**, 9, 136-211.

[106] Swope, W. C.; Andersen, H. C.; Berens, P. H.; Wilson, K. R. *J. Chem. Phys.*, **1982**, 76, 637-649.

[107] people.virginia.edu/~lz2n/mse627/notes/Boundary.pdf

[108] Adelman, S. A.; Doll, J. D. *Chem. Phys. Lett.*,**1982**, 90, 215.

[109] Rahimi, M.; Karimi-Varzaneh, H. A.; Böhm, M. C.; Müller-Plathe, F.; Pfaller, S.; Possart, G.; Steinmann, P. *J. Chem. Phys.*, **2011**, 134, 154108.

[110] Born, M.; Von Karman, Th. *Physik. Z.*, **1912**, 13, 297-309.

[111] Allen, M. P.; Tildesley, T. J. *Computer simulations of liquids,* Clarendon Press, Oxford, **1987**.

[112] Leach, A. R. *Molecular Modeling: principles and application*, 2nd ed. Prentice Hall, England **2001**.

[113] Berendsen, H. J. C.; Postma, J. P. M.; van Gunsteren, W. F.; Di Nola, A.; Haak, J. R. *J.Chem. Phys.*, **1984**, 81, 3684-3690.

[114] Anderson, H. C. *J. Chem. Phys.*, **1983**, 72, 2384-2393.

[115] Nosé, S. *Mol. Phys.*, **1984**, 53, 255-268.

[116] Hoover, W. G. *Phys. Rev. A*, **1985**, 31, 1695-1697.

[117] Bussi, G.; Donadio, D.; Parinello, M. *J. Chem. Phys.*, **2007**, 126, 014101.

[118] Cole, D. *Surface Chemistry and Adhesive Properties of Oxidised Si surfaces*, PhD Thesis, Queens' College, University of Cambridge, **2007**.

[119] Stillinger, F. H.; Weber, T. A. *Phys. Rev. B*, **1985**, 31, 5262-5271.

[120] Stillinger, F. H.; Weber, T. A. *J. Chem. Phys. B*, **1988**, 88, 5123-5133.

[121] Watanabe, T.; Fujiwara, H.; Noguchi, H.; Hoshino, T.; Ohdomari, I. *Jpn. J. Appl. Phys.*, **1999**, 38, L366.

[122] Tersoff, J. *Phys. Rev. Lett.*, **1986**, 56, 632-635.

[123] Tersoff, J. *Phys. Rev. B*, **1989**, 39, 5566-5568.

[124] Bazant, M. Z.; Kaxiras, E. *Phys. Rev. Lett.*, **1996**, 77, 4370.

[125] Justo, J. F.; Bazant, M. Z.; Kaxiras, E.; Bulatov, V. V.; Yip, S. *Phys. Rev*. B, **1998**, 58, 2539.

[126] Muralidharan, K.; Cao, C.; Wan, Y-X.; Runge, K.; Cheng, H.-P. *Chem. Phys. Lett.*, **2007**, 437, 92–98.

[127] Flikkema, E.; Bromley, S. T. *Chem. Phys. Lett.*, **2003**, 378 622–629.

[128] van Duin, A. C. T.; Dasgupta, S.; Lorant, F.; Goddard III, W. A. *J. Phys. Chem. A*, **2001**, 105, 9396-9409.

[129] van Duin, A. C. T.; Strachan, A.; Stewman, S.; Zhang, Q.; Xu, X.; Goddard III, W. A. *J. Phys. Chem. A*, **2003**, 107, 3803-3811.

[130] Buehler, M. J. *J. Comput. Theor. Nanosci.*, **2006**, 3, 603-623.

[131] Chenoweth, K.; van Duin, A. C. T.; Goddard III, W. A. *J. Phys. Chem. A*, **2008**, 112 1040-1053.

[132] Neyts, E. C.; Shibuta, Y.; van Duin, A. C. T.; Bogaerts A. *ACS Nano*, **2010**, 4, 6665-6672.

[133] Neyts, E. C.; van Duin, A. C. T.; Bogaerts A. *J. Am. Chem. Soc.*, **2011**, 133, 17225-17231.

[134] Neyts, E. C.; van Duin, A. C. T.; Bogaerts A. *J. Am. Chem. Soc.*, **2012**, 134, 1256-1260.

[135] Valentini, P.; Schwartzentruber, T. E.; Cozmuta, I. *J. Chem. Phys.*, **2010**, 133, 084703.

[136] Mueller J. E.; van Duin A. C. T.; Goddard III, W. A. *J. Phys. Chem. C*, **2010**, 114, 5675-5685.

[137] Buehler, M.J.; van Duin, A.C.T.; Goddard III, W. A. *Phys. Rev. Lett.*, **2006**, 96, 095505.

[138] Ning, N.; Calvo, F.; van Duin, A. C. T.; Wales, D. J.; Vach, H. *J. Phys. Chem. C*, **2009**, 113, 518-523.

[139] Khalilov, U.; Neyts, E.C.; Pourtois, G.; van Duin, A.C.T. *J. Phys. Chem. C*, **2011**, 115, 24839–24848.

[140] Khalilov, U.; Pourtois, G.; van Duin, A.C.T.; Neyts, E.C. *Chem. Mater*., **2012**, 24, 2141–2147.

[141] Fogarty, J.C.; Aktulga, H.M.; Grama, A. Y.; van Duin, A.C.T.; Pandit, S. *J. Chem. Phys.*, **2010**, 132, 174704.

[142] Rahaman, O.; van Duin, A.C.T.; Goddard III, W.A.; Doren, D.J. *J. Phys. Chem. B*, **2011**, 115, 249-261.

[143] Monti, S.; van Duin, A.C.T.; Kim, S.Y.; Barone, V. *J. Phys. Chem. C*, **2012**, 116, 5141-5150.

[144] Abolfath, R. M.; van Duin, A. C. T.; Brabec, T. *J. Phys. Chem. A*, **2011**, 115, 11045.

[145] de Vos Burchart, E. *Studies on Zeolites: Molecular Mechanics, Framework Stability, and Crystal Growth*. PhD Thesis, Delft University of Technology, Delft, The Netherlands, **1992**.

[146] Mortier, W. J.; Ghosh, S. K.; Shankar, S. J. *J. Am. Chem. Soc.*, **1986**, 108, 4315.

[147] http://www.charmm.org

[148] Nomura, K.; Kalia, R. K.; Nakano, A.; Vashista, P., van Duin, A. C. T.; Goddard III, W.A. *Phys. Rev. Lett.*, **2007**, 99, 148303.

[149] Vashista, P.; Kalia, R. K.; Nakano, A. *J. Phys. Chem.* B, **2006**, 110, 3727-3733.

[150] Engstrom, J. R.; Engel, T. *Phys. Rev B*, **1990**, 41, 1038-1041.

[151] Engstrom, J. R.; Nelson, M. M.; Engel, T. *J. Vac. Sci. Technol. A*, **1989**, *7*, 1837-1840.

[152] Engel, T. *Surf. Sci. Rep.* **1993**, 18, 91-144.

[153] Watanabe, H.; Kato, K.; Uda, T.; Fujita, K.; Ichikawa, M.; Kawamura, T.; Terakura, K. *Phys. Rev. Let.*, **1998**, 80, 345-348.

[154] Ferguson, B. A.; Reeves, C. T.; Mullins, C. B. *J. Chem. Phys.*, **1999**, 110, 11574-11584.

[155] Miyake, T.; Soeki, S.; Kato, H.; Nakamura, T.; Namiki, A.; Kamba, H.; Suzaki, T. *Phys. Rev B*, **1990**, *42*, 11801-11807.

[156] Hoshino, T.; Tsuda, M.; Oikawa, S.; Ohdomari, I. *Phys. Rev. B*, **1994**, 50, 14999-15008.

[157] Kato, K.; Uda, T. *Phys. Rev B*, **2000**, 62, 15978-15988.

[158] Mazzone, A. M. *Eur. Phys. J. B*, **2003**, 35, 125-132.

[159] Osipov, A. V.; Patzner, P.; Hess, P. *Appl. Phys. A*, **2006**, 82, 275-280.

[160] Massoud, H. Z. *Microelectronic Engineering*, **1995**, 28, 109-116.

[161] Quinteros, C. L.; Tzvetkov, T.; Jacobs, C. C. *J. Chem. Phys.*, **2000**, 113, 5119-5121.

[162] Stefanov, B.; Raghavachari, K. *Surf. Sci.*, **1997**, 389, L1159-L1164.

[163] Neyts, E. C.; Khalilov, U.; Pourtois, G.; van Duin, A. C. T. *J. Phys. Chem. C*, **2011**, 115, 4818–4823.

[164] Dereli, G.; Yalabik, M. C.; Ellialtioglu, S. *Physica Scripta*, **1989**, 40, 117-121.

[165] Timonova M.; Groenewegen J.; Thijsse B. J. *Phys. Rev. B*, **2010**, 81, 144107.

[166] Loferski J.; Rappaport, P. *Phys. Rev.*, **1958**, 111, 432-439.

[167] Corbett J. W.; Watkins, G. D. *Phys. Rev.*, **1965**, 138, A555-A560.

[168] Hemment, P.; Stevens, P. *J. Appl. Phys.*, **1969**, 40, 4893-4901.

[169] Rabalais, J. W. *Low Energy Ion-Surface Interactions*, Wiley, Chester, **1994**.

[170] Holmström, E.; Kuronen, A.; Nordlund, K. *Phys. Rev. B*, **2008**, *78*, 045202.

[171] International Technology Roadmap for Semiconductors **2010** edition (http://www.public.itrs.net/).

[172] Massoud, H. Z.; Plummer, J. D.; Irene, E. A. *J. Electrochem. Soc.*, **1985**, 132, 1745.

[173] Cerofolini, G. F.; Mascolo, D.; Vlad, M. O. J. Appl. Phys., **2006**, 100, 054308.

[174] Elovich, S. J. *Proceedings of the Second International Congress on Surface Activity, ed. by Schulman JH, Academic Press, Inc, New York*, **1959**, 11, 253.

[175] McLintock, I. S. *Nature,* **1967**, 216, 1204-1205.

[176] Atkinson, R. J.; Hingston, F. J.; Posner, A. M.; Quirk, J. P. *Nature,* **1970**, 226, 148-149.

[177] Ganster, P.; Treglia, G.; Saul, A. *Phys. Rev. B,* **2010**, 81, 045315.

[178] Murad, E. *J. Spacecr. Rockets,* **1996**, 33, 131.

[179] Kageshima, H.; Shiraishi, K. *Phys. Rev. Lett.*, **1998**, 81, 5936-5939.

[180] Kato, K.; Uda, T.; Terakura, K. *Phys. Rev. Lett.*, **1998**, 80, 2000.

[181] Oh, J. H.; Nakamura, K.; Ono, K. ; Oshima, M.; Hirashita, N.; Niwa, M.; Toriumi, A.; Kakizaki, A. *J. Elec. Spec. and Rel. Phen.*, **2001**, 114-116, 395-399.

[182] Tu, Y.; Tersoff, J. *Phys. Rev. Lett.*, **2000**, 84, 4393.

[183] Bongiorno, A.; Pasquarello, A. *Mat. Sci. and Eng. B*, **2002**, 96, 102-106.

[184] van Ginhoven, R. M.; Hjalmarson, H. P. *NIM B.*, **2007**, 255, 183-187.

[185] Stoneham, A. M.; Szymanski, M. A.; Shluger, A. L. *Phys. Rev. B,* **2001**, 63, 221304-07.

[186] Ng, Kwok-On; Vanderbilt, David *Phys. Rev. B*, **1999**, 59, 10132-10137.

[187] Newton, M. D.; Gibbs, G. V. *Phys. Chem. Minerals*, **1980**, 6, 221.

[188] Irene, E. *Solid-State Electronics,* **2001**, 45, 1207-1217.

[189] Pasquarello, A.; Hybertsen, M.; Car, R. *Appl. Surf. Sci.*, **1996**, 104/105, 317-322.

[190] Mozzi, R. L.; Warren, B. E. *J. Appl. Crystall.*, **1969**, 2, 164-172.

[191] Bakos, T.; Rashkeev, S. N.; Pantelides, S. T. *Phys. Rev. Lett.*, **2002**, 88, 5, 055508.

[192] Watanabe, T.; Tatsumura, K.; Ohdomari, I. *Appl. Surf. Sci.*, **2004**, 237, 125-133.

[193] Mauri, F.; Pasquarello, A.; Pfrommer, B. G.; Yoon, Y.-G.; Louie, S. G. *Phys. Rev. B*, **2000**, 62, 4786-4789.

[194] Pantalides, S.T. *The Physics of* SiO_2 *and its Interfaces,* Pergamon, **1978**.

[195] Green, M.A. *Third Generation Photovoltaics: Advanced Solar Energy Conversion,* 2nd ed., Springer, Berlin, **2005**.

[196] Ourmazd, A.; Taylor, D. W.; Rentschler, J. A.; Bevk, J. *Phys. Rev. Lett.*, **1987**, 59, 213.

[197] Grunthaner, F. J; Grunthaner, P. J *Chemical and Electronic Structure Of* SiO_2 *interface,* North Holland - Amsterdam, **1986**.

[198] Rabedeau, T. A.; Tidswell, I. M.; Pershan, P. S.; Bevk, J.; Freer, B. S. *Phys. Rev. Lett.*, **1991**, 59, 706.

[199] Himpsel F. J.; McFeely, F. R.; Taleb-Ibrahimi, A.; Yarmoff, J. A.; Hollinger, G. *Phys. Rev. B*, **1988**, 38, 6084.

[200] Ohdomari, I.; Akatsu, H.; Yamakoshi, Y.; Kishimoto, K. *J. Non-Cryst. Solids,* **1987**, 89, 239-248.

[201] Pasquarello, A.; Hybertsen, M.; Car, R. *Phys. Rev. Lett.*, **1995**, 74, 1024.

[202] Oh, J. H.; Yeom, H. W.; Hagimoto, Y.; Ono, K.; Oshima, M.; Hirashita, N.; Nywa, M.; Toriumi, A.; Kakizaki, A. *Phys. Rev. B*, **2001**, 63, 205310.

[203] Orellana, W.; Antonio, J. R.; da Silva; Fazzio A. , J. *Phys. Rev. Lett.*, **2003**, 90, 016103.

[204] Khalilov, U.; Pourtois, G.; van Duin, A. C. T.; Neyts, E. C. *J. Phys. Chem. C,* **2012**, 116, 8649–8656.

[205] Khalilov, U.; Pourtois, G.; van Duin, A. C. T. ; Neyts, E. C. *J. Phys. Chem. C*, **2012**, 116, 21856–21863.

[206] Ohta, H.; Watanabe, T.; Ohdomari, I. *Jpn. J. Appl. Phys*., **2007**, 46, 3277-3282.

[207] Hollinger, G.; Himpsel, F. J. *Appl. Phys. Lett.*, **1984**, 44, 93.

[208] Grunthaner, P. J.; Hecht, M. H.; Grunthaner, F. J.; Johnson, N. M. *J. Appl. Phys.*, **1987**, 61, 629.

[209] Derrien, J.; Commandre, M. *Surf. Sci.*, **1982**, 118, 32-46.

[210] Giustino, F. *Infrared Properties of the Si-SiO$_2$ Interface from First Principles*, PhD thesis, Lausanne, EPFL, **2005**.

[211] Mao, L.-F.; Yao, Y.; Wei, J.-L.; Zhang, Xu, M.-Z.; Tan, C.-H. *Microelectronics Reliability*, **2001**, 41, 1903-1907.

[212] Hayashi Y.; Hasunuma, R.; Kikuo, Y. *Key Engineering Materials*, **2011**, 470, 110-116.

[213] Cundiff, S. T.; Knox, W. H.; Baumann, F. H.; Evans-Lutterodt, K. W.; Tang, M. T.; Green, M. L.; van Driel, H. M. *Appl. Phys. Lett.*, **1997**, 70, 1414-1416.

[214] Da Silva, J.; Pinatti, D.; Anderson, C.; Rudee, M. *Philos. Mag.*, **1975**, 31, 713.

[215] Stefanov, B. B.; Gurevich, A. B.; Weldon, M. K.; Raghavachari, K.; Chabal, Y. J. *Phys. Rev. Lett.*, **1998**, 81, 3908-3911.

[216] Yang, T.-C.; Saraswat, K. C. *IEEE Trans. Elect. Dev.*, **2000**, 47, 746-755.

[217] Murray, P.; Carey, G. F. *J. Appl. Phys.*, **1989**, 65, 3667-3670.

[218] Korkin, A.; Greer, J. C.; Bersuker, G.; Karasiev, V. V.; Bartlett, R. J. *Phys. Rev. B*, **2006**, 73, 165312.

[219] Daruka, I.; Barabási, A.-L.; Zhou, S. J.; Germann, T. C.; Lomdahl, P. S.; Bishop, A. R. *Phys. Rev. B*, **1999**, 60, R2150-R2153.

[220] Donnadieu, P.; Blanquet, E.; Jakse, N.; Mur, P. *Appl. Phys. Lett.*, **2004**, 85, 5574.

[221] Liu, H. I.; Biegelsen, D. K.; Johnson, N. M.; Ponce, F. A.; Pease, R. F. W. *J. Vac. Sci. Technol. B*, **1993**, 11, 6.

[222] Ferguson, B. A.; Reeves, C. T.; Mullins, C. B. *J. Chem. Phys.* **1999**, 110, 11574-11577.

[223] Hamann, D. R. *J. Phys. Rev. Lett.*, **1998**, 81, 3447-3450.

[224] Kajihara, K.; Miura, T.; Kamioka, H.; Aiba, A.; Uramoto, M.; Morimoto, Y.; Hirano, M.; Skuja, L.; Hosono, H. *Journal of Non-Crystalline Solids*, **2008**, 354, 224-232.

[225] Bongiorno, A.; Pasquarello, A. *J. Mat. Sci.*, **2005**, 40, 3047-3050.

[226] Stoneham, A. M.; Grovenor, C. R. M.; Carezzo, A. *Philos. Mag. B*, **1985**, 55, 201-10.

[227] Uematsu, M.; Kageshima, H.; Shiraishi, K. *Comp. Mat. Sci*., **2002**, 24, 229-234.

[228] Massoud, H. Z. *Solid-State Elect.*, **1997**, 41, 929–934.

[229] Büttner, C. C.; Zacharias, M. *Appl. Phys. Lett.*, **2006**, 89, 263106.

[230] Konagai, M *Jpn. J. Appl. Phys*., **2011**, 50, 030001.

[231] Khalilov, U.; Pourtois, G.; van Duin, A. C. T.; Neyts, E. C. *Nanoscale*, **2013**, 5, 719–725.

[232] Okumura, I. "*On the stress field in orthogonal curvilinear coordinates,*" Memoirs of the Kitami Institute of Technology, **2000**, 32, 51–65.

[233] Denn, M. M. *Process Fluid Mechanics*, Englewood Cliffs, NJ: Prentice-Hall, **1980.**